SLAC-417
SLAC/SSRL-0027
UC-411, 413
(SSRL-M)

NUCLEAR DYNAMICAL DIFFRACTION USING SYNCHROTRON RADIATION*

Dennis Eugene Brown

Stanford Linear Accelerator Center
Stanford Synchrotron Radiation Laboratory
Stanford University, Stanford, California 94309

May 1993

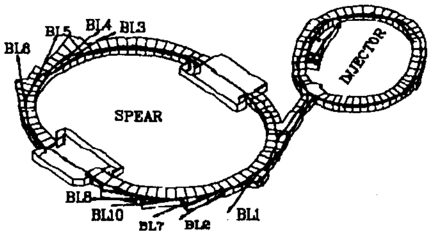

Prepared for the Department of Energy under contract number DE-AC03-76SF00515

Printed in the United States of America. Available from the National Technical Information Service, U.S. Department of Commerce, 5285 Port Royal Road, Springfield, Virginia 22161

---

* Ph.D. thesis

This thesis is dedicated to Mom and Dad:

Joyce and Isaiah Brown

ABSTRACT

The scattering of synchrotron radiation by nuclei is extensively explored in this thesis. From the multipole electric field expansion resulting from time-dependent nonrelativistic perturbation theory, a dynamical scattering theory is constructed. This theory is shown, in the many particle limit, to be equivalent to the semi-classical approach where a quantum mechanical scattering amplitude is used in the Maxwell inhomogeneous wave equation. The Mössbauer specimen whose low-lying energy levels were probed is a ferromagnetic lattice of ^{57}Fe embedded in a yttrium iron garnet (YIG) crystal matrix. The hyperfine fields in YIG thin films were studied at low and room temperature using time-resolved quantum beat spectroscopy. Nuclear hyperfine structure quantum beats were measured using a fast plastic scintillator coincidence photodetector and associated electronics having a time resolution of 2.5 nsec. The variation of the quantum beat patterns near the Bragg [0 0 2] diffraction peak gave a Lamb-Mössbauer factor of 8.2 ± 0.4 . Exploring characteristic dynamical features in the higher order YIG [0 0 10] reflection revealed that one of the YIG crystals had bifurcated into two different layers. The dynamics of nuclear superradiance was explored. This phenomenon includes the radiative speedup exhibited by a collective state of particles, and, in striking concurrence, resonance frequency shifts. A speedup of a factor of 4 in the total decay rate and a beat frequency shift of $1\frac{1}{2}$ natural resonance linewidths were observed. Nuclear resonance scattering was also found to be a useful way of performing angular interferometry experiments, and it was used to observe the phase shift of a rotated quantum state. On the whole, nuclear dynamical diffraction theory has superbly explained many of the fascinating features of resonant magnetic dipole radiation scattered by a lattice of nuclei.

ACKNOWLEDGMENTS

I wish to thank all the members of the nuclear resonance scattering group at the Stanford Synchrotron Radiation Laboratory (SSRL) for their help in making this research possible. I give special thanks to George Brown, my research advisor, for giving me the opportunity to do this thesis. I greatly appreciate his tireless, diplomatic efforts that lead to doing experiments on PEP and on SPEAR (whose arms he had to twist to obtain special timing mode runs on SPEAR are unknown, but hopefully his efforts will have contributed to making timing mode operations a necessary feature on all synchrotrons). I also must thank John Arthur for all the help he provided me throughout my project--he had an unerring, keen insight into understanding the multitude of interesting physical phenomena and puzzles frequently faced by the nuclear scattering group. I also must thank Stan Ruby for the wealth of ideas he provided me--he had a seemingly uncanny ability to come up with fascinating, novel ideas in fundamental physics almost weekly. I also thank Alfred Baron for many thoughtful discussions and for trudging through portions of this thesis paper and correcting some of the formulas in the text.

I give thanks and praise to the members of the staff at SSRL (such as Arthur Bienenstock for allowing timing mode runs on SPEAR, Sean Brennan for his SUPER 4-circle diffractometer program and his database of Cromer and Liberman's electronic scattering factors, Teresa Troxel for initial beamline support, Glen Kerr and Pierre Capeder for electronics support, and Hans Przybylski and Chuck Troxel, Jr. who were machine shop wizards at constructing the precision apparatus needed to do crystal diffraction experiments, and to many others), at SLAC (such as Burt Richter for allowing parasitic synchrotron user runs on PEP during high energy physics runs), and at CHESS (such as Bob Batterman who provided a bright and dilligent grad student, Sarvjit Shastri, to collaborate with during a run on CESR). I also thank Gopal Shenoy and Ercan Alp from Argonne National Labs for their collaborative help during initial nuclear resonance scattering experiments on SPEAR. I thank Dr. D. M. Gualtieri from the Electronic Materials and Devices Lab at Allied-Signal and William Lavender for the preparation and construction of the ^{57}Fe-enriched YIG crystals used in this thesis.

From the Stanford Physics Department, I am greatly indebted to Fanny VanBuren for her esteemed advice and precious help during my initial, unsteady years at Stanford. Her abrupt departure from the physics administration is a truly incalculable loss to the Stanford Physics Department and to future physics grad students.

Support for this research was provided by the U.S. Department of Energy, Office of Basic Energy Science, Division of Materials Sciences.

TABLE OF CONTENTS

Table of Contents

LIST OF TABLES

LIST OF ILLUSTRATIONS

List of Illustrations

List of Illustrations

NUCLEAR DYNAMICAL DIFFRACTION USING SYNCHROTRON RADIATION

1. INTRODUCTION

The field of nuclear resonance fluorescence has developed considerably since Kuhn initiated the first search for this phenomena in 1929.[1] In the late 1950's, a variety of techniques were developed to probe the low-lying energy levels of nuclei. One method used Coulomb-excitation reactions where nuclei were excited by the electromagnetic fields of bombarding particles[2,3] (this later developed into the field of perturbed angular correlations[4]). Another method used nuclear reactions as a gamma ray source for exciting nuclei.[5,6] However, it was Mössbauer's discovery in 1958 of the recoil free resonance absorption of nuclei excited by radioactive sources that enabled the field of nuclear resonance fluorescence to blossom and to become useful in a wide variety of disciplines, ranging from biology to chemistry and physics.[7]

The construction of man-made x-ray sources provided a new way to excite nuclear transitions. Use of betatron bremsstrahlung radiation as an x-ray source was first proposed in 1945,[8] but it was not until 1962 that nuclear fluorescence radiation was observed using a conventional x-ray tubes as a source.[9] The problem of detecting the nuclear signal resulted mainly from the huge photoelectric background that occurred when x-rays were simultaneously scattered from the electrons. For this reason, pulsed x-ray sources and time-gated detectors were proposed.[9] Because electrons scatter x-rays promptly compared to nuclear lifetimes, properly gating out the effects due to electronically scattered x-rays leaves the nuclear signal with almost no background. The pulsed nature of synchrotron storage rings made them highly desirable candidates as x-ray sources for exciting nuclei. The first proposal for using synchrotron x-rays was made in 1974,[10] and the first observation of nuclear fluorescence radiation using synchrotron x-rays was made in 1978.[11]

In this first experiment, an iron foil was used in reflection geometry as a target, and the foil was enriched with ^{57}Fe to enhance the nuclear resonance signal. The experiment was performed on a bending magnet beamline which produced, when using a silicon monochromator having a 2 eV wide bandpass, roughly 10^9 electronically scattered photons for each nuclear scattered photon. Since the gating method was not completely effective, background problems produced serious difficulties limiting the usefulness of this technique. Crystals were introduced to further suppress the electronic background. For certain crystals, the ^{57}Fe ferromagnetic or antiferromagnetic lattice is distinct from the electronic lattice. This allows, for certain crystal orientations, the electronic reflection to be forbidden while the nuclear reflection is still allowed. The first observations of nuclear scattered radiation from perfect crystals using synchrotron x-rays were made in the early and mid 1980's.[12,13] Since then, many nuclear resonance fluorescence experiments have followed at synchrotron radiation facilities to explore the dynamics of nuclear diffraction from crystals.[14-19]

The question usually arises as to why should one use multi-million dollar synchrotron storage rings to do Mössbauer experiments when much cheaper radioactive sources costing a few hundred dollars can be used. For instance, Bragg diffraction off polycrystalline materials using radioactive sources was observed more than two decades earlier in 1960 and off perfect crystals in 1969.[20,21] As described earlier, what makes synchrotron storage rings useful is the pulsed nature of the photons. This allows one to use gated photodetectors and electronics to reduce the electronic background. Also, unlike a radioactive source, the energy bandwidth of the synchrotron radiation is much larger than the nuclear energy bandwidth. This allows all resonant nuclear hyperfine lines to be excited, and results in nuclear hyperfine quantum beats that reveal information about the internal hyperfine fields and the collective nature of the excitation. And, unlike synchrotron sources, time-resolved resonance fluorescence experiments using radioactive sources require deconvoluting out the time response of the source which can significantly alter the resonance signal from the target. Also, synchrotron radiation can provide radiation over a broad range of energies which, with present day undulators and wigglers, can be up to 50 keV. The design of longer, high powered, undulators and wigglers can extend this energy range up to 250 keV,[22] thus making it feasible to perform experiments with most types of Mössbauer samples. Also, synchrotron rings provide linearly polarized beams of x-rays that can be used for doing polarization sensitive experiments.

However, a radioactive source can produce many more resonant photons than present day synchrotrons. For instance, a readily obtainable ^{57}Co source having a strength of 250 mCi produces about 10^{10} resonant photons/sec. However, these photons radiate into 4π steradians, so a better measure of photon production is spectral brilliance--the number of photons per second per square millimeter of source size per square milliradian of photon beam size per 0.1% frequency bandwidth. A 250 mCi source having an emission area of $1\,\mathrm{mm}^2$ produces about $250\,\mathrm{photons/sec\cdot mm^2\cdot mrad^2}$. For an energy bandwidth of

$$\Delta E/E = 4.67\times10^{9}\,\mathrm{eV}/14413\,\mathrm{eV} \approx 3\times10^{-13},$$

the spectral brilliance is about $10^{12}\,\mathrm{photons/sec\cdot mm^2\cdot mrad^2}(0.1\%\ \mathrm{bandwidth})$. Examining Fig. 1-1, the brilliance of radioactive sources is better than x-ray tubes, but is

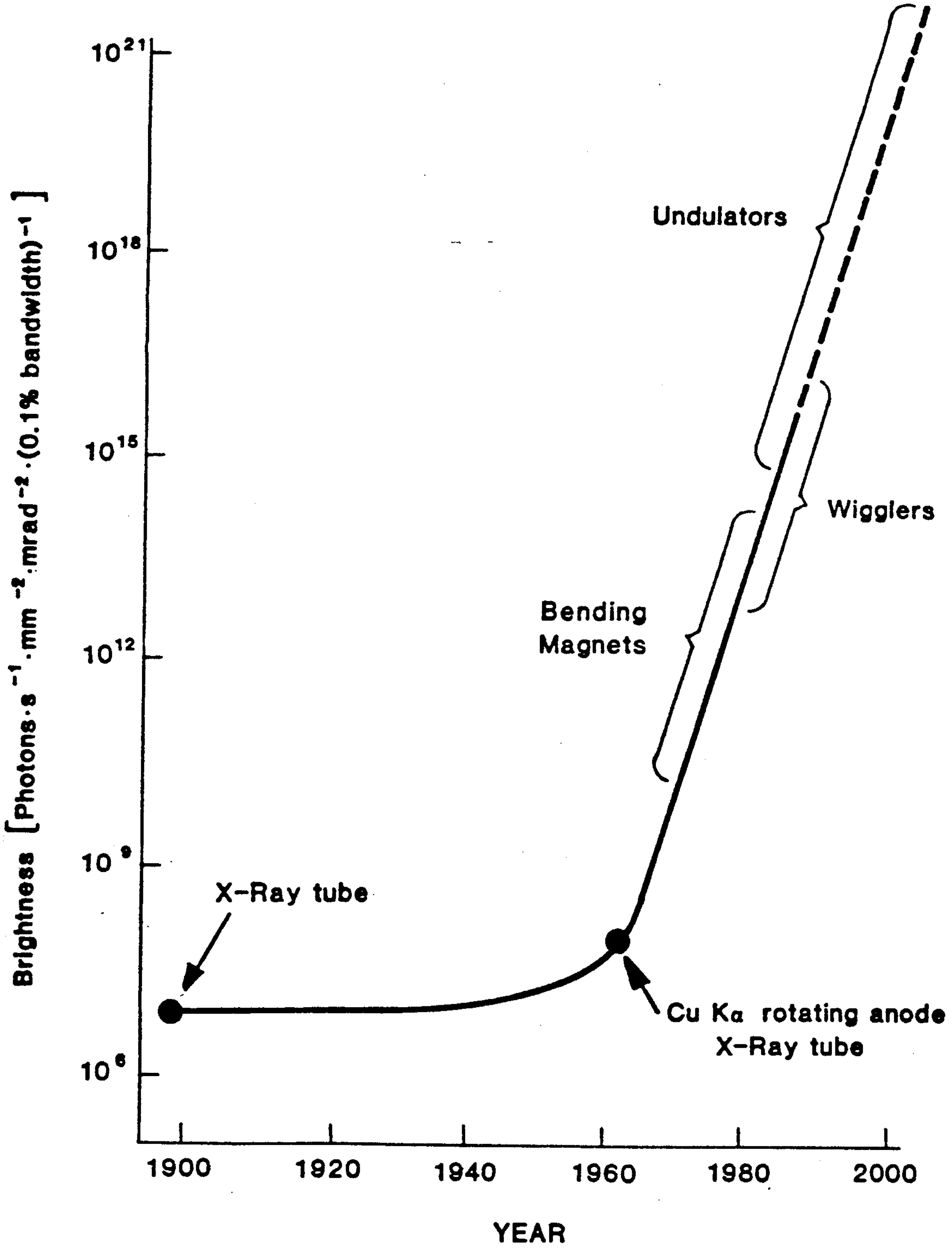

Fig. 1-1. Exponential increase in the spectral brilliance from man-made sources of x-rays. Free electron lasers (FELs) currently in the design phase are estimated to yield a spectral brilliance on the order of 10^{31}. In comparison, the strongest radioactive sources yield a spectral brilliance on the order of 10^{12}. (Reprinted with permission from H. Winick)[23]

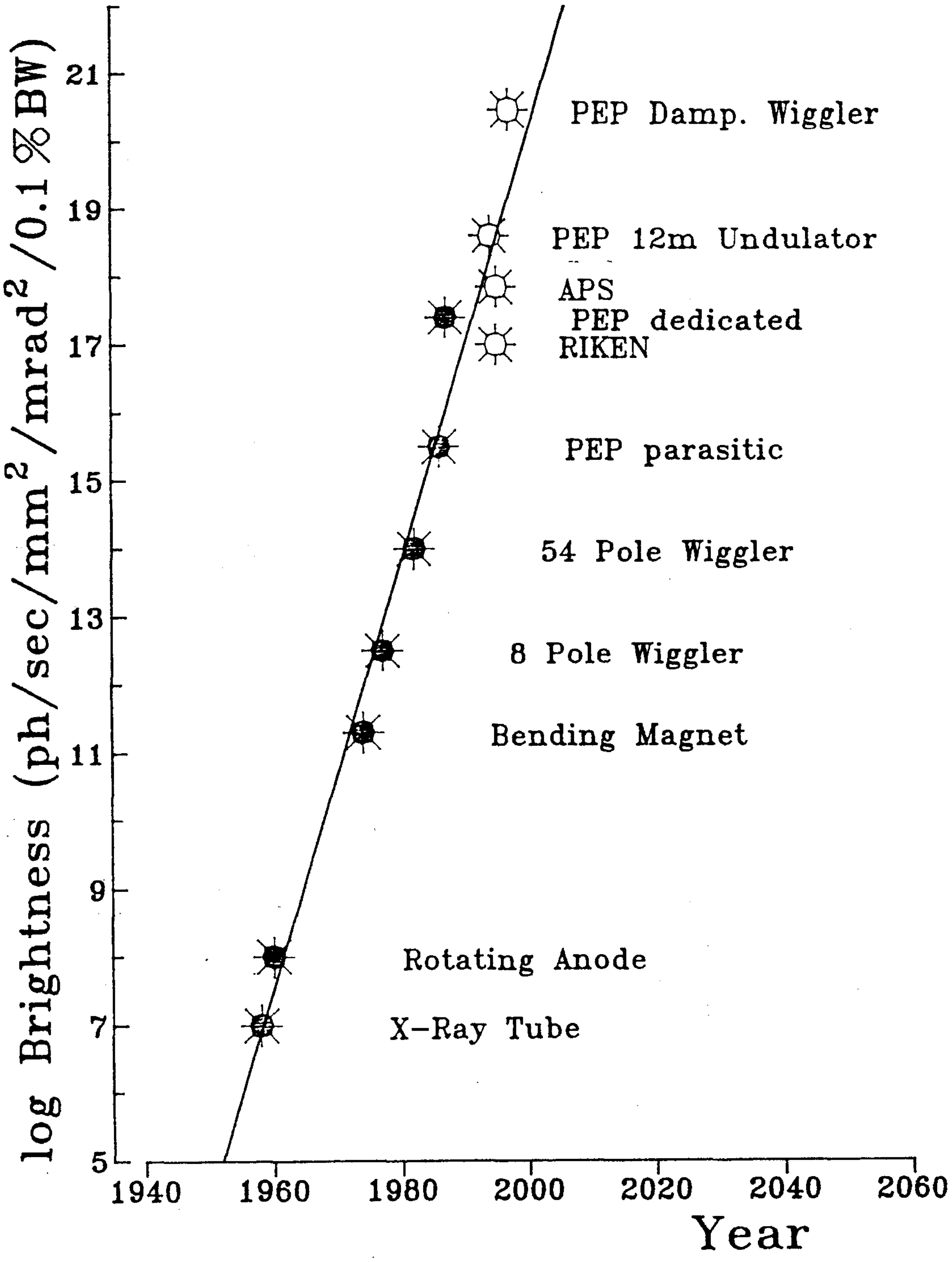

Fig. 1-2. Optimistic 1988 forcast of the spectral brilliance from the PEP synchrotron ring. The bending magnet and the 8 and 54 pole wigglers are insertion devices on the SPEAR ring. PEP parasitic and dedicated were calculated using a 2 m undulator. The open circles are proposed operations which never came about, and PEP was never run in a dedicated mode at 14 GeV. For the experiments completed in this thesis project, PEP was operated in a colliding beam optics mode (parasitic running), and a 2 meter undulator was used. (Reprinted with permission from H. Wiedemann)[24]

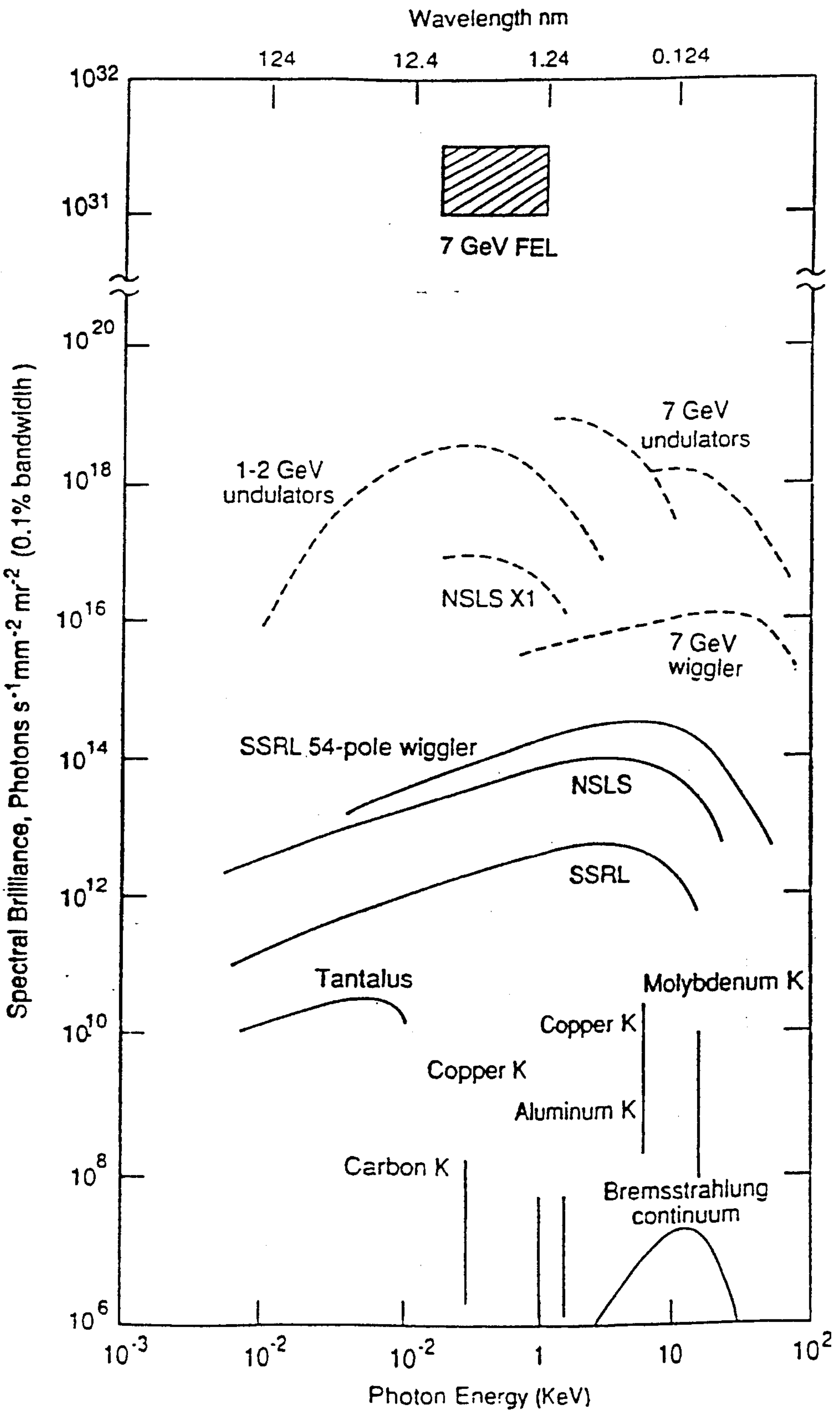

Fig. 1-3. Spectral brilliance curves for various x-ray sources. Note the break of 11 orders of magnitude in the chart to include the FEL results. (Reprinted with permission from K.-J. Kim)[25]

only comparable with synchrotron beamlines having bending magnet sources. However, when wigglers and undulators are used, dramatic increases in the brilliance many orders of magnitude greater than radioactive sources can be achieved, thus making synchrotron sources much more desirable than radioactive sources.

In this thesis, synchrotrons having wiggler and undulator devices were used for the first time to do nuclear diffraction experiments. For bending magnet beamlines, the nuclear counting rate is no more than a few counts/sec. On wiggler and undulator beamlines, the counting rate increased by a factor of 100 (for the 10-2 wiggler at the 3 GeV SPEAR storage ring, counting rates of 80 counts/sec were observed, and for the PBF1 undulator at the 15 GeV PEP storage ring, counting rates as high as 800 counts/sec were obtained, but these rates are highly dependent upon the quality of the monochromator (heating problems occur at high x-ray intensities), the x-ray beam optics, the detector efficiency, and the electron beam current and optics). As seen in Figs. 1-2 and 1-3, the SPEAR 54 pole wiggler has a spectral brilliance of about 10^{14} photons/sec$\cdot$mm$^2\cdot$mrad^2(0.1% bandwidth) at 14.4 keV, while the brilliance of the 2 meter PEP undulator is a factor of 10 greater when run in parasitic, or colliding beam, mode (When run in a dedicated, or nonparasitic, low emittance optics mode, the brilliance of the PEP undulator is expected to be 10,000 times greater than the SPEAR wiggler. Unfortunately, before PEP could be run at 14 GeV in this low emittance optics mode, PEP was decommissioned by the Stanford Linear Accelerator Center (SLAC) for fiscal reasons).[24-26]

The development of high energy storage rings specifically dedicated for synchrotron experiments is expected to push counting rates even higher. Already, the 6.5 GeV Accumulator Ring at the KEK high energy facility in Japan that has recently been outfitted with a 3.6 meter undulator, and there are reports of nuclear signal rates as high as 10,000 counts/sec.[27,28] The 7 GeV APS ring under construction at Argonne, the 6 GeV ESRF ring under construction in France, and the 8 GeV Spring-8 ring under construction in Japan will have beamlines equipped with 4 to 5 meter long undulators that are expected to be 1000 times more brilliant (see Fig. 1-4) than the PEP undulator (when, that is, PEP is operated in colliding beam mode--the brilliance would be comparable to PEP were it to be operated in a very low emittance optics mode). A feasibility study under way at KEK is looking into the possibility of converting the electron-positron Tristan Collider Main Ring into a dedicated, exceptionally intense, synchrotron light source called the TSLF (Tristan Super Light Facility).[29] The TSLF, with a 6 meter undulator operating at 10 GeV, is expected to provide an extremely brilliant source of x-rays that is 3 orders of magnitude greater than the third generation synchrotron sources under construction described above and 6 orders of magnitude greater than PEP (The design of TSLF envisages using damping wigglers to reduce the electron beam emittance. If PEP were outfitted with damping wigglers, its brilliance would be comparable to TSLF--see Figs. 1-2 and 1-4). Also in the conceptual design stage is an effort to insert a 50-60 meter FEL undulator into the SLAC linac.[25] If the technical difficulties of operating FELs near 1 Å are overcome (such as modulating the electron bunch structure to a 1 Å periodicity), the SLAC FEL is expected to have an extraordinary brilliance of 10^{31} photons/sec·mm^2·mrad^2(0.1% bandwidth)--this is 15 orders of magnitude brighter than PEP and makes the nuclear photon flux alone (from nuclear resonance scattering experiments) greater than the photon flux generated by present day synchrotron light sources! The prospects of doing useful physics across many science disciplines using the highly monochromatic (micro eV energy width), very collimated (20 μrad or 4 arcsec angular spread), extremely coherent (30 m coherence length) fluorescence radiation from nuclear systems looks very encouraging.

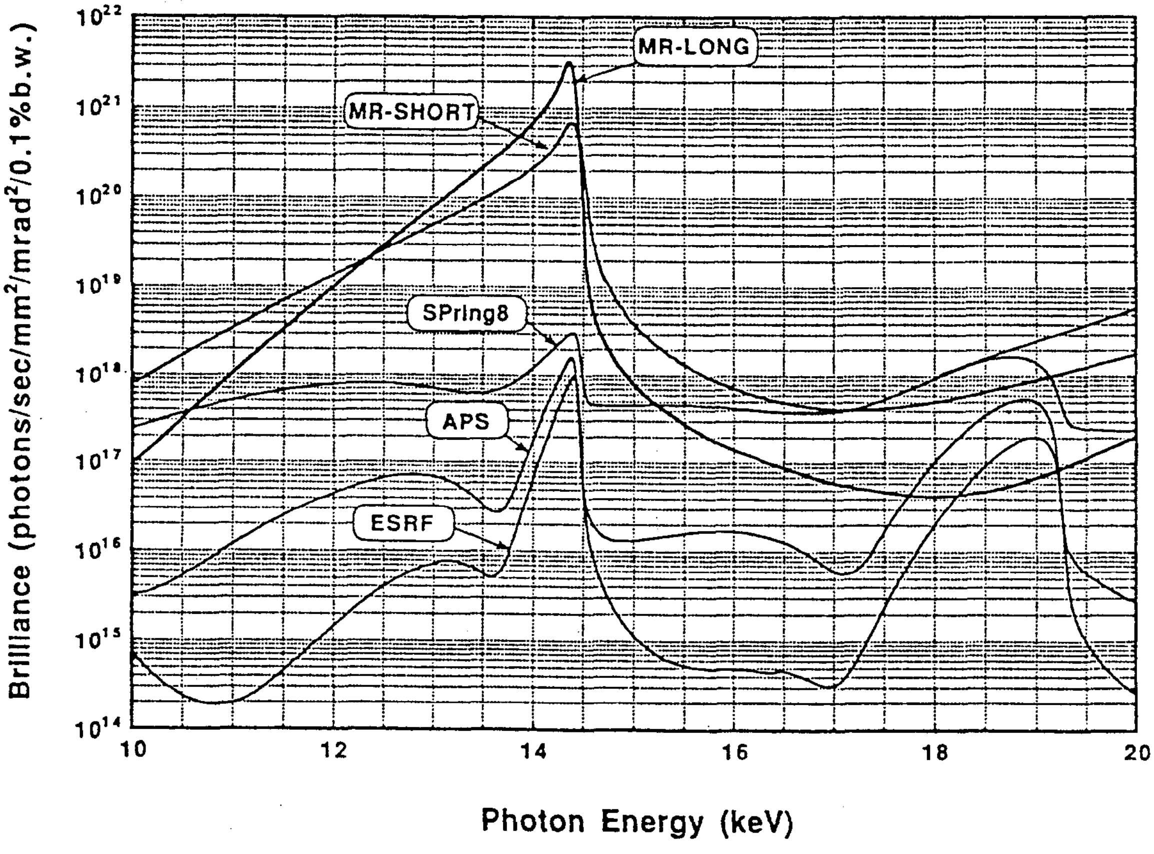

Fig. 1-4. Spectral brilliance curves for various synchrotron storage rings. MR-short and MR-long correspond to a 6 m short undulator and a 70 m long undulator on the TSLF ring. The APS and ESRF calculations were done for a 4.5 m undulator, a 5 m undulator was used for the Spring-8 calculations, and all calculations used an electron beam current of 100 mA. (Reprinted with permission from T. Ishikawa)[29]

This thesis is organized in the following manner. In Chapters 1-4, elementary scattering theory is reviewed, culminating in the construction of the spherical multipole electric fields scattered by resonant particles. In Chapter 5, I have constructed the complete form of the multipole polarization tensor for magnetic dipole scattering in a linear polarization basis. Nuclear level mixing is reviewed, and I give several interesting examples of magnetic dipole scattering. In Chapter 6, I have worked out a novel formulation of dynamical scattering from resonant systems using the principles of linearity and time invariance present in system theory. This theory is used to examine the interaction between two resonant particles, and it reveals that superradiance is due to very elementary multiple scattering effects. I also show that the dynamical scattering equations, in the many particle limit, give the same results as the Maxwell equations for a medium, thus connecting quantum mechanics with classical electrodynamics. Chapter 7 reviews nuclear dynamical diffraction theory, with an emphasize on the superradiant effects of radiative speedup and resonance frequency shifts. Chapter 8 describes the EWALD computer code I wrote to perform the numerically intensive nuclear dynamical diffraction theory calculations. The program is written generally enough to handle any crystal type, to handle reflections from multiple crystals, and can be used for systems containing nuclei other than ^{57}Fe. Chapter 9 describes the general experimental setup along with details about the detector and fast timing electronics.

Chapters 10 and 11 summarize my analysis of the results of the experiments carried out by the Stanford nuclear resonance scattering group composed of myself along with Dr. G. S. Brown (my thesis advisor), Dr. S. Ruby, Dr. J. Arthur, and A. Q. R. Baron. The experiments done on the SPEAR and PEP rings were done in collaboration with Dr. E. Alp and Dr. G. K. Shenoy of Argonne National Labs, and S. Sastri from the Cornell High Energy Synchrotron Source (CHESS) collaborated in experiments done on the CESR ring.

In the Appendices, a copy of a Physical Review Letter article titled "Phase Shift of a Rotated Quantum State Observed in an X-Ray Scattering Experiment" is given. Also given are two time domain calculations using the dynamical scattering equations I formulated. These calculations illustrate that the dynamical scattering equations can be used to examine and understand the physics behind multiple scattering in a way that is not possible using the conventional, index of refraction, approach where the Maxwell equations for a medium are solved in the frequency domain and Fourier transformed into the time domain.

REFERENCES

[1] W. Kuhn, *Phil. Mag.* **8**, 625 (1929).

[2] A. Abragam and R. V. Pound, *Phys. Rev.* **92**, 943 (1953).

[3] K. Alder, A. Bohr, T. Huus, B. Mottelson, and A. Winther, *Revs. Mod. Phys.* **28**, 432 (1956).

[4] R. M. Steffen and H. Frauenfelder, *Perturbed Angular Correlations*, edited by E. Karisson, E.Matthias, K. Siegbahn (North-Holland, Amsterdam, 1964).

[5] C. P. Swann and F. R. Metzger, *Phys. Rev.* **108**, 982 (1957).

[6] P. B. Smith and P. M. Endt, *Phys. Rev.* **110**, 397 (1958).

[7] R. L. Mössbauer, *Z. Physik* **151**, 124 (1958).

[8] L. I. Schiff, *Phys. Rev.* **70**, 761 (1946).

[9] E. J. Seppi and F. Boehm, *Phys. Rev.* **128**, 2334 (1962).

[10] S. L. Ruby, *J. Phys. (Paris) Colloq.* **6**, 209 (1974).

[11] R. L. Cohen, G. L. Miller, and K. W. West, *Phys. Rev. Lett.* **41**, 381 (1978).

[12] A. I. Chechin, N. V. Andronova, M. V. Zelepukhin, A. N. Artem'ev, and E. P. Stepanov, *JETP Lett.* **37**, 633 (1983).

[13] E. Gerdau, R. Rüffer, H. Winkler, W. Tolksdorf, C. P. Klages, and J. P. Hannon, *Phys. Rev. Lett.* **54**, 835 (1985).

[14] E. Gerdau and R. Rüffer, *Hyp. Int.* **27**, 59 (1986).

[15] R. Rüffer, E. Gerdau, and R. Hollatz, *Phys. Rev. Lett.* **58**, 2359 (1987).

[16] U. van Bürck, R. L. Mössbauer, E. Gerdau, R. Rüffer, R. Hollatz, G. V. Smirnov, and J. P. Hannon, *Phys. Rev. Lett.* **59**, 355 (1987).

[17] G. Faigel, D. P. Siddons, J. B. Hastings, P. E. Haustein, J. R. Grover, and L. E. Berman, *Phys. Rev. Lett.* **61**, 2794 (1988).

[18] J. Arthur, G. S. Brown, D. E. Brown, and S. L. Ruby, *Phys. Rev. Lett.* **63**, 1629 (1989).

[19] S. Kikuta, Y. Yoda, Y. Kudo, K. Izumi, T. Ishikawa, C. K. Suzuki, H. Ohno, H. Takei, K. Nakayama, X. W. Zhang, T. Matsushita, S. Kishimoto, and M. Ando, *Jpn. J. App. Phys.* **30**, L 1686 (1991).

[20] P. J. Black and P. B. Moon, *Nature (London)* **188**, 481 (1960).

[21] G. V. Smirnov, V. V. Sklyarevskii, R. A. Voskanyan, and A. N. Artem'ev, *JETP Lett.* **9**, 123 (1969).

[22] J. M. Paterson, *PEP as a Synchrotron Radiation Source: Status and Review,* SSRL ACD-NOTE **68**, (1989) [SLAC-PUB-4899, March 1989].

[23] H. Winick, *Synchrotron Radiation*, Physics of Particle Accelerators (AIP Conference

Proceedings No. **184**), vol. 2, edited by M. Month and M. Dienes (American Institute of Physics, New York, 1989).

[24] H. Wiedemann, *Storage Ring Optimization,* Handbook on Synchrotron Radiation, vol. 3, edited by G. S. Brown and D. E. Moncton (North-Holland, Amsterdam, 1991).

[25] K. Bane, K. Halbach, K.-J. Kim, J. Kirz, P. Morton, H.-D. Nuhn, C. Pellegrini, J. Rosenzweig, J. Seeman, R. Tatchyn, and H. Winick, *The 2 to 4 nm High Power Linear Coherent Light Source*, Workshop on Applications of X-ray FELs (Stanford Synchrotron Radiation Laboratory, Stanford University, 1992).

[26] R. Coisson, private communications and PEP paper (Stanford Synchrotron Radiation Laboratory, Stanford University, 1987).

[27] T. Ishikawa, Y. Yoda, K. Izumi, C. K. Suziki, X. W. Zhang, M. Ando, and S. Kikuta, *Rev. Sci. Instrum.* **63**, 1015 (1992).

[28] X. W. Zhang, T. Mochizuki, H. Sugiyama, S. Yamamoto, H. Kitamura, T. Sioya, M. Ando, Y. Yoda, T. Ishikawa, S. Kikuta, and C. K. Suzuki, *Rev. Sci. Instrum.* **63**, 404 (1992).

[29] H. Sugawara, *The Tristan Super Light Facility*, KEK Progress Report 92-1, (National Laboratory for High Energy Physics, Tsukuba, Japan, 1992).

2. TIME DEPENDENT NONRELATIVISTIC PERTURBATION THEORY

2.1 Perturbation Theory

The essential problem in nuclear dynamical diffraction is to adequately describe the interaction of a charged particle with an electromagnetic field. This chapter will develop the fundamentals of a time dependent perturbation theory that will be used to explore this interaction process.[1-8] The following approach leads to a direct form of a scattering amplitude in terms of a series expansion. Once the scattering amplitude is formulated, many types of scattering processes can be examined.

In determining the quantum mechanical behavior of a charged particle in the presence of a time-varying interaction potential, $V(\mathbf{x},t)$, the time independent part, $H_0(\mathbf{x})$, is separated from the total Hamiltonian,

$$H(\mathbf{x},t) = H_0(\mathbf{x}) + V(\mathbf{x},t). \tag{2-1.1}$$

If the solution of the time independent Schrödinger equation can be found, then the time dependent solution can be written in terms of a perturbative expansion of the known solution. The time independent Schrödinger equation obeys the relation

$$H_0(\mathbf{x})\phi_n(\mathbf{x}) = E_n(\mathbf{x}), \tag{2-1.2}$$

where ϕ_n are the stationary eigenstates of the unperturbed Hamiltonian and satisfies the orthonormal relation

$$\int_V \phi_m^*(\mathbf{x})\phi_n(\mathbf{x})d^3x = \delta_{mn}. \tag{2-1.3}$$

The solutions of the time dependent Schrödinger equation,

$$i\hbar\frac{\partial}{\partial t}\psi(\mathbf{x},t) = \left[H_0(\mathbf{x}) + V(\mathbf{x},t)\right]\psi(\mathbf{x},t), \tag{2-1.4}$$

expressed in terms of an expansion of the stationary states are

$$\psi(\mathbf{x},t) = \sum_n a_n(t)\phi_n(\mathbf{x})e^{-iE_n t/\hbar}. \tag{2-1.5}$$

To determine the coefficients, $a_n(t)$, this solution is inserted back into the Schrödinger equation. The result of this operation is

$$i\hbar\sum_n \dot{a}_n(t)\phi_n(\mathbf{x})e^{-iE_n t/\hbar} = V(\mathbf{x},t)\sum_n a_n(t)\phi_n(\mathbf{x})e^{-iE_n t/\hbar}.$$

Multiplying both sides of the equation above by $\phi_f^*(\mathbf{x})$ and integrating over all space gives

$$\dot{a}_f(t) = -\frac{i}{\hbar}\sum\nolimits_n a_n(t) V_{fn}(t) e^{i\omega_{fn}t}, \tag{2-1.6}$$

where

$$V_{fn}(t) = \int_V \phi_f^*(\mathbf{x}) V(\mathbf{x},t) \phi_n(\mathbf{x}) d^3x \tag{2-1.7}$$

and

$$\omega_{fn} = \left(E_f - E_n\right)/\hbar. \tag{2-1.8}$$

So far, this formalism is exact, and solving the coupled differential equations, Eq. 2-1-6, is equivalent to solving the Schrödinger equation. However, in general, an analytical solution to $a_f(t)$ cannot be found, and thus $a_f(t)$ must be expressed in terms of a series expansion. The convergence of this series will be determined by whether the perturbation $V(\mathbf{x},t)$ is small enough. The series expansion of $a_f(t)$ will be defined as

$$a_f(t) \equiv a_f^{(0)}(t) + a_f^{(1)}(t) + a_f^{(2)}(t) + \cdots + a_f^{(N-1)}(t). \tag{2-1.9}$$

Using the information that the system is definitely in a stationary eigenstate, $\phi_i(\mathbf{x})$, at time $t = -\infty$, the zeroth order term in the expansion can be found. At time $t = -\infty$, the solution to Eq. 2-1.5,

$$\psi(\mathbf{x}, t = -\infty) = \phi_i(\mathbf{x}) e^{-iE_i t/\hbar}\Big|_{t=-\infty} = \sum\nolimits_n a_n(t) \phi_n(\mathbf{x}) e^{-iE_n t/\hbar}\Big|_{t=-\infty},$$

is $a_n(-\infty) = \delta_{ni}$. The zeroth order term in the expansion is the solution to the Schrödinger equation when the perturbation is absent:

$$\dot{a}_f^{(0)}(t) = 0 \tag{2-1.10}$$

$$a_f^{(0)}(t) = \delta_{ni}. \tag{2-1.11}$$

The next order term in the expansion is obtained by substituting the zeroth order term into the relation for $\dot{a}_f(t)$, Eq. 2-1.6:

$$\dot{a}_f^{(1)}(t) = (-i/\hbar) V_{fi}(t) e^{i\omega_{fi}t} \tag{2-1.12}$$

$$a_f^{(1)}(t) = (-i/\hbar) \int_{-\infty}^{t} V_{fi}(t') e^{i\omega_{fi}t'} dt'. \tag{2-1.13}$$

This substitution process can be done recursively to obtain all the other higher orders. The second order terms are:

$$\dot{a}_f^{(2)}(t) = (-i/\hbar)^2 \sum_{n \neq i} V_{fn}(t) e^{i\omega_{fn}t} \int_{-\infty}^{t} V_{ni}(t') e^{i\omega_{ni}t'} dt' \tag{2.1-14}$$

$$a_f^{(2)}(t) = (-i/\hbar)^2 \sum_{n \neq i} \int_{-\infty}^{t} dt_1 V_{fn}(t_1) e^{i\omega_{fn}t_1} \int_{-\infty}^{t_1} dt_2 V_{ni}(t_2) e^{i\omega_{ni}t_2}. \tag{2.1-15}$$

The constraint on the sum, $n \neq i$, forces any intermediate state, $|n\rangle$, to be different from the initial state (there is also the constraint that $n \neq f$). Thus the intermediate state transitions do not conserve energy: $\omega_{fn} \neq 0$ and $\omega_{ni} \neq 0$. The self energy terms, V_{ii}, will be partially ignored. They are described by single particle scattering loops in Feynman scattering diagrams, and, when they are more carefully evaluated in a covariant perturbation theory, they will only contribute energy shifts to the scattering amplitude. No attempt will be made to calculate such energy shifts--they will simply be lumped with the experimentally measured isomer shifts and appropriately inserted into the scattering amplitude.

The third order amplitude is listed below:

$$\dot{a}_f^{(3)}(t) = (-i/\hbar)^3 \sum_{m\neq i} \sum_{n\neq m} V_{fn}(t) e^{i\omega_{fn}t} \int_{-\infty}^{t} dt_1 V_{nm}(t_1) e^{i\omega_{nm}t_1} \int_{-\infty}^{t_1} dt_2 V_{mi}(t_2) e^{i\omega_{mi}t_2} \tag{2-1.16}$$

$$a_f^{(3)}(t) = (-i/\hbar)^3 \sum_{m\neq i} \sum_{n\neq m} \int_{-\infty}^{t} dt_1 V_{fn}(t_1) e^{i\omega_{fn}t_1} \int_{-\infty}^{t_1} dt_2 V_{nm}(t_2) e^{i\omega_{nm}t_2} \int_{-\infty}^{t_2} dt_3 V_{mi}(t_3) e^{i\omega_{mi}t_3} . \tag{2-1.17}$$

2.2 The Scattering S and T Matrices

After the interaction perturbation ceases, the system resides in a definite stationary state, $\phi_f(\mathbf{x},t)$. Then the transition amplitude for a transition from an initial state to a final state can be defined in terms of the elements of a scattering operator S,

$$\begin{aligned} S_{fi} &= \langle \phi_f | S | \phi_i \rangle = \langle \phi_f(\mathbf{x},t) | \psi(\mathbf{x},t) \rangle = \sum_n a_n(t) e^{-iE_n t/\hbar} \int_V \phi_f^*(\mathbf{x}) \phi_n(\mathbf{x}) e^{iE_f t/\hbar} \\ &= a_f(t) \end{aligned} \tag{2-2.1}$$

The S-operator is then a unitary operator that describes the evolution of an initial state, $|\phi_i(\mathbf{x},t)\rangle$, to a final state, $|\psi(\mathbf{x},t)\rangle$, during the action of the perturbation:

$$S|\phi_i(\mathbf{x},t)\rangle = |\psi(\mathbf{x},t)\rangle . \tag{2-2.2}$$

The unitarity of S can be seen by noting that

$$\langle \psi | \psi \rangle = 1 = \langle \phi_i | S^\dagger S | \phi_i \rangle . \tag{2-2.3}$$

This is true only if $S^\dagger S = 1$. Summing over all the possible final states gives a total probability for a scattering event to occur of unity,

$$\sum_f [S^\dagger S]_{fi} = \sum_f \langle \psi | \phi_f \rangle \langle \phi_f | \psi \rangle = \langle \psi | \psi \rangle = 1 . \tag{2-2.4}$$

The matrix elements of the scattering operator can be found by evaluating the perturbative expansion terms of $a_f(t)$, Eqs. 2-1.10 to 2-1.17. The transition probability is

$|S_{fi}|^2$, and the transition probability per unit time, or transition rate, is the time rate of change of the transition probability,[5]

$$\Gamma_{fi} = \frac{\partial}{\partial t}|S_{fi}|^2 = S_{fi}^{*}\dot{S}_{fi} + \dot{S}_{fi}^{*}S_{fi}. \qquad (2\text{-}2.5)$$

The other interesting quantity desired is the T-matrix element, T_{fi}, which should be differentiated from the transition probability in that it describes the amplitude of a scattered wave rather than the probability for a transition from an initial state to a final state. The structure of the T-matrix can be seen by evaluating the transition rate for the simple case of a constant interaction perturbation,

$$V(\mathbf{x},t) = \begin{cases} 0 & t \to -\infty \\ V(\mathbf{x}) & \end{cases}. \qquad (2\text{-}2.6)$$

The zeroth and first order terms of the S-matrix elements can be found using the perturbative expansions of Eqs. 2-1.10 to 2-1.13:

$$S_{fi} = \delta_{fi} + (-i/\hbar)\int_{-\infty}^{t} V_{fi}e^{i\omega_{fi}t'}\,dt' \qquad (2\text{-}2.7)$$

$$\dot{S}_{fi} = (-i/\hbar)V_{fi}e^{i\omega_{fi}t}. \qquad (2\text{-}2.8)$$

The transition rate is then

$$\Gamma_{fi} = (i/\hbar)V_{fi}^{*}e^{-i\omega_{fi}t}\left[\delta_{fi} + (-i/\hbar)\int_{-\infty}^{t} V_{fi}e^{i\omega_{fi}t'}\,dt'\right]$$
$$+(-i/\hbar)V_{fi}e^{i\omega_{fi}t}\left[\delta_{fi} + (i/\hbar)\int_{-\infty}^{t} V_{fi}^{*}e^{-i\omega_{fi}t'}\,dt'\right].$$

The δ-function terms yield

$$(i/\hbar)\left[V_{ii}^{*} - V_{ii}\right] = (i/\hbar)\left[\langle\phi_i|V^{\dagger}|\phi_i\rangle - \langle\phi_i|V|\phi_i\rangle\right] = 0$$

since the interaction perturbation Hamiltonian, $V(\mathbf{x},t)$, is Hermetian: $V^{\dagger} = V$. Then,

$$\Gamma_{fi} = \left(1/\hbar^2\right)V_{fi}^{*}V_{fi}\left[\int_{-\infty}^{t} e^{i\omega_{fi}(t'-t)}\,dt' + \int_{-\infty}^{t} e^{i\omega_{fi}(t-t')}\,dt'\right].$$

Making the change of variables $u = t' - t$ for the first integral and $u = t - t'$ for the second integral results in

$$\Gamma_{fi} = \left(1/\hbar^2\right)V_{fi}^{*}V_{fi}\left[\int_{-\infty}^{0} e^{i\omega_{fi}u}\,du - \int_{\infty}^{0} e^{i\omega_{fi}u}\,du\right] = \left(1/\hbar^2\right)|V_{fi}|^2\int_{-\infty}^{\infty} e^{i\omega_{fi}u}\,du$$

$$= \frac{2\pi}{\hbar}|V_{fi}|^2\,\delta\left(E_f - E_i\right), \qquad (2\text{-}2.9)$$

where the following relations were used:

$$\int_{-\infty}^{\infty} e^{ikx}\, dx = 2\pi\delta(k) \tag{2-2.10}$$

$$\delta(ax) = \frac{1}{|a|}\delta(x). \tag{2-2.11}$$

Equation 2-2.9 is the Fermi Golden Rule to first order. Also the δ-function preserves the conservation of energy condition--this is usually termed in the scattering language as the on-energy-shell condition.

To obtain the Fermi Golden Rule to second order, the S-matrix elements must be evaluated to second order:

$$S_{fi} = \delta_{fi} + (-i/\hbar)\int_{-\infty}^{t} V_{fi} e^{i\omega_{fi}t'}\, dt' + (-i/\hbar)^2 \sum_{n\neq i} \int_{-\infty}^{t} dt_1 V_{fn} e^{i\omega_{fn}t_1} \int_{-\infty}^{t_1} dt_2 V_{ni} e^{i\omega_{ni}t_2}. \tag{2-2.12}$$

Inserting a small positive imaginary quantity, $i\varepsilon$ where $\varepsilon > 0$, into the exponent of the last integral allows one to perform the integral to get a meaningful result. After integration, taking the limit as $\varepsilon \to 0$ gives the final result. This procedure, though seemingly ad hoc, is very important in ensuring that the S-matrix obeys the accepted rules of causality for incoming and outgoing particles. The last integral in the third term above then integrates to

$$\int_{-\infty}^{t_1} dt_2 V_{ni} e^{i\omega_{ni}t_2} = \lim_{\varepsilon\to 0} \int_{-\infty}^{t_1} dt_2 V_{ni} e^{i(E_n - E_i - i\varepsilon)t_2/\hbar} = i\hbar V_{ni} \frac{e^{i(E_n - E_i)t_1/\hbar}}{E_i - E_n}.$$

Then,

$$S_{fi} = \delta_{fi} + (-i/\hbar)\left[V_{fi} + \sum_{n\neq i} \frac{V_{fn}V_{ni}}{E_i - E_n}\right] \int_{-\infty}^{t} e^{i\omega_{ni}t'}\, dt' \tag{2-2.13}$$

and

$$\dot{S}_{fi} = (-i/\hbar)\left[V_{fi} + \sum_{n\neq i} \frac{V_{fn}V_{ni}}{E_i - E_n}\right] e^{i\omega_{fi}t}. \tag{2-2.14}$$

S_{fi} and $\dot{S}_{fi}$ have the same form as their first order expressions for the substitution

$$V_{fi} \to V_{fi} + \sum_{n\neq i} \frac{V_{fn}V_{ni}}{E_i - E_n}.$$

Then employing the same techniques as before gives

$$\Gamma_{fi} = \frac{2\pi}{\hbar} \left| V_{fi} + \sum_{n\neq i} \frac{V_{fn}V_{ni}}{E_i - E_n} \right|^2 \delta(E_f - E_i). \tag{2-2.15}$$

This gives the on-energy-shell T-matrix elements to second order,

$$T_{fi} = V_{fi} + \sum_{n \neq i} \frac{V_{fn} V_{ni}}{E_i - E_n}. \qquad \text{(2-2.16)}$$

The Fermi Golden rule to all orders can now be written in a compact form:

$$\Gamma_{fi} = \frac{2\pi}{\hbar} \left| T_{fi} \right|^2 \delta\left(E_f - E_i\right), \qquad \text{(2-2.17)}$$

where

$$T_{fi} = V_{fi} + \sum_{n \neq i} \frac{V_{fn} V_{ni}}{E_i - E_n} + \sum_{m \neq i} \sum_{n \neq m} \frac{V_{fn} V_{nm} V_{mi}}{\left(E_i - E_n\right)\left(E_i - E_m\right)} + \cdots. \qquad \text{(2-2.18)}$$

2.3 The Scattering Amplitude

In dealing with scattering problems, knowledge of the total cross section of a scattering event is very useful. The total cross section can be evaluated from the transition rate using the following definition:

$$\sigma_{tot} = \frac{\text{all scattered photons/sec}}{\text{flux of incident photons}} \equiv \frac{\sum_f \Gamma_{fi}}{n_i v_i / V_0}, \qquad \text{(2-3.1)}$$

where n_i and v_i are the number and velocity of the incident particles, and V_0 is the volume of space enclosing the interaction region. Summing over all the possible final states gives the total cross section. Using the Fermi Golden rule, the total cross section can be expressed in the form

$$\sigma_{tot} = \frac{2\pi/\hbar}{n_i v_i / V_0} \sum_f \left| T_{fi} \right|^2 \delta\left(E_f - E_i\right). \qquad \text{(2-3.2)}$$

Notice that T_{fi} in the expression above is in units of energy. The expression for a scattering amplitude in units of length can be obtained by showing that σ_{tot} satisfies the optical theorem. To do so, first note that the S-matrix elements, for $t \to \infty$, follows the relation

$$S_{fi} = \delta_{fi} - 2\pi i T_{fi} \delta\left(E_f - E_i\right). \qquad \text{(2-3.3)}$$

Using the unitarity properties of the S-matrix yields

$$\begin{aligned} \left(S^{\dagger} S\right)_{fi} &= \delta_{fi} = \sum_n S^*_{nf} S_{ni} \\ &= \sum_n \Big[\delta_{fn} \delta_{ni} + 2\pi i \delta_{ni} T^*_{nf} \delta\left(E_f - E_n\right) - 2\pi i \delta_{nf} T_{ni} \delta\left(E_n - E_i\right) \end{aligned}$$

$$+ (2\pi)^2 T_{nf}^* T_{ni} \delta(E_f - E_n)\delta(E_n - E_i)\Big].$$

Then,

$$\Big[(T_{if}^* - T_{fi}) - 2\pi i \sum\nolimits_n T_{nf}^* T_{ni} \delta(E_n - E_i)\Big]\delta(E_f - E_i) = 0,$$

where the identity $\delta(E_f - E_n)\delta(E_n - E_i) = \delta(E_f - E_i)\delta(E_n - E_i)$ has been used. The above expression is true on the energy shell if

$$(T_{if}^* - T_{fi}) - 2\pi i \sum\nolimits_n T_{nf}^* T_{ni} \delta(E_n - E_i) = 0. \tag{2-3.4}$$

This is simply an equivalent expression of the unitary condition expressed in terms of the scattering amplitude. The diagonal elements yield the meaningful result

$$T_{ii} - T_{ii}^* = 2i\,\mathrm{Im}\{T_{ii}\} = -2\pi i \sum\nolimits_n |T_{ni}|^2 \delta(E_n - E_i). \tag{2-3.5}$$

The total cross section is then

$$\sigma_{tot} = -\frac{2V_0}{\hbar n_i v_i}\mathrm{Im}\{T_{ii}\}. \tag{2-3.6}$$

This is the optical theorem, and it relates the total cross section to the imaginary part of the scattering amplitude. The photons have been elastically scattered since the final state of the system is identical to the initial state.

A normalized scattering amplitude in units of length can then be defined as

$$F_{fi}(\mathbf{k}_f, \mathbf{k}_i) = -A_0 T_{fi}, \tag{2-3.7}$$

where

$$A_0 = \frac{1}{\sqrt{n_i}}\frac{V_0 k_f}{2\pi\hbar v_i}. \tag{2-3.8}$$

The factor $1/\sqrt{n_i}$ normalizes the square modulus of the scattering amplitude to the number of incoming particles, and $\mathbf{k}_i$ and $\mathbf{k}_f$ are the incoming and outgoing photon wavectors respectively. Then, for one incoming particle undergoing elastic scattering

$$\sigma_{tot} = \frac{4\pi}{k_f}\mathrm{Im}\{F_{ii}(\mathbf{k}_f, \mathbf{k}_i)\}. \tag{2-3.9}$$

This is the familiar form of the optical theorem seen in classical electrodynamics. However, when many scatterers are present, the total cross section is proportional to the forward scattering amplitude, $F(\mathbf{k}_f = \mathbf{k}_i)$. This multiparticle scattering behavior will explored later.

Basic assumptions about certain symmetry laws in physics have been made in the construction of σ_{tot}. For instance, a generalized scattering cross section can be constructed from Eq. 2-3.4

$$\sigma_{tot}^{gen} = -\frac{2\pi i}{k_f}\left[F_{fi}(\mathbf{k}_f,\mathbf{k}_i) - F_{if}^*(\mathbf{k}_i,\mathbf{k}_f)\right]. \qquad (2\text{-}3.10)$$

This expression can be put in a form similar to Eq. 2-3.9 by applying the law of reciprocity for systems possessing space-inversion symmetry.[9] The law of reciprocity states that a scattering event in which an incoming particle scatters from $\mathbf{k}_i$ to $\mathbf{k}_f$ is identical to a scattering event in which the particle scatters in the reverse direction from $-\mathbf{k}_f$ to $-\mathbf{k}_i$. Then

$$F_{fi}(\mathbf{k}_f,\mathbf{k}_i) = F_{if}(-\mathbf{k}_i,-\mathbf{k}_f) \qquad (2\text{-}3.11)$$

satisfies the principle of reciprocity (see Fig 2-3.1). As long as one remains on the energy shell, reciprocity is simply another way of stating that time reversal invariance holds.[10]

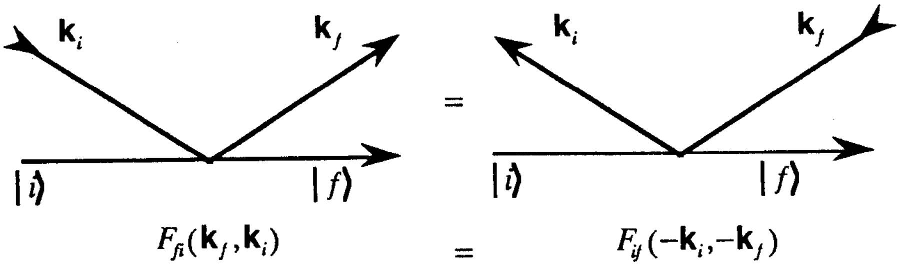

Fig. 2-3.1. Illustration of reciprocity where the scattering amplitudes for a scattering process and its time reversed process are equivalent.

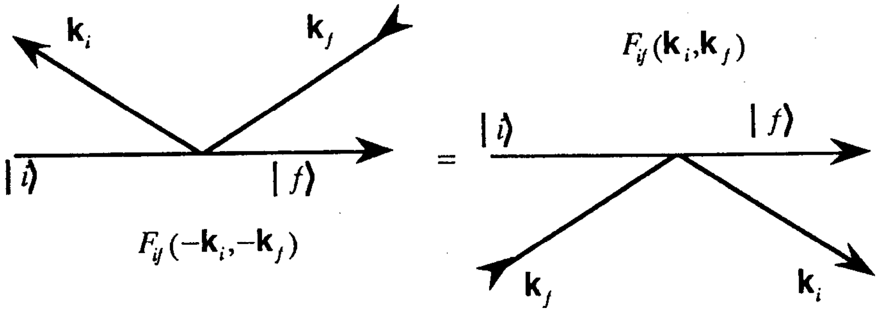

Fig. 2-3.2. Illustration of space inversion symmetry. Photons traveling in the **x** direction sees the same interaction as those traveling in the $-\mathbf{x}$ directon.

If the scattering system possesses space inversion symmetry (that is, the interaction perturbation satisfies $V(\mathbf{x}) = V(-\mathbf{x})$) then, from Fig 2-3.2, the scattering amplitude obeys the relation

$$F_{if}\left(-\mathbf{k}_i,-\mathbf{k}_f\right) = F_{if}\left(\mathbf{k}_i,\mathbf{k}_f\right). \tag{2-3.12}$$

This makes the scattering amplitude (and the scattering T-matrix) symmetric

$$T_{if} = T_{fi} \quad \text{or} \quad F_{if}\left(\mathbf{k}_i,\mathbf{k}_f\right) = F_{fi}\left(\mathbf{k}_f,\mathbf{k}_i\right). \tag{2-3.13}$$

Under such conditions, the generalized cross section reduces to

$$\sigma_{tot}^{gen} = \frac{4\pi}{k_f}\operatorname{Im}\left\{F_{fi}\left(\mathbf{k}_f,\mathbf{k}_i\right)\right\}. \tag{2-3.14}$$

The generalized cross section reduces to the elastic cross section, Eq. 2-3.9, when the initial and final states are identical. This also shows that the elastic cross section is valid only when the scattering system possesses space-inversion symmetry and time reversal invariance holds.

REFERENCES

[1] M. L. Goldberger and K. M. Watson, *Collision Theory* (Wiley, New York, 1964).

[2] F. Halzen and A. D. Martin, *Quarks and Leptons* (Wiley, New York, 1984).

[3] W. Heitler, *The Quantum Theory of Radiation* (Clarendon Press, Oxford, 1954).

[4] M. Lax, *Rev. Mod. Phys.* **23**, 287 (1951).

[5] B. A. Lippmann and J. Schwinger, *Phys. Rev.* **79**, 469 (1950).

[6] J. J. Sakurai, *Advanced Quantum Mechanics* (Addison-Wesley, Reading, Mass., 1967).

[7] H. Frauenfelder, *Subatomic Physics* (Prentice-Hall, Englewood Cliffs, N. J., 1974).

[8] C. Cohen-Tannoudji, B. Diu, and F. Laloë, *Quantum Mechanics* (Wiley, New York, 1977).

[9] L. I. Schiff, *Quantum Mechanics* (McGraw-Hill, New York, 1968).

[10] A. Messiah, *Quantum Mechanics* (Wiley, New York, 1962), vol. 2.

3. SCATTERING THEORY

3.1 Semiclassical Wave Theory

So far, a quantum mechanical, microscopic description of the scattering amplitude has been derived for a single incoming particle interacting with a scatterer. The goal is to derive a macroscopic description of the scattering amplitude for one or more incoming particles interacting with many scatterers. And, if the scatterers are densely distributed in space such that their interparticle separation is on the order of or less than the wavelength of the incoming particle, multiple scattering events must be taken in to account. Purely quantum mechanical calculations become quite difficult to compute when dealing with the interaction of more than two particles, and are, in many cases, impossible to compute when the number of particles exceeds several hundred. A small solid target with interatomic distances on the order of 1 Å and that is 10 μm thick with a surface area of 1 mm will have on the order of 10^{19} scatterers. Clearly, a purely quantum mechanical approach toward solving the scattering problem is not possible.

One must therefore rely upon some other approach, such as a semiclassical theory, to obtain a macroscopic scattering amplitude. Fortunately, the inhomogeneous classical wave equation inherently describes multiple scattering--it describes the propagation of a wave (a packet of many incoming particles) in a many particle medium. Its superb success in describing wave phenomena in classical physics is why the semiclassical framework is commonly used to make the bridge between classical and quantum physics.

From here on, the emphasis will mainly be on scattering processes in which photons are the incoming particles (with the knowledge that inhomogeneous wave equations can be constructed for other particles, such as electrons). In the classical picture, their interaction with matter is adequately described by the Maxwell equations. Jackson[1] shows how to go from the microscopic Maxwell equations,

$$\nabla \cdot \mathbf{b} = 0 \qquad \nabla \times \mathbf{e} + \frac{1}{c}\frac{\partial \mathbf{b}}{\partial t} = 0$$

$$\nabla \cdot \mathbf{e} = 4\pi\eta \qquad \nabla \times \mathbf{b} - \frac{1}{c}\frac{\partial \mathbf{e}}{\partial t} = \frac{4\pi}{c}\mathbf{j}, \tag{3-1.1}$$

where $\mathbf{e}$ and $\mathbf{b}$ are the microscopic electric and magnetic fields and η and $\mathbf{j}$ are the microscopic charge and current densities, to the macroscopic Maxwell equations,

$$\nabla\cdot\mathbf{B}=0 \qquad \nabla\times\mathbf{E}+\frac{1}{c}\frac{\partial\mathbf{B}}{\partial t}=0$$

$$\nabla\cdot\mathbf{D}=4\pi\rho \qquad \nabla\times\mathbf{H}-\frac{1}{c}\frac{\partial\mathbf{D}}{\partial t}=\frac{4\pi}{c}\mathbf{J}, \tag{3-1.2}$$

where ρ and $\mathbf{J}$ are the macroscopic free charge and current densities. The transition from the classical microscopic equations to a semiclassical macroscopic description is done by taking the expectation values and spatially averaging over all microscopic quantities. Spatially averaging over the microscopic fluctuations due to thermal motion, zero point fluctuations, and orbital motion, gives the smooth, slowly varying macroscopic quantities present in the Maxwell equations for a medium. The macroscopic picture is taken to be on the order of Avagadro's number of atoms per cubic centimeter, 10^{24} atoms/cm^3, where the length scale, 100 Å, is taken as an absolute lower limit to the macroscopic domain. The macroscopic electric displacement, $\mathbf{D}$, and magnetic field, $\mathbf{H}$, come from the spatial average over the microscopic charge and current densities

$$D_\alpha = E_\alpha + 4\pi\left\{P_\alpha - \sum_\beta \frac{\partial Q'_{\alpha\beta}}{\partial x_\beta} + \cdots\right\} \tag{3-1.3}$$

$$H_\alpha = B_\alpha - 4\pi\{M_\alpha + \cdots\} \tag{3-1.4}$$

where $\mathbf{P}(\mathbf{x},t)$, $\mathbf{Q}'(\mathbf{x},t)$, and $\mathbf{M}(\mathbf{x},t)$ are the macroscopic electric polarization, quadrupole density, and magnetization. For a substance that has a linear response (that is, any induced electric or magnetic polarization is proportional to the magnitude of the applied field),

$$\mathbf{D}=\boldsymbol{\varepsilon}\mathbf{E} \tag{3-1.5}$$

$$\mathbf{H}=\boldsymbol{\mu}^{-1}\mathbf{B} \tag{3-1.6}$$

where $\boldsymbol{\varepsilon}$ and $\boldsymbol{\mu}$ are the dielectric and magnetic permeability tensors. Note that the dielectric and permeability tensors are proportional to the electric and magnetic multipole moments.

As a simple example, let both tensors be diagonal, with all diagonal elements equal, as for an isotropic medium. Then

$$D_\alpha = \varepsilon_0 E_\alpha \quad , \; H_\alpha = \mu_0^{-1} B_\alpha \tag{3-1.7}$$

and thus

$$\varepsilon_0 = 1 + 4\pi\left\{\frac{P_\alpha}{E_\alpha} - \frac{1}{E_\alpha}\sum_\beta \frac{\partial Q'_{\alpha\beta}}{\partial x_\beta} + \cdots\right\} \tag{3-1.8}$$

and
$$\mu_0^{-1} = 1 - 4\pi\left\{\frac{M_\alpha}{B_\alpha} + \cdots\right\}. \tag{3-1.9}$$

For multipole moments small in comparison to the electric and magnetic fields that generate them, the quantity $\varepsilon_0\mu_0$, which is the square of the index of refraction, is then

$$n^2 = \varepsilon_0\mu_0 = 1 + 4\pi\left\{\frac{P_\alpha}{E_\alpha} + \frac{M_\alpha}{B_\alpha} - \frac{1}{E_\alpha}\sum_\beta \frac{\partial Q'_{\alpha\beta}}{\partial x_\beta} + \cdots\right\}$$
$$+(4\pi)^2 \times \text{Multipole Mixtures}. \tag{3-1.10}$$

This shows that the index of refraction of a medium is proportional to the electric and magnetic multipole moments generated by that medium, and it also has terms proportional to mixtures, or products, of electric and magnetic multipoles. The quantum mechanical expectation value of this quantity will be taken to produce a semiclassical theory for the scattering amplitude.

3.2 Inhomogeneous Wave Equation

The inhomogeneous wave equation can be constructed from the Maxwell macroscopic equations. However, one must note that the relationship between **D** and **E** can be nonlocal. In other words, **D** at time t and position $\mathbf{x}$ can depend upon **E** at times and positions other than t and $\mathbf{x}$. The relationship between the sources, $\boldsymbol{\varepsilon}(\mathbf{x},t)$, and the fields they generate, $\mathbf{D}(\mathbf{x},t)$, must be causal to ensure that the fields do not instantaneously propagate from one point in space to another. For the electric displacement[1]

$$D_\alpha(\mathbf{x},t) = \sum_\beta \int d^3x' \int dt' \varepsilon_{\alpha\beta}(\mathbf{x}',t')E_\beta(\mathbf{x}-\mathbf{x}',t-t'). \tag{3-2.1}$$

In frequency space,

$$D_\alpha(\mathbf{k},\omega) = \sum_\beta \varepsilon_{\alpha\beta}(\mathbf{k},\omega)E_\beta(\mathbf{k},\omega) \tag{3-2.2}$$

and similarly

$$H_\alpha(\mathbf{k},\omega) = \sum_\beta \mu_{\alpha\beta}^{-1}(\mathbf{k},\omega)B_\beta(\mathbf{k},\omega) \tag{3-2.3}$$

where the Fourier transform is defined as

$$f(\mathbf{k},\omega) = \int d^3x \int dt f(\mathbf{x},t)e^{-i\mathbf{k}\cdot\mathbf{x}+i\omega t}. \tag{3-2.4}$$

The inhomogeneous wave equation in frequency space can now be constructed. The Fourier transform of the $\mathbf{E}$ and $\mathbf{B}$ fields in the second relation of Eq. 3-1.2 gives

$$\nabla\times\mathbf{E}(\mathbf{x},\omega)-i\frac{\omega}{c}\mathbf{B}(\mathbf{x},\omega)=0. \tag{3-2.5}$$

Doing the same for the fourth relation of Eq. 3-1.2, for no free current, gives

$$\int d\omega\, e^{-i\omega t}\int d^3x'\, e^{i\mathbf{k}\cdot\mathbf{x}'}\left\{\nabla\times\left[\boldsymbol{\mu}^{-1}(\mathbf{x}',\omega)\mathbf{B}(\mathbf{x}-\mathbf{x}',\omega)\right]+i\frac{\omega}{c}\boldsymbol{\varepsilon}(\mathbf{x}',\omega)\mathbf{E}(\mathbf{x}-\mathbf{x}',\omega)\right\}=0.$$

The dielectric and permeability tensors depend upon the observation point $\mathbf{x}$ since they may have an overall spatial distribution throughout the interaction volume. If the spatial frequencies of the inverse magnetic permeability are far smaller than those of the magnetic field, spatial derivatives of the inverse permeability tensor can be neglected. If the sources that generate the multipole fields have dimensions that are small compared to the spatial variation of the $\mathbf{E}$ and $\mathbf{B}$ fields in the medium, then they can be considered to be sharply localized around the points $\mathbf{x}'$ with negligible effects outside a small volume around $\mathbf{x}'$. Then, for particles such as electrons and nuclei that have diameters much smaller than the spatial variation of light down to X-ray wavelengths, the tensor quantities can be approximated as

$$\boldsymbol{\mu}^{-1}(\mathbf{x}',\omega)=\delta(\mathbf{x}-\mathbf{x}')\boldsymbol{\mu}^{-1}(\mathbf{x},\omega) \tag{3-2.6}$$

$$\boldsymbol{\varepsilon}(\mathbf{x}',\omega)=\delta(\mathbf{x}-\mathbf{x}')\boldsymbol{\varepsilon}(\mathbf{x},\omega). \tag{3-2.7}$$

Then the expression above reduces to

$$\nabla\times\mathbf{B}(\mathbf{x},\omega)+i\frac{\omega}{c}\boldsymbol{\mu}(\mathbf{x},\omega)\boldsymbol{\varepsilon}(\mathbf{x},\omega)\mathbf{E}(\mathbf{x},\omega)=0. \tag{3-2.8}$$

Taking the curl of Eq.3-2.5 and substituting the results into Eq.3-2.8 give the Maxwell wave equation for a medium:

$$\nabla^2\mathbf{E}(\mathbf{x},\omega)+(\omega/c)^2\boldsymbol{\mu}(\mathbf{x},\omega)\boldsymbol{\varepsilon}(\mathbf{x},\omega)\mathbf{E}(\mathbf{x},\omega)=0 \tag{3-2.9}$$

where the observation point has been placed far from the scatterer to make the longitudinal components of the $\mathbf{E}$ field negligible so that $\nabla\cdot\mathbf{E}\approx 0$.

A quantity $2\boldsymbol{\varepsilon}_0$ will be defined where

$$n^2=1+2\boldsymbol{\varepsilon}_0(\mathbf{x},\omega)=\boldsymbol{\mu}(\mathbf{x},\omega)\boldsymbol{\varepsilon}(\mathbf{x},\omega). \tag{3-2.10}$$

The quantity $2\boldsymbol{\varepsilon}_0$ carries all the information about the electric and magnetic multipoles. This leads to an expression of the inhomogeneous wave equation for transverse electric fields within a medium

$$\left(\nabla^2+k_{0v}^2+k_{0v}^2\left[2\boldsymbol{\varepsilon}_0(\mathbf{x},\omega)\right]\right)\mathbf{E}(\mathbf{x},\omega)=0, \tag{3-2.11}$$

where
$$k_{0\nu} = \omega / c \tag{3-2.12}$$
and
$$\nabla \cdot \mathbf{E} = 0. \tag{3-2.13}$$

3.3 Integral Scattering Equation

There is a scalar wave equation for each component of **E**. Let φ be one of those components of the **E** field in a basis that diagonalizes the index of refraction tensor. Also define

$$U(\mathbf{x},\omega) = k_{0\nu}^2 [2\varepsilon_0(\mathbf{x},\omega)]. \tag{3-3.1}$$

The scalar wave equation is then

$$\left(\nabla^2 + k_{0\nu}^2\right)\varphi(\mathbf{x},\omega) = -U(\mathbf{x},\omega)\varphi(\mathbf{x},\omega). \tag{3-3.2}$$

The Green function techniques can be used to solve this inhomogeneous scalar wave equation. Constructing a Green function that satisfies

$$\left(\nabla^2 + k_{0\nu}^2\right)G(\mathbf{x},\mathbf{x}') = -4\pi\delta(\mathbf{x}-\mathbf{x}') \tag{3-3.3}$$

leads to the solution of Eq.3-3.2:

$$\varphi(\mathbf{x},\omega) = \phi_i(\mathbf{x},\omega) + \int G(\mathbf{x},\mathbf{x}')U(\mathbf{x}',\omega)\varphi(\mathbf{x}',\omega)\,d^3x', \tag{3-3.4}$$

where $\phi_i(\mathbf{x},\omega)$ is the solution to homogeneous wave equation

$$\left(\nabla^2 + k_{0\nu}^2\right)\phi_i(\mathbf{x},\omega) = 0. \tag{3-3.5}$$

Thus $\phi_i(\mathbf{x},t)$ represents the state of the system, or the wavefield in the medium, before the perturbation $U(\mathbf{x},t)$ exists -- $\phi_i(\mathbf{x},t)$ is the initial, or incoming, wavefield.

Equation 3-3.4 is commonly referred to as the integral scattering equation or the Lippmann-Schwinger integral equation.[2-4] The second term describes the scattered part of the incoming wave. To see this more clearly, note that the Green function for outgoing spherical waves is[1]

$$G(\mathbf{x},\mathbf{x}') = \frac{e^{ik_{0\nu}|\mathbf{x}-\mathbf{x}'|}}{4\pi|\mathbf{x}-\mathbf{x}'|}. \tag{3-3.6}$$

For observation distances far from the scatterer, $|\mathbf{x}| >> |\mathbf{x}'|$, then

$$|\mathbf{x}-\mathbf{x}'| = \sqrt{x^2 + x'^2 - 2\mathbf{x}\cdot\mathbf{x}'} \approx x - \frac{\mathbf{x}\cdot\mathbf{x}'}{x}.$$

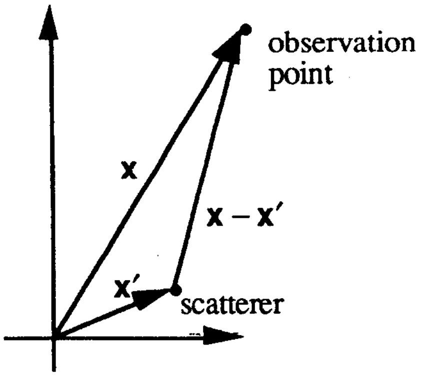

Fig. 3-3.1. Scattering Geometry

Also note that $\mathbf{x}$ is approximately the direction of the fields emanating from the scatterer. Defining a propagation vector

$$\mathbf{k}_f = k_{0v}(\mathbf{x}/x), \tag{3-3.7}$$

gives

$$\varphi(\mathbf{x},\omega) = \phi_i(\mathbf{x},\omega) + \frac{1}{4\pi}\frac{e^{ik_{0v}x}}{x}\int e^{i\mathbf{k}_f\cdot\mathbf{x}'}U(\mathbf{x}',\omega)\varphi(\mathbf{x}',\omega)d^3x'. \tag{3-3.8}$$

Letting the final wavefunction, which exists when the perturbation $U(\mathbf{x},\omega)$ ceases, be a normalized plane wave state

$$\phi_f(\mathbf{x},\omega) = \frac{e^{i\mathbf{k}_f\cdot\mathbf{x}}}{(2\pi)^{3/2}}, \tag{3-3.9}$$

and, assuming that $\varphi(\mathbf{x},\omega)$ will also have a normalized plane wave structure, then

$$\varphi(\mathbf{x},\omega) = \phi_i(\mathbf{x},\omega) + \frac{e^{ik_{0v}x}}{x}f(\mathbf{k}_f,\mathbf{k}_i) \tag{3-3.10}$$

where a scattering amplitude, $f(\mathbf{k}_f,\mathbf{k}_i)$, has been defined as

$$f(\mathbf{k}_f,\mathbf{k}_i) = 2\pi^2\int \phi_f(\mathbf{x}',\omega)U(\mathbf{x}',\omega)\varphi(\mathbf{x}',\omega)d^3x', \tag{3-3.11}$$

and the incoming wavector is defined as

$$\mathbf{k}_i = k_{0v}(\mathbf{x}'/x). \tag{3-3.12}$$

So far, only a classical approach towards scattering has been followed. To obtain a semiclassical formalism that is general enough to deal with many types of incoming particles and scatterers, the scattering amplitude is related to the expectation value of a perturbation operator

$$f(\mathbf{k}_f,\mathbf{k}_i) = 2\pi^2\langle\phi_f|U|\psi\rangle \tag{3-3.13}$$

where $|\phi_f\rangle$ is the total final quantum state of the system which includes both the incoming particle and the scatterer, and $|\psi\rangle$ is the total quantum state of the system during the perturbation.

The form of the operator $U(\mathbf{x},\omega)$ can easily be obtained from quantum mechanics. For instance, nonrelativistic particles with mass obey the Schrödinger equation which can be put into the form of a scalar inhomogeneous wave equation. In frequency space the Schrödinger equation can be written in the form

$$\left(\nabla^2 + k_{0v}^2\right)\psi(\mathbf{x},\omega) = \left(2m/\hbar^2\right)V(\mathbf{x},\omega)\psi(\mathbf{x},\omega) \qquad (3\text{-}3.14)$$

where

$$k_{0v}^2 = 2mE/\hbar^2 . \qquad (3\text{-}3.15)$$

The scattering amplitude for particles with mass is then

$$f\left(\mathbf{k}_f,\mathbf{k}_i\right) = -\left(4\pi^2 m/\hbar^2\right)\langle\phi_f|V|\psi\rangle . \qquad (3\text{-}3.16)$$

3.4 Scattering Amplitude for Photons

To derive the scattering amplitude for massless incoming particles, a relativistic Schrödinger equation must be developed. This can be done by utilizing the Schrödinger time dependent equation

$$i\hbar\frac{\partial}{\partial t}\psi(\mathbf{x},t) = H\psi(\mathbf{x},t). \qquad (3\text{-}4.1)$$

The relativistic energy-momentum equation allows the construction of a Lorentz invariant Hamiltonian for the photon:

$$H^2 = p^2c^2 \qquad (3\text{-}4.2)$$

where $\mathbf{p} = -i\hbar\nabla$ and, from the Schrödinger time dependent equation,

$$H = i\hbar\frac{\partial}{\partial t}. \qquad (3\text{-}4.3)$$

Then Eq. 3-4.2 reduces to

$$\left(\frac{1}{c^2}\frac{\partial^2}{\partial t^2} - \nabla^2\right)\psi(\mathbf{x},t) = 0 \qquad (3\text{-}4.4)$$

when it operates on a wavefunction $\psi(\mathbf{x},t)$.

Define the space-time 4-momentum operator product as

$$-p^{\mu}p_{\mu}=\frac{1}{c^2}\frac{\partial^2}{\partial t^2}-\nabla^2=-\partial^{\mu}\partial_{\mu} \tag{3-4.5}$$

where
$$\partial_{\mu}=\left(\frac{1}{c}\frac{\partial}{\partial t},\mathbf{\nabla}\right),\ \partial^{\mu}=\left(\frac{1}{c}\frac{\partial}{\partial t},-\mathbf{\nabla}\right) \tag{3-4.6}$$

and
$$p^{\mu}=i\partial^{\mu}. \tag{3-4.7}$$

Then, the relativistic operator wave equation for a photon can be written in the form

$$\partial^{\mu}\partial_{\mu}\psi(\mathbf{x},t)=0. \tag{3-4.8}$$

The first quantization condition instructs one to perform a gauge transformation on the 4-momentum

$$p^{\mu}\rightarrow p^{\mu}+(e/c)A^{\mu} \tag{3-4.9}$$

where A^{μ} is the 4-vector potential, $A^{\mu}=(\Phi,\mathbf{A})$, and Φ and $\mathbf{A}$ are the scalar and vector potentials of the state consisting of both the photon and the scatterer. The gauge transformation then results in

$$p^{\mu}p_{\mu}=(i\partial^{\mu})(i\partial_{\mu})\rightarrow\left(i\partial^{\mu}+\frac{e}{c}A^{\mu}\right)\left(i\partial_{\mu}+\frac{e}{c}A_{\mu}\right).$$

Then

$$\partial^{\mu}\partial_{\mu}\psi(\mathbf{x},t)=V(\mathbf{x},t)\psi(\mathbf{x},t) \tag{3-4.10}$$

where
$$V(\mathbf{x},t)=i(e/c)\left[\partial_{\mu}A^{\mu}+A^{\mu}\partial_{\mu}\right]+(e/c)^2A^{\mu}A_{\mu}. \tag{3-4.11}$$

Equation 3-4.10 is the Klein-Gordon wave equation for a massless particle. Written out explicitly, it has the form of an inhomogeneous wave equation

$$\left(\nabla^2-\frac{1}{c^2}\frac{\partial^2}{\partial t^2}+V(\mathbf{x},t)\right)\psi(\mathbf{x},t)=0. \tag{3-4.12}$$

This expression can be written in frequency space by using the same methods as in Section 3.2 where, to maintain causality between sources and the fields they emit, the product $V(\mathbf{x},t)\psi(\mathbf{x},t)$ is more accurately expressed as the convolution in space and time of the two quantities. The frequency space representation of the Klein-Gordon wave equation is then

$$\left[\nabla^2+k_{0v}^2+V(\mathbf{x},\omega)\right]\psi(\mathbf{x},\omega)=0. \tag{3-4.13}$$

This equation has the same form as the classical wave equation, Eq. 3-2.11. Both equations must be equivalent in the many particle limit where the quantum and classical pictures converge. Thus, the index of refraction effect is the physical observable found by taking the expectation value and spatially averaging over the interaction volume of the interaction perturbation Hamiltonian

$$k_{0v}^2[2\varepsilon_0(\mathbf{x},\omega)] = const \times \overline{\langle \phi_f | V | \psi \rangle}. \tag{3-4.14}$$

The constant can be determined though the optical theorem. From the Maxwell equations the exponential decay of the intensity of a field traversing a distance d through a medium is related to a macroscopic total cross section

$$I = I_0 e^{-n_f \overline{\sigma_{tot}} d / V_0} \tag{3-4.15}$$

where n_f is the number of scatterers, I_0 is the incoming field intensity, and the macroscopic total cross section is the spatial average of the microscopic cross section derived in Section 2.3. But,

$$I = I_0 \left| e^{in\mathbf{k}_f \cdot \mathbf{x}} \right|^2 = I_0 e^{-k_f d \,\mathrm{Im}\{2\varepsilon_o\}}. \tag{3-4.16}$$

Then, for one scatterer

$$\mathrm{Im}\{2\varepsilon_0\} = \overline{\sigma_{tot}} / k_f V_0 = \frac{4\pi}{k_f^2 V_0} \mathrm{Im}\left\{ \overline{F(\mathbf{k}_f, \mathbf{k}_i)} \right\}. \tag{3-4.17}$$

If the imaginary parts of the two quantities are related by the expression above, then by analytical continuation both the real and imaginary parts are related by

$$2\varepsilon_0(\mathbf{x},\omega) = \frac{4\pi}{k_f^2 V_0} \overline{F(\mathbf{k}_f, \mathbf{k}_i)} = -\frac{4\pi}{k_f^2 V_0} A_0 \overline{T_{fi}}. \tag{3-4.18}$$

This is a form of the Lorentz relation seen in classical electrodynamics.[5] The constant in Eq. 3-4.14 has then been determined along with a direct form of the T-matrix elements

$$T_{fi} = \langle \phi_f | V | \psi \rangle. \tag{3-4.19}$$

The T-matrix elements on the energy shell are given in Eq. 2-2.18. A more general expression can now be derived by making use of the series expansion of the perturbed wavefunction, Eq. 2-1.5

$$\langle \phi_f(\mathbf{x},t) | V(\mathbf{x},t) | \psi(\mathbf{x},t) \rangle = \sum\nolimits_n a_n(t) e^{-iE_n t/\hbar} e^{iE_f t/\hbar} \int_{V_0} \phi_f^*(\mathbf{x}) V(\mathbf{x},t) \phi_n(\mathbf{x}) \, d^3x$$

$$= i\hbar \dot{S}_{fi}(t). \tag{3-4.20}$$

Thus, the T-matrix elements are proportional to the time rate of change of the transition amplitude from the final to the initial state. Also note that

$$\langle \phi_f | V | \psi \rangle = \langle \phi_f | T | \phi_i \rangle \tag{3-4.21}$$

which leads to
$$T | \phi_i \rangle = V | \psi \rangle = VS | \phi_i \rangle \tag{3-4.22}$$

and thus
$$T = VS. \tag{3-4.23}$$

The T-operator is then a scattering operator that describes the combined effect of a perturbation and an S-scattering operator.

3.5 Coherence Properties of the Scattering Amplitude

An examination of the S-matrix elements for a constant perturbation will yield useful information about the coherence properties of the scattering amplitude. From Eqs. 2-1.10 to 2-1.17 in the section on perturbation theory, and using the $i\varepsilon$ convergence factor to do the integrals as was done in Section 2.2, gives an expression for T_{fi} up to third order for the constant perturbation, Eq. 2-2.6:

$$T_{fi} = i\hbar\dot{S}_{fi}(t) = i\hbar\Big[(-i/\hbar)V_{fi}e^{i\omega_{fi}t} + (-i/\hbar)^2\sum_{n\neq i}V_{fn}e^{i\omega_{fn}t}\int_{-\infty}^{t}V_{ni}e^{i\omega_{ni}t'}\,dt'$$

$$+(-i/\hbar)^3\sum_{m\neq i}\sum_{n\neq m}V_{fn}e^{i\omega_{fn}t}\int_{-\infty}^{t}V_{nm}e^{i\omega_{nm}t_1}\,dt_1\int_{-\infty}^{t_1}V_{mi}e^{i\omega_{mi}t_2}\,dt_2+\cdots\Big]$$

$$= e^{i\omega_{fi}t}\left[V_{fi} + \sum_{n\neq i}\frac{V_{fn}V_{ni}}{E_i - E_n} + \sum_{m\neq i}\sum_{n\neq m}\frac{V_{fn}V_{nm}V_{mi}}{(E_i - E_m)(E_i - E_n)} + \cdots\right]. \qquad (3\text{-}5.1)$$

The variable t in the expressions above is simply a parameter that indicates when the perturbation is turned off. Since the lower limit of the integral in the evaluation of T_{fi} was $t = -\infty$, an assumption was made that the perturbation was left on for a time long compared to the period of the oscillator (many oscillations occured during the perturbation)

$$t >> \frac{1}{\omega_{fi}}. \qquad (3\text{-}5.2)$$

The coherence properties of T_{fi} are now readily evident. On the energy shell, or for energy conserving transitions where $E_i = E_f$, the overall phase factor disappears and gives, as expected, the on-energy-shell T-matrix elements expressed in Eq. 2-2.18. Off the energy shell, or for non-energy conserving transitions where $E_i \neq E_f$, the overall phase factor remains attached to T_{fi}. At this point one should note that there are no physical systems that can instantaneously turn off a perturbation--sources have an effective decay time associated with the lifetime of the atomic systems comprising the sources. There is then an uncertainty relation associated with when the perturbation is turned off which will

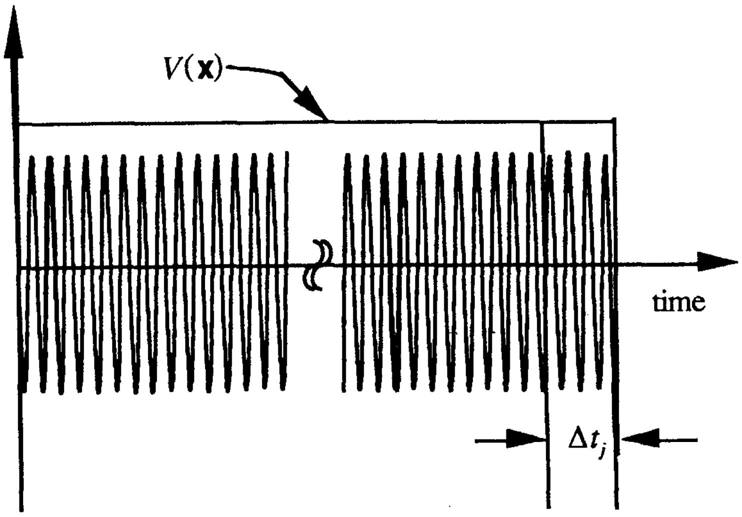

Fig. 3-5.1. Uncertainty, Δt_j, in when constant perturbation ceases.

be called a jitter, Δt_j. The jitter should be on the order of the inverse spontaneous linewidth, or decay rate, of the source

$$\Delta t_j \sim 1/\Gamma . \tag{3-5.3}$$

Typically Γ is on the order of or greater than $10^9/\mathrm{sec}$ (for atomic sources). Photons with frequencies in the visible to X-ray regime have energies $E > 0.1$ eV or frequencies $\nu > 10^{14}$ cycles/sec. Thus, for X-ray photons, the jitter will cover many periods of oscillation. Since the time parameter, t, is uncertain to within Δt_j, the phase is then essentially random. If $\omega_{fi} \neq 0$, then T_{fi} will exhibit a type of temporal incoherence.

The coherence properties can be observed in the definition of the differential scattering cross section

$$\frac{d\sigma}{d\Omega} = \left|F(\mathbf{k}_f, \mathbf{k}_i)\right|^2 = A_0^2 \left|T_{fi}\right|^2 . \tag{3-5.4}$$

If there is more than one final and initial state, then the total differential cross section is the sum over all possible states

$$\frac{d\sigma}{d\Omega} = A_0^2 \left|\sum_{fi} T_{fi}\right|^2 = A_0^2 \left|\sum_{fi} B_{fi} e^{i\phi_{fi}}\right|^2 \tag{3-5.5}$$

where B_{fi} is some complex scattering factor for the transition from $i \to f$ and $\phi_{fi} = \omega_{fi} t$ is a random phase factor. For the example in this section,

$$B_{fi} = V_{fi} + \sum_{n \neq i} \frac{V_{fn} V_{ni}}{E_i - E_n} + \sum_{m \neq i} \sum_{n \neq m} \frac{V_{fn} V_{nm} V_{mi}}{(E_i - E_m)(E_i - E_n)} + \cdots \tag{3-5.6}$$

Since ϕ_{fi} is a random phase, all the interference terms average to zero and

$$\frac{d\sigma}{d\Omega} = A_0^2 \left| \sum_{i,f=i} B_{fi} \right|^2 + A_0^2 \sum_{i,f\neq i} \left| B_{fi} \right|^2 . \qquad (3\text{-}5.7)$$

The total differential cross section is composed of two terms. The first term is a coherent sum of amplitudes that have the same temporal phase factor: $\phi_{fi} = 0$. Since each amplitude always lies on the energy shell, the scattering is elastic. The second term is an incoherent sum of amplitudes with nonzero random temporal phase factors. Since each amplitude always lies off the energy shell, the scattering is inelastic. Imbedded within each of the terms in Eq. 3-5.7 is a coherent sum over all possible intermediate states as represented by the expression for B_{fi} in Eq. 3-5.6. For this reason, calling the scattering process represented by each term in Eq. 3-5.7 as either a coherent or an incoherent process is misleading and ambiguous. For elastic scattering all scattering amplitudes are coherent with each other, whereas for inelastic scattering the scattering amplitudes may or may not be coherent with each other. This discussion is summarized below :

$$\left.\begin{array}{l}\text{Transition 1: } i \to f_1 \\ \text{Transition 2: } i \to f_2 \\ \text{Transition 3: } j \to k\end{array}\right\}$$

Amplitudes T_1 and T_2 are incoherent with respect to each other for $f_1 \neq f_2$. If $f_1 \neq f_2 \neq i$ the scattering amplitudes are inelastic $(\omega_{fi} \neq 0)$. If $\omega_{kj} = \omega_{f_1 i}$ then T_1 and T_3 are coherent with respect to each other (and inelastic if $f_1 \neq i$ and $k \neq j$)

$$\left.\begin{array}{l}\text{Transition 1: } i \to n_1 \to f \\ \text{Transition 2: } i \to n_2 \to f \\ \text{Transition 3: } j \to k \to m\end{array}\right\}$$

Amplitudes T_1 and T_2 are coherent with respect to each other, and if $f \neq i$ the scattering is inelastic. If $\omega_{mj} = \omega_{fi}$ then T_3 is coherent with respect to both T_1 and T_2.

$$\left.\begin{array}{l}\text{Transition 1: } i \to n_1 \to i \\ \text{Transition 2: } i \to n_2 \to i \\ \text{Transition 3: } j \to k \to j\end{array}\right\}$$

Amplitudes T_1 , T_2 , and T_3 are all coherent with respect to each other and the scattering is elastic.

3.6 Harmonic Perturbation

The interaction of a photon with a scatterer is modeled in perturbation theory by forcing the interaction perturbation to be a harmonic potential. Before second quantizing the scattering theory, important information can be extracted by examining the semiclassical perturbation of a monochromatic harmonic potential

$$V(\mathbf{x},t)=\begin{cases}0 & t\to-\infty \\ 2V(\mathbf{x})\cos\omega t & \end{cases}. \tag{3-6.1}$$

The T-matrix elements, to second order, are then

$$T_{fi}=V_{fi}\left[e^{i(\omega_{fi}+\omega)t}+e^{i(\omega_{fi}-\omega)t}\right]+\sum_{n\neq i}V_{fn}V_{ni}\left[\frac{e^{i\omega_{fi}t}+e^{i(\omega_{fi}+2\omega)t}}{E_i-(E_n+\hbar\omega)}+\frac{e^{i\omega_{fi}t}+e^{i(\omega_{fi}-2\omega)t}}{E_i-(E_n-\hbar\omega)}\right]. \tag{3-6.2}$$

Examining only the T-matrix elements that lie on the energy shell reveals that there can be both elastic and inelastic scattering processes (in the constant perturbation case of the last section only elastic scattering processes existed on the energy shell). These processes are summarized in the diagrams below.

(1). Single photon absorption (inelastic scattering):

$\omega_{fi}-\omega=0$ $\quad T_{fi}=V_{fi}$

$\underbrace{E_i+\hbar\omega}_{\text{initial state energy}}=\underbrace{E_f}_{\text{final state energy}}$ $\quad \Omega_{fi}=\omega_{\mathbf{k}_i}$

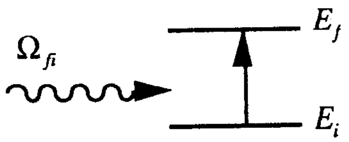

Fig. 3–6.1. Single photon absorption.

(2) Single photon emission (inelastic scattering):

$\omega_{fi}+\omega=0$ $\quad T_{fi}=V_{fi}$

$\underbrace{E_i}_{\text{initial state energy}}=\underbrace{E_f+\hbar\omega}_{\text{final state energy}}$ $\quad \Omega_{fi}=-\omega_{\mathbf{k}_f}$

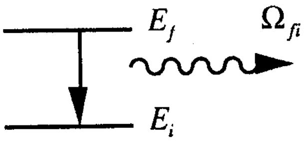

Fig. 3–6.2. Single photon emission.

(3) Two photon absorption (inelastic scattering):

$\omega_{fi} - 2\omega = 0$ $\qquad T_{fi} = \sum_{n \neq i} \frac{V_{fn} V_{ni}}{E_i - E_n + \hbar\Omega_{ni}}$

$E_i + 2\hbar\omega = E_f$ $\qquad \Omega_{ni} = \omega_{\mathbf{k}_i}$

$2\omega = \omega_{\mathbf{k}_i} + \omega'_{\mathbf{k}_i}$ $\qquad \Omega_{fn} = \omega'_{\mathbf{k}_i}$

For monochromatic incoming beam: $\omega_{\mathbf{k}_i} = \omega'_{\mathbf{k}_i}$

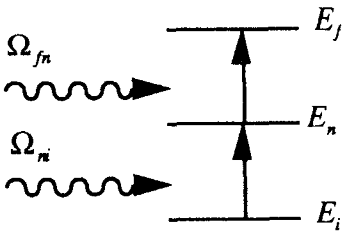

Fig. 3–6.3. Two photon absorption.

(4) Two photon emission (inelastic scattering):

$\omega_{fi} + 2\omega = 0$ $\qquad T_{fi} = \sum_{n \neq i} \frac{V_{fn} V_{ni}}{E_i - E_n + \hbar\Omega_{ni}}$

$E_i = E_f + 2\hbar\omega$ $\qquad \Omega_{ni} = -\omega_{\mathbf{k}_f}$

$2\omega = \omega_{\mathbf{k}_f} + \omega'_{\mathbf{k}_f}$ $\qquad \Omega_{fn} = -\omega'_{\mathbf{k}_f}$

For monochromatic outgoing beam: $\omega_{\mathbf{k}_f} = \omega'_{\mathbf{k}_f}$

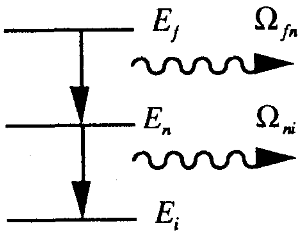

Fig. 3–6.4. Two photon emission.

(5) Absorption reemission (elastic if $\omega_{\mathbf{k}_i} = \omega_{\mathbf{k}_f}$):

$\omega_{fi} = 0$ $\qquad T_{fi} = \sum_{n \neq i} \frac{V_{fn} V_{ni}}{E_i - E_n + \hbar\Omega_{ni}}$

$E_i = E_f$ $\qquad \Omega_{ni} = \omega_{\mathbf{k}_i}$

$\Omega'_{ni} = -\omega_{\mathbf{k}_f}$

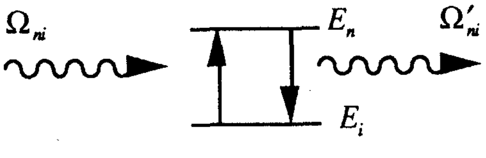

Fig. 3–6.5. Absorption reemission.

(6) Emission reabsorption (elastic if $\omega_{\mathbf{k}_i} = \omega_{\mathbf{k}_f}$):

$$\omega_{fi} = 0 \qquad T_{fi} = \sum_{n \neq i} \frac{V_{fn} V_{ni}}{E_i - E_n + \hbar\Omega_{ni}}$$

$$E_i = E_f \qquad \Omega_{ni} = -\omega_{\mathbf{k}_f}$$

$$\Omega'_{ni} = \omega_{\mathbf{k}_i}$$

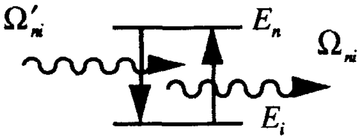

Fig. 3–6.6. Emission reabsorption.

Notice that even though the harmonic potential describes a single incoming particle, some of the processes (and all of the higher order terms) have more than one photon interacting with the oscillator. Perturbation theory then allows for many photon transitions to occur. Even though the semiclassical perturbation was not second quantized, it must consist of many discrete photons in order for the perturbation expansion to make sense. This is then a reconfirmation of what a classical field is--a distribution of quantum particles.

Note that the emission reabsorption case is simply the time reversed process of the absorption reemission case. There are also time reversed processes for the two photon absorption and emission cases that have been omitted. Performing a coherent sum over all these different processes leads to a total scattering amplitude which is similar to that derived in the constant perturbation case restricted to the energy shell

$$T_{fi} = V_{fi} + \sum_{n \neq i} \frac{V_{fn} V_{ni}}{E_i - (E_n - \hbar\Omega_{ni})} + \sum_{m \neq i} \sum_{n \neq m} \frac{V_{fn} V_{nm} V_{mi}}{\left[E_i - (E_m - \hbar\Omega_{mi})\right]\left[E_i - (E_n - \hbar\Omega_{ni})\right]} + \cdots. \tag{3-6.3}$$

3.7 Resonant Transitions

The expression in Eq. 3-6.3 is valid as long as all possible time ordered events are included. However, there appears to be a major problem for resonant transitions. For instance, for resonant two-photon processes, $\hbar\Omega_{ni} \approx E_n - E_i$, thus the second and all higher order terms in Eq. 3-6.3 go to infinity--the expansion appears to diverge. To keep the perturbation expansion convergent, a sum over many higher order terms must be performed. To do this, note that T_{fi} can be rewritten in a form similar to the Lippman-Schwinger equation

$$T_{fi} = V_{fi} + \sum_{n \neq i} \frac{V_{fn} T_{ni}}{E_i - E_n + \hbar\Omega_{ni}}. \qquad (3\text{-}7.1)$$

For instance, the third order term can be constructed by inserting the second order term in for T_{ni}. Doing so results in Eq. 3-6.3 when T_{mi} is set equal to V_{mi}. This procedure can be done indefinitely to obtain all the higher order terms.

Another problem that must be properly dealt with is the correct expression for $1/x$. From Dirac one finds that[6]

$$1/x = \mathrm{P}\{1/x\} - i\pi\delta(x) \qquad (3\text{-}7.2)$$

where P is the principal value and $\delta(x)$ is a Dirac delta function. This relationship can be inferred from noting that one would usually expect that

$$\frac{d}{dx} \ln x = 1/x. \qquad (3\text{-}7.3)$$

However, upon integrating both sides of the expression near $x = 0$ gives

$$\int_{-\eta}^{+\eta} d(\ln x) = \ln(-1) \quad \text{and} \quad \int_{-\eta}^{+\eta} 1/x \, dx = 0,$$

where the second integral is zero because $1/x$ is a well behaving odd function. The integration then leads to the contradiction: $\ln(-1) = 0$.

Using the relation for the log of a complex number

$$\ln x = \ln|x| + i \arg(x) \qquad (3\text{-}7.4)$$

allows the correction of Eq. 3-7.3 by setting $1/x$ to its expression in Eq. 3-7.2. This is the justification for Eq 3-7.2 (Note that $\arg(-1) = \pm\pi$. The minus sign was chosen for Eq. 3-7.2 because $1/x \sim 1/(E_i - E_n + \hbar\Omega_{ni} + i\varepsilon)$. The $i\varepsilon$ factor discussed in Section 2.2 has been suppressed in all preceding equations for convenience, but when it is considered in the integration above, one finds the minus sign to be the appropriate sign for Eq. 3-7.2. The $i\varepsilon$ factor, as discussed earlier, ensures that causality is obeyed.). For compactness define, as Heitler does, a ζ-function:[7]

$$\zeta(x) \equiv 1/x = \mathrm{P}\{1/x\} - i\pi\delta(x). \qquad (3\text{-}7.5)$$

If only two photon processes are of interest, then the second order term in Eq. 3-6.3 must be split from all the other terms. This is accomplished by summing up two photon and all higher two photon scattering processes. Noting that there is no first order term, V_{fi}, for two photon processes gives (converting Eq. 3-7.1 to operator form)

$$T = V\frac{1}{E-H_0}T$$

$$= V\frac{1}{E-H_0}V + V\frac{1}{E-H_0}V\frac{1}{E-H_0}V\frac{1}{E-H_0}V + \cdots \qquad (3\text{-}7.6)$$

where $H_0|n\rangle = E'_n|n\rangle = (E_n - \hbar\Omega_{ni})|n\rangle$ gives the energy of the intermediate state.

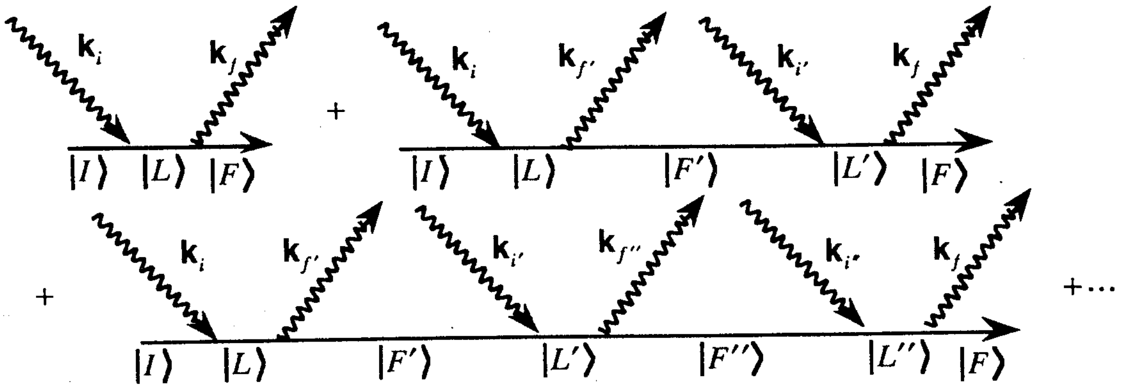

Fig. 3-7.1. Two photon absorption reemission scattering diagrams to all orders. The sum of all the scattering diagrams gives the total two photon scattering T-matrix elements.

This expansion is equivalent to summing two photon processes to all orders as shown in Fig.3-7.1 (for absorption reemission). This is a common procedure in quantum field theory, and there are plenty of tools available for performing the infinite sum (yielding, unfortunately, the same problems with ultraviolet divergences that must be dealt properly with renormalization theory). Using the identity[8]

$$\frac{1}{X+Y} = \frac{1}{X} - \frac{1}{X}Y\frac{1}{X} + \frac{1}{X}Y\frac{1}{X}Y\frac{1}{X} - \cdots \qquad (3\text{-}7.7)$$

gives

$$T = V\frac{1}{E-H_0+V\frac{1}{E-H_0}V}V \qquad (3\text{-}7.8)$$

or, in matrix element form,

$$T_{fi} = \sum_{n\neq i}\frac{\langle f|V|n\rangle\langle n|V|i\rangle}{E_i - E_n + \hbar\Omega_{ni} - \sum_{f\neq n}\frac{\langle n|V|f\rangle\langle f|V|n\rangle}{E_n - E_f + \hbar\Omega_{fn}}}$$

$$= \sum_{n\neq i} \frac{V_{fn}V_{ni}}{E_i - E_n + \hbar\Omega_{ni} - \dfrac{\Gamma_n\left(E_{nf}\right)}{2}} \qquad (3\text{-}7.9)$$

When adding up all higher order terms (as shown in Fig. 3-7.1), the two photon T-matrix elements acquires a term, $\Gamma_n\left(E_{nf}\right)$, in the denominator which prevents it from diverging on resonance ($E_i = E_n - \hbar\Omega_{ni}$). $\Gamma_n\left(E_{nf}\right)$ is the sum of all transitions from some intermediate state, $|n\rangle$, to all possible final states, $|f\rangle$. It is therefore usually called a complex spontaneous transition rate. Its real and imaginary parts can be examined in more detail by using the ζ-function in Eq. 3-7.5:

$$\Gamma_n\left(E_{nf}\right) = 2\sum_{f\neq n} V_{nf}V_{fn}\left[\mathrm{P}\left\{\frac{1}{E_n - E_f + \hbar\Omega_{fn}}\right\} - i\pi\delta\left(E_n - E_f + \hbar\Omega_{fn}\right)\right]. \qquad (3\text{-}7.10)$$

For absorption reemission, the resulting photon, Ω_{fn}, is an emitted photon, $-\omega_{\mathbf{k}_f}$. Then

$$\Gamma_n\left(E_{nf}\right) = \Gamma_n\left(E_{\mathbf{k}_f}\right) = \mathrm{P}\left\{2\sum_{f\neq n}\frac{\left|V_{fn}\right|^2}{E_n - E_f - \hbar\omega_{\mathbf{k}_f}}\right\} - 2\pi i\sum_{f\neq n}\left|V_{fn}\right|^2\delta\left(E_n - E_f - \hbar\omega_{\mathbf{k}_f}\right). \qquad (3\text{-}7.11)$$

The real part of $\Gamma_n\left(E_{\mathbf{k}_f}\right)$ is a level shift which is due to the self-energy of the scatterer and has a magnitude on the order of the natural linewidth.[5] The imaginary part corresponds to the natural linewidth and is a damping term caused by the effect of the emitted radiation on the oscillator--the oscillator produces its own damping self-force. This expression can be rewritten by substituting the non-physical, infinitely sharp δ-function by a density of states.

Let $d\rho(E)dE$ be the number of states in the interval E to $E + dE$. The density of states, $d\rho(E)$, can be obtained by solving for a particle in a box with sides of length L and imposing periodic boundary conditions. This gives rise to a discrete set of modes within the box:

$$e^{i\mathbf{k}\cdot\mathbf{x}} = e^{i\mathbf{k}\cdot(\mathbf{x}+\mathbf{L})}. \qquad (3\text{-}7.12)$$

This is satisfied if

$$k_i = (2\pi/L)N_i \qquad i = x,y,z; \quad N = 0,\pm 1,\pm 2,\ldots \ . \qquad (3\text{-}7\text{-}13)$$

The number of modes in the interval $N_x + dN_x$, $N_y + dN_y$, and $N_z + dN_z$ is then

$$dN = dN_x dN_y dN_z = (L/2\pi)^3 dk_x dk_y dk_z = \left[V_0/(2\pi)^3\right]k^2 dk d\Omega \qquad (3\text{-}7.14)$$

where V_0 is the volume of the box. The number of states in the wavevector interval **k** and $\mathbf{k}+d\mathbf{k}$ is then

$$d\rho(k)dk = \left[V_0/(2\pi)^3\right]k^2 dk d\Omega. \tag{3-7.15}$$

Since $d\rho(E)dE = d\rho(k)dk$, then for $E = \hbar ck$ the density of states is

$$d\rho(E) = \frac{V_0}{(2\pi)^3}(E/\hbar)^2 \frac{d\Omega}{\hbar c^3}. \tag{3-7.16}$$

Notice that $d\rho(E)$ is defined only within a narrow cone of angles $d\Omega$. For a single isolated oscillator, the emitted photon can travel in any direction, thus the spontaneous transition probability is obtained by integrating over all the possible final photon states and all possible final photon directions

$$\Gamma_n\left(E_{\mathbf{k}_f}\right) = \mathrm{P}\left\{2\sum_{f\neq n}\int dE_{\mathbf{k}_f}\frac{\left|V_{fn}\right|^2}{E_n - E_f - E_{\mathbf{k}_f}}d\rho\left(E_{\mathbf{k}_f}\right)\right\}$$

$$-2\pi i\sum_{f\neq n}\int dE_{\mathbf{k}_f}\left|V_{fn}\right|^2\delta\left(E_n - E_f - E_{\mathbf{k}_f}\right)d\rho\left(E_{\mathbf{k}_f}\right)$$

$$= 2D_n^+\left(E_{\mathbf{k}_f}\right) - i\Gamma_n^+\left(E_{\mathbf{k}_f}\right) \tag{3-7.17}$$

where,

$$D_n^+\left(E_{\mathbf{k}_f}\right) = \mathrm{P}\left\{\sum_{f\neq n}\int dE_{\mathbf{k}_f}d\Omega_{\mathbf{k}_f}\frac{\left|V_{fn}\right|^2}{E_n - E_f - E_{\mathbf{k}_f}}\rho\left(E_{\mathbf{k}_f}\right)\right\} \tag{3-7.18}$$

$$\Gamma_n^+\left(E_{\mathbf{k}_f}\right) = 2\pi\sum_{f\neq n}\int d\Omega_{\mathbf{k}_f}\left|V_{fn}\right|^2\rho\left(E_{nf}\right) \tag{3-7.19}$$

and

$$\rho(E) = \frac{V_0}{(2\pi)^3\hbar c^3}(E/\hbar)^2. \tag{3-7.20}$$

The energy level shift is $2D_n^+\left(E_{\mathbf{k}_f}\right)$, $\Gamma_n^+\left(E_{\mathbf{k}_f}\right)$ is the natural linewidth, and $\rho\left(E_n - E_f = E_{nf}\right)$ is the density of states. Note that $\Gamma_n^+\left(E_{\mathbf{k}_f}\right)$ is independent of the outgoing photon energy--this is because the δ-function is infinitely sharp at $E_{\mathbf{k}_f} = E_n - E_f$. Broadening out the delta function will yield a natural linewidth that slowly varies with the photon energy.

In the case of emission reabsorption (Fig. 3-6.6), $\Gamma_n\left(E_{\mathbf{k}_i}\right)$ is now a spontaneous absorption probability

$$\Gamma_n\left(E_{\mathbf{k}_i}\right)=2D_n^-\left(E_{\mathbf{k}_i}\right)-i\Gamma_n^-\left(E_{\mathbf{k}_i}\right), \tag{3-7.21}$$

where

$$D_n^-\left(E_{\mathbf{k}_i}\right)=\mathrm{P}\left\{\sum_{f\neq n}\int dE_{\mathbf{k}_i}d\Omega_{\mathbf{k}_i}\frac{\left|V_{fn}\right|^2}{E_n-E_f+E_{\mathbf{k}_i}}\rho\left(E_{\mathbf{k}_i}\right)\right\} \tag{3-7.22}$$

$$\Gamma_n^-\left(E_{\mathbf{k}_i}\right)=2\pi\sum_{f\neq n}\int d\Omega_{\mathbf{k}_i}\left|V_{fn}\right|^2\rho\left(E_{fn}\right). \tag{3-7.23}$$

The first order two photon T-matrix element is the sum of all allowable two photon processes (absorption reemission, emission reabsorption, two photon absorption, two photon emission)

$$T_{fi}=\sum_{n\neq f}\left\{\frac{V_{fn}^aV_{ni}^a}{E_i-E_n+\hbar\omega_{\mathbf{k}_i}-D_n^+\left(E_{\mathbf{k}_f}\right)+i\Gamma_n^+/2}+\frac{V_{fn}^bV_{ni}^b}{E_i-E_n-\hbar\omega_{\mathbf{k}_f}-D_n^-\left(E_{\mathbf{k}_i}\right)+i\Gamma_n^-/2}\right.$$

$$\left.+\left[\frac{V_{fn}^cV_{ni}^c}{E_i-E_n+\hbar\omega_{\mathbf{k}_i}-D_n^-\left(E_{\mathbf{k}_i'}\right)+i\Gamma_n^-/2}+\frac{V_{fn}^dV_{ni}^d}{E_i-E_n-\hbar\omega_{\mathbf{k}_f}-D_n^+\left(E_{\mathbf{k}_f'}\right)+i\Gamma_n^+/2}\right]_{f\neq i}\right\}. \tag{3-7.24}$$

When $i=f$, elastic scattering occurs and the last two terms become zero. When $i\neq f$, the first two terms describe inelastic spin-flip scattering since usually the exiting photon has a different spin that the incoming photon. However, in such a case, the scattering process is off the energy shell, and one would therefore have to multiply the two terms by a random phase factor as described in Section 3.5. When $i\neq f$, the last two terms describe an inelastic scattering process than can still lie on the energy shell if energy conservation is satisfied, $\hbar\left(\omega_{\mathbf{k}}+\omega_{\mathbf{k}}'\right)=\pm\left(E_f-E_i\right)$ as described in Figs. 3-6.3 and 3-6.4. For instance, the third term conserves energy as long as the oscillator stays in the excited state for the duration of one's observation. However, when both of the last two terms are considered on the energy shell, they describe a scattering process that appears elastic since now two photons enter and leave the system.

Finally, notice that the natural linewidth, $\Gamma_n^{\pm}$, is the sum of all transitions from an intermediate state to all possible final states. Thus $\Gamma_n^{\pm}$ contains contributions from both elastic and inelastic transitions. Then, $\Gamma_n^\pm$ can be described as the sum of the transitions rates for all the elastic and inelastic channels

$$\Gamma_n^\pm = \sum_i \Gamma_{\text{elastic}}^i + \sum_i \Gamma_{\text{inelastic}}^i \,. \tag{3-7.25}$$

The level shift $D_n^\pm$ is discussed in Goldberger and Watson.[5] It linearly diverges since the limits of integration in the expression is taken from $E_k = \infty \to 0$. This is an example of the common problem of ultraviolet divergences found in quantum field theory. Through renormalization of the scatterer's mass when taking care of the scatterer's self-energy, the divergence can be eliminated. In doing so one will find that the level shift is on the order of a natural linewidth, $\Gamma_n^\pm$.

REFERENCES

[1] J. D. Jackson, *Classical Electrodynamics* (Wiley, New York, 1975).

[2] H. Frauenfelder, *Subatomic Physics* (Prentice-Hall, Englewood Cliffs, N.J., 1974).

[3] B. A. Lippmann and J. Schwinger, *Phys. Rev.* **79**, 469 (1950).

[4] C. Cohen-Tannoudji, B. Diu, and F. Lalöe, *Quantum Mechanics* (Wiley, New York, 1977).

[5] M. L. Goldberger and K. M. Watson, *Collision Theory* (Wiley, New York, 1964).

[6] P. A. M. Dirac, *The Principles of Quantum Mechanics* (Clarendon Press, Oxford, 1958).

[7] W. Heitler, *The Quantum Theory of Radiation* (Clarendon Press, Oxford, 1954).

[8] J. J. Sakurai, *Advanced Quantum Mechanics* (Addison-Wesley, Reading, Mass., 1967).

4. MULTIPOLE FIELDS

4.1 Interaction Perturbation Hamiltonian

A multipole scattering amplitude can be constructed through evaluating the T-matrix elements described in Section 3.4.[1-8] In that section the T-matrix elements were shown to be proportional to the inhomogeneous term in the Klein-Gordon wave equation, or the interaction perturbation Hamiltonian described by Eq. 3-4.11, which describes the interaction of the electromagnetic field of a photon with a charged scatterer. Noting that the total wavefunction includes both the photon and the scatterer's wavefunction, the following decomposition can be made:

$$|\phi\rangle = |\phi^p;\phi^s\rangle \tag{4-1.1}$$

where $|\phi^p\rangle$ is the photon wavefunction, $|\phi^s\rangle$ is the scatterer's wavefunction, and $|\phi\rangle$ is the total stationary state wavefunction.

To compute T_{fi} the expectation value of the interaction perturbation over the initial and final stationary states must be evaluated. The contribution from only the scatterer's part of the total wavefunction is

$$V_{fi}^s = \int_{V_0} \phi_f^{s*} V \phi_i^s \, d^3x \, . \tag{4-1.2}$$

Then inserting Eq. 3-4.11 yields

$$V_{fi}^s = (ie/c)\int_{V_0} d^3x \left\{\phi_f^{s*}\left[\partial_\mu\left(A^\mu \phi_i^s\right)\right] + \phi_f^{s*} A^\mu \left(\partial_\mu \phi_i^s\right)\right\} + (e/c)^2 \int_{V_0} d^3x \, \phi_f^{s*} A^\mu A_\mu \phi_i^s \, . \tag{4-1.3}$$

Integrating the first term by parts leads to

$$\int_{V_0} \phi_f^{s*}\left[\partial_\mu\left(A^\mu \phi_i^s\right)\right] d^3x = \phi_f^{s*} A^\mu \phi_i^s \Big|_{V_0} - \int_{V_0} \left(\partial_\mu \phi_f^{s*}\right) A^\mu \phi_i^s \, d^3x \, .$$

The surface term goes to zero as the volume expands to infinity since the potential varies as $1/|\mathbf{x}|$. Then

$$V_{fi}^s = \frac{1}{c}\int_{V_0} d^3x \, j_\mu^{fi} A^\mu + (e/c)^2 \int_{V_0} d^3x \, \phi_f^{s*} A^\mu A_\mu \phi_i^s \tag{4-1.4}$$

where

$$j_\mu^{fi} = ie\left[\phi_f^{s*}\left(\partial_\mu \phi_i^s\right) - \left(\partial_\mu \phi_f^{s*}\right)\phi_i^s\right] \tag{4-1.5}$$

and j_μ^{fi} is the electromagnetic current of the charged spinless scatterer.

The Dirac equation can be used to evaluate j_μ^{fi} for a charged particle with spin:

$$\left(\gamma_\mu p^\mu - m\right)\psi^s = 0 \tag{4-1.6}$$

where γ_μ is a Dirac γ-matrix and m is the mass of the particle. Applying a gauge transformation on the 4-momentum, Eq. 3-4.9, leads to the expression

$$\left[\gamma_\mu p^\mu - m + (e/c)\gamma_\mu A^\mu\right]\psi^s = 0. \tag{4-1.7}$$

Defining the perturbation as[9]

$$\gamma^0 V(\mathbf{x},t) = (e/c)\gamma_\mu A^\mu(\mathbf{x},t) \tag{4-1.8}$$

leads to an interaction perturbation term similar to Eq. 4-1.4:

$$V_{fi}^s = \frac{1}{c}\int_{V_0} d^3x\, j_\mu^{fi} A^\mu + (e/c)^2 \int_{V_0} d^3x\, \psi_f^{s\dagger} A^\mu A_\mu \psi_i^s \tag{4-1.9}$$

where

$$j_\mu^{fi} = e\overline{\psi}_f^s \gamma_\mu \psi_i^s \tag{4-1.10}$$

and the quadratic potential term obtained from the Klein-Gordon equation has been simply added on (the Dirac equation is simply a linearized form of the Klein-Gordon equation and therefore does not yield this quadratic term). In this formalism, the wavefunction, ψ^s, of a charged particle is a 4-component spinor where each component satisfies the Klein-Gordon wave equation. The covariant normalization of fermions is usually defined as

$$\int \psi^\dagger \psi\, d^3x = 2E \approx 2m \tag{4-1.11}$$

where, in the nonrelativistic case, $E \approx m$.

When the photon wavefunctions are included, the matrix elements of the interaction perturbation becomes

$$V_{fi} = \left\langle \phi_f^p \middle| \frac{1}{c}\int_{V_0} d^3x\, j_\mu^{fi} A^\mu \middle| \phi_i^p \right\rangle + \frac{e^2}{2mc^2}\left\langle \phi_f^p;\phi_f^s \middle| A^\mu A_\mu \middle| \phi_i^p;\phi_i^s \right\rangle. \tag{4-1.12}$$

The timelike component of A^μ, or the scalar electrostatic potential, will be partially ignored. The scalar electrostatic potential contributes to an energy level shift called the isomer shift, and its effect will be included in the scattering amplitude where appropriate. Therefore, when computing the scattering amplitude, the 4-potential will be assumed to be

$$A^\mu = (0,\mathbf{A}) \tag{4-1.13}$$

where $\mathbf{A}$ is the magnetic vector potential.

4.2 Second Quantization

To conveniently manipulate the photon wavefunctions, the technique of second quantization will be applied. Here, the fields are quantized in a Hilbert space in which the basis states are the eigenstates of the number operator

$$N_{\mathbf{k}\lambda} = a_{\mathbf{k}\lambda}^{\dagger} a_{\mathbf{k}\lambda} \tag{4-2.1}$$

$$N_{\mathbf{k}\lambda} \left| n_{\mathbf{k}\lambda} \right\rangle = n_{\mathbf{k}\lambda} \left| n_{\mathbf{k}\lambda} \right\rangle \tag{4-2.2}$$

$$a_{\mathbf{k}\lambda} \left| n_{\mathbf{k}\lambda} \right\rangle = \sqrt{n_{\mathbf{k}\lambda}} \left| n_{\mathbf{k}\lambda} - 1 \right\rangle \tag{4-2.3}$$

$$a_{\mathbf{k}\lambda}^{\dagger} \left| n_{\mathbf{k}\lambda} \right\rangle = \sqrt{n_{\mathbf{k}\lambda} + 1} \left| n_{\mathbf{k}\lambda} + 1 \right\rangle \tag{4-2.4}$$

$$n_{\mathbf{k}\lambda} = 0, 1, 2, \ldots .$$

The operators $a_{\mathbf{k}\lambda}$ and $a_{\mathbf{k}\lambda}^{\dagger}$ are the familiar annihilation and creation operators, $\mathbf{k}$ is a photon propagation vector, λ is a polarization index, $n_{\mathbf{k}\lambda}$ is an occupation number, and $\hat{\boldsymbol{\varepsilon}}_{\mathbf{k}\lambda}$ is the polarization of the photon of frequency $\omega_{\mathbf{k}}$.

In this notation (the notation used in Weissbluth[7]), the vector potential is the sum over all the normal modes and polarizations of the system

$$\mathbf{A}(\mathbf{x},t) = \sum_{\mathbf{k}\lambda} \sqrt{\frac{2\pi\hbar c^2}{V_0 \omega_{\mathbf{k}}}}\, \hat{\boldsymbol{\varepsilon}}_{\mathbf{k}\lambda} \left[a_{\mathbf{k}\lambda} e^{i(\mathbf{k}\cdot\mathbf{x} - \omega_{\mathbf{k}} t)} + a_{\mathbf{k}\lambda}^{\dagger} e^{-i(\mathbf{k}\cdot\mathbf{x} - \omega_{\mathbf{k}} t)} \right]. \tag{4-2.5}$$

The basis states for the system will be written, for the sake of clarity, as

$$\left|\phi_i\right\rangle = \left|\phi_i^p; \phi_i^s\right\rangle = |\mathrm{I}\rangle = \left|n_{\mathbf{k}_i\lambda}; i_s\right\rangle \tag{4-2.6}$$

$$\left|\phi_f\right\rangle = \left|\phi_f^p; \phi_f^s\right\rangle = |\mathrm{F}\rangle = \left|n_{\mathbf{k}_f\lambda}; f_s\right\rangle . \tag{4-2.7}$$

The T-matrix elements, Eq. 2-2.18, can now be evaluated with the help of the scattering diagrams shown in Fig. 4-2.1.

Examining just the quadratic A^2 term in the interaction perturbation, Eq. 4-1.12, the T-matrix elements, up to first order, are

$$\begin{aligned} T_{fi} &= \frac{q^2}{2m_q c^2} \left\langle \phi_f^p; \phi_f^s \middle| \mathbf{A}\cdot\mathbf{A}^* \middle| \phi_i^p; \phi_i^s \right\rangle \\ &= \frac{q^2}{2m_q c^2} \sum_{\mathbf{k}\lambda} \sum_{\mathbf{k}'\lambda'} \frac{2\pi\hbar c}{V_0\sqrt{kk'}}\, \hat{\boldsymbol{\varepsilon}}_{\mathbf{k}\lambda} \cdot \hat{\boldsymbol{\varepsilon}}_{\mathbf{k}'\lambda'}^{*} \langle \mathrm{I} | \left[a_{\mathbf{k}\lambda} e^{i(\mathbf{k}\cdot\mathbf{x} - \omega_{\mathbf{k}} t)} + a_{\mathbf{k}\lambda}^{\dagger} e^{-i(\mathbf{k}\cdot\mathbf{x} - \omega_{\mathbf{k}} t)} \right] \\ &\quad \times \left[a_{\mathbf{k}'\lambda'} e^{i(\mathbf{k}'\cdot\mathbf{x} - \omega_{\mathbf{k}'} t)} + a_{\mathbf{k}'\lambda'}^{\dagger} e^{-i(\mathbf{k}'\cdot\mathbf{x} - \omega_{\mathbf{k}'} t)} \right] | \mathrm{F} \rangle \end{aligned} \tag{4-2.8}$$

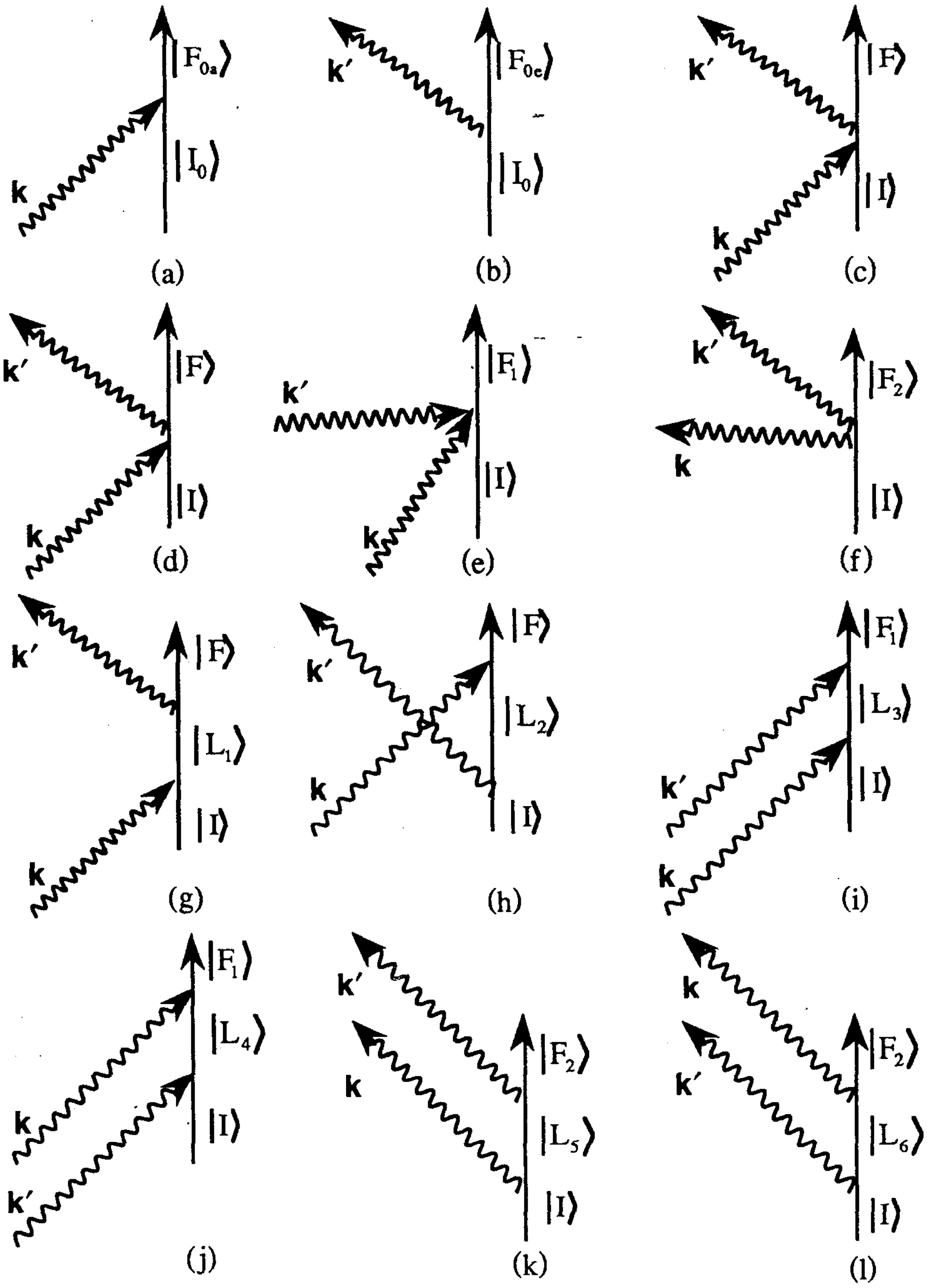

Fig. 4-2.1. Scattering diagrams: (a) and (b) single photon absorption and emission, (c) and (d) prompt two photon scattering [that the diagrams for prompt scattering and its time reversed process are the same can be seen by shrinking the intermediate state lifetime of diagrams (g) and (h) to zero], (e) and (f) prompt two photon absorption and emission [omitted the time reversed process since it corresponds to an equivalent diagram], (g) absorption reemission, (h) emission reabsorption [the time reversed diagram of (g)], (i) and (j) two photon absorption and its time reversed diagram, (k) and (l) two photon emission and its time reversed diagram.

Let the initial state of the system have occupation numbers $n_{\mathbf{k}\lambda}$ and $n_{\mathbf{k}'\lambda'}$:

$$|\mathrm{I}\rangle = |n_{\mathbf{k}\lambda}, n_{\mathbf{k}'\lambda'}; i_s\rangle. \tag{4-2.9}$$

For prompt scattering the final state of the system has occupation numbers $n_{\mathbf{k}'\lambda'}+1$ and $n_{\mathbf{k}\lambda}-1$ where one photon mode has gained a photon (the scattered photon) and another mode has lost a photon (the incoming photon):

$$|\mathrm{F}\rangle = |n_{\mathbf{k}\lambda}-1, n_{\mathbf{k}'\lambda'}+1; f_s\rangle. \tag{4-2.10}$$

The diagrams for this process and its time reversed process are shown in Figs. 4-2.1 (c) and (d).

The bilinear combinations of $a_{\mathbf{k}\lambda}$ and $a_{\mathbf{k}'\lambda'}$ and their Hermetian conjugates in Eq. 4-2.8 gives

$$\langle n_{\mathbf{k}\lambda}-1, n_{\mathbf{k}'\lambda'}+1|a_{\mathbf{k}\lambda}a_{\mathbf{k}'\lambda'}|n_{\mathbf{k}\lambda}, n_{\mathbf{k}'\lambda'}\rangle = 0$$

$$\langle n_{\mathbf{k}\lambda}-1, n_{\mathbf{k}'\lambda'}+1|a^\dagger_{\mathbf{k}\lambda}a^\dagger_{\mathbf{k}'\lambda'}|n_{\mathbf{k}\lambda}, n_{\mathbf{k}'\lambda'}\rangle = 0$$

$$\langle n_{\mathbf{k}\lambda}-1, n_{\mathbf{k}'\lambda'}+1|a_{\mathbf{k}\lambda}a^\dagger_{\mathbf{k}'\lambda'}|n_{\mathbf{k}\lambda}, n_{\mathbf{k}'\lambda'}\rangle = \sqrt{n_{\mathbf{k}\lambda}(n_{\mathbf{k}'\lambda'}+1)}.$$

Acknowledging that prompt scattering and its time reversed process are equivalent and associating $\mathbf{k}$ with the incoming photon $\mathbf{k}_i$, and $\mathbf{k}'$ with the outgoing photon $\mathbf{k}_f$, leads to the scattering amplitude

$$F(\mathbf{k}_f,\mathbf{k}_i) = -r_q\sqrt{k_f/k_i}\sqrt{n_f+1}\left(\hat{\varepsilon}^*_f\cdot\hat{\varepsilon}_i\right)\langle f_s|e^{-i(\mathbf{k}_f-\mathbf{k}_i)\cdot\mathbf{x}}|i_s\rangle \tag{4-2.11}$$

where

$$r_q = \frac{q^2}{m_q c^2} \tag{4-2.12}$$

and q is the charge of the scatterer with mass m_q. For electrons $r_q = r_e$ -- the electron radius. The minus comes from the optical theorem, Eq. 2-3.6, and it is expected since an oscillator tends to resist driving fields by producing induced fields that partially cancel the incoming fields--the induced fields are 180° out of phase with the driving fields.

The differential scattering cross section is related to the scattering amplitude by the relation shown in Eq. 3-5.4. It has a term proportional to the number of scattered photons n_f. This term is the result of stimulated scattering and is only significant at high intensities. For elastic scattering $k_i = k_f$ and, in the dipole approximation, the differential scattering cross section reduces to the familiar Thomson cross section

$$\frac{d\sigma}{d\Omega} = r_q^2\left(\hat{\varepsilon}^*_f\cdot\hat{\varepsilon}_i\right)|f_0|^2 \tag{4-2.13}$$

where

$$f_0 = \langle i_s|e^{-i(\mathbf{k}_f-\mathbf{k}_i)\cdot\mathbf{x}}|i_s\rangle \tag{4-2.14}$$

and f_0 is a scattering angle dependent form factor.

There is also a T-matrix element term for prompt two-photon absorption and emission arising from the bilinear combinations $a_{\mathbf{k}\lambda}a_{\mathbf{k}'\lambda'}$ and $a^\dagger_{\mathbf{k}\lambda}a^\dagger_{\mathbf{k}'\lambda'}$ of the interaction perturbation [see Figs. 4-2.1 (e) and (f)]. The final state occupation numbers for prompt two photon absorption are $n_{\mathbf{k}\lambda}-1$ and $n_{\mathbf{k}'\lambda'}-1$, and for prompt two photon emission the occupation numbers are $n_{\mathbf{k}\lambda}+1$ and $n_{\mathbf{k}'\lambda'}+1$. Each mode **k** and **k′** in the final state have either simultaneously lost or gained a photon. The scattering amplitude is then

$$F(\mathbf{k}_i',\mathbf{k}_i)=-r_q\sqrt{k_i'/k_i}\sqrt{n_i'}\left(\hat{\boldsymbol{\varepsilon}}_i'^{*}\cdot\hat{\boldsymbol{\varepsilon}}_i\right)\langle f_s|e^{i(\mathbf{k}_i'+\mathbf{k}_i)\cdot\mathbf{x}}|i_s\rangle \tag{4-2.15}$$

for prompt two photon absorption, and

$$F(\mathbf{k}_f',\mathbf{k}_f)=-r_e\sqrt{k_f'/k_f}\sqrt{(n_f'+1)(n_f+1)/n_f}\left(\hat{\boldsymbol{\varepsilon}}_f'^{*}\cdot\hat{\boldsymbol{\varepsilon}}_f\right)\langle f_s|e^{-i(\mathbf{k}_f'+\mathbf{k}_f)\cdot\mathbf{x}}|i_s\rangle \tag{4-2.16}$$

for prompt two photon emission. Since prompt two photon absorption and emission are inelastic processes, they can be safely ignored when considering only elastic processes.

Second order A^2 scattering gives rise to scattering of more than two photons and will therefore not be investigated.

For the current-vector potential coupling term in the interaction perturbation, Eq. 4-1.12, the T-matrix elements, up to second order, are

$$T_{fi}=\left\langle\phi_f^p;f_\alpha\left|\frac{1}{c}\int_{V_0}d^3x\,\mathbf{j}_{fi}\cdot\mathbf{A}\right|\phi_i^p;i_\alpha\right\rangle$$
$$+\sum_n\frac{\left\langle\phi_f^p;f_\alpha\left|\frac{1}{c}\int_{V_0}d^3x\,\mathbf{j}_{fn}\cdot\mathbf{A}\right|\phi_n^p;n_\alpha\right\rangle\left\langle\phi_n^p;n_\alpha\left|\frac{1}{c}\int_{V_0}d^3x\,\mathbf{j}_{ni}\cdot\mathbf{A}\right|\phi_i^p;i_\alpha\right\rangle}{E_\mathrm{I}-E_\mathrm{N}}. \tag{4-2.17}$$

States with the index α have been added to include quantum processes not described so far (such as phonon scattering). The scattering diagrams (along with their time reversed processes) are shown in Figs. 4-2.1 (g) through (l).

For the absorption reemission and its time reversed emission reabsorption process, the initial, final, and intermediate states shown in Figs. 4-2.1 (g) and (h) are

$$|\mathrm{I}\rangle=|n_{\mathbf{k}\lambda},n_{\mathbf{k}'\lambda'};i_\alpha\rangle$$
$$|\mathrm{L}_1\rangle=|n_{\mathbf{k}\lambda}-1,n_{\mathbf{k}'\lambda'};\ell_{1\alpha}\rangle$$
$$|\mathrm{L}_2\rangle=|n_{\mathbf{k}\lambda},n_{\mathbf{k}'\lambda'}+1;\ell_{2\alpha}\rangle$$
$$|\mathrm{F}\rangle=|n_{\mathbf{k}\lambda}-1,n_{\mathbf{k}'\lambda'}+1;f_\alpha\rangle.$$

Since these scattering events have intermediate states, they are properly described only by the second order T-matrix element term

$$F(\mathbf{k}_f,\mathbf{k}_i) = -A_0 \sum_{\ell} \frac{\langle \mathrm{F}|\frac{1}{c}\int_{V_0} d^3x\, \mathbf{j}_{f\ell} \cdot \mathbf{A}|\mathrm{L}\rangle\langle \mathrm{L}|\frac{1}{c}\int_{V_0} d^3x\, \mathbf{j}_{\ell i} \cdot \mathbf{A}|\mathrm{I}\rangle}{E_{\mathrm{I}} - E_{\mathrm{L}}} \tag{4-2.18}$$

where

$$\mathbf{A} = \sum_{\mathbf{k}\lambda} \sqrt{2\pi\hbar c/V_0 k}\, \hat{\boldsymbol{\varepsilon}}_{\mathbf{k}\lambda}\left[A_{\mathbf{k}\lambda} + A^{\dagger}_{\mathbf{k}\lambda}\right] \tag{4-2.19}$$

and

$$A_{\mathbf{k}\lambda} = a_{\mathbf{k}\lambda} e^{i\mathbf{k}\cdot\mathbf{x}}\,, \quad A^{\dagger}_{\mathbf{k}\lambda} = a^{\dagger}_{\mathbf{k}\lambda} e^{-i\mathbf{k}\cdot\mathbf{x}}. \tag{4-2.20}$$

One must now find those combinations of the matrix elements of $\mathbf{A}$ that yield nonzero values for each scattering process. For the case where $|\mathrm{L}_1\rangle$ is an intermediate state, $A_{\mathbf{k}\lambda}$ must be used to decrease the number of $\mathbf{k}$ photons by one in the state $|\mathrm{L}_1\rangle$, and $A^{\dagger}_{\mathbf{k}'\lambda'}$ must be used to increase the number of $\mathbf{k}'$ photons by one in the state $|\mathrm{F}\rangle$. Thus, the only nonzero matrix element combination is

$$\langle n_{\mathbf{k}\lambda} - 1, n_{\mathbf{k}'\lambda'} + 1; f_\alpha | A^{\dagger}_{\mathbf{k}'\lambda'} | n_{\mathbf{k}\lambda} - 1, n_{\mathbf{k}'\lambda'}; \ell_{1\alpha}\rangle\langle n_{\mathbf{k}\lambda} - 1, n_{\mathbf{k}'\lambda'}; \ell_{1\alpha} | A_{\mathbf{k}\lambda} | n_{\mathbf{k}\lambda}, n_{\mathbf{k}'\lambda'}; i_\alpha\rangle$$
$$= \langle f_\alpha | e^{-i\mathbf{k}'\cdot\mathbf{x}} | \ell_{1\alpha}\rangle\langle \ell_{1\alpha} | e^{i\mathbf{k}\cdot\mathbf{x}} | i_\alpha\rangle \sqrt{n_{\mathbf{k}\lambda}(n_{\mathbf{k}'\lambda'} + 1)}\,.$$

The initial and intermediate state energies can be read right off the scattering diagram, Fig. 4-2.1 (g).

$$E_{\mathrm{I}} = E_i + \hbar\omega_{\mathbf{k}} \tag{4-2.21}$$

$$E_{\mathrm{L}_1} = E_{\ell_1}. \tag{4-2.22}$$

Then the scattering amplitude is

$$F_{\ell_1}(\mathbf{k}_f,\mathbf{k}_i) = -\sqrt{k_f/k_i}\sqrt{n_f + 1}\, \frac{\langle f_\alpha | 1/c \int d^3x\, \hat{\boldsymbol{\varepsilon}}_f \cdot \mathbf{j}_{f\ell_1} e^{-i\mathbf{k}_f\cdot\mathbf{x}} | \ell_{1\alpha}\rangle\langle \ell_{1\alpha} | 1/c \int d^3x\, \hat{\boldsymbol{\varepsilon}}_i \cdot \mathbf{j}_{\ell_1 i} e^{i\mathbf{k}_i\cdot\mathbf{x}} | i_\alpha\rangle}{E_i - \left(E_{\ell_1} - \hbar\omega_{\mathbf{k}_i}\right)}. \tag{4-2.23}$$

For the emission reabsorption case, there is a loss of a $\mathbf{k}$ photon in the state $|\mathrm{F}\rangle$ and a gain of a $\mathbf{k}'$ photon in the state $|\mathrm{L}_2\rangle$. From the scattering diagram, Fig. 4-2.1 (h), the initial and intermediate state energies are

$$E_{\mathrm{I}} = E_i + \hbar\omega_{\mathbf{k}} \tag{4-2.24}$$

$$E_{\mathrm{L}_2} = E_{\ell_2} + \hbar\omega_{\mathbf{k}'} + \hbar\omega_{\mathbf{k}}. \tag{4-2.25}$$

The scattering amplitude for this process is then

$$F_{\ell_2}(\mathbf{k}_f,\mathbf{k}_i)=-\sqrt{k_f/k_i}\sqrt{n_f+1}\,\frac{\langle f_\alpha|1/c\int d^3x\,\hat{\boldsymbol{\varepsilon}}_i\cdot\mathbf{j}_{f\ell_2}\,e^{i\mathbf{k}_i\cdot\mathbf{x}}|\ell_{2\alpha}\rangle\langle\ell_{2\alpha}|1/c\int d^3x\,\hat{\boldsymbol{\varepsilon}}_f\cdot\mathbf{j}_{\ell_2 i}\,e^{-i\mathbf{k}_f\cdot\mathbf{x}}|i_\alpha\rangle}{E_i-\left(E_{\ell_2}+\hbar\omega_{\mathbf{k}_f}\right)}. \tag{4-2.26}$$

For the other scattering events in Fig. 4-2.1:

$$|\mathrm{I}_0\rangle=|n_{\mathbf{k}\lambda};i_\alpha\rangle$$

$$|\mathrm{F}_{0a}\rangle=|n_{\mathbf{k}\lambda}-1;f_\alpha\rangle$$

$$|\mathrm{F}_{0e}\rangle=|n_{\mathbf{k}'\lambda'}+1;f_\alpha\rangle$$

$$|\mathrm{L}_3\rangle=|n_{\mathbf{k}\lambda}-1,n_{\mathbf{k}'\lambda'};\ell_{3\alpha}\rangle\;;\quad E_{\mathrm{L}_3}=E_{\ell_3}+\hbar\omega_{\mathbf{k}'}\;;\quad E_{\mathrm{I}}=E_i+\hbar\omega_{\mathbf{k}}+\hbar\omega_{\mathbf{k}'}$$

$$|\mathrm{L}_4\rangle=|n_{\mathbf{k}\lambda},n_{\mathbf{k}'\lambda'}-1;\ell_{4\alpha}\rangle\;;\quad E_{\mathrm{L}_4}=E_{\ell_4}+\hbar\omega_{\mathbf{k}}\;;\quad E_{\mathrm{I}}=E_i+\hbar\omega_{\mathbf{k}}+\hbar\omega_{\mathbf{k}'}$$

$$|\mathrm{L}_5\rangle=|n_{\mathbf{k}\lambda}+1,n_{\mathbf{k}'\lambda'};\ell_{5\alpha}\rangle\;;\quad E_{\mathrm{L}_5}=E_{\ell_5}+\hbar\omega_{\mathbf{k}}\;;\quad E_{\mathrm{I}}=E_i$$

$$|\mathrm{L}_6\rangle=|n_{\mathbf{k}\lambda},n_{\mathbf{k}'\lambda'}+1;\ell_{6\alpha}\rangle\;;\quad E_{\mathrm{L}_6}=E_{\ell_6}+\hbar\omega_{\mathbf{k}'}\;;\quad E_{\mathrm{I}}=E_i$$

$$|\mathrm{F}_1\rangle=|n_{\mathbf{k}\lambda}-1,n_{\mathbf{k}'\lambda'}-1;f_\alpha\rangle$$

$$|\mathrm{F}_2\rangle=|n_{\mathbf{k}\lambda}+1,n_{\mathbf{k}'\lambda'}+1;f_\alpha\rangle$$

and their scattering amplitudes are found to be

$$F_{0a}(\mathbf{k}_i)=-\sqrt{V_0k_i/2\pi\hbar c}\,\langle f_\alpha|1/c\int d^3x\,\hat{\boldsymbol{\varepsilon}}_i\cdot\mathbf{j}_{fi}\,e^{i\mathbf{k}_i\cdot\mathbf{x}}|i_\alpha\rangle \tag{4-2.27}$$

$$F_{0e}(\mathbf{k}_f)=-\sqrt{V_0k_f/2\pi\hbar c}\sqrt{(n_f+1)/n_f}\,\langle f_\alpha|1/c\int d^3x\,\hat{\boldsymbol{\varepsilon}}_f\cdot\mathbf{j}_{fi}\,e^{-i\mathbf{k}_f\cdot\mathbf{x}}|i_\alpha\rangle \tag{4-2.28}$$

$$F_{\ell_3}(\mathbf{k}_i',\mathbf{k}_i)=-\sqrt{k_i'/k_i}\sqrt{n_i'}$$
$$\times\frac{\langle f_\alpha|1/c\int d^3x\,\hat{\boldsymbol{\varepsilon}}_i'\cdot\mathbf{j}_{f\ell_3}\,e^{i\mathbf{k}_i'\cdot\mathbf{x}}|\ell_{3\alpha}\rangle\langle\ell_{3\alpha}|1/c\int d^3x\,\hat{\boldsymbol{\varepsilon}}_i\cdot\mathbf{j}_{\ell_3 i}\,e^{i\mathbf{k}_i\cdot\mathbf{x}}|i_\alpha\rangle}{E_i-\left(E_{\ell_3}-\hbar\omega_{\mathbf{k}_i}\right)} \tag{4-2.29}$$

$$F_{\ell_4}(\mathbf{k}_i,\mathbf{k}_i')=-\sqrt{k_i'/k_i}\sqrt{n_i'}$$
$$\times\frac{\langle f_\alpha|1/c\int d^3x\,\hat{\boldsymbol{\varepsilon}}_i\cdot\mathbf{j}_{f\ell_4}\,e^{i\mathbf{k}_i\cdot\mathbf{x}}|\ell_{4\alpha}\rangle\langle\ell_{4\alpha}|1/c\int d^3x\,\hat{\boldsymbol{\varepsilon}}_i'\cdot\mathbf{j}_{\ell_4 i}\,e^{i\mathbf{k}_i'\cdot\mathbf{x}}|i_\alpha\rangle}{E_i-\left(E_{\ell_4}-\hbar\omega_{\mathbf{k}_i'}\right)} \tag{4-2.30}$$

$$F_{\ell_5}\left(\mathbf{k}'_f,\mathbf{k}_f\right)=-\sqrt{k'_f/k_f}\sqrt{\left(n_f+1\right)\left(n'_f+1\right)/n_f}$$

$$\times\frac{\left\langle f_\alpha\right|1/c\int d^3x\,\hat{\varepsilon}'_f\cdot\mathbf{j}_{f\ell_5}\,e^{-i\mathbf{k}'_f\cdot\mathbf{x}}\left|\ell_{5\alpha}\right\rangle\left\langle\ell_{5\alpha}\right|1/c\int d^3x\,\hat{\varepsilon}_f\cdot\mathbf{j}_{\ell_5 i}\,e^{-i\mathbf{k}_f\cdot\mathbf{x}}\left|i_\alpha\right\rangle}{E_i-\left(E_{\ell_5}+\hbar\omega_{\mathbf{k}_f}\right)} \tag{4-2.31}$$

$$F_{\ell_6}\left(\mathbf{k}_f,\mathbf{k}'_f\right)=-\sqrt{k'_f/k_f}\sqrt{\left(n_f+1\right)\left(n'_f+1\right)/n_f}$$

$$\times\frac{\left\langle f_\alpha\right|1/c\int d^3x\,\hat{\varepsilon}_f\cdot\mathbf{j}_{f\ell_6}\,e^{-i\mathbf{k}_f\cdot\mathbf{x}}\left|\ell_{6\alpha}\right\rangle\left\langle\ell_{6\alpha}\right|1/c\int d^3x\,\hat{\varepsilon}'_f\cdot\mathbf{j}_{\ell_6 i}\,e^{-i\mathbf{k}'_f\cdot\mathbf{x}}\left|i_\alpha\right\rangle}{E_i-\left(E_{\ell_6}+\hbar\omega_{\mathbf{k}'_f}\right)} \tag{4-2.32}$$

When considering only elastic scattering, the inelastic scattering amplitudes expressed by Eqs. 4-2.27 to 4.2-32 can be ignored.

For resonant transitions, all of the higher order terms of all the on-energy-shell scattering amplitudes must be taken into account as was done in Section 3.7. Following precisely the same procedures used in that section produces a natural linewidth that prevents the scattering amplitudes from becoming infinite on resonance.

4.3 Multipole Scattering Amplitude

The next step needed to be taken in investigating the scattering amplitude is the examination of its multipole structure. Following Frauenfelder's approach,[2] this can be accomplished by applying a spherical wave expansion on the plane wave

$$e^{i\mathbf{k}\cdot\mathbf{x}}=4\pi\sum_{\ell=0}^{\infty}i^\ell j_\ell(kr)\sum_{m=-\ell}^{\ell}Y^*_{\ell m}(\theta_\mathbf{k},\phi_\mathbf{k})Y_{\ell m}(\theta_r,\phi_r) \tag{4-3.1}$$

where

$$j_\ell(kr)=(\pi/2kr)^{1/2}J_{\ell+\frac{1}{2}}(kr) \tag{4-3.2}$$

and $j_\ell(kr)$ is a spherical Bessel function, the coordinate $\left(\theta_\mathbf{k},\phi_\mathbf{k}\right)$ is the direction of the wavector $\mathbf{k}$, and the coordinate $\left(r,\theta_r,\phi_r\right)$ is the location of the observation point in a coordinate system attached to the scatterer. The sum over ℓ, as will be shown later, gives the various multipole components of the plane wave (for instance, the dipole field corresponds to the $\ell=0$, 1, and 2 terms, the quadrupole field corresponds to the $\ell=1$, 2, and 3 terms, etc.) A matrix element U_{ni} defined as (temporarily dropping the f_α and n_α quantum numbers)

$$U_{ni} = 1/c \int d^3x\, \hat{\boldsymbol{\varepsilon}} \cdot \mathbf{j}_{ni}\, e^{i\mathbf{k}\cdot\mathbf{x}} \tag{4-3.3}$$

can then be expressed as

$$U_{ni} = \hat{\boldsymbol{\varepsilon}} \cdot \sum_{\ell=0}^{\infty} \sum_{m=-\ell}^{\ell} \sum_{q=-1}^{1} Y_{\ell m}^{*}(\theta_{\mathbf{k}}, \phi_{\mathbf{k}})(-1)^q \hat{\mathbf{e}}_{-q} \left[1/c \int d\mathbf{r}\ j_q^{ni}(\mathbf{r}) Y_{\ell m}(\theta_{\mathbf{r}}, \phi_{\mathbf{r}}) g_\ell(kr) \right] \tag{4-3.4}$$

where the current $\mathbf{j}_{ni}$ of the scatterer has been expressed in a spherical basis

$$\mathbf{j}_{ni} = \sum_{q=-1}^{1} (-1)^q j_q^{ni} \hat{\mathbf{e}}_{-q} \tag{4-3.5}$$

where

$$\hat{\mathbf{e}}_{\pm 1} = \mp 1/\sqrt{2}\left(\hat{\mathbf{e}}_x \pm i\hat{\mathbf{e}}_y\right) \tag{4-3.6}$$

$$\hat{\mathbf{e}}_0 = \hat{\mathbf{e}}_z \tag{4-3.7}$$

$$(-1)^q \hat{\mathbf{e}}_{-q} = \hat{\mathbf{e}}_q^{*} \tag{4-3.8}$$

and

$$g_\ell(kr) = 4\pi i^\ell j_\ell(kr) \tag{4-3.9}$$

The notation used in this section will closely follow the notation used by Weissbluth and Edmonds.[7, 10]

Note that the tensor product of two tensor operators of rank l and l' can be expressed as

$$V_Q^{(K)} = \left[\mathbf{T}^{(l)}\mathbf{U}^{(l')}\right]_Q^{(K)} = \sum_{qq'} T_q^{(l)} U_{q'}^{(l')} \langle lql'q' | ll'KQ \rangle. \tag{4-3.10}$$

The spherical harmonic $Y_{\ell m}(\theta_r, \phi_r)$ is a component of an irreducible tensor operator of rank ℓ. Then, since $\mathbf{j}_{ni}$ is a vector and therefore an irreducible tensor operator of rank 1,

$$\left[\mathbf{Y}^{(\ell)}\mathbf{j}^{(1)}\right]_M^{(L)} = \sum_{mq} Y_m^{(\ell)} j_q^{(1)} \langle \ell m 1 q | \ell 1 L M \rangle \tag{4-3.11}$$

where the ni index on $\mathbf{j}_{ni}$ is momentarily suppressed. Using the orthogonality relation for Clebsch-Gordan coefficients,

$$\sum\nolimits_{jm} \langle j_1 m_1' j_2 m_2' | j_1 j_2 j m \rangle \langle j_1 m_1 j_2 m_2 | j_1 j_2 j m \rangle = \delta_{m_1' m_1} \delta_{m_2' m_2}, \tag{4-3.12}$$

gives

$$\sum_{LM}\left[\mathbf{Y}^{(\ell)}\mathbf{j}^{(1)}\right]_M^{(L)}\langle \ell m 1 q|\ell 1 L M\rangle = \sum_{m'q'} Y_{m'}^{(\ell)} j_{q'}^{(1)} \sum_{LM}\langle \ell m' 1 q'|\ell 1 L M\rangle\langle \ell m 1 q|\ell 1 L M\rangle$$
$$= Y_m^{(\ell)} j_q^{(1)}. \tag{4-3.13}$$

Using this relation U_{ni} becomes

$$U_{ni} = \hat{\boldsymbol{\varepsilon}}\cdot\sum_{\ell=0}^{\infty}\sum_{m=-\ell}^{\ell}\sum_{q=-1}^{1}\sum_{LM} Y_{\ell m}^{*}(\Omega_{\mathbf{k}})\hat{\mathbf{e}}_q^{*}\langle \ell m 1 q|\ell 1 L M\rangle\langle j_n, m_n|1/c\int d\mathbf{r}\left[\mathbf{Y}^{(\ell)}\mathbf{j}^{(1)}\right]_M^{(L)} g_\ell(kr)|j_i, m_i\rangle \tag{4-3.14}$$

where the matrix elements of the current are defined in terms of the scatterer's spin and angular momentum components

$$\mathbf{j}_{ni} = \langle \phi_n^s|\mathbf{j}|\phi_i^s\rangle = \langle j_n, m_n|\mathbf{j}|j_i, m_i\rangle. \tag{4-3.15}$$

Note that the tensor product in Eq. 4-3.13 can be written in terms of a dot product of a vector spherical harmonic with the current. A vector spherical harmonic of rank J follows the relation

$$\mathbf{Y}_{JLSM} = \sum_{mq} Y_{Lm}\hat{\mathbf{e}}_q\langle L m S q|L S J M\rangle. \tag{4-3.16}$$

The vector spherical harmonic is proportional to the amplitude of the incoming particle. The total angular momentum of the particle is the sum of the orbital and spin angular momentum

$$\mathbf{J} = \mathbf{L} + \mathbf{S}, \tag{4-3.17}$$

and the vector spherical harmonic is the simultaneous eigenfunction of J^2, L^2, S^2, J_z, L_z, and S_z. The numbers M, m, and q are the projection quantum numbers of the total orbital, orbital, and spin angular momentum vectors respectively. For a photon vector field, $S = 1$, and the photon vector spherical harmonic, with the S subscript suppressed, is

$$\mathbf{Y}_{JLM} = \sum_{mq} Y_{Lm}\hat{\mathbf{e}}_q\langle L m 1 q|L 1 J M\rangle. \tag{4-3.18}$$

The tensor product in Eq. 4-3.14 can be written in the more convenient form of a dot product between a vector spherical harmonic and the current

$$\mathbf{Y}_{L\ell M}\cdot\mathbf{j} = \sum_{mq} Y_{\ell m}\langle \ell m 1 q|\ell 1 L M\rangle\sum_{q'} j_{q'}\hat{\mathbf{e}}_q\cdot\hat{\mathbf{e}}_{q'}^{*}. \tag{4-3.19}$$

But, unit vectors in the spherical basis follow the orthogonality rule

$$\hat{\mathbf{e}}_q\cdot\hat{\mathbf{e}}_p^{*} = \delta_{pq}, \tag{4-3.20}$$

so

$$\mathbf{Y}_{L\ell M} \cdot \mathbf{j} = \sum_{mq} Y_{\ell m} j_q \langle \ell m 1 q | \ell 1 L M \rangle = \left[\mathbf{Y}^{(\ell)} \mathbf{j}^{(1)} \right]_M^{(L)} \tag{4-3.21}$$

by comparison with Eq. 4-3.11.

Applying the Wigner-Eckart theorem,

$$\langle \alpha\, j\, m | T_q^{(k)} | \alpha'\, j'\, m' \rangle = \frac{1}{\sqrt{2j+1}} \langle j'\, m'\, k\, q | j'\, k\, j\, m \rangle \langle \alpha\, j \| \mathbf{T}^{(k)} \| \alpha'\, j' \rangle \tag{4-3.22}$$

and using the relation in Eqs. 4-3.18 and 4-3.21, the matrix elements can be written in terms of its reduced matrix elements

$$U_{ni} = \sum_{\ell=0}^{\infty} \sum_{LM} \left[\hat{\boldsymbol{\varepsilon}} \cdot \mathbf{Y}_{L\ell M}^{*}(\Omega_{\mathbf{k}}) \right] \frac{\langle j_i\, m_i\, L\, M | j_i\, L\, j_n\, m_n \rangle}{\sqrt{2j_n+1}} \chi(L,\ell) \tag{4-3.23}$$

where $$\chi(L,\ell) = \left| \left\langle j_n \left\| 1/c \int d\mathbf{r}\ \mathbf{A}_{L\ell M}(r,\Omega_{\mathrm{r}}) \cdot \mathbf{j}(\mathbf{r}) \right\| j_i \right\rangle \right| e^{i\eta(L,\ell)} \tag{4-3.24}$$

and $$\mathbf{A}_{L\ell M}(r,\Omega_{\mathrm{r}}) = \mathbf{Y}_{L\ell M}(\Omega_{\mathrm{r}}) g_\ell(kr). \tag{4-3.25}$$

The quantity $\chi(L,\ell)$ with phase $\eta(L,\ell)$ is a reduced matrix element that no longer depends upon m_n or m_f. Note that the z-axis of the coordinate system in which the angles $(\theta_{\mathbf{k}}, \phi_{\mathbf{k}}) = \Omega_{\mathbf{k}}$ are measured is now the quantum axis of the scatterer (such as an electron or nucleon).

Since

$$\mathbf{Y}_{L\ell M}(\Omega_{\mathbf{k}}) = \sum_{mq} Y_{\ell m} \hat{\mathbf{e}}_q \langle \ell m 1 q | \ell 1 L M \rangle, \tag{4-3.26}$$

the Clebsch-Gordan coefficient gives a constraint on the possible values of ℓ due to the selection rules for the coupling of two angular momentum

$$|\ell - 1| \le L \le \ell + 1. \tag{4-3.27}$$

Then, the only possible values of ℓ for a given L are

$$\ell = L, L \pm 1 \tag{4-3.28}$$

The selection rules also constrain the possible values of M

$$M = m + q. \tag{4-3.29}$$

The expression for U_{ni} in Eq. 4-3.23 contains information about transverse electric and magnetic and longitudinal multipole fields. To see this, first examine the $\ell = L$ component of $\mathbf{Y}_{L\ell M}$:

$$
\begin{aligned}
\mathbf{Y}_{LLM} &= \sum_q Y_{L,M-q}\hat{\mathbf{e}}_q \langle L, M-q, 1, q | L 1 L M\rangle \\
&= (-1)^{1-L-M}\sqrt{2L+1}\left\{\begin{pmatrix} L & 1 & L \\ M-1 & 1 & -M \end{pmatrix} Y_{\ell,M-1}\hat{\mathbf{e}}_{+1} + \begin{pmatrix} L & 1 & L \\ M & 0 & -M \end{pmatrix} Y_{\ell M}\hat{\mathbf{e}}_0 \right. \\
&\quad \left. + \begin{pmatrix} L & 1 & L \\ M+1 & -1 & -M \end{pmatrix} Y_{\ell,M+1}\hat{\mathbf{e}}_{-1} \right\} \\
&= \sqrt{2L+1}\left\{(-1)\sqrt{\frac{(L+M)(L-M+1)}{(L+1)(2L+1)2L}}\, Y_{\ell,M-1}\hat{\mathbf{e}}_{+1} + \frac{M}{\sqrt{(2L+1)(L+1)L}}\, Y_{\ell M}\hat{\mathbf{e}}_0 \right. \\
&\quad \left. + (-1)^{-2(L+M)}\sqrt{\frac{(L-M)(L+M+1)}{(L+1)(2L+1)2L}}\, Y_{\ell,M+1}\hat{\mathbf{e}}_{-1} \right\}
\end{aligned}
\tag{4-3.30}
$$

where the following identity between the Clebsch-Gordan coefficients and the Wigner $3\text{-}j$ symbol was used:

$$
\langle j_1 m_1\, j_2 m_2 | j_1\, j_2\, j m\rangle = (-1)^{j_2-j_1-m}\sqrt{2j+1}\begin{pmatrix} j_1 & j_2 & j \\ m_1 & m_2 & -m \end{pmatrix}. \tag{4-3.31}
$$

Tables , such as in Weissbluth or Edmonds,[7, 10, 11] give formulas for special types of $3\text{-}j$ symbols. The exponent $2(L+M)$ is an even integer because if L is either integral or half integral then so is M since $M = L, L-1, \ldots, -L$. Utilizing the properties of the lowering and raising operators of angular momentum

$$
L_{\pm}Y_{\ell m} = \mp\frac{1}{\sqrt{2}}\sqrt{\ell(\ell+1) - m(m\pm 1)}\; Y_{\ell,m\pm 1} \tag{4-3.32}
$$

$$
L_0 Y_{\ell m} = m Y_{\ell m} \tag{4-3.33}
$$

yields

$$
\begin{aligned}
\mathbf{Y}_{LLM} &= \frac{-\left(1/\sqrt{2}\right)\sqrt{L(L+1) - M(M-1)}}{\sqrt{L(L+1)}}\, Y_{\ell,M-1}\hat{\mathbf{e}}_{+1} + \frac{M}{\sqrt{L(L+1)}}\, Y_{\ell M}\hat{\mathbf{e}}_0 \\
&\quad + \frac{\left(1/\sqrt{2}\right)\sqrt{L(L+1) - M(M+1)}}{\sqrt{L(L+1)}}\, Y_{\ell,M+1}\hat{\mathbf{e}}_{-1}
\end{aligned}
$$

$$= \frac{-L_- Y_{\ell,M-1}\hat{\mathbf{e}}_{+1} + L_0 Y_{\ell M}\hat{\mathbf{e}}_0 + L_+ Y_{\ell,M+1}\hat{\mathbf{e}}_{-1}}{\sqrt{L(L+1)}} = \frac{1}{\sqrt{L(L+1)}}\left(\sum\nolimits_q (-1)^q L_q \hat{\mathbf{e}}_{-q}\right) Y_{LM}$$

$$= \frac{\mathbf{L} Y_{LM}}{\sqrt{L(L+1)}}. \tag{4-3.34}$$

The angular momentum operator can be written as

$$\mathbf{L} = \mathbf{r} \times \mathbf{p} = -i(\mathbf{r} \times \nabla) \tag{4-3.35}$$

where $\mathbf{r}$ a radial vector. Then

$$\hat{\mathbf{r}} \cdot \mathbf{Y}_{LLM} = \left(-i/\sqrt{L(L+1)}\right)\hat{\mathbf{r}} \cdot (\mathbf{r} \times \nabla) = \left(-i/\sqrt{L(L+1)}\right)\nabla \cdot (\hat{\mathbf{r}} \times \mathbf{r})$$

$$= 0. \tag{4-3.36}$$

Thus, $\mathbf{Y}_{LLM}$ is a transverse vector spherical harmonic, and, since it is related to the angular momentum operator, it is associated with the magnetic multipole electric field. Akhiezer and Berestetskii[8] define this field as $\mathbf{Y}_{LM}^{(0)}$ and Rose[5] as a magnetic multipole field $\mathbf{Y}_{LM}^{(\mathrm{m})}$. Thus, depending upon notation

$$\mathbf{Y}_{LLM} = \mathbf{Y}_{LM}^{(0)} = \mathbf{Y}_{LM}^{(\mathrm{m})}. \tag{4-3.37}$$

To obtain the electric multipole electric field, the cross product between the magnetic multipole field and $\hat{\mathbf{r}}$ is taken as defined below

$$i\mathbf{Y}_{LM}^{(\mathrm{e})} = \hat{\mathbf{r}} \times \mathbf{Y}_{LM}^{(\mathrm{m})}. \tag{4-3.38}$$

Also similarly

$$i\mathbf{Y}_{LM}^{(\mathrm{m})} = \hat{\mathbf{r}} \times \mathbf{Y}_{LM}^{(\mathrm{e})}. \tag{4-3.39}$$

From Akhiezer and Berestetskii, the electric multipole field is related to the vector spherical harmonics as follows

$$\mathbf{Y}_{jm}^{(1)} = \mathbf{Y}_{jm}^{(\mathrm{e})} = \sqrt{\frac{j}{2j+1}}\,\mathbf{Y}_{j,j+1,m} + \sqrt{\frac{j+1}{2j+1}}\,\mathbf{Y}_{j,j-1,m}. \tag{4-3.40}$$

From the differential properties of the gradient of a scalar[8, 12]

$$r\nabla Y_{jm} = j\sqrt{\frac{j+1}{2j+1}}\,\mathbf{Y}_{j,j+1,m} + (j+1)\sqrt{\frac{j}{2j+1}}\,\mathbf{Y}_{j,j-1,m}, \tag{4-3.41}$$

one can see that the electric multipole electric field is related to the linear momentum operator

$$\mathbf{Y}_{jm}^{(e)} = \frac{ir}{\hbar\sqrt{j(j+1)}}\,\mathbf{p} Y_{jm} \tag{4-3.42}$$

where $\mathbf{p} = -i\hbar\nabla$.

The other vector field has only longitudinal components along $\hat{\mathbf{r}}$:

$$\mathbf{Y}^{(-1)}_{jm} = \mathbf{Y}^{(l)}_{jm} = \hat{\mathbf{r}} Y_{jm} = \sqrt{\frac{j}{2j+1}}\,\mathbf{Y}_{j,j-1,m} - \sqrt{\frac{j+1}{2j+1}}\,\mathbf{Y}_{j,j+1,m}. \tag{4-3.43}$$

These three vector fields form an orthogonal basis about which any field can be expanded.

Going back to the expression for U_{ni}, there is a summation term

$$\sum_{\ell=L-1}^{L+1} \mathbf{Y}_{L\ell M}(\Omega_{\mathbf{k}})\mathbf{Y}_{L\ell M}(\Omega_{\mathbf{r}}) g_\ell(kr) = \mathbf{Y}_{LLM}(\Omega_{\mathbf{k}})\mathbf{Y}_{LLM}(\Omega_{\mathbf{r}}) g_L(kr)$$
$$+ \mathbf{Y}_{L,L-1,M}(\Omega_{\mathbf{k}})\mathbf{Y}_{L,L-1,M}(\Omega_{\mathbf{r}}) g_{L-1}(kr) + \mathbf{Y}_{L,L+1,M}(\Omega_{\mathbf{k}})\mathbf{Y}_{L,L+1,M}(\Omega_{\mathbf{r}}) g_{L+1}(kr).$$

The first term can be expressed in terms of the magnetic multipole field $\mathbf{Y}^{(\mathrm{m})}_{LM}$. The next two terms give the electric and longitudinal fields. First note that the vector spherical harmonics of angular momenta $j \pm 1$ can be expressed in terms of the multipole fields

$$\mathbf{Y}_{j,j+1,m} = \left(1/\sqrt{2j+1}\right)\left(\sqrt{j}\,\mathbf{Y}^{(1)}_{jm} - \sqrt{j+1}\,\mathbf{Y}^{(-1)}_{jm}\right) \tag{4-3.44}$$

$$\mathbf{Y}_{j,j-1,m} = \left(1/\sqrt{2j+1}\right)\left(\sqrt{j+1}\,\mathbf{Y}^{(1)}_{jm} + \sqrt{j}\,\mathbf{Y}^{(-1)}_{jm}\right). \tag{4-3.45}$$

Then

$$\sum_{\ell=L-1}^{L+1} \mathbf{Y}_{L\ell M}(\Omega_{\mathbf{k}})\mathbf{Y}_{L\ell M}(\Omega_{\mathbf{r}}) g_\ell(kr) = \sum_{\lambda=-1}^{1} \mathbf{Y}^{(\lambda)}_{LM}(\Omega_{\mathbf{k}})\mathbf{A}^{(\lambda)}_{LM}(r,\Omega_{\mathbf{r}}) \tag{4-3.46}$$

where

$$\mathbf{A}^{(0)}_{LM}(r,\Omega_{\mathbf{r}}) = \mathbf{Y}_{LLM}(\Omega_{\mathbf{r}}) g_L(kr) \tag{4-3.47}$$

$$\mathbf{A}^{(\pm)}_{LM}(r,\Omega_{\mathbf{r}}) = \frac{1}{2L+1}\Big\{\left[L g_{L\pm 1}(kr) + (L+1) g_{L\mp 1}(kr)\right]\mathbf{Y}^{(\pm)}_{LM}(\Omega_{\mathbf{r}})$$
$$+ \sqrt{L(L+1)}\left[g_{L-1}(kr) - g_{L+1}(kr)\right]\mathbf{Y}^{(\mp)}_{LM}(\Omega_{\mathbf{r}}). \tag{4-3.48}$$

The matrix elements, U_{ni}, can now be expressed as a sum of the transverse and longitudinal multipole fields

$$U_{ni} = \sum_{\lambda=-1}^{1} \sum_{LM} \left[\hat{\varepsilon} \cdot \mathbf{Y}^{(\lambda)*}_{LM}(\Omega_{\mathbf{k}})\right] \frac{\langle j_i m_i LM | j_i L j_n m_n \rangle}{\sqrt{2j_n+1}} \chi(L,\lambda) \tag{4-3.49}$$

where $$\chi(L,\lambda) = \left| \left\langle j_n \middle\| 1/c \int d\mathbf{r}\; \mathbf{A}^{(\lambda)}_{LM}(r,\Omega_{\mathbf{r}}) \cdot \mathbf{j}(\mathbf{r}) \middle\| j_i \right\rangle \right| e^{i\eta(L,\lambda)}. \tag{4-3.50}$$

Another expression for the expansion of a vector field plane wave has thus been derived

$$\hat{\boldsymbol{\varepsilon}} e^{i\mathbf{k}\cdot\mathbf{x}} = \sum_{LM} \sum_{\lambda=-1}^{1} \left[\hat{\boldsymbol{\varepsilon}} \cdot \mathbf{Y}_{LM}^{(\lambda)*}(\Omega_{\mathbf{k}})\right] \mathbf{A}_{LM}^{(\lambda)}(r,\Omega_{\mathbf{r}})$$

$$= \sum_{LM} \left\{\left[\hat{\boldsymbol{\varepsilon}} \cdot \mathbf{Y}_{LM}^{(\mathrm{e})*}(\Omega_{\mathbf{k}})\right] \mathbf{A}_{LM}^{(\mathrm{e})}(r,\Omega_{\mathbf{r}}) + \left[\hat{\boldsymbol{\varepsilon}} \cdot \mathbf{Y}_{LM}^{(\mathrm{m})*}(\Omega_{\mathbf{k}})\right] \mathbf{A}_{LM}^{(\mathrm{m})}(r,\Omega_{\mathbf{r}}) + \left[\hat{\boldsymbol{\varepsilon}} \cdot \mathbf{Y}_{LM}^{(l)*}(\Omega_{\mathbf{k}})\right] \mathbf{A}_{LM}^{(l)}(r,\Omega_{\mathbf{r}})\right\}. \tag{4-3.51}$$

This shows the decomposition of a vector field into its transverse electric and magnetic $(\text{e and m or } \lambda = 1 \text{ and } 0)$ and longitudinal $(l \text{ or } \lambda = -1)$ multipole components. This is basically what Rose has done but in a different manner.[5] Another expression for the vector potential is then

$$\mathbf{A}(\mathbf{x},t) = \sum_{\mathbf{k}\lambda} \sqrt{\frac{2\pi\hbar c^2}{V_0 \omega_{\mathbf{k}}}} \left\{ \sum_{LM} \sum_{\ell=L-1}^{L+1} \Big(a_{\mathbf{k}\lambda} \left[\hat{\boldsymbol{\varepsilon}}_{\mathbf{k}\lambda} \cdot \mathbf{Y}_{L\ell M}^{*}(\Omega_{\mathbf{k}})\right] \mathbf{A}_{L\ell M}(r,\Omega_{\mathbf{r}}) e^{-i\omega_{\mathbf{k}} t} \right.$$

$$\left. + \, a_{\mathbf{k}\lambda}^{\dagger} \left[\hat{\boldsymbol{\varepsilon}}_{\mathbf{k}\lambda}^{*} \cdot \mathbf{Y}_{L\ell M}(\Omega_{\mathbf{k}})\right] \mathbf{A}_{L\ell M}^{*}(r,\Omega_{\mathbf{r}}) e^{i\omega_{\mathbf{k}} t} \Big) \right\} \tag{4-3.52}$$

$$= \sum_{\mathbf{k}\lambda} \sqrt{\frac{2\pi\hbar c^2}{V_0 \omega_{\mathbf{k}}}} \left\{ \sum_{LM} \sum_{p=-1}^{1} \Big(a_{\mathbf{k}\lambda} \left[\hat{\boldsymbol{\varepsilon}}_{\mathbf{k}\lambda} \cdot \mathbf{Y}_{LM}^{(p)*}(\Omega_{\mathbf{k}})\right] \mathbf{A}_{LM}^{(p)}(r,\Omega_{\mathbf{r}}) e^{-i\omega_{\mathbf{k}} t} \right.$$

$$\left. + \, a_{\mathbf{k}\lambda}^{\dagger} \left[\hat{\boldsymbol{\varepsilon}}_{\mathbf{k}\lambda}^{*} \cdot \mathbf{Y}_{LM}^{(p)}(\Omega_{\mathbf{k}})\right] \mathbf{A}_{LM}^{(p)*}(r,\Omega_{\mathbf{r}}) e^{i\omega_{\mathbf{k}} t} \Big) \right\} \tag{4-3.53}$$

where the vector spherical harmonics are constructed in the quantum coordinate system of the scatterer.

The scattering amplitude can now be expressed in terms of multipole fields. For the case of spontaneous absorption reemission $(n_f = 0)$, the scattering amplitude on the energy shell is

$$F_n(\mathbf{k}_f,\mathbf{k}_i) = \frac{U_{fn} U_{ni}}{E_i - E_n + \hbar\omega_{\mathbf{k}_i} + i\Gamma_n/2} \tag{4-3.54}$$

where

$$U_{fn} = \left\langle j_f, m_f; f_\alpha \middle| 1/c \int d^3x \, \hat{\boldsymbol{\varepsilon}}_f^{*} \cdot \mathbf{j} e^{-i\mathbf{k}_f\cdot\mathbf{x}} \middle| j_n, m_n; n_\alpha \right\rangle \tag{4-3.55}$$

$$U_{ni} = \left\langle j_n, m_n; n_\alpha \middle| 1/c \int d^3x \, \hat{\boldsymbol{\varepsilon}}_i \cdot \mathbf{j} e^{i\mathbf{k}_i\cdot\mathbf{x}} \middle| j_i, m_i; i_\alpha \right\rangle. \tag{4-3.56}$$

The polarization of the scattered photon has been complex conjugated to handle complex polarizations.

The natural linewidth, Γ_n, described in Section 3.7, can be readily evaluated in terms of the reduced matrix elements $\chi(L,\ell)$. In terms of the matrix elements U_{fn},

$$\Gamma_n = 2\pi \sum_{f\neq n} \int d\Omega_{\mathbf{k}_f} \frac{|U_{fn}|^2}{A_0}\rho(E_{in}) \qquad (4\text{-}3.57)$$

where A_0 is given by Eq. 2-3.8, and the density of states, $\rho(E_{in})$, is given by Eq. 3-7.25. $U_{fn} = U^*_{ni}$ with the interchange of indices $i \rightarrow f$, and U_{ni} is given by Eq. 4-3.23 or 4-3.49. The sum over all final states is the sum over all final angular momentum, spin, photon modes, and polarization states: $\sum_{f\neq n} = \sum_{j_f m_f} \sum_{\mathbf{k}_f \lambda}$. For only one photon mode, $\mathbf{k}_f$, the sum over photon modes can be ignored. With the help of the orthogonality of spherical harmonics,

$$\int d\Omega\, Y^*_{\ell m}(\Omega) Y_{\ell' m'}(\Omega) = \delta_{\ell\ell'}\,\delta_{mm'}, \qquad (4\text{-}3.58)$$

the angular integral in Γ_n is then

$$\begin{aligned}
\sum_{\lambda} \int d\Omega_{\mathbf{k}_f} \left|\hat{\boldsymbol{\varepsilon}}_\lambda \cdot \mathbf{Y}^*_{\ell LM}\left(\Omega_{\mathbf{k}_f}\right)\right|^2 &= \sum_{\lambda} \int d\Omega_{\mathbf{k}_f} \left[\sum_{mq} Y^*_{\ell m} \langle \ell m 1 q | \ell 1 L M\rangle \hat{\boldsymbol{\varepsilon}}_\lambda \cdot \hat{\mathbf{e}}^*_q\right] \\
&\quad \times \left[\sum_{m'q'} Y_{\ell' m'} \langle \ell' m' 1 q' | \ell' 1 L' M'\rangle \hat{\boldsymbol{\varepsilon}}^*_\lambda \cdot \hat{\mathbf{e}}_{q'}\right] \\
&= \sum_{\lambda m m'} \int d\Omega_{\mathbf{k}_f} Y^*_{\ell m}\left(\Omega_{\mathbf{k}_f}\right) Y_{\ell' m'}\left(\Omega_{\mathbf{k}_f}\right) \langle \ell m 1 \lambda | \ell 1 L M\rangle \langle \ell' m' 1 \lambda | \ell' 1 L' M'\rangle \\
&= \delta_{\ell\ell'}\delta_{LL'}\delta_{MM'}.
\end{aligned} \qquad (4\text{-}3.59)$$

The natural linewidth then reduces to

$$\begin{aligned}
\Gamma_n &= \left(k_f/2\pi\right) \sum\sum_{j_f m_f \ell L M} \sum_{\ell' L' M'} \frac{\langle j_i m_i L M | j_i L j_n m_n\rangle \langle j_f m_f L' M' | j_f L' j_n m_n\rangle}{(2j_n+1)} \\
&\qquad \times \chi(L,\ell)\chi^*(L',\ell')\delta_{\ell\ell'}\delta_{LL'}\delta_{MM'} \\
&= \left(k_f/2\pi\right) \sum_{j_f} \sum_{\ell L} \sum_{m_f M} \frac{\langle j_i m_i L M | j_i L j_n m_n\rangle \langle j_f m_f L M | j_f L j_n m_n\rangle}{(2j_n+1)} |\chi(L,\ell)|^2
\end{aligned}$$

$$= (k_f/2\pi)\sum_{L\ell}\sum_{j_f}|\chi(L,\ell)|^2/(2j_n+1)$$

$$\equiv \sum_{L\ell}\Gamma(L,\ell) \tag{4-3.60}$$

The multipole linewidth, $\Gamma(L,\ell)$, is a function of the multipole index L and an index ℓ which determines whether the process is transverse magnetic, transverse electric, or longitudinal scattering (see Table 4-3.1). Then, the reduced matrix element expressed in terms of the multipole linewidth is

$$\sum_{j_f}|\chi(L,\ell)|^2 = (2\pi/k_f)(2j_n+1)\Gamma(L,\ell). \tag{4-3.61}$$

For a two level system the sum over j_f can be ignored.

Multipole index		Electric: $\lambda=1$	Magnetic: $\lambda=0$
$L=1$	$\ell=0,2$	dipole	
	$\ell=1$		dipole
$L=2$	$\ell=1,3$	quadrupole	
	$\ell=2$		quadrupole
$L=3$	$\ell=2,4$	sextupole	
	$\ell=3$		sextupole

Table 4-3.1. Multipole fields designated by multipole index L.

The spontaneous absorption reemission on-energy-shell scattering amplitude can now be expressed in terms of the multipole spontaneous radiative linewidth[1-3]

$$F_n(\mathbf{k}_f,\mathbf{k}_i,\mathbf{x}_0) = -(2\pi/k_f)e^{-i(\mathbf{k}_f-\mathbf{k}_i)\cdot\mathbf{x}_0}\sum_{\ell LM}\sum_{\ell' L'M'}\left[\hat{\varepsilon}_f^*\cdot\mathbf{Y}_{L\ell M}(\Omega_{\mathbf{k}_f})\right]\left[\mathbf{Y}^*_{L'\ell'M'}(\Omega_{\mathbf{k}_i})\cdot\hat{\varepsilon}_i\right]$$

$$\times\frac{\sqrt{\Gamma(L,\ell)\Gamma(L',\ell')}\,e^{i[\eta(L,\ell)-\eta(L',\ell')]}}{E_i-E_n+\hbar\omega_{\mathbf{k}_i}+i\Gamma_n/2}\langle j_f m_f LM|j_f L j_n m_n\rangle\langle j_i m_i L'M'|j_i L' j_n m_n\rangle \tag{4-3.62}$$

or

$$F_n(\mathbf{k}_f,\mathbf{k}_i,\mathbf{x}_0) = -(2\pi/k_f)e^{-i(\mathbf{k}_f-\mathbf{k}_i)\cdot\mathbf{x}_0}\sum_{\lambda LM}\sum_{\lambda' L'M'}\left[\hat{\boldsymbol{\varepsilon}}_f^*\cdot\mathbf{Y}_{LM}^{(\lambda)}(\Omega_{\mathbf{k}_f})\right]\left[\mathbf{Y}_{L'M'}^{(\lambda')*}(\Omega_{\mathbf{k}_i})\cdot\hat{\boldsymbol{\varepsilon}}_i\right]$$

$$\times\frac{\sqrt{\Gamma(L,\lambda)\Gamma(L',\lambda')}\,e^{i[\eta(L,\lambda)-\eta(L',\lambda')]}}{E_i-E_n+\hbar\omega_{\mathbf{k}_i}+i\Gamma_n/2}\langle j_f\,m_f\,L\,M|j_f\,L\,j_n\,m_n\rangle\langle j_i\,m_i\,L'\,M'|j_i\,L'\,j_n\,m_n\rangle \quad (4\text{-}3.63)$$

For convenience of notation in later sections, $F_n(\mathbf{k}_f,\mathbf{k}_i)\equiv F_n(\mathbf{k}_f,\mathbf{k}_i,\mathbf{x}_0=0)$. If the scattering process preserves time reversal invariance, the phase difference, $\eta(L,\lambda)-\eta(L',\lambda')$, between two multipoles is zero or π.[13, 14] The spatial phase factor, $\phi_{\mathbf{x}}=-(\mathbf{k}_f-\mathbf{k}_i)\cdot\mathbf{x}_0$, comes from shifting the scatterer from the origin by the displacement $\mathbf{x}_0$ as shown in Fig.4-3.1.

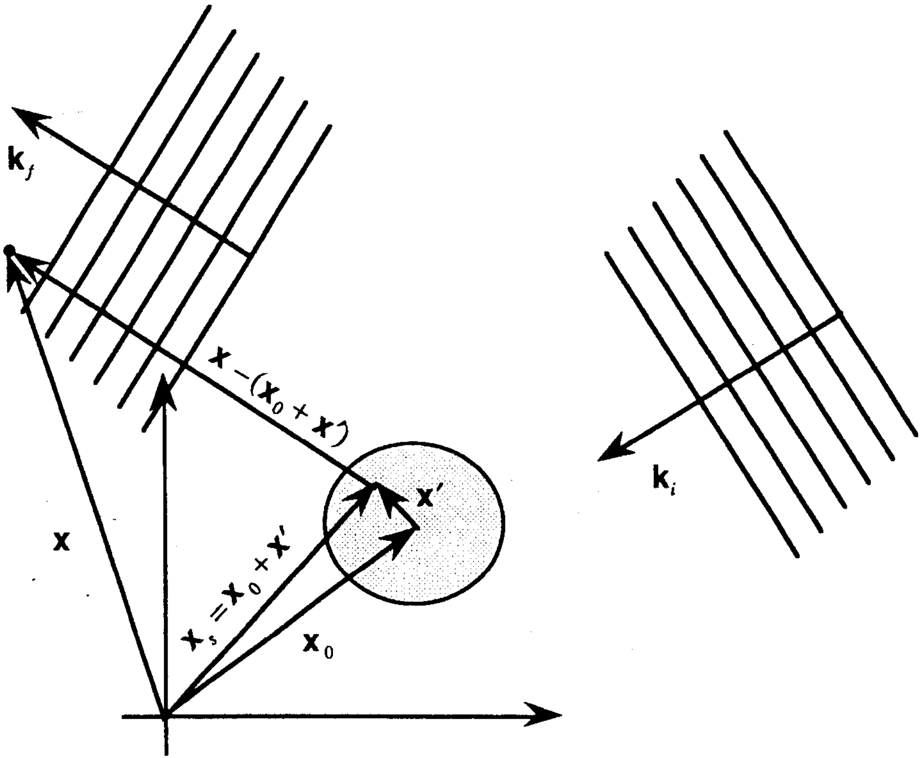

Fig. 4-3.1. Incoming transverse plane waves with direction $\mathbf{k}_i$ scatterers off particle located at $\mathbf{x}_0$ to produce outgoing transverse plane waves traveling in direction $\mathbf{k}_f$.

In general, the scattering is usually expressed as

$$F_n^{f_\alpha i_\alpha}=\langle f_\alpha|F_n|i_\alpha\rangle \quad (4\text{-}3.64)$$

where the matrix elements of F_n must be summed over other quantum states not discussed so far (such as phonon states) to arrive at a final value for the scattering amplitude. For instance, in phonon scattering,[3, 6, 15, 16] the plane wave can be approximated as having an additional oscillatory spatial function, $\mathbf{u}$, that describes displacements about an equilibrium position $\mathbf{x}$ of a scatterer

$$e^{i\mathbf{k}\cdot\mathbf{x}} \rightarrow e^{i\mathbf{k}\cdot(\mathbf{x}+\mathbf{u})}. \tag{4-3.65}$$

In such a case, the scattering amplitude changes to

$$F_n^{f_\alpha i_\alpha} = F_n' \sum_{n_\alpha} \left\langle f_\alpha \middle| e^{-i\mathbf{k}_f\cdot\mathbf{u}} \middle| n_\alpha \right\rangle \left\langle n_\alpha \middle| e^{i\mathbf{k}_i\cdot\mathbf{u}} \middle| i_\alpha \right\rangle \tag{4-3.66}$$

The vibrational factor usually lead to a diminution in the scattering amplitude, and, for nuclear scattering, is called a Lamb-Mössbauer factor, or, for electronic scattering, a Debye-Waller factor. The resonant denominator of F_n also changes to include frequency terms that give rise to frequency sidebands.

4.4 Spherical Multipole Electric Fields

In the computations done so far, the incoming and exiting waves have been described as plane waves. Such a description is inadequate for a single scatterer since it usually scatters waves spherically that fall off as $1/R$ where R is the distance from the scatterer to an observation point. To include this effect, the incoming and outgoing vector fields of the photon are described as spherical Green functions

$$\mathbf{A}_{out}(\mathbf{x},\mathbf{x}') = \hat{\varepsilon}_f^* \frac{e^{ik|\mathbf{x}-\mathbf{x}'|}}{|\mathbf{x}-\mathbf{x}'|} \tag{4-4.1}$$

$$\mathbf{A}_{in}(\mathbf{x}_0,\mathbf{x}') = \hat{\varepsilon}_i \frac{e^{ik|\mathbf{x}_0+\mathbf{x}'|}}{|\mathbf{x}_0+\mathbf{x}'|} \tag{4-4.2}$$

where the incoming spherical wave originates at point $\mathbf{x}_0$ in Fig.4-3.1, the scattered spherical is observed at point $\mathbf{x}$, and $\mathbf{x}'$ are the internal coordinates of the scatterer. Inserting these vector potentials into the expressions for U_{fn} and U_{ni} in Eqs. 4-3.55 and 4-3.56 will give the spherical multipole electric field amplitudes scattered from a particle.

The spherical wave expansion of the spherical Green function is[17]

$$\frac{e^{ik|\mathbf{x}-\mathbf{x}'|}}{|\mathbf{x}-\mathbf{x}'|} = 4\pi ik \sum_{\ell=0}^{\infty} j_\ell(kr_<) h_\ell^{(1)}(kr_>) \sum_{m=-\ell}^{\ell} Y_{\ell m}(\theta_\mathbf{k},\phi_\mathbf{k}) Y_{\ell m}^*(\theta_\mathbf{r},\phi_\mathbf{r}) \tag{4-4.3}$$

where $h_\ell^{(1)}(kr)$ is a spherical Hankel function

$$h_\ell^{(1)}(kr) = \sqrt{\frac{\pi}{2x}}\left[J_{\ell+1/2}(x) + iN_{\ell+1/2}(x)\right]. \tag{4-4.4}$$

Inserting the spherical wave expansions into the expressions for U_{fn} and U_{ni} and carrying out computations similar to those performed in Section 4.3 leads to the spherical multipole electric fields in a form very similar to Eq. 4-3.62

$$\mathbf{E}_n(\mathbf{k}_f,\mathbf{k}_i) = \hat{\boldsymbol{\varepsilon}}_f F_n'(\mathbf{k}_f,\mathbf{k}_i) = \hat{\boldsymbol{\varepsilon}}_f F_n(\mathbf{k}_f,\mathbf{k}_i)\Big|_{\mathbf{Y}_{L\ell M}(\Omega_\mathbf{k})\to\mathbf{Z}_{L\ell M}(r_\mathbf{k},\Omega_\mathbf{k})} \tag{4-4.5}$$

where $F_n'(\mathbf{k}_f,\mathbf{k}_i)$ is similar to $F_n(\mathbf{k}_f,\mathbf{k}_i)$ in Eq. 4-3.62 but with the substitution $\mathbf{Y}_{L\ell M}(\Omega_\mathbf{k}) \to \mathbf{Z}_{L\ell M}(r_\mathbf{k},\Omega_\mathbf{k})$ (the spatial phase is now contained in the spherical Hankel functions). The spherical Hankel harmonics follow the relation

$$\mathbf{Z}_{L\ell M}(r_\mathbf{k},\Omega_\mathbf{k}) = kf_\ell(kr_\mathbf{k})\mathbf{Y}_{L\ell m}(\theta_\mathbf{k},\phi_\mathbf{k}) \tag{4-4.6}$$

$$f_\ell(kr_\mathbf{k}) = i(-i)^{-\ell}h_\ell(kr_\mathbf{k}) \tag{4-4.7}$$

$$r_{\mathbf{k}_f} \approx |\mathbf{x}-\mathbf{x}_0| \quad \text{for} \quad |\mathbf{x}-\mathbf{x}_0| >> |\mathbf{x}'| \tag{4-4.8}$$

$$r_{\mathbf{k}_i} \approx |\mathbf{x}_0| \quad \text{for} \quad |\mathbf{x}_0| >> |\mathbf{x}'| \tag{4-4.9}$$

One can also construct magnetic, electric, and longitudinal multipole electric fields in a manner similar to that in the last section:[12]

$$\mathbf{Z}_{jm}^{(\mathrm{m})} = \mathbf{Z}_{jjm} = kf_j(kr)\mathbf{Y}_{jjm} \tag{4-4.10}$$

$$i\mathbf{Z}_{jm}^{(\mathrm{e})} = -\frac{i}{k}\nabla\times\mathbf{Z}_{jm}^{(\mathrm{m})} = i(-i)^{-j}\left\{\sqrt{\frac{j+1}{2j+1}}h_{j-1}(kr)\mathbf{Y}_{j,j-1,m} - \sqrt{\frac{j}{2j+1}}h_{j+1}(kr)\mathbf{Y}_{j,j+1,m}\right\} \tag{4-4.11}$$

$$\mathbf{Z}_{jm}^{(l)} = -\frac{i}{k}\nabla Z_{jm} \qquad = i(-i)^{-j}\left\{\sqrt{\frac{j}{2j+1}}h_{j-1}(kr)\mathbf{Y}_{j,j-1,m} - \sqrt{\frac{j+1}{2j+1}}h_{j+1}(kr)\mathbf{Y}_{j,j+1,m}\right\} \tag{4-4.12}$$

The magnetic multipole field is still a transverse field, but, since the electric and longitudinal multipoles now have spherical Hankel functions multiplying the vector spherical harmonics, they are no longer purely transverse or longitudinal fields--they both now have mixtures of transverse and longitudinal field components. The spherical multipole electric field expressed in terms of these multipoles can still be cast in a form very similar to that in Eq. 4-3.63

$$\mathbf{E}_n(\mathbf{k}_f,\mathbf{k}_i) = \hat{\boldsymbol{\varepsilon}}_f F_n'(\mathbf{k}_f,\mathbf{k}_i) = \hat{\boldsymbol{\varepsilon}}_f F_n(\mathbf{k}_f,\mathbf{k}_i)\Big|_{\mathbf{Y}_{LM}^{(\lambda)}(\Omega_\mathbf{k})\to\mathbf{Z}_{LM}^{(\lambda)}(_\mathbf{k},\Omega_\mathbf{k})}. \tag{4-4.13}$$

Typically the approximation is made that the incoming fields are plane waves and the scattered fields are spherical waves. Also, if the observation point is far from the scatterer compared to a wavelength, a far field approximation can be made for the scattered spherical field. The spherical Hankel functions, to all multipoles, approaches

$$f_\ell(kr) \xrightarrow[kr>>1]{} \frac{e^{ikr}}{kr} \tag{4-4.14}$$

and

$$\mathbf{Z}_{LM}^{(\lambda)} \xrightarrow[kr>>1]{} \frac{e^{ikr}}{r}\mathbf{Y}_{LM}^{(\lambda)}. \tag{4-4.15}$$

In the far field limit, the electric and magnetic multipoles now become purely transverse fields, and the longitudinal multipoles are purely longitudinal fields. The total electric field at the point $\mathbf{x}$ is then

$$\mathbf{E}(\mathbf{x}) = \hat{\varepsilon}_i E_0 e^{i\mathbf{k}_i\cdot\mathbf{x}} + \hat{\varepsilon}_f E_0 \frac{e^{ikr_{\mathbf{k}_f}}}{r_{\mathbf{k}_f}} e^{i\mathbf{k}_i\cdot\mathbf{x}_0} F_n(\mathbf{k}_f,\mathbf{k}_i) \tag{4-4.16}$$

where the first term is the incoming plane wave field of amplitude E_0, the second term is the spherically scattered multipole electric field with F_n given by Eq. 4-3.62 or 4-3.63, and $r_{\mathbf{k}_f}$ is given by Eq. 4-4.8. Notice that the expression for each transverse electric field component is now equivalent to the solution of the integral scattering equation discussed in Section 3.3 (see Eq. 3-3.10) when $|\mathbf{x}| >> |\mathbf{x}_0|$. Now that the scattered fields from a single particle have been found, one can then go on to solve for the net field scattered from several particles (this is done in Chapters 6 and 7). When there are many particles and frequent multiple scatterings, the computations become too time consuming, and one must rely upon the Maxwell inhomogeneous wave equation for transverse electric fields. Fortunately, a wide range of problems involving many particle media can be handled well by the Maxwell inhomogeneous wave equation (as shown in Chapters 6 and 7).

REFERENCES

[1] M. Blume and O. C. Kistner, *Phys. Rev.* **171**, 417 (1968).

[2] H. Frauenfelder, D. E. Nagle, R. D. Taylor, D. R. F. Cochran, and W. M. Visscher, *Phys. Rev.* **126**, 1065 (1962).

[3] J. P. Hannon and G. T. Trammell, *Phys. Rev.* **186**, 306 (1969).

[4] R. M. Housley, R. W. Grant, and U. Gonser, *Phys. Rev.* **178**, 514 (1969).

[5] M. E. Rose, *Elementary Theory of Angular Momentum* (Wiley, New York, 1957).

[6] G. T. Trammell, *Phys. Rev.* **126**, 1045 (1962).

[7] M. Weissbluth, *Atoms and Molecules* (Academic Press, New York, 1978).

[8] A. I. Akhiezer, *Quantum Electrodynamics* (Interscience Publishers, New York, 1965).

[9] F. Halzen and A. D. Martin, *Quarks and Leptons* (Wiley, New York, 1984).

[10] A. R. Edmonds, *Angular Momentum in Quantum Mechanics* (Princeton University Press, Princeton, New Jersey, 1960).

[11] D. M. Brink and G. R. Satchler, *Angular Momentum* (Clarendon Press, Oxford, 1968).

[12] J. Mathews, *Tensor Spherical Harmonics* (California Institute of Technology, 1981).

[13] S. P. Lloyd, *Phys. Rev.* **81**, 161 (1950).

[14] J. P. Hannon and G. T. Trammell, *Phys. Rev. Lett.* **21**, 726 (1968).

[15] A. M. Afanas'ev and Y. Kagan, *Sov. Phys. JETP* **21**, 215 (1965).

[16] A. Y. Dzyublik, *Phys. stat. sol. (b)* **123**, 53 (1984).

[17] J. D. Jackson, *Classical Electrodynamics* (Wiley, New York, 1975).

5. DIPOLE POLARIZATION PROPERTIES AND STATIC FIELD INTERACTIONS

5.1 Polarization Properties of Electric and Magnetic Dipole Scattering

For the case of Thomson scattering, the scattering amplitude, Eq. 4-2.11, can be written in tensor form where a polarization matrix contains all the polarization information about the scattering process

$$\mathbf{F}_T(\mathbf{k}_f,\mathbf{k}_i) = -r_q f_0 P_T \tag{5-1.1}$$

where

$$P_T = \hat{\boldsymbol{\varepsilon}}^i \cdot \hat{\boldsymbol{\varepsilon}}^{f*} = \begin{pmatrix} \hat{\boldsymbol{\varepsilon}}^i_x \cdot \hat{\boldsymbol{\varepsilon}}^{f*}_x & \hat{\boldsymbol{\varepsilon}}^i_x \cdot \hat{\boldsymbol{\varepsilon}}^{f*}_y \\ \hat{\boldsymbol{\varepsilon}}^i_y \cdot \hat{\boldsymbol{\varepsilon}}^{f*}_x & \hat{\boldsymbol{\varepsilon}}^i_y \cdot \hat{\boldsymbol{\varepsilon}}^{f*}_y \end{pmatrix}. \tag{5-1.2}$$

Since there are two directions corresponding to the incoming and outgoing photons, there are two separate polarization bases for each direction, and the orientation of each basis with respect to one another is arbitrary. Usually a convenient orientation is chosen that diagonalizes the polarization matrix and simplifies calculations. Constraining one polarization component, say the x-component of both the incoming and outgoing fields, to be perpendicular to the scattering plane--$\hat{\boldsymbol{\varepsilon}}_x = \hat{\boldsymbol{\sigma}}$ = sigma polarized--forces the other component to lie in the scattering plane--$\hat{\boldsymbol{\varepsilon}}_y = \hat{\boldsymbol{\pi}}$ = pi polarized--(see Fig. 5-1.1). Under such conditions the polarization matrix diagonalizes to

$$P_T = \begin{pmatrix} \hat{\boldsymbol{\sigma}}_i \cdot \hat{\boldsymbol{\sigma}}_f & \hat{\boldsymbol{\sigma}}_i \cdot \hat{\boldsymbol{\pi}}_f \\ \hat{\boldsymbol{\pi}}_i \cdot \hat{\boldsymbol{\sigma}}_f & \hat{\boldsymbol{\pi}}_i \cdot \hat{\boldsymbol{\pi}}_f \end{pmatrix} = \begin{pmatrix} 1 & 0 \\ 0 & \cos 2\theta_B \end{pmatrix} \tag{5-1.3}$$

where $2\theta_B$ is the scattering angle between $\mathbf{k}_i$ and $\mathbf{k}_f$. The polarization matrix reveals that Thomson radiation has an angular distribution commonly associated with electric dipole scattering--horizontally polarized fields are reflected by the same amount regardless of scattering angle while vertically polarized fields suffer a decrease in amplitude proportional to the cosine of the scattering angle between the incoming and outgoing wave directions.

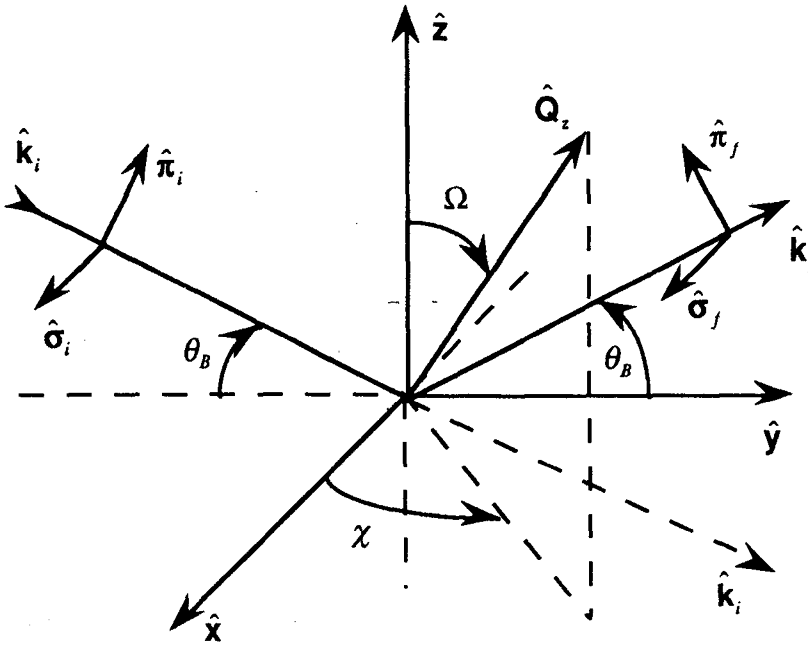

Fig. 5-1.1. Scattering geometry for a particle at the origin. Sigma (pi) polarizations are perpendicular (parallel) to the yz scattering plane. $\mathbf{Q}_z$ is the quantization axis direction with polar and azimuthal angles Ω and χ. $2\theta_B$ is the scattering angle.

For dipole scattering (and no polarization mixing), the tensor form of the scattering amplitude is (from Eq. 4-3.63)

$$\mathbf{F}(\mathbf{k}_f,\mathbf{k}_i,\mathbf{x}_0) = -(2\pi/k_f)e^{-i(\mathbf{k}_f-\mathbf{k}_i)\cdot\mathbf{x}_0}\sum_{\lambda LM} P_{LM}^{(\lambda)}\frac{\Gamma(L,\lambda)}{E_i - E_n + \hbar\omega_{\mathbf{k}_i} + i\Gamma_n/2}\langle j_f m_f LM | j_f L j_n m_n\rangle^2 \tag{5-1.4}$$

where the polarization matrix is of the form

$$P_{LM}^{(\lambda)} = \hat{\boldsymbol{\varepsilon}}^i \cdot \mathbf{Y}_{LM}^{(\lambda)*}(\Omega_{\mathbf{k}_i})\mathbf{Y}_{LM}^{(\lambda)}(\Omega_{\mathbf{k}_f}) \cdot \hat{\boldsymbol{\varepsilon}}^{f*}$$

$$= \begin{pmatrix} [\hat{\boldsymbol{\varepsilon}}_x^i \cdot \mathbf{Y}_{LM}^{(\lambda)*}(\Omega_{\mathbf{k}_i})][\mathbf{Y}_{LM}^{(\lambda)}(\Omega_{\mathbf{k}_f}) \cdot \hat{\boldsymbol{\varepsilon}}_x^{f*}] & [\hat{\boldsymbol{\varepsilon}}_x^i \cdot \mathbf{Y}_{LM}^{(\lambda)*}(\Omega_{\mathbf{k}_i})][\mathbf{Y}_{LM}^{(\lambda)}(\Omega_{\mathbf{k}_f}) \cdot \hat{\boldsymbol{\varepsilon}}_y^{f*}] \\ [\hat{\boldsymbol{\varepsilon}}_y^i \cdot \mathbf{Y}_{LM}^{(\lambda)*}(\Omega_{\mathbf{k}_i})][\mathbf{Y}_{LM}^{(\lambda)}(\Omega_{\mathbf{k}_f}) \cdot \hat{\boldsymbol{\varepsilon}}_x^{f*}] & [\hat{\boldsymbol{\varepsilon}}_y^i \cdot \mathbf{Y}_{LM}^{(\lambda)*}(\Omega_{\mathbf{k}_i})][\mathbf{Y}_{LM}^{(\lambda)}(\Omega_{\mathbf{k}_f}) \cdot \hat{\boldsymbol{\varepsilon}}_y^{f*}] \end{pmatrix}, \tag{5-1.5}$$

and $\lambda = 1 \equiv \mathrm{e}$ for electric dipole scattering, $\lambda = 0 \equiv \mathrm{m}$ for magnetic dipole scattering, and $L = 1$ for dipole scattering. The vector spherical harmonics for dipole (and also quadrupole) scattering are given in Table 5-1.1. The scattering geometry presented in Fig. 5-1.1 will be used to examine the structure of the dipole polarization matrix.

			$\mathbf{Y}^{e*}_{jm}$		$\mathbf{Y}^{m}_{jm}$	
j	m	factor	$\hat{\boldsymbol{\theta}}$	$\hat{\boldsymbol{\phi}}$	$\hat{\boldsymbol{\theta}}$	$\hat{\boldsymbol{\phi}}$
1	1	$\sqrt{\frac{3}{16\pi}}e^{i\phi}$	$-\cos\theta$	$-i$	1	$i\cos\theta$
1	0	$\sqrt{\frac{3}{8\pi}}\sin\theta$	-1	0	0	i
1	-1	$\sqrt{\frac{3}{16\pi}}e^{-i\phi}$	$\cos\theta$	$-i$	1	$-i\cos\theta$
2	2	$\sqrt{\frac{5}{16\pi}}\sin\theta e^{2i\phi}$	$\cos\theta$	i	-1	$-i\cos\theta$
2	1	$\sqrt{\frac{5}{16\pi}}e^{i\phi}$	$1-2\cos^2\theta$	$-i\cos\theta$	$\cos\theta$	$i(2\cos^2\theta-1)$
2	0	$\sqrt{\frac{15}{8\pi}}\sin\theta$	$-\cos\theta$	0	0	$i\cos\theta$
2	-1	$\sqrt{\frac{5}{16\pi}}e^{-i\phi}$	$2\cos^2\theta-1$	$-i\cos\theta$	$\cos\theta$	$i(1-2\cos^2\theta)$
2	-2	$\sqrt{\frac{5}{16\pi}}\sin\theta e^{-2i\phi}$	$\cos\theta$	$-i$	1	$-i\cos\theta$

Table 5-1.1. Electric and magnetic dipole, $j=1$, and quadrupole, $j=2$, vector spherical harmonics.[1]

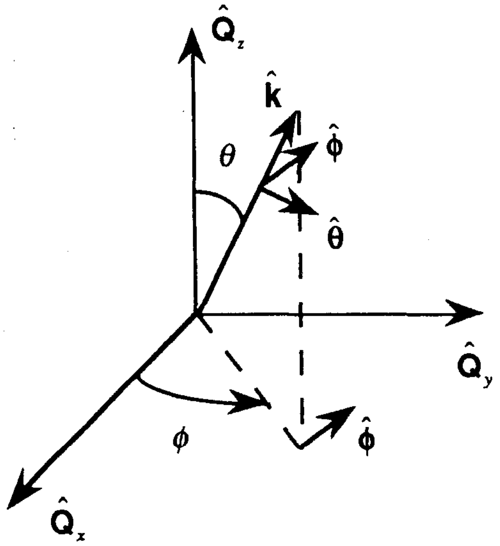

Fig. 5-1.2. Wavector in quantization system defines the spherical coordinates and unit vectors of a vector spherical harmonic.

The dipole direction, or quantization axis $\hat{\mathbf{Q}}_z$, points in some arbitrary direction specified by the polar and azimuthal angles Ω and χ:

$$\hat{\mathbf{Q}}_z = \cos\chi \sin\Omega\,\hat{\mathbf{x}} + \sin\chi \sin\Omega\,\hat{\mathbf{y}} + \cos\Omega\,\hat{\mathbf{z}}. \qquad (5\text{-}1.6)$$

Recall that the spherical coordinate system for the vector spherical harmonics is defined by the quantum axis of the scatterer. The polar angle, $\theta_{(i,f)}$, is the angle between the incoming or outgoing photon and the quantization axis--see Fig. 5-1.2.

$$\cos\theta_{(i,f)} = \hat{\mathbf{Q}}_z \cdot \hat{\mathbf{k}}_{(i,f)} = \cos\theta_B \sin\chi \sin\Omega \mp \sin\theta_B \cos\Omega \qquad (5\text{-}1.7)$$

where

$$\hat{\mathbf{k}}_{(i,f)} = \cos\theta_B\,\hat{\mathbf{y}} \mp \sin\theta_B\,\hat{\mathbf{z}}, \qquad (5\text{-}1.8)$$

and the top sign in the $\mp$ corresponds to $\hat{\mathbf{k}}_i$ and the bottom sign corresponds to $\hat{\mathbf{k}}_f$. Since the $\left(\hat{\mathbf{Q}}_x, \hat{\mathbf{Q}}_y\right)$ basis can be arbitrarily oriented in a plane perpendicular to the quantization axis, only the azimuthal phase difference, $\Delta\phi = \phi_f - \phi_i$, is meaningful. This phase difference can be found through the angle addition rule

$$\cos 2\theta_B = \cos\theta_f \cos\theta_i + \sin\theta_f \sin\theta_i \cos\left(\phi_f - \phi_i\right). \qquad (5\text{-}1.9)$$

To perform the dot products in the polarization matrix, Eq. 5-1.5, the spherical unit vectors must be transformed into Cartesian unit vectors. This transformation can be accomplished by noting that the azimuthal unit vector, $\hat{\boldsymbol{\phi}}$, is perpendicular to both $\hat{\mathbf{k}}$ and $\hat{\mathbf{Q}}_z$

$$\hat{\boldsymbol{\phi}} = \hat{\mathbf{Q}}_z \times \hat{\mathbf{k}} \Big/ \left|\hat{\mathbf{Q}}_z \times \hat{\mathbf{k}}\right|, \qquad (5\text{-}1.10)$$

and the polar unit vector, $\hat{\boldsymbol{\theta}}$,is perpendicular to both $\hat{\boldsymbol{\phi}}$ and $\hat{\mathbf{k}}$

$$\hat{\boldsymbol{\theta}} = \hat{\boldsymbol{\phi}} \times \hat{\mathbf{k}} \Big/ \left|\hat{\boldsymbol{\phi}} \times \hat{\mathbf{k}}\right|. \qquad (5\text{-}1.11)$$

After some algebra, the spherical unit vectors can be written down as

$$\hat{\boldsymbol{\phi}}_{(i,f)} = \frac{-(\cos\theta_B \cos\Omega \pm \sin\theta_B \sin\chi \sin\Omega)\hat{\mathbf{x}} + \cos\chi \sin\Omega\left(\cos\theta_B\,\hat{\mathbf{z}} \pm \sin\theta_B\,\hat{\mathbf{y}}\right)}{\sqrt{N_{(i,f)}}} \qquad (5\text{-}1.12)$$

$$\hat{\boldsymbol{\theta}}_{(i,f)} = \frac{-\cos\chi \sin\Omega\,\hat{\mathbf{x}} - (\sin\theta_B \sin\chi \sin\Omega \pm \cos\theta_B \cos\Omega)\left(\sin\theta_B\,\hat{\mathbf{y}} \cos\theta_B\,\hat{\mathbf{z}} \pm \cos\theta_B\,\hat{\mathbf{z}}\right)}{\sqrt{N_{(i,f)}}}$$

where (5-1.13)

$$N_{(i,f)} = \left(\cos\theta_B \cos\Omega \pm \sin\theta_B \sin\chi \sin\Omega\right)^2 + \left(\cos\chi \sin\Omega\right)^2. \qquad (5\text{-}1.14)$$

The polarization vector directions can be read directly from Fig. 5-1.1

$$\hat{\boldsymbol{\varepsilon}}_x^{(i,f)} \equiv \hat{\boldsymbol{\sigma}}_{(i,f)} = \hat{\mathbf{x}} \tag{5-1.15}$$

$$\hat{\boldsymbol{\varepsilon}}_y^{(i,f)} \equiv \hat{\boldsymbol{\pi}}_{(i,f)} = \pm\sin\theta_B\,\hat{\mathbf{y}} + \cos\theta_B\,\hat{\mathbf{z}}. \tag{5-1.16}$$

Then, all of the dot products in the dipole polarization matrix can be put in the form (see Fig. 5-1.3)

$$\hat{\boldsymbol{\sigma}}_{(i,f)}\cdot\hat{\boldsymbol{\phi}}_{(i,f)} = \hat{\boldsymbol{\pi}}_{(i,f)}\cdot\hat{\boldsymbol{\theta}}_{(i,f)} = \cos\beta_{(i,f)} = -\left(\cos\theta_B\cos\Omega \pm \sin\theta_B\sin\chi\sin\Omega\right)\Big/\sqrt{N_{(i,f)}} \tag{5-1.17}$$

$$\hat{\boldsymbol{\sigma}}_{(i,f)}\cdot\hat{\boldsymbol{\theta}}_{(i,f)} = -\left(\hat{\boldsymbol{\pi}}_{(i,f)}\cdot\hat{\boldsymbol{\phi}}_{(i,f)}\right) = \sin\beta_{(i,f)} = -\cos\chi\sin\Omega\Big/\sqrt{N_{(i,f)}}\,. \tag{5-1.18}$$

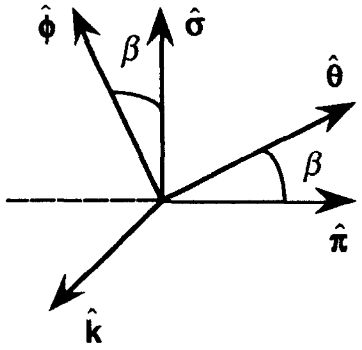

Fig. 5-1.3. Orientation of polarization vectors with respect to spherical unit vectors lying in the $(\hat{\boldsymbol{\sigma}},\hat{\boldsymbol{\pi}})$ plane and the wavector direction.

There is now enough information to construct the dipole polarization matrix. For magnetic dipole scattering, the $M=0$ term is

$$P_{10}^{(\mathrm{m})} = \frac{3}{8\pi}\begin{pmatrix} \sin\theta_i\sin\theta_f\cos\beta_i\cos\beta_f & -\sin\theta_i\sin\theta_f\cos\beta_i\sin\beta_f \\ -\sin\theta_i\sin\theta_f\sin\beta_i\cos\beta_f & \sin\theta_i\sin\theta_f\sin\beta_i\sin\beta_f \end{pmatrix}, \tag{5-1.19}$$

the $M=1$ term is

$$P_{11}^{(\mathrm{m})} = \frac{3}{16\pi}e^{i(\phi_f-\phi_i)}$$

$$\times\begin{pmatrix} (\sin\beta_i - i\cos\theta_i\cos\beta_i)(\sin\beta_f + i\cos\theta_f\cos\beta_f) & (\sin\beta_i - i\cos\theta_i\cos\beta_i)(\cos\beta_f - i\cos\theta_f\sin\beta_f) \\ (\cos\beta_i - i\cos\theta_i\sin\beta_i)(\sin\beta_f + i\cos\theta_f\cos\beta_f) & (\cos\beta_i - i\cos\theta_i\sin\beta_i)(\cos\beta_f + i\cos\theta_f\sin\beta_f) \end{pmatrix} \tag{5-1.20}$$

and the $M=-1$ term is obtained by taking the complex conjugate of the $M=1$ term because a linear polarization basis was chosen

$$P_{1,-1}^{(\mathrm{m})} = \left(P_{11}^{(\mathrm{m})}\right)^{*}. \tag{5-1.21}$$

For electric dipole scattering, the polarization matrices are equivalent except for the substitution $\beta \to \beta - \pi/2$ since the electric dipole vector fields are orthogonal to the magnetic dipole vector fields. For simple orientations of the quantization axis with respect to the photon directions, three examples illustrating the structure of polarization matrices are given below.

CASE 1: Quantization axis is perpendicular to the scattering plane: $\hat{\mathbf{Q}}_z = \hat{\mathbf{x}}$.

$$\Omega = \pi/2, \quad \chi = 0, \quad \theta_i = \theta_f = \pi/2, \quad \phi_f - \phi_i = 2\theta_B$$

$$\hat{\sigma}_{(i,f)} = -\hat{\boldsymbol{\theta}}_{(i,f)}, \quad \hat{\boldsymbol{\pi}}_{(i,f)} = \hat{\boldsymbol{\phi}}_{(i,f)}, \quad \beta_{(i,f)} = -\pi/2$$

Then,

$$P_{10}^{(m)} = \frac{3}{8\pi}\begin{pmatrix} 0 & 0 \\ 0 & 1 \end{pmatrix}, \qquad P_{1,\pm1}^{(m)} = \frac{3}{16\pi} e^{\pm i2\theta_B}\begin{pmatrix} 1 & 0 \\ 0 & 0 \end{pmatrix} \tag{5-1.22}$$

$$P_{10}^{(e)} = \frac{3}{8\pi}\begin{pmatrix} 1 & 0 \\ 0 & 0 \end{pmatrix}, \qquad P_{1,\pm1}^{(e)} = \frac{3}{16\pi} e^{\pm i2\theta_B}\begin{pmatrix} 0 & 0 \\ 0 & 1 \end{pmatrix} \tag{5-1.23}$$

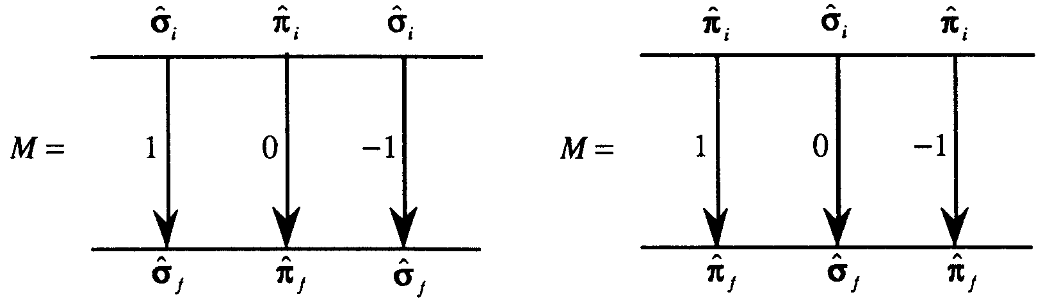

(*a*) (*b*)

Fig. 5-1.4. For a dipole transition $M = m_n - m_f$, incoming linearly polarized fields scatter into outgoing linearly polarized fields: (a) magnetic dipole transitions, (b) electric dipole transitions.

The polarization matrices show that the $M = m_n - m_f$ transitions emit only linearly polarized light. For $M = 0$, the scattered magnetic dipole radiation is vertically, or pi, polarized while for $M = \pm 1$ the scattered radiation is horizontally, or sigma, polarized. For scattered electric dipole radiation the situation is opposite to that of magnetic dipole radiation as shown in Fig. 5-1.4.

CASE 2: Quantization axis is parallel to the scattering plane but vertically oriented: $\hat{\mathbf{Q}}_z = \hat{\mathbf{z}}$.

$$\Omega = \chi = 0, \quad \theta_{(i,f)} = \theta_B \pm \pi/2, \quad \phi_f - \phi_i = \pi$$

$$\hat{\sigma}_{(i,f)} = -\hat{\boldsymbol{\phi}}_{(i,f)}, \quad \hat{\boldsymbol{\pi}}_{(i,f)} = -\hat{\boldsymbol{\theta}}_{(i,f)}, \quad \beta_{(i,f)} = \pi$$

Then

$$P_{10}^{(\mathrm{m})} = \frac{3}{8\pi}\begin{pmatrix} -\cos^2\theta_B & 0 \\ 0 & 0 \end{pmatrix}, \qquad P_{1,\pm1}^{(\mathrm{m})} = -\frac{3}{16\pi}\begin{pmatrix} -\sin^2\theta_B & \pm i\sin\theta_B \\ \pm i\sin\theta_B & 1 \end{pmatrix} \tag{5-1.24}$$

$$P_{10}^{(\mathrm{e})} = \frac{3}{8\pi}\begin{pmatrix} 0 & 0 \\ 0 & -\cos^2\theta_B \end{pmatrix}, \qquad P_{1,\pm1}^{(\mathrm{e})} = -\frac{3}{16\pi}\begin{pmatrix} 1 & \mp i\sin\theta_B \\ \mp i\sin\theta_B & -\sin^2\theta_B \end{pmatrix} \tag{5-1.25}$$

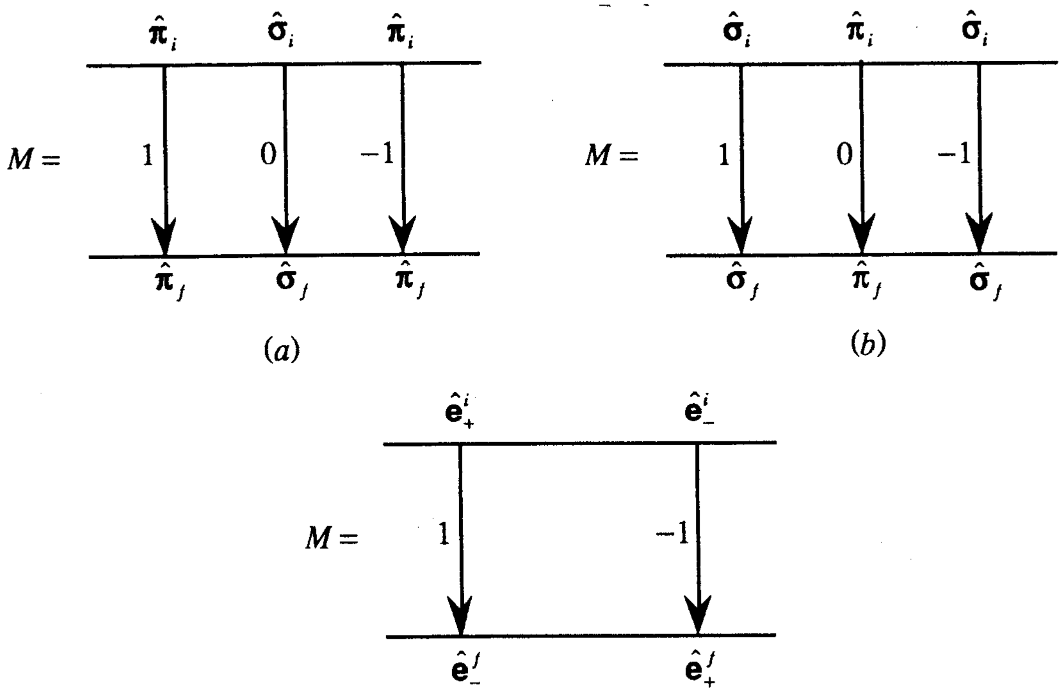

(*a*) (*b*)

(*c*)

Fig. 5-1.5. For forward scattering $(2\theta_B = 0)$ incoming fields scatter into outgoing linearly polarized fields: (a) magnetic dipole transitions, (b) electric dipole transitions. For backscattering $(2\theta_B = 180°)$ polarization reversal occurs for circularly polarized fields: (c) magnetic and electric dipole transitions.

For $M = 0$, the scattered magnetic (electric) dipole radiation is horizontally (vertically) polarized. For $M = \pm 1$, the scattered dipole radiation is generally elliptically polarized--this is an example of polarization mixing where an incoming polarized field can be scattered into an outgoing field of a different polarization. However, for forward scattering, $(2\theta_B = 0)$, the scattered field is linearly polarized (no polarization mixing occurs), and for backscattering, $(2\theta_B = 180°)$, the scattered field is circularly polarized.

For backscattering the polarization matrix for both magnetic (upper sign) and electric (lower sign) dipole radiation is (for $M = 1$)

$$P_{11}^{(\mathrm{m,e})} = -\frac{3}{16\pi}\begin{pmatrix} \mp 1 & \pm i \\ \pm i & \pm 1 \end{pmatrix}. \tag{5-1.26}$$

If the incoming field is left circularly polarized

$$\hat{\boldsymbol{\varepsilon}}_i = \hat{\mathbf{e}}_+^i = -\frac{1}{\sqrt{2}}\left(\hat{\boldsymbol{\sigma}}_i + i\hat{\boldsymbol{\pi}}_i\right), \tag{5-1.27}$$

then the scattered field has polarization

$$P_{11}^{(\mathrm{m,e})}\cdot\hat{\mathbf{e}}_+^i = \frac{3}{16\pi}\frac{1}{\sqrt{2}}\begin{pmatrix} \mp 1 & \pm i \\ \pm i & \pm 1 \end{pmatrix}\begin{pmatrix} 1 \\ i \end{pmatrix} = \mp\frac{3}{8\pi}\frac{1}{\sqrt{2}}\begin{pmatrix} 1 \\ -i \end{pmatrix} = \mp\left(\frac{3}{8\pi}\right)\hat{\mathbf{e}}_-^f.$$

This shows that left circularly polarized fields scatter into right circularly polarized fields for $M = 1$. However, right circularly polarized fields do not scatter since

$$P_{11}^{(\mathrm{m,e})}\cdot\hat{\mathbf{e}}_-^i = -\frac{3}{16\pi}\frac{1}{\sqrt{2}}\begin{pmatrix} \mp 1 & \pm i \\ \pm i & \pm 1 \end{pmatrix}\begin{pmatrix} 1 \\ -i \end{pmatrix} = 0.$$

This is an extreme case of polarization mixing--it corresponds to complete polarization reversal.

For $M = -1$, the converse happens--incoming right circularly polarized fields scatter into left circularly polarized fields whereas incoming left circularly polarized radiation does not scatter at all. This is all shown schematically in Fig. 5-1.5 (c).

CASE 3: Quantization axis is parallel to the scattering plane but horizontally oriented: $\hat{\mathbf{Q}}_z = \hat{\mathbf{y}}$.

$$\Omega = \chi = \pi/2, \qquad \theta_{(i,f)} = \theta_B, \qquad \phi_f - \phi_i = \pi$$

$$\hat{\boldsymbol{\sigma}}_i = -\hat{\boldsymbol{\phi}}_i, \qquad \hat{\boldsymbol{\sigma}}_f = \hat{\boldsymbol{\phi}}_f, \qquad \hat{\boldsymbol{\pi}}_i = -\hat{\boldsymbol{\theta}}_i, \qquad \hat{\boldsymbol{\pi}}_f = \hat{\boldsymbol{\theta}}_f, \qquad \beta_i = \pi, \qquad \beta_f = 0$$

Then

$$P_{10}^{(\mathrm{m})} = \frac{3}{8\pi}\begin{pmatrix} -\sin^2\theta_B & 0 \\ 0 & 0 \end{pmatrix}, \qquad P_{1,\pm1}^{(\mathrm{m})} = -\frac{3}{16\pi}\begin{pmatrix} -\cos^2\theta_B & \pm i\cos\theta_B \\ \mp i\cos\theta_B & -1 \end{pmatrix} \tag{5-1.28}$$

$$P_{10}^{(\mathrm{e})} = \frac{3}{8\pi}\begin{pmatrix} 0 & 0 \\ 0 & -\sin^2\theta_B \end{pmatrix}, \qquad P_{1,\pm1}^{(\mathrm{e})} = -\frac{3}{16\pi}\begin{pmatrix} -1 & \pm i\cos\theta_B \\ \mp i\cos\theta_B & -\cos^2\theta_B \end{pmatrix} \tag{5-1.29}$$

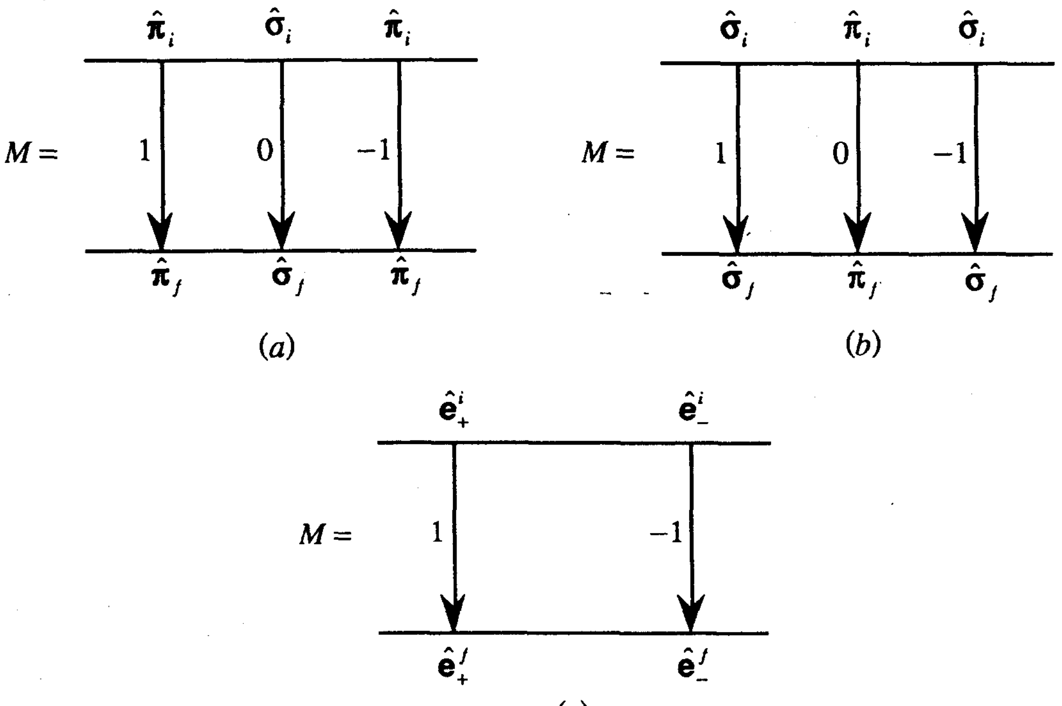

(*a*) (*b*)

(*c*)

Fig. 5-1.6. For backscattering $(2\theta_B = 180^\circ)$ incoming fields scatter into outgoing linearly polarized fields: (a) magnetic dipole transitions, (b) electric dipole transitions. For forward scattering $(2\theta_B = 0)$ incoming fields scatter into outgoing circularly polarized fields: (c) magnetic and electric dipole transitions.

For $M = 0$, the scattered magnetic (electric) dipole radiation is horizontally (vertically) polarized. For $M = \pm 1$, the scattered dipole radiation is generally elliptically polarized. However, for forward scattering the scattered field is circularly polarized, and for backscattering the scattered field is linearly polarized (this the reverse of Case 2).

For forward scattering the polarization matrix for both magnetic and electric dipole radiation is the same:

$$P_{1,\pm 1}^{(\mathrm{m})} = P_{1,\pm 1}^{(\mathrm{e})} = -\frac{3}{16\pi}\begin{pmatrix} -1 & \pm i \\ \mp i & -1 \end{pmatrix}, \tag{5-1.30}$$

and for $M = 0$ the polarization matrices are zero. For $M = 1$, incoming left circularly polarized fields scatter into outgoing left circularly polarized fields since

$$P_{11}^{(\mathrm{m,e})} \cdot \hat{\mathbf{e}}_+^i = \frac{3}{16\pi}\frac{1}{\sqrt{2}}\begin{pmatrix} -1 & i \\ -i & -1 \end{pmatrix}\begin{pmatrix} 1 \\ i \end{pmatrix} = -\frac{3}{8\pi}\frac{1}{\sqrt{2}}\begin{pmatrix} 1 \\ i \end{pmatrix} = \left(\frac{3}{8\pi}\right)\hat{\mathbf{e}}_+^f,$$

while incoming right circularly polarized fields do not scatter. Similarly, for $M = -1$, the converse occurs (see Fig. 5-1.6). No polarization reversal occurs as happened in Case 2.

There can be no polarization reversal for sigma or pi polarized fields because scattering can only change the amplitude or phase of the incoming field. There is no way a phase change can transform a sigma polarized field to a pi polarized field. However, by introducing an additional quantization axis, and arranging a set of scatterers in a convenient lattice structure, this limitation can be overcome. This is discussed in Section 5.2 and 5.3.

The scattering amplitude, Eq. 5-1.4, can be greatly simplified for those cases in which all the angular momentum spin states are degenerate, or when operating far from any dipole resonance. The scattering amplitude can then be spin averaged by summing over all intermediate, final, and initial state projection quantum numbers, or spins, m_f, m_i, m_n, and averaging over all initial state spins

$$\mathbf{F}^{(\lambda)}_{ave}(\mathbf{k}_f,\mathbf{k}_i) = \sum_{m_f m_n m_i} \mathbf{F}^{(\lambda)}(\mathbf{k}_f,\mathbf{k}_i) \Big/ (2j_i+1) \qquad (5\text{-}1.31)$$

where $2j_i+1$ is the number of initial state spins, m_i.

For elastic scattering $j_f = j_i$ and $m_f = m_i$, and thus the sum over m_i in the triple sum above can be omitted. Since all of the angular momentum spin states are degenerate, or nearly degenerate, the energy, E_n, of the state with spin m_n is the energy of the unsplit angular momentum state with angular momentum quantum number j_n

$$E_n = E_{j_n}. \qquad (5\text{-}1.32)$$

The resonance denominator of the scattering amplitude is then the same for all spins m_n and can therefore be pulled out of the sum (assuming also that the total decay rates, Γ_n, from each state with spin m_n are all the same). Since the quantization axis is now unimportant--it can point in an arbitrary direction--let it point in the same direction as in Case 3:

$$\hat{\mathbf{Q}}_z = \hat{\mathbf{y}}. \qquad (5\text{-}1.33)$$

Then the polarization matrices of Case 3, Eqs. 5-1.28 and 5-1.29, can be used to perform the spin average.

Concentrating on just magnetic dipole scattering, the main part of the spin average calculation involves the term

$$\sum_{m_f m_n M} P^{(m)}_{1M} \langle j_f m_f 1\, M | j_f 1\, j_n m_n \rangle^2 = \frac{3}{16\pi}\begin{pmatrix} s_{11} & s_{12} \\ s_{21} & s_{22} \end{pmatrix}, \qquad (5\text{-}1.34)$$

where (since $m_n = m_f + M$ the sum over m_n can be suppressed)

$$s_{11} = s_{22}\cos^2\theta_B - \sum_{m_f} 2\sin^2\theta_B \langle j_f, m_f, 1, 0 | j_f, 1, j_n, m_f \rangle^2 \qquad (5\text{-}1.35)$$

$$s_{12} = \sum_{m_f} i\cos\theta_B\left(\left\langle j_f,m_f,1,-1\middle|j_f,1,j_n,m_f-1\right\rangle^2 - \left\langle j_f,m_f,1,1\middle|j_f,1,j_n,m_f+1\right\rangle^2\right) \tag{5-1.36}$$

$$s_{21} = s_{12}^{*} \tag{5-1.37}$$

$$s_{22} = \sum_{m_f}\left(\left\langle j_f,m_f,1,1\middle|j_f,1,j_n,m_f+1\right\rangle^2 + \left\langle j_f,m_f,1,1\middle|j_f,1,j_n,m_f+1\right\rangle^2\right) \tag{5-1.38}$$

Since, for dipole transitions, $j_n = j_f + 1$, the Clebsch-Gordan coefficients reduce to simple relations[2]

$$\left\langle j_f,m_f,1,0\middle|j_f,1,j_f+1,m_f\right\rangle^2 = \frac{(j_f-m_f+1)(j_f+m_f+1)}{(2j_f+1)(j_f+1)} \tag{5-1.39}$$

$$\left\langle j_f,m_f,1,\pm1\middle|j_f,1,j_f+1,m_f\pm1\right\rangle^2 = \frac{(j_f\pm m_f+1)(j_f\pm m_f+2)}{2(2j_f+1)(j_f+1)}. \tag{5-1.40}$$

Then the off-diagonal elements sum to zero since

$$s_{12} = -\frac{i\cos\theta_B(2j_f+3)}{(2j_f+1)(j_f+1)}\sum_{m_f=-j_f}^{j_f} m_f = 0. \tag{5-1.41}$$

This result already shows that polarization mixing is not possible for the spin averaged scattering amplitude since the polarization matrix is diagonal.

For the diagonal element s_{22}:

$$\begin{aligned} s_{22} &= \frac{1}{2(2j_f+1)(j_f+1)}\left[(2j_f^2+6j_f+4)(2j_f+1)+2\sum_{m_f} m_f^2\right] \\ &= \frac{1}{2(2j_f+1)(j_f+1)}\left[2(j_f+2)(j_f+1)(2j_f+1)+4\frac{j_f(j_f+1)(2j_f+1)}{6}\right] \\ &= \frac{2}{3}(2j_f+3) = \frac{2}{3}(2j_n+1). \end{aligned} \tag{5-1.42}$$

Noting that

$$\sum_{m_f}\left\langle j_f,m_f,1,0\middle|j_f,1,j_f+1,m_f\right\rangle^2 = \frac{1}{(2j_f+1)(j_f+1)}\left[(j_f^2+2j_f+1)(2j_f+1)-\sum_{m_f} m_f^2\right]$$

$$= \frac{1}{3}(2j_n + 1) \tag{5-1.43}$$

gives

$$s_{11} = \cos^2\theta_B\left[\frac{2}{3}(2j_n + 1)\right] - 2\sin^2\theta_B\left[\frac{1}{3}(2j_n + 1)\right]$$

$$= \frac{2}{3}(2j_n + 1)\cos 2\theta_B \tag{5-1.44}$$

The spin average scattering amplitude is then

$$\mathbf{F}^{(\mathrm{m})}_{ave}(\mathbf{k}_f, \mathbf{k}_i) = -\frac{1}{4k_f}\frac{(2j_n + 1)}{(2j_i + 1)}\frac{\Gamma_{rad}}{\hbar}P^{(\mathrm{m})}_{ave}\frac{1}{\omega_{\mathbf{k}_i} - \omega_0 + i\Gamma/2\hbar} \tag{5-1.45}$$

where $$P^{(\mathrm{m})}_{ave} = \begin{pmatrix} \cos 2\theta_B & 0 \\ 0 & 1 \end{pmatrix}, \tag{5-1.46}$$

and $\Gamma_{rad} = \Gamma(1, \mathrm{m})$, and Γ is the total decay rate from the angular momentum state with angular momentum number j_n. For electric dipole scattering, the average scattering amplitude is of the same form as Eq. 5-1.45 except that the polarization matrix is now

$$P^{(\mathrm{e})}_{ave} = \begin{pmatrix} 1 & 0 \\ 0 & \cos 2\theta_B \end{pmatrix}. \tag{5-1.47}$$

Note that the polarization matrix for spin averaged electric dipole scattering is equivalent to that for Thomson scattering--this is one reason why Thomson scattering is sometimes called electric dipole scattering at high photon energies. The scattering amplitude for dipole radiation can then be written (in nontensor form) in a manner similar to that for Thomson radiation

$$F^{(\lambda)}_{ave}(\mathbf{k}_f, \mathbf{k}_i) = -\frac{1}{4k_f}\frac{(2j_n + 1)}{(2j_i + 1)}\frac{\Gamma_{rad}}{\hbar}\left(\hat{\mathbf{u}}^{(\lambda)*}_f \cdot \hat{\mathbf{u}}^{(\lambda)}_i\right)\frac{1}{\omega_{\mathbf{k}_i} - \omega_0 + i\Gamma/2\hbar} \tag{5-1.48}$$

where for electric dipole scattering

$$\hat{\mathbf{u}}^{(\mathrm{e})} = \hat{\boldsymbol{\varepsilon}}, \tag{5-1.49}$$

and for magnetic dipole scattering

$$\hat{\mathbf{u}}^{(\mathrm{m})} = \hat{\mathbf{h}} = \hat{\mathbf{k}} \times \hat{\boldsymbol{\varepsilon}}. \tag{5-1.50}$$

If the polarization of an electric field is $\hat{\boldsymbol{\varepsilon}}$, then the polarization of the corresponding magnetic field is $\hat{\mathbf{h}}$. Then, the scattering amplitude reveals that magnetic dipole electric fields have the same polarization characteristics as electric dipole magnetic fields.

The total cross section for electric or magnetic dipole scattering is, from the optical theorem,

$$\sigma_{tot} = \frac{4\pi}{k_f}\mathrm{Im}\left\{F_{ave}(\mathbf{k}_f,\mathbf{k}_i)\right\} = \sigma_0 \frac{(\Gamma/2\hbar)^2}{\left(\omega_{\mathbf{k}_i} - \omega_0\right)^2 + (\Gamma/2\hbar)^2} \tag{5-1.51}$$

where σ_0 is the total cross section on resonance

$$\sigma_0 = \frac{2\pi}{k_f^2}\left(\frac{2j_n+1}{2j_i+1}\right)\left(\frac{\Gamma_{rad}}{\Gamma}\right)\left(\hat{\mathbf{u}}_f^* \cdot \hat{\mathbf{u}}_i\right). \tag{5-1.52}$$

This is the familiar form for the spin averaged total cross section for dipole scattering.[3]

For nuclear scattering, the ratio of the radiative decay rate to the total decay rate is a measure of how dominant the internal conversion rate is

$$\frac{\Gamma_{rad}}{\Gamma} = \frac{1}{1+\alpha_{ic}}, \tag{5-1.53}$$

where α_{ic} is the internal conversion coefficient. In nuclear scattering, since the photon energy is so high, the probability that the nuclear excited state will emit an electron, rather than a photon, to decay back to the ground state (that is, will result in internal conversion) can be quite high. For instance, for ^{57}Fe, a common Mössbauer isotope, $\alpha_{ic} = 8.23$, thereby limiting to 11% the chance that an isolated atom will scatter a photon instead of emitting an electron.[4] However, when there is a collection of atoms, this limitation can be overcome and there can be more than an 11% chance of photon emission through a collective phased excitation effect. This is discussed in the dynamical scattering theory of Chapters 6 and 7.

For nuclei having simple two-level systems, the total decay rate and the internal conversion coefficient can be easily measured, and the total cross section, Eq. 5-1.51, can be readily computed. However, electronic systems usually have many level systems with many radiative decay schemes and cascades of Auger emissions from many different angular momentum states. Performing a spin average over all the possible transitions is a formidable task for multielectron systems (recall Eq. 5-1.48 was only for a two level system with initial and intermediate states specified by j_i and j_n). Therefore, the total cross section is usually decomposed into a sum of all the possible types of scattering processes, and the dominant processes are selected

$$\sigma_{tot} = \sigma_{photoelectric}^{elas+inelas} + \sigma_{Compton}^{elas+inelas} + \sigma_{Thomson} + \sigma_{pair\ production} + \cdots. \tag{5-1.54}$$

The photoelectric cross section describes a scattering event in which an incoming photon causes an electron to be ejected into the continuum, and the atom subsequently decays to a final state through radiative or Auger emissions. If the final state is identical to the initial state, the scattering is "elastic" even though the incoming and outgoing particles are different particles--energy conservation still holds. The Compton cross section describes elastic or inelastic absorption reemission for a multilevel system (these are bound state transitions)--the elastic, or Rayleigh, part is expressed in Eq. 5-1.51 for a two level system. Pair production, where an incoming photon scatters into an outgoing photon but changes the electron into its antiparticle in the process, becomes important at energies greater than one MeV. In the dipole approximation, the Thomson cross section is zero since the scattering amplitude is real. Cases for nonzero Thomson cross sections are discussed later in this chapter.

As will be shown in the next chapter, the elastic cross sections are greatly enhanced over the inelastic cross sections in scattering channel directions, such as in the forward direction. When operating far from any bound state resonances, mainly photoelectric scattering occurs, and Compton scattering can be neglected. Cromer and Liberman have made self-consistent Hartree Fock calculations of the relativistic photoelectric cross section of individual atoms for scattering into the forward direction.[5] The imaginary part of the scattering amplitude is proportional to the total cross section, and the real part of the scattering amplitude can be obtained by using the Kramer-Kronig relations (which is equivalent to performing a Hilbert transform). Cromer and Liberman have made these calculations along with a computation of the nonrelativistic Thomson scattering amplitude and tabulated them in the form of parameters f_0, f', and f''.[5] Their parameters are related to the scattering amplitude as follows:

$$F_T(\mathbf{k}_f,\mathbf{k}_i)+F_{photoel}(\mathbf{k}_f,\mathbf{k}_i)=-r_e(\hat{\boldsymbol{\varepsilon}}_f^*\cdot\hat{\boldsymbol{\varepsilon}}_i)(e^{-2W}f_0+f'-if'') \qquad (5\text{-}1.55)$$

where e^{-2W} is a Debye Waller factor that takes into account the vibrations of the atoms about their equilibrium positions. The major contribution to f_0 comes from Thomson scattering described by Eq. 5-1.1 with small relativistic corrections from the photoelectric cross section. The Debye Waller factor is essentially the form factor, Eq. 4-2.14, modified to take into account vibrating scatterers

$$e^{-2W}=\langle i_s|e^{-i(\mathbf{k}_f-\mathbf{k}_i)\cdot\mathbf{u}}|i_s\rangle, \qquad (5\text{-}1.56)$$

where $\mathbf{u}$ is a displacement vector describing the vibrations of the atoms about their equilibrium positions. The factor W turns out to be proportional to the mean square displacement of the atom from equilibrium in the direction of the momentum transfer[6]

$$\mathbf{H} = \left(\mathbf{k}_f - \mathbf{k}_i\right) \tag{5-1.57}$$

$$W = 8\pi^2 \left\langle u_{\mathbf{H}}^2 \right\rangle \left(\sin\theta_B/\lambda\right). \tag{5-1.58}$$

The form factor is essentially the Fourier transform of the charge density

$$f_0(\mathbf{H}) = \int d^3x \rho_s(\mathbf{x}) e^{-i\mathbf{H}\cdot\mathbf{x}}, \tag{5-1.59}$$

where $\mathbf{H}$ is given by Eq. 5-1.57, and $\rho_s(\mathbf{x}) = \phi_s^*(\mathbf{x})\phi_s(\mathbf{x})$. Since the charge density is a real function of the spatial coordinates, the form factor is in general Hermitian

$$f_0(\mathbf{H}) = f_0^*(-\mathbf{H}). \tag{5-1.60}$$

If the charge density has space inversion symmetry (the assumed case for all Cromer and Liberman calculations), the form factor is real and symmetric

$$\rho_s(\mathbf{x}) = \rho_s(-\mathbf{x}) \Rightarrow f_0(\mathbf{H}) = f_0^*(\mathbf{H}) = f_0(-\mathbf{H}). \tag{5-1.61}$$

However, when atoms are brought together into a solid, the electronic charge distributions of an atom may be distorted by the electronic and magnetic potentials of nearby atoms, thereby, possibly breaking space inversion symmetry.[7]

5.2 Hyperfine Interactions for Magnetostatic and Electrostatic Fields

If the incoming electric field is a small perturbation, too small to significantly shift energy levels or cause level splitting of those states that existed before the perturbation, the eigenenergies during the perturbation can be approximated as being the eigenenergies before the perturbation. The major effect of the perturbation will then be to cause transitions between the various energy levels as described by the transition probability, or S-matrix elements. In this approximation, the resonant frequencies, $\omega_{ni} = \left(E_n - E_i\right)/\hbar$, in the multipole scattering amplitude are simply the eigenvalues of the constant perturbation, H_0, in Eq. 2-1.1. For magnetostatic and electrostatic interactions, the constant perturbation can be written in the form

$$H_0 = H_0' + H_{mag} + H_{el} \tag{5-2.1}$$

where

$$H_0' = p^2/2m + H_{Int}, \tag{5-2.2}$$

and H_{Int} includes other possible interactions not discussed so far.

Under the assumption that a nucleus is a pointlike magnetic dipole, H_{mag} can be constructed by examining how the nuclear dipole interacts with the magnetic dipole field of the electron

$$H_{mag} = -\boldsymbol{\mu} \cdot \mathbf{B}_{dipole} - \boldsymbol{\mu} \cdot \mathbf{B}_{F}. \tag{5-2.3}$$

The first term represents the dipole interaction between an electron's orbital and spin momentum with the magnetic moment of the nucleus[8]

$$\mathbf{B}_{dipole} = -2\beta\left[\frac{\mathbf{L}-\mathbf{S}}{r^3} + \frac{3\mathbf{r}(\mathbf{S}\cdot\mathbf{r})}{r^5}\right] \tag{5-2.4}$$

where $\mathbf{L}$ and $\mathbf{S}$ are the orbital and spin angular momenta of an electron, and β is the electron Bohr magneton

$$\beta = e\hbar/2m_e c. \tag{5-2.5}$$

Only the orbital electrons that do not lie in an s-state, $l \neq 0$, contribute to the dipolar magnetic field.

The second term in Eq. 5-2.3 represents the Fermi contact interaction between an s orbital electron and the nucleus[8]

$$\mathbf{B}_F = -\frac{16\pi}{3}\beta\delta(\mathbf{r})\mathbf{S}. \tag{5-2.6}$$

The computation of the total magnetic field at the nucleus can be quite involved for multielectron atoms embedded in a medium because one must take into account the exchange interactions among all the internal electrons and between the internal and external conduction electrons.[9, 10] For example, examination of Eq. 5-2.6 will show that the net Fermi contact field is zero for a filled s shell because the two electrons in that shell have opposite spin. The exchange interaction between electrons from outer unfilled shells and the filled s shells polarizes the s shell electrons to produce a nonzero net Fermi contact field at the nucleus.[10] The polarization of s electrons is a small effect, but since the Fermi contact field for an unpaired $1s$ electron can be hundreds of megagauss, the polarization effect can easily produce sizable fields on the order of hundreds of kilogauss. The field strength of the dipole fields is an order to two orders of magnitude smaller that the net Fermi contact field, and there is also a contribution from the polarization of the conduction s electrons that can also produce Fermi contact fields on the order of a hundred kilogauss.[9]

For the purpose of constructing the magnetostatic interaction Hamiltonian, the detailed structure of the dipole and Fermi contact fields will be not be investigated, and the magnetostatic interaction Hamiltonian will simply be expressed as

$$H_{mag} = -\boldsymbol{\mu} \cdot \mathbf{B}_{\text{int}} \tag{5-2.7}$$

where $\mathbf{B}_{\text{int}}$ is the total magnetic field at the nucleus.

The electrostatic interaction Hamiltonian is

$$H_{el} = -\sum_{pc} \frac{e^2}{|r_p - r_c|} \tag{5-2.8}$$

where r_p is the position of a proton within the nucleus, and r_c is the position of an electron outside the nucleus (including those from surrounding atoms). Expanding $1/|r_p - r_c|$ in terms of spherical harmonics enables H_{el} to be rewritten as[11, 12]

$$H_{el} = \sum_{l=0}^{\infty} \mathbf{T}^{(l)} \cdot \mathbf{V}^{(l)} \tag{5-2.9}$$

where $\mathbf{T}^{(l)}$ and $\mathbf{V}^{(l)}$ are nuclear and electronic multipole electrostatic operators

$$\mathbf{T}_q^{(l)} = \sqrt{\frac{4\pi}{2l+1}} \sum_p e r_p^l Y_{lq}(\theta_p, \phi_p) \tag{5-2.10}$$

$$\mathbf{V}_q^{(l)} = -\sqrt{\frac{4\pi}{2l+1}} \sum_c e \frac{1}{r_c^{l+1}} Y_{lq}(\theta_c, \phi_c) \tag{5-2.11}$$

Since the nuclear states have a well defined parity, the odd nuclear multipole operators (those with odd l) give vanishing matrix elements. The even nuclear operators yield nonvanishing matrix elements, and the major contribution come from the lowest order multipoles--the Coulomb and electric quadrupoles ($l = 0$ and 2).

The Coulomb interaction is

$$H_{coul} = -Ze_p \sum_c \frac{e_c}{r_c} \tag{5-2.12}$$

where Z is the number of protons within the nucleus. To this a correction term must be added that is due to the finite size of the nucleus--the isomer shift[8]

$$H_{isomer} = \frac{2}{3} \pi e^2 Z |\phi(0)|^2 \langle R^2 \rangle \tag{5-2.13}$$

where $\langle R^2 \rangle$ is the mean square charge radius of the nucleus and $e^2|\phi(0)|^2$ is the electronic charge density at the nucleus.

The introduction of the electric quadrupole interaction produces additional complexities. The electric quadrupole Hamiltonian has matrix elements that are proportional the electric field gradient at the nucleus. However, the electric field gradient tensor has a principal axis that may not be aligned with the quantum axis of the nucleus. Then, there are two possible quantum axes. This arrangement gives rise to nuclear level mixing (a competition between quantum axes towards defining the state of the system) in which there no longer exists any well defined, or "good", quantum numbers describing the nuclear or electronic states. Matthias, Schneider, and Steffen have extensively worked out this problem.[13]

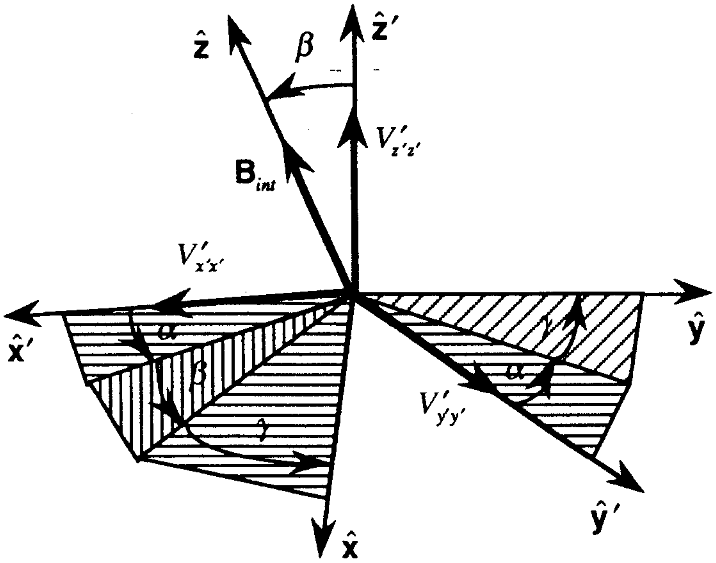

Fig. 5-2.1. Orientation of electric field gradient axes (primed system) to the quantization axes (unprimed system).[13]

Fig. 5-2.1 shows the orientation of the electric field gradient system, system S' with principal axes $(\hat{\mathbf{x}}', \hat{\mathbf{y}}', \hat{\mathbf{z}}')$, with respect to the nuclear quantum axis system, system S, in which the magnetic field direction specifies the quantum $\hat{\mathbf{z}}$ axis. The Euler angles, (α, β, γ), specify how to rotate system S' so that it coincides with system S. For an electric field gradient that has axial symmetry with respect to the $\hat{\mathbf{z}}'$ axis, the angle α can be set to zero. For nonaxial symmetry, an asymmetry parameter η is introduced

$$\eta = \frac{V'_{x'x'} - V'_{y'y'}}{V'_{z'z'}} \tag{5-2.14}$$

where

$$V'_{uv} = \frac{\partial^2 V'}{\partial u \partial v} \qquad u, v = x, y, z. \tag{5-2.15}$$

Using the rotation matrix, $D^{(2)}_{mm'}(\alpha, \beta, \gamma)$, to rotate the electric field gradient principal axis system upon the quantum axis system gives the matrix elements of the quadrupole electrostatic Hamiltonian. (The nuclear dipole magnetostatic matrix elements are also included below. Also, nuclear total angular momentum quantum numbers are conventionally represented as I.)

$$H_{mm} = -\hbar\omega_B m + \hbar\omega_E \frac{1}{2}\left(3\cos^2\beta - 1 + \eta\sin^2\beta\cos 2\alpha\right)\left[3m^2 - I(I+1)\right] \tag{5-2.16}$$

$$\begin{aligned} H_{m,m\pm1} = \hbar\omega_E \frac{3}{2}\sin\beta\left\{\cos\beta \mp \frac{\eta}{6}\left[(1\pm\cos\beta)e^{i2\alpha} - (1\mp\cos\beta)e^{-i2\alpha}\right]\right\} \\ \times e^{\pm i\gamma}(2m\pm1)\sqrt{(I\mp m)(I\pm m+1)} \end{aligned} \tag{5-2.17}$$

$$\begin{aligned} H_{m,m\pm2} = \hbar\omega_E \frac{3}{4}\left\{\sin^2\beta + \frac{\eta}{6}\left[(1\pm\cos\beta)^2 e^{i2\alpha} + (1\mp\cos\beta)^2 e^{-i2\alpha}\right]\right\} \\ \times e^{\pm i2\gamma}\sqrt{(I\pm m+2)(I\pm m+1)(I\mp m)(I\mp m-1)} \end{aligned} \tag{5-2.18}$$

where $\hbar\omega_B = \mu B_{int}/I$ (5-2.19)

$$\hbar\omega_E = \frac{e^2qQ}{4I(2I-1)}. \tag{5-2.20}$$

The magnetic moment of the nucleus has been defined as

$$\mu = \langle I, m_I = I|\mu_0^{(1)}|I, m_I = I\rangle = \begin{pmatrix} I & 1 & I \\ -I & 0 & I \end{pmatrix}\langle I\|\boldsymbol{\mu}^{(1)}\|I\rangle = \frac{I}{\sqrt{(2I+1)(I+1)I}}\langle I\|\boldsymbol{\mu}^{(1)}\|I\rangle, \tag{5-2.21}$$

the nuclear electric quadrupole moment has been defined as

$$\begin{aligned} eQ/2 &= \langle I, m_I = I|T_0^{(2)}|I, m_I = I\rangle = \begin{pmatrix} I & 2 & I \\ -I & 0 & I \end{pmatrix}\langle I\|\mathbf{T}^{(2)}\|I\rangle \\ &= \frac{I(2I-1)}{\sqrt{(2I+3)(I+1)(2I+1)2I(2I-1)}}\langle I\|\mathbf{T}^{(2)}\|I\rangle, \end{aligned} \tag{5-2.22}$$

and the electronic electric quadrupole has been defined as (averaging over space)

$$eq/2 = \langle V_0'^{(2)}\rangle \tag{5-2.23}$$

where $V_0'^{(2)} = V'_{z'z'}/2$ (5-2.24)

$$V_{\pm1}'^{(2)} = \mp\frac{1}{2}\sqrt{\frac{2}{3}}\left(V'_{z'x'} \pm iV'_{y'z'}\right) = 0 \tag{5-2.25}$$

$$V_{\pm2}'^{(2)} = \frac{1}{4}\sqrt{\frac{2}{3}}\left(V'_{x'x'} - V'_{y'y'} \pm 2iV'_{x'y'}\right) = \frac{1}{4}\sqrt{\frac{2}{3}}\eta V'_{z'z'}, \tag{5-2.26}$$

and a coordinate system has been chosen so that $V'_{uv} = 0$ when $u \neq v$. The angular factors come from the rotation relation

$$V_q^{(2)} = \sum_{l=-2}^{2} V_l'^{(2)} D_{lq}^{(2)}(\alpha,\beta,\gamma). \tag{5-2.27}$$

When the electric quadrupole interaction is small compared to the magnetic dipole interaction, a first order approximation can be made by dropping all of the off diagonal matrix elements of the total Hamiltonian. In such a first order approximation, the eigenvalues are given by H_{mm}, and the eigenfunctions can be written in column form as

$$\boldsymbol{\phi}_{mn}^{(0)T} = (0,0,0,\cdots,1,\cdots,0) \tag{5-2.28}$$

where the unity factor is in the n^{th} place for $1 \le n \le 2I+1$, and $2I+1$ is the number of eigenvalues. Each quantum number m is then a "good" quantum number in that they all define a unique state of the system--the n^{th} state is specified by only one number: m.

When no approximations are made to the total Hamiltonian, the eigenfunctions become a linear combination of the first order states of the system

$$\boldsymbol{\phi}_{mn} = \sum_{q=-m'}^{m'} c_{nq} \boldsymbol{\phi}_{qn}^{(0)} \tag{5-2.29}$$

where c_{nq} is a complex number and m' ranges from the minimum to the maximum possible value of m. Each quantum number m is now a "poor" quantum number since they no longer well define the states of the system--the n^{th} state is now specified by a sum over all possible m quantum numbers.

The polarization matrix of Eq. 5-1.5 must now be modified to include these changes

$$\left(P_{Ln}^{(\lambda)}\right)_{xy} = \left[\hat{\boldsymbol{\varepsilon}}_x^{f*} \cdot \sum_{q=-m'}^{m'} \mathbf{Y}_{LM}^{(\lambda)}\left(\Omega_{\mathbf{k}_f}\right)\left(\boldsymbol{\phi}_{mn} \cdot \boldsymbol{\phi}_{qn}^{(0)}\right)\right]\left[\sum_{q'=-m'}^{m'}\left(\boldsymbol{\phi}_{mn}^{*} \cdot \boldsymbol{\phi}_{q'n}^{(0)}\right)\mathbf{Y}_{LM'}^{(\lambda)*}\left(\Omega_{\mathbf{k}_i}\right) \cdot \hat{\boldsymbol{\varepsilon}}_y^{i}\right] \tag{5-2.30}$$

where $\boldsymbol{\phi}_{mn} \cdot \boldsymbol{\phi}_{qn}^{(0)} = c_{nq}$ of Eq. 5-2.29, $M = q - m_f$, and $M' = q' - m_f$ (the scattering amplitude in Eq. 5-1.4 must now be summed over L and n rather than L and M as before). Examples of magnetic dipole scattering for ^{57}Fe are given in the following sections.

5.3 Linear Polarization Reversal of Fields Scattered from a Ferromagnetic Lattice

The hyperfine energy level diagram for ^{57}Fe is shown in Fig. 5-3.1 (all energy shifts are greatly exaggerated). The isomer shifts for the excited and ground states are designated by ΔE_{Is}^{e} and ΔE_{Is}^{g}. The excited and ground state magnetic splittings are $\hbar\omega_B^e = 2\mu_e B_{int}/3$ and $\hbar\omega_B^g = 2\mu_g B_{int}$. The ground and excited state quadrupole shifts are $\Delta E_Q^g = 0$ and

$$\Delta E_Q^e = \frac{1}{4} e^2 qQ \left(\frac{3\cos^2\beta - 1}{2} \right). \tag{5-3.1}$$

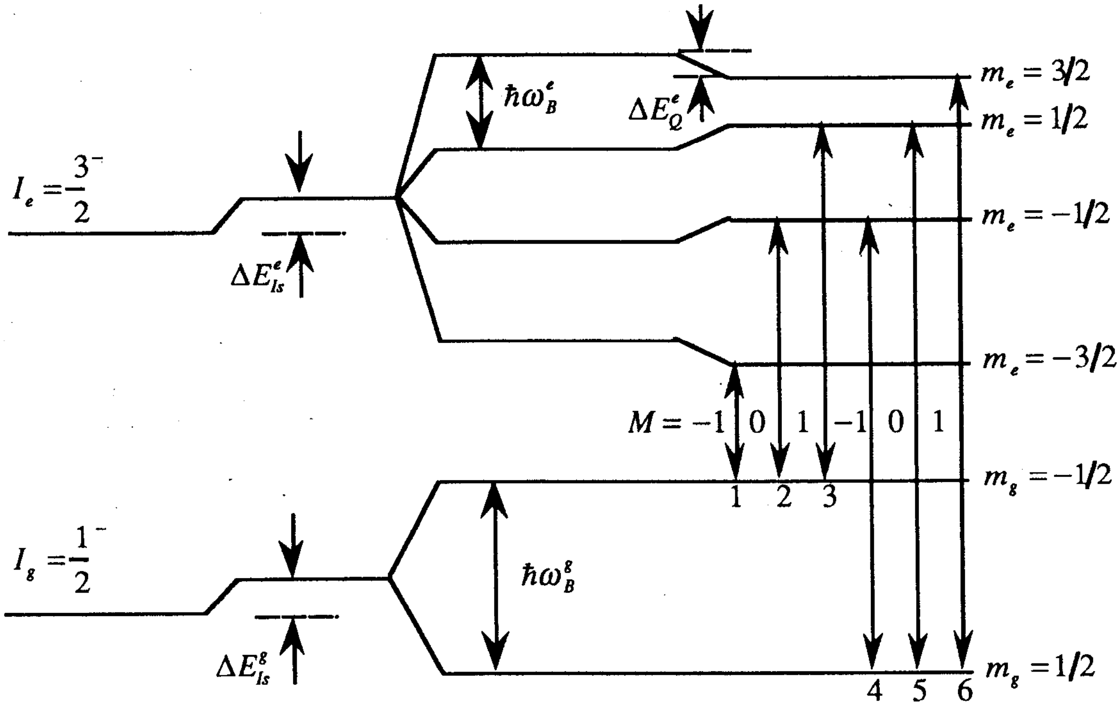

Fig. 5-3.1. Hyperfine energy levels of ^{57}Fe of d-sites in a YIG crystal. Quadrupole shift for ground states is zero, and $\mu_e < 0$ and $B_{int} < 0$.

where the electric field gradient tensor is assumed to be axially symmetric so that $\eta = 0$.

The electric quadrupole shift is small compared to the magnetic dipole shift for ^{57}Fe, so in most cases first order perturbation theory is adequate. The excited states are then labeled by good quantum numbers, and the unitary eigenvector matrix (whose columns are the eigenfunctions) that diagonalizes the Hamiltonian is diagonal

$$\Phi^{(0)} = \left(\phi^{(0)}_{\frac{3}{2},1}, \phi^{(0)}_{\frac{1}{2},2}, \phi^{(0)}_{-\frac{1}{2},3}, \phi^{(0)}_{-\frac{3}{2},4}\right) = \begin{pmatrix} 1 & & & \\ & 1 & \multicolumn{2}{c}{0} \\ \multicolumn{2}{c}{0} & 1 & \\ & & & 1 \end{pmatrix}. \qquad (5\text{-}3.2)$$

When the full theory is employed, the unitary eigenvector matrix that diagonalizes the Hamiltonian is no longer diagonal

$$\Phi = \left(\phi_{\frac{3}{2},1}, \phi_{\frac{1}{2},2}, \phi_{-\frac{1}{2},3}, \phi_{-\frac{3}{2},4}\right) = \begin{pmatrix} c_{1,\frac{3}{2}} & c_{2,\frac{3}{2}} & c_{3,\frac{3}{2}} & c_{4,\frac{3}{2}} \\ c_{1,\frac{1}{2}} & c_{2,\frac{1}{2}} & c_{3,\frac{1}{2}} & c_{4,\frac{1}{2}} \\ c_{1,-\frac{1}{2}} & c_{2,-\frac{1}{2}} & c_{3,-\frac{1}{2}} & c_{4,-\frac{1}{2}} \\ c_{1,-\frac{3}{2}} & c_{2,-\frac{3}{2}} & c_{3,-\frac{3}{2}} & c_{4,-\frac{3}{2}} \end{pmatrix}. \qquad (5\text{-}3.3)$$

Since the ground states have no electric quadrupole interaction, their eigenvector matrix is always diagonal. The Φ-matrix elements for the excited states are found by diagonalizing the full Hamiltonian matrix to get the eigenvectors. The magnitude of the diagonal elements are close to unity, and the off diagonal terms are small (magnitudes on the order of 0.1 or less). The energy level diagram is negligibly changed (the energy levels change by about 1% of a natural linewidth). The change in the nuclear states, though, is large enough to produce noticeable effects.

One interesting effect is the case of complete polarization reversal of the linear polarization basis of an incoming electric field. In Section 5.1, where nuclear level mixing was neglected, incoming right circularly polarized fields could be scattered into left circularly polarized fields and visa-versa for a convenient orientation of the quantization axis. Nuclear level mixing now enables vertically polarized fields to scatter into horizontally polarized fields and visa-versa.

For example, for the $[0\ 0\ 2]$ reflection of a YIG crystal, two ^{57}Fe sublattices within the unit cell, called $d1$ and $d2$ sites, contribute to a nonzero diffracted beam. The iron in these sites have identical hyperfine environments except that the electric field gradients lying in the $[0\ 0\ 2]$ plane are oriented 90° with respect to each site. Also, the two sublattices are situated such that the reflected wave from each site is 180° out of phase. Each site produces a six line emission pattern which will be labeled $(\ell_1, \ell_2, \ell_3, \ell_4, \ell_5, \ell_6)$ for the $d1$ sites and $(\ell_1', \ell_2', \ell_3', \ell_4', \ell_5', \ell_6')$ for the $d2$ sites (see Fig. 5-3.1). In first order perturbation theory, if the internal magnetic field was oriented by an external magnetic field so that it bisected the angle between the electric field gradients, see Fig. 5-3.2, the quadrupole shifts of the iron atoms in the two sites would be identical for each pair of lines (ℓ_i, ℓ_i') since $\beta = \pm 45°$ and $(3\cos^2\beta - 1)/2 = 1/4$. Then, to first order, no net reflected intensity is possible because the reflected field amplitudes from each site would cancel as a result of the 180° phase difference and because each pair of lines lie at the same energy.

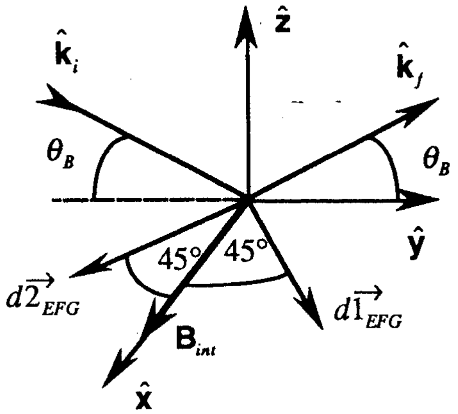

Fig. 5-3.2. Orientation of YIG electric field gradient directions for $d1$ and $d2$ sites lying in the xy plane. Internal magnetic field direction bisects angle between them.

However, when nuclear level mixing is accounted for, there is no complete cancellation. For instance, the polarization matrix of line ℓ_1 is (using Eq. 5-2.30 for the case where $n = 1$, keeping only terms that satisfy the dipole selection rules $M = 0, \pm 1$, and knowing that ^{57}Fe radiates only magnetic dipole fields)

$$\left(P_{11}^{(\mathrm{m})}\right)_{xy} = \left[\hat{\boldsymbol{\varepsilon}}_x^{f*} \cdot \left(\mathbf{Y}_{1,1}^{(\mathrm{m})} c_{1,\frac{3}{2}} + \mathbf{Y}_{1,0}^{(\mathrm{m})} c_{1,\frac{1}{2}} + \mathbf{Y}_{1,-1}^{(\mathrm{m})} c_{1,-\frac{1}{2}}\right)\right]\left[\left(\mathbf{Y}_{1,1}^{(\mathrm{m})*} c_{1,\frac{3}{2}}^* + \mathbf{Y}_{1,0}^{(\mathrm{m})*} c_{1,\frac{1}{2}}^* + \mathbf{Y}_{1,-1}^{(\mathrm{m})*} c_{1,-\frac{1}{2}}^*\right) \cdot \hat{\boldsymbol{\varepsilon}}_y^i\right]. \tag{5-3.4}$$

The scattering geometry is exactly that of Case 1 in Section 5.1. Then, using Eqs. 5-1.19 to 5-1.21 and the results of Case 1 gives the polarization matrix elements:

$$\left(P_{11}^{(\mathrm{m})}\right)_{xx} = \frac{3}{16\pi}\left(-e^{i2\theta_B} c_{1,\frac{3}{2}} - e^{-i2\theta_B} c_{1,-\frac{1}{2}}\right)\left(-e^{i2\theta_B} c_{1,\frac{3}{2}}^* - e^{-i2\theta_B} c_{1,-\frac{1}{2}}^*\right) \tag{5-3.5}$$

$$\left(P_{11}^{(\mathrm{m})}\right)_{xy} = \frac{3}{16\pi}\left(i\sqrt{2}\, c_{1,\frac{1}{2}}\right)\left(-e^{i2\theta_B} c_{1,\frac{3}{2}}^* - e^{-i2\theta_B} c_{1,-\frac{1}{2}}^*\right) \tag{5-3.6}$$

$$\left(P_{11}^{(\mathrm{m})}\right)_{yx} = \frac{3}{16\pi}\left(-e^{i2\theta_B} c_{1,\frac{3}{2}} - e^{-i2\theta_B} c_{1,-\frac{1}{2}}\right)\left(-i\sqrt{2}\, c_{1,\frac{1}{2}}^*\right) \tag{5-3.7}$$

$$\left(P_{11}^{(\mathrm{m})}\right)_{yy} = \frac{3}{8\pi}\left|c_{1,\frac{1}{2}}\right|^2. \tag{5-3.8}$$

Note that the Euler azimuthal angle for ℓ_1 is $\gamma_1 = -\pi/2$ and for ℓ_1' is $\gamma_1' = \pi/2$. Applying a unitary transformation upon the Hamiltonian, Eqs. 5-2.16 to 5-2.18, gives in matrix form [12]

$$H(\alpha,\beta,0) = A(\gamma)H(\alpha,\beta,\gamma)A^{-1}(\gamma) \tag{5-3.9}$$

where $$A_{kl}(\gamma) = \delta_{kl}e^{il\gamma} \qquad (k,l = I, I-1,\ldots,-I). \tag{5-3.10}$$

The eigenvectors can then be written in the form

$$\Phi(\alpha,\beta,\gamma) = \Phi(\alpha,\beta,0)A(\gamma). \tag{5-3.11}$$

Since $\alpha = 0$, $\Phi(\alpha = 0,\beta,0)$ is a real matrix. So, when $\gamma \to -\gamma$, the eigenvectors transform into their complex conjugates. Therefore, the eigenfunction associated with ℓ_1 is the complex conjugate of the one associated with ℓ_1'

$$c'_{nq} = c^*_{nq}. \tag{5-3.12}$$

Attaching a minus sign to the amplitude of line ℓ_1' to take care of the phase difference of the reflected fields from each sublattice, and summing the polarization matrices for lines ℓ_1 and ℓ_1' gives

$$P_{11}^{(m)}\Big|_{\ell_1} + P_{11}^{(m)}\Big|_{\ell_1'} = \begin{pmatrix} 0 & C \\ C & 0 \end{pmatrix} \tag{5-3.13}$$

where $$C = 2\sqrt{2}\,\frac{3}{16\pi}\left(e^{i2\theta_B}\,\mathrm{Im}\left\{c_{1,\frac{1}{2}}c^*_{1,\frac{3}{2}}\right\} + e^{-i2\theta_B}\,\mathrm{Im}\left\{c_{1,\frac{1}{2}}c^*_{1,-\frac{1}{2}}\right\}\right). \tag{5-3.14}$$

Because the polarization matrix has only off diagonal matrix elements, complete linear polarization reversal occurs. For example,

$$\begin{pmatrix} 0 & C \\ C & 0 \end{pmatrix} \cdot \hat{\boldsymbol{\sigma}}_i = \begin{pmatrix} 0 & C \\ C & 0 \end{pmatrix} \cdot \begin{pmatrix} 1 \\ 0 \end{pmatrix} = C\begin{pmatrix} 0 \\ 1 \end{pmatrix} = C\hat{\boldsymbol{\pi}}_f.$$

This shows that incoming horizontally polarized fields scatter into vertically polarized fields with an amplitude proportional to C. However, since the off diagonal elements of the eigenvector matrix are small, $|C|$ is small, and thus the scattered intensity is very low. The nuclear resonance scattering group at Hamburg[14, 15] has observed the effect of nonzero cancellation, but to date no polarization analysis has been done to observe the effect of polarization reversal.

5.4 Linear Polarization Reversal of Fields Scattered from an Antiferromagnetic Lattice

The added complexity of nuclear level mixing is not needed to produce linear polarization reversal for scattering from an antiferromagnetic lattice. However, similar to the case for a ferromagnetic lattice, one still relies upon the phase difference between the reflected fields from different iron sites within the lattice.

For this example, take the case of ^{57}FeBO$_3$: It has a rhombohedral unit cell structure containing two iron atoms located at two different b-sites. For certain reflections, such as $[n\ n\ n]$ reflections where n is an odd integer, the reflected fields from the two sites are 180° out of phase. However, because of the antiferromagnetic structure of the crystal lattice (further explained in Chapter 8), the electric fields scattered from the nuclei do not cancel out.

Let the internal magnetic field at each nuclei at the two b-sites be parallel to both the scattering plane and the $[n\ n\ n]$ planes (this corresponds to Case 3 in Section 5.1). The polarization matrices for the iron site in which the internal magnetic field lies in the $\hat{\mathbf{y}}$ direction (see Fig. 5-1.1) is given by Eq. 5-1.28, and the polarization matrices for the other site in which the internal magnetic field lies in the $-\hat{\mathbf{y}}$ direction is given by the complex conjugate of Eq. 5-1.28:

$$P_{10}^{(m)} = \frac{3}{8\pi}\begin{pmatrix} -\sin^2\theta_B & 0 \\ 0 & 0 \end{pmatrix}, \qquad P_{1,\pm1}^{(m)} = -\frac{3}{16\pi}\begin{pmatrix} -\cos^2\theta_B & \mp i\cos\theta_B \\ \pm i\cos\theta_B & -1 \end{pmatrix}. \tag{5-4.1}$$

For incident horizontally polarized fields, the polarization of lines ℓ_i for the case $\hat{\mathbf{B}}_{int} = +\hat{\mathbf{y}}$ is:

$$\ell_2 \text{ and } \ell_5 \Rightarrow \frac{3}{8\pi}\begin{pmatrix} -\sin^2\theta_B & 0 \\ 0 & 0 \end{pmatrix}\begin{pmatrix} 1 \\ 0 \end{pmatrix} = -\frac{3}{8\pi}\sin^2\theta_B\begin{pmatrix} 1 \\ 0 \end{pmatrix},$$

$$\ell_1 \text{ and } \ell_4 \Rightarrow -\frac{3}{16\pi}\begin{pmatrix} -\cos^2\theta_B & +i\cos\theta_B \\ -i\cos\theta_B & -1 \end{pmatrix}\begin{pmatrix} 1 \\ 0 \end{pmatrix} = \frac{3}{16\pi}\begin{pmatrix} \cos^2\theta_B \\ i\cos\theta_B \end{pmatrix},$$

and

$$\ell_3 \text{ and } \ell_6 \Rightarrow \frac{3}{16\pi}\begin{pmatrix} \cos^2\theta_B \\ -i\cos\theta_B \end{pmatrix}.$$

The polarization of lines ℓ_i' for the case $\hat{\mathbf{B}}_{int} = -\hat{\mathbf{y}}$ is the complex conjugate of the expressions above. Pictorially, the polarizations the lines for the two b-sites are shown in Fig. 5-4.1 where, for the lines ℓ_i', a minus sign was included to take into account that the fields reflected the iron sites giving rise to these lines are 180° out of phase with those fields reflected from the other iron sites giving rise to the lines ℓ_i.

Since pairs of resonance lines lie at the same energy, the superposition of each pair of lines ℓ_i and ℓ_i' gives the net amplitude. As shown in Fig. 5-4.1, the net resultant field is completely vertically polarized. Incident horizontally polarized fields are scattered into outgoing vertically polarized fields, and visa-versa. Unlike the case for a ferromagnet, linear polarization reversal of fields scattered from an antiferromagnet is a strong effect and has been clearly observed in an experiment using $^{57}\mathrm{Fe_2O_3}$.[16]

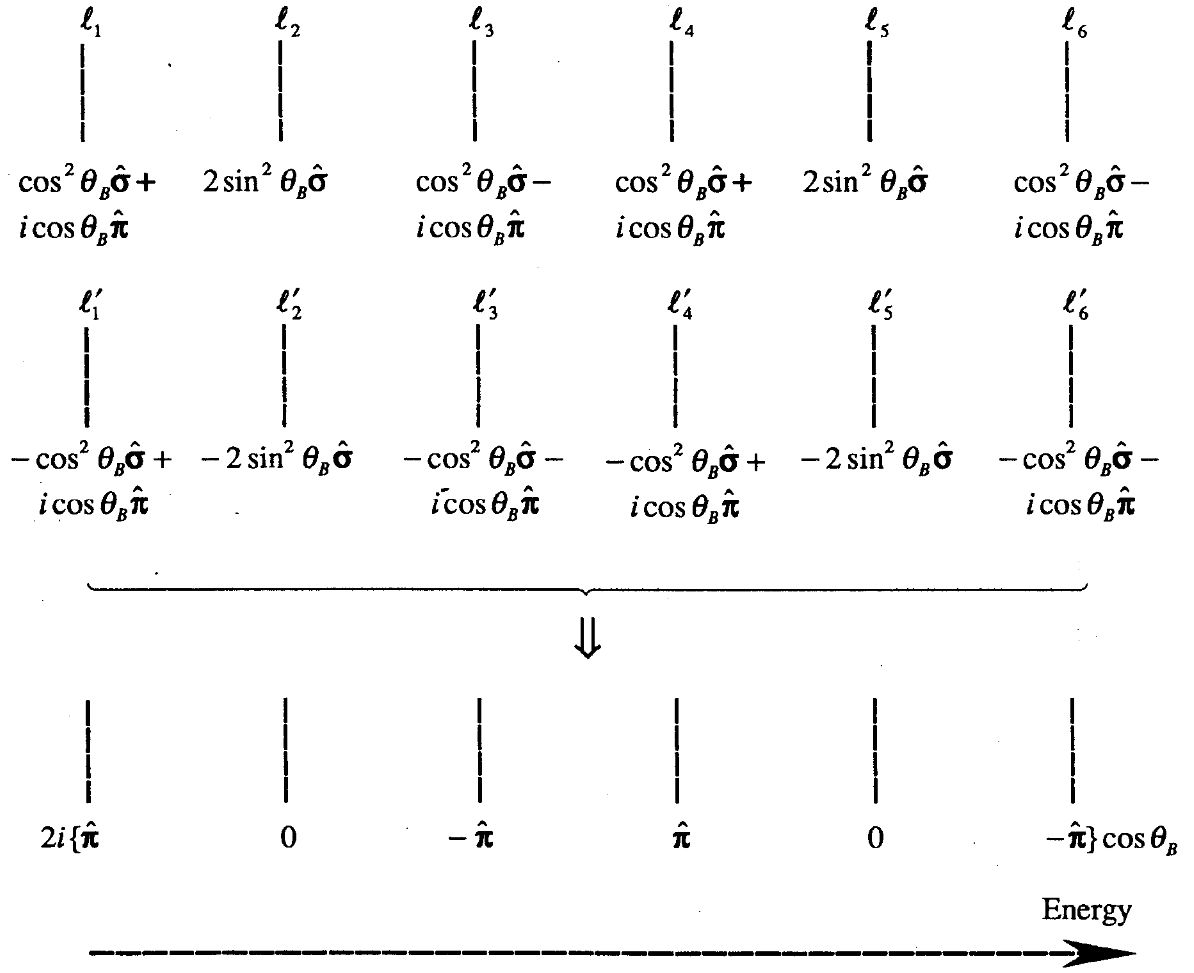

Fig. 5-4.1 Demonstration of linear polarization reversal. An incident $\hat{\sigma}$ polarized field is scattered by iron nuclei in an antiferromagnetic lattice. The sum of the scattered fields is a resultant field that is $\hat{\pi}$ polarized.

5.5 Angular Interferometry

As shown in Section 5.1, the direction of the quantization axis strongly influences the nature of the scattered fields. Major differences in the spectra of scattered fields can also be seen when the internal magnetic field is oriented to lie in an antiparallel direction. This phenomena allows one to do angular interferometry where quantum beat interference patterns depend not upon the spatial distances photons travel such as in a Michelson-Morley interferometer, but upon the angles through which photons are rotated. The example below describes this type of interferometry using the scattering theory developed in this chapter. An alternate description of this phenomena utilizing the rotational symmetry properties of free space is given in Appendix A.[17]

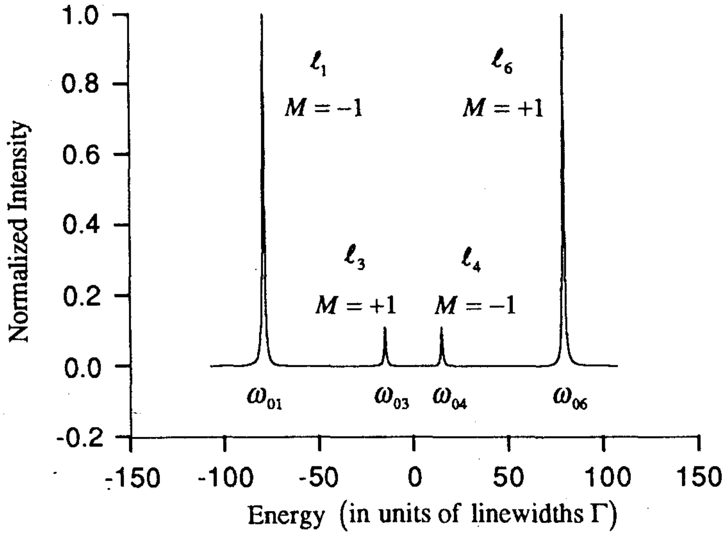

Fig. 5-5.1. Four line magnetic dipole energy spectrum when incoming field is horizontally polarized.

As an example, consider just one site in YIG, such as the d 1-site discussed in the last section. When the internal magnetic field is oriented perpendicular to the scattering plane (see Fig. 5-1.1 where $\hat{\mathbf{B}}_{\text{int}}$ is now the quantization axis $\hat{\mathbf{Q}}_z$),

$$\hat{\mathbf{B}}_{\text{int}} = \hat{\mathbf{x}}, \tag{5-5.1}$$

and, for incoming horizontally polarized fields, the intensity of the scattered fields exhibits the 4-line spectrum shown in Fig. 5-5.1. The orientation corresponds to Case 1 in Section 5.1, and thus lines ℓ_2 and ℓ_5 are forbidden by polarization selection rules.

In the kinematical limit, the total electric field amplitude scattered from the crystal is simply the sum of the amplitudes from each particle within the crystal. Since the scattered field from each particle is proportional to the scattering amplitude, the field amplitude of the four allowed lines for a single particle are as follows (from Eqs. 5-1.4, 5-1.22, and 5-1.23):

$$\ell_1(\omega) = a_1 e^{-i2\theta_B} / (\omega - \omega_{01} + i\Gamma/2\hbar) \qquad (5\text{-}5.2)$$

$$\ell_3(\omega) = a_3 e^{i2\theta_B} / (\omega - \omega_{03} + i\Gamma/2\hbar) \qquad (5\text{-}5.3)$$

$$\ell_4(\omega) = a_3 e^{-i2\theta_B} / (\omega - \omega_{04} + i\Gamma/2\hbar) \qquad (5\text{-}5.4)$$

$$\ell_6(\omega) = a_1 e^{i2\theta_B} / (\omega - \omega_{06} + i\Gamma/2\hbar) \qquad (5\text{-}5.5)$$

where $a_1 = c_0 \cdot 1$, $a_3 = c_0 \cdot 1/3$, and c_0 is a quantity proportional to the incoming field amplitude. The factors multiplying c_0 are the squares of the Clebsch-Gordan coefficients for those lines (see Eqs. 5-1.39 and 5-1.40).

When the internal magnetic field is oriented into an antiparallel direction,

$$\hat{\mathbf{B}}_{\text{int}} = -\hat{\mathbf{x}}, \qquad (5\text{-}5.6)$$

the phase of the amplitudes will change, but their magnitudes stay the same. For such an orientation, from Fig. 5-5.2, the conditions in Case 1 in Section 5.1 change to

$$\theta_i = \theta_f = \pi/2, \qquad \phi_f - \phi_i = -2\theta_B,$$

$$\hat{\boldsymbol{\sigma}}_{(i,f)} = \hat{\boldsymbol{\theta}}_{(i,f)}, \qquad \hat{\boldsymbol{\pi}}_{(i,f)} = -\hat{\boldsymbol{\phi}}_{(i,f)}, \qquad \beta_{(i,f)} = \pi/2.$$

Because the azimuthal phase difference is now minus the scattering angle, the polarization matrices in Eqs. 5-1.22 and 5-1.23 change to their complex conjugates. As a result, the amplitudes of the lines for this new orientation are

$$\ell_1'(\omega) = a_1 e^{i2\theta_B} / (\omega - \omega_{01} + i\Gamma/2\hbar) \qquad (5\text{-}5.7)$$

$$\ell_3'(\omega) = a_3 e^{-i2\theta_B} / (\omega - \omega_{03} + i\Gamma/2\hbar) \qquad (5\text{-}5.8)$$

$$\ell_4'(\omega) = a_3 e^{i2\theta_B} / (\omega - \omega_{04} + i\Gamma/2\hbar) \qquad (5\text{-}5.9)$$

$$\ell_6'(\omega) = a_1 e^{-i2\theta_B} / (\omega - \omega_{06} + i\Gamma/2\hbar). \qquad (5\text{-}5.10)$$

Far off resonance where $\omega - \omega_{0i} >> \Gamma/2\hbar$, the amplitudes for the two inverted orientations of the internal magnetic field are the phase conjugates of each other: $\ell_i' = \ell_i^*$. This is so because the amplitudes a_i are real. This calculation has neglected nuclear level mixing, however, if it were included the amplitudes would still be the complex conjugates of each other even though the amplitudes a_i are now complex (this is because the Euler γ angle undergoes the transformation $\gamma \rightarrow -\gamma$ upon an inversion of the quantum axis, and

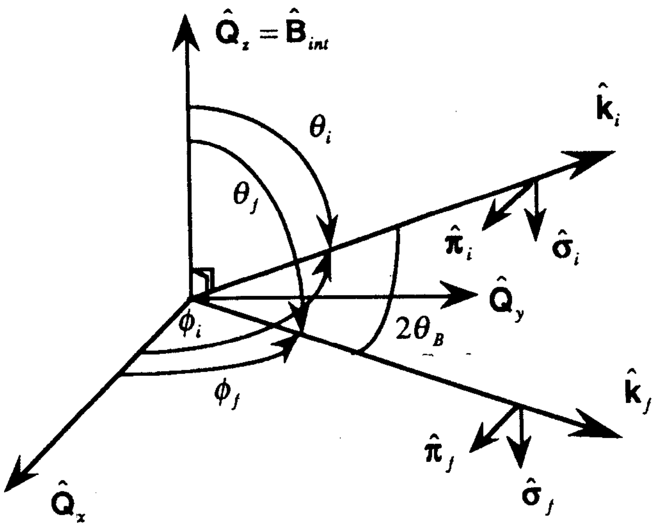

Fig. 5-5.2. Scattering geometry for inverted quantization axis. Wavectors $\mathbf{k}_i$ and $\mathbf{k}_f$ lie in the Q_xQ_y-plane.

by Eqs. 5-3.10 and 5-3.11 the amplitudes a_i change to their complex conjugates). Because of the resonant denominator, resonant systems cannot experience true phase conjugate scattering.

In frequency space this phase effect is not easily observed for spectra having resonance lines separated by many natural linewidths--one would have to carefully examine the interference between widely spaced lines that have little overlap. However, in the time domain the effect stands out more because the phase of the beat patterns due to the interference of two oscillators with different frequencies can be more easily measured.

This can be seen by examining the beating between the two dominant resonance lines ℓ_1 and ℓ_6. The Fourier transform of their frequency amplitudes gives the familiar damped sinusoidal expressions

$$\ell_1(t) = -ia_1 e^{-i\Gamma t/2\hbar} e^{-i(\omega_{01}t+2\theta_B)} \tag{5-5.11}$$

$$\ell_6(t) = -ia_1 e^{-i\Gamma t/2\hbar} e^{-i(\omega_{06}t-2\theta_B)}. \tag{5-5.12}$$

For just these two lines, the kinematic intensity from crystal is then proportional to

$$\begin{aligned} I(t) &\sim \left[\ell_1(t)+\ell_6(t)\right]\left[\ell_1^*(t)+\ell_6^*(t)\right] \\ &= 2a_1^2 e^{-\Gamma t/\hbar}\left\{1+\cos\left[(\omega_{06}-\omega_{01})t-4\theta_B\right]\right\}. \end{aligned} \tag{5-5.13}$$

When the internal magnetic field is inverted, the phase of the intensity pattern changes sign so that

$$I'(t) \sim 2a_1^2 e^{-\Gamma t/\hbar}\left\{1+\cos\left[(\omega_{03}-\omega_{01})t+4\theta_B\right]\right\}. \tag{5-5.14}$$

Thus, adjusting the Bragg angle tunes the phase difference, $\Delta\varphi = 8\theta_B$, between the beat patterns of the two intensity distributions. For Bragg angles near 22.5° this is a very noticeable effect. For instance, if $2\theta_B = \pi/4$ then the intensity distributions are 180° out of phase and, therefore, the the peaks of one intensity pattern will lie in the valleys of the other. This is one of the kinematical effects investigated experimentally in this thesis, and the results are given in Chapter 10.

REFERENCES

[1] J. Mathews, *Tensor Spherical Harmonics* (California Institute of Technology,1981).

[2] A. R. Edmonds, *Angular Momentum in Quantum Mechanics* (Princeton University Press, Princeton, New Jersey, 1960).

[3] H. Frauenfelder, *The Mössbauer Effect* (W. A. Benjamin, New York, 1962).

[4] C. M. Lederer and V. S. Shirley, *Table of Isotopes* (Wiley, New York, 1978).

[5] D. T. Cromer and D. Liberman, *J. Chem. Phys.* **53**, 1891 (1970).

[6] R. W. James, *The Optical Principles of the Diffraction of X-Rays* (Ox Bow Press, Woodbridge, Connecticut, 1982).

[7] B. E. Warren, *X-Ray Diffraction* (Dover, New York, 1990).

[8] M. Weissbluth, *Atoms and Molecules* (Academic Press, New York, 1978).

[9] V. I. Goldanskii and R. H. Herber, *Chemical Applications of Mössbauer Spectroscopy* (Academic Press, New York, 1968).

[10] A. J. Freeman and R. B. Frankel, *Hyperfine Interactions* (Academic Press, New York, 1967).

[11] R. V. Pound, *Phys. Rev.* **79**, 685 (1950).

[12] E. Matthias, W. Schneider, and R. M. Steffen, *Phys. Rev.* **125**, 261 (1962).

[13] E. Matthias, W. Schneider, and R. M. Steffen, *Arkiv Fur Fysik* **24**, 97 (1963).

[14] H. D. Rüter, R. Rüffer, R. Hollatz, W. Sturhahn, and E. Gerdau, *Hyp.Int.* **58**, 2477 (1990).

[15] R. Hollatz, W. Sturhahn, H. D. Rüter, and E. Gerdau, *International Conference on the Applications of the Mössbauer Effect* (Budapest, Hungary, 1989), vol. 2, 14.11

[16] D. P. Siddons, J. B. Hastings, G. Faigel, L. E. Berman, P. E. Haustein, and J. R. Grover, *Phys. Rev. Lett.* **62**, 1384 (1989).

[17] D. E. Brown, J. Arthur, A. Q. R. Baron, G. S. Brown, and S. Shastri, *Phys. Rev. Lett.* **69**, 699 (1992).

6. DYNAMICAL SCATTERING BY RESONANT SYSTEMS

6.1 Kinematical Scattering Theory

In kinematical scattering a photon scattered from one particle does not interact with other particles-multiple scattering is nonexistent. The field amplitude at a point $\mathbf{x}$ is then just the sum of the individually scattered fields emanating from each scatterer within the medium. From the spherical multipole electric field equation, Eq. 4-4.16, this sum (over N identical particles) is

$$
\begin{aligned}
I(\mathbf{x}) &= I_0 \left| F\left(\mathbf{k}_f, \mathbf{k}_i\right) \right|^2 \left| \sum_{n=1}^{N} e^{-i\left(\mathbf{k}_f - \mathbf{k}_i\right)\cdot \mathbf{x}_n} \right|^2 \\
&= I_0 \left| F\left(\mathbf{k}_f, \mathbf{k}_i\right) \right|^2 \left(N + \sum_{n=1}^{N} \sum_{m=1}^{N} e^{-i\left(\mathbf{k}_f - \mathbf{k}_i\right)\cdot\left(\mathbf{x}_n - \mathbf{x}_m\right)} \right)
\end{aligned} \qquad (6.1\text{-}1)
$$

where $\mathbf{x}$ is far from any scatterer, I_0 is a constant proportional to the incoming beam intensity, and the incoming field term has been excluded so that only the properties of the scattered fields are examined. The scattering amplitude is given by Eq. 4-3.63 or 4-3.64 with $\mathbf{x}_0 = 0$.

For scattering into the forward direction, $\mathbf{k}_f = \mathbf{k}_i$, all spatial phases, $\phi_{\mathbf{x}} = -\left(\mathbf{k}_f - \mathbf{k}_i\right)\cdot \mathbf{x}$, are zero. This is a scattering channel direction--a scattering direction in which the scattered fields from all the particles in a medium have the same spatial phase. In the forward direction, the intensity is proportional to the square of the number of scatterers. To find the scattered intensity in other directions, the second term in Eq. 6-1.1 must be evaluated. As $N \to \infty$ this term, for an isotropic medium, can be approximated as a sum over a random distribution of spatial phases which averages to zero--in such a case, the nonforward scattered field intensity is formed from an incoherent sum of the scattered fields from each scatterer. Then, the nonforward scattered intensity is proportional to the number of scatterers, and the net intensity for elastic scattering is

$$
I^{elas}(\mathbf{x}) = I_0 N \left| F\left(\mathbf{k}_f \neq \mathbf{k}_i\right) \right|^2 + I_0 N^2 \left| F\left(\mathbf{k}_f = \mathbf{k}_i\right) \right|^2 . \qquad (6\text{-}1.2)
$$

For off-energy-shell inelastic scattering where $k_f \neq k_i$, a random temporal phase, ϕ_n^{fi}, must be added to the field as discussed in Section 3.5. Because of this factor, irrespective of the scattering direction, the scattered intensity is formed from an incoherent sum over all the scattered fields from each scatterer

$$I^{inel}(\mathbf{x}) = I_0\left|F_{inel}(\mathbf{k}_f,\mathbf{k}_i)\right|^2\left|\sum_{n=1}^{N} e^{i(\mathbf{k}_f-\mathbf{k}_i)\cdot\mathbf{x}_n} e^{i\phi_n^{fi}}\right|^2 = I_0 N\left|F_{inel}(\mathbf{k}_f,\mathbf{k}_i)\right|^2 \qquad (6\text{-}1.3)$$

where $F_{inel}(\mathbf{k}_f,\mathbf{k}_i)$ is an inelastic scattering amplitude.

For an anisotropic medium, such as a crystal, there can be many scattering channel directions (such as those resulting from Bragg diffraction in a crystal) in addition to the forward direction. Normally, a structure factor for a unit cell is constructed to calculate the total field scattered from a crystal.

The structure factor is the sum of the scattering amplitudes from all of the particles in the unit cell. For electronic scattering (operating far from any any bound state resonances or absorption edges) or for nuclear scattering the structure factor of a unit cell with scatterers of type α located at $\mathbf{r}_{n_\alpha}$ is

$$F_H = -r_e\left(\hat{\varepsilon}_f^*\cdot\hat{\varepsilon}_i\right)\sum_{\alpha n_\alpha}\left(e^{-2W_\alpha} f_{0\alpha} + f'_\alpha - i f''_\alpha\right)e^{-i\mathbf{H}\cdot\mathbf{r}_{n_\alpha}} \qquad \text{(electronic scattering)} \quad (6\text{-}1.4)$$

$$F_H = \sum_{\alpha n_\alpha} F_\alpha(\mathbf{k}_f,\mathbf{k}_i)e^{-i\mathbf{H}\cdot\mathbf{r}_{n_\alpha}} \qquad \text{(nuclear scattering)} \quad (6\text{-}1.5)$$

where $\mathbf{H} = \mathbf{k}_f - \mathbf{k}_i$, (6-1.6)

and the scattering amplitudes are given by Eq. 5-1.55 (electronic scattering) and Eqs 4-3.62 or 4-3.63 (nuclear scattering). If the origin is placed at the corner, $\mathbf{x}_0$, of one of the unit cells in the crystal, then any other unit cell can be found through an integral number of lattice displacements

$$\mathbf{x}' = \mathbf{x}_0 + n_1\mathbf{a}_1 + n_2\mathbf{a}_2 + n_3\mathbf{a}_3. \qquad (6\text{-}1.7)$$

After calculating the structure factor for one unit cell, then, for one scattering channel, the total scattering amplitude from the whole crystal is constructed by summing the scattering amplitude from each cell multiplied by a phase factor, $e^{-i\mathbf{H}\cdot(n_i\mathbf{a}_i)}$ ($n_i = 0,1,2,\ldots,N_i-1$ and $i = 1,2,3$), each cell acquires. The resulting scattered intensity is given by[1, 2]

$$I(\mathbf{x}) = I_0\left|F_{tot}(\mathbf{x})\right|^2 = I_0\left|F_H\right|^2\prod_{i=1}^{3}\frac{\sin^2(N_i\mathbf{H}\cdot\mathbf{a}_i/2)}{\sin^2(\mathbf{H}\cdot\mathbf{a}_i/2)}. \qquad (6\text{-}1.8)$$

The reflectivity is maximized at the Bragg peaks according to the Laue equation

$$\mathbf{H}\cdot\mathbf{a}_i = 2\pi H_i \qquad (6\text{-}1.9)$$

where H_i are integers and $\mathbf{H}$ is a reciprocal lattice vector

$$\mathbf{H} = h\mathbf{b}_1 + k\mathbf{b}_2 + \ell\mathbf{b}_3. \qquad (6\text{-}1.10)$$

When the Bragg condition is satisfied, the scattered fields travel mainly in scattering channel directions, $\hat{\mathbf{H}}$, and have narrow angular spreads. At the Bragg peaks, the intensity is again proportional to the square of the number of scatterers

$$I(\mathbf{x}) = I_0 N^2 |F_H|^2 \tag{6-1.11}$$

where $N = N_1 N_2 N_3$ is the total number of unit cells within the crystal. The angular width of an outgoing beam is inversely proportional to the number of scatters. Since most materials studied are macroscopic in size (as discussed in Section 3.1)--their dimensions are much greater than 100 Å and $N >> 10^6$--the angular widths are essentially delta functions at the scattering angle $2\theta_B$. Examination of Eq. 6-1.8 shows that the average intensity off the Bragg peaks is half the scattered intensity from a single unit cell--this extremely small factor can be safely ignored.

In the kinematic domain, crystalline and isotropic media give reflectivities proportional to the square of the number of scatterers when examining fields traveling in scattering channel directions. However, when examining fields not traveling in scattering channel directions, isotropic media give intensities proportional to the number of scatterers, while crystalline material give intensities that are essentially zero. Inelastic scattering in crystalline media is identical to that in isotropic media because of the effect of the random temporal phase factors of the scattering amplitude.

6.2 Dynamical Scattering Theory

Dynamical scattering includes the multiple scattering effects that are ignored in kinematical scattering theory. For linear time-invariant causal systems, multiple scattering can be handled by linear system theory. In such a theory, if the impulse response of a system is known (that is, the response of a system to a delta function in time), then the response of the system to any arbitrary analytic function is known (this is proved by imposing linearity, or using superposition arguments).[3] The frequency response of a scatterer to an incoming plane wave is described by the spherical multipole electric field in Eq. 4-4.16

$$H_\alpha\left(\omega, \mathbf{x}_{n_\alpha}, \mathbf{x}\right) = \frac{e^{ikr_{n_\alpha}}}{r_{n_\alpha}} F_\alpha\left(\mathbf{k}_f, \mathbf{k}_i\right) \tag{6-2.1}$$

where $\mathbf{x}_{n_\alpha}$ is the position of scatterer of type α, and $r_{n_\alpha} = |\mathbf{x} - \mathbf{x}_{n_\alpha}|$ is the distance from the scatterer to an observation point.

In multiple scattering, the spherical wave generated by a scatterer can interact with all other scatterers which in turn produce spherical waves that can interact with the original scatterer and all other scatterers. This multiple scattering behavior can be investigated by examining each step in the scattering process. For instance, for an incoming wave (the zeroth order scattered wave)

$$\mathbf{a}_0(\omega,\mathbf{x}) = \mathbf{E}_0(\omega,\mathbf{x}), \tag{6-2.2}$$

the response of the system (first order, or single scattering), is

$$\mathbf{a}_1(\omega,\mathbf{x}) = \sum_{\alpha=1}^{N_t} \sum_{n_\alpha=1}^{N_\alpha} \mathbf{a}_0(\omega,\mathbf{x}_{n_\alpha}) H(\omega,\mathbf{x}_{n_\alpha},\mathbf{x}) \tag{6-2.3}$$

where N_α is the number of scatterers of type α, and N_t is the number of different types of scatterers. Note that Eq. 6-2.3 represents a symmetric state of excited scatterers since interchanging the indices of identical scatters, $\mathbf{x}_{i_\alpha} \leftrightarrow \mathbf{x}_{j_\alpha}$, does not change the final sum. Double scattering (second order scattering) occurs when the single scattered wave interacts with all the particles

$$\mathbf{a}_2(\omega,\mathbf{x}) = \sum_{\alpha=1}^{N_t} \sum_{n_\alpha=1}^{N_\alpha} \mathbf{a}_1(\omega,\mathbf{x}_{n_\alpha}) H(\omega,\mathbf{x}_{n_\alpha},\mathbf{x}). \tag{6-2.4}$$

By iteration, one can determine the amplitudes for triple and all higher order scattered fields

$$\mathbf{a}_m(\omega,\mathbf{x}) = \sum_{\alpha=1}^{N_t} \sum_{n_\alpha=1}^{N_\alpha} \mathbf{a}_{m-1}(\omega,\mathbf{x}_{n_\alpha}) H(\omega,\mathbf{x}_{n_\alpha},\mathbf{x}) \qquad (m \geq 1). \tag{6-2.5}$$

For some problems, working in the time picture rather than in frequency space may be more convenient or illustrative. In the time picture multiple scattering involves the convolution of the frequency response with the incoming wave

$$\mathbf{a}_m(t,\mathbf{x}) = \sum_{\alpha=1}^{N_t} \sum_{n_\alpha=1}^{N_\alpha} \int_0^t \mathbf{a}_{m-1}(t',\mathbf{x}_{n_\alpha}) H(t-t',\mathbf{x}_{n_\alpha},\mathbf{x})\, dt' \qquad (m \geq 1) \tag{6-2.6}$$

where the limits of the convolution integral were constrained by assuming the functions are causal:

$$\mathbf{a}_m(t',\mathbf{x}) = 0 \qquad \text{for} \quad t' < 0 \tag{6-2.7}$$

$$H(t-t',\mathbf{x}_{n_\alpha},\mathbf{x}) = 0 \qquad \text{for} \quad t-t' < 0 \quad \text{or} \quad t' > t. \tag{6-2.8}$$

Working in the time domain, the multiple scattering formalism can be shown to be equivalent to a Feynman path integral approach where a sum is made over all the possible scattering paths of a collection of scatterers.[4]

The total scattered wavefield emanating from the medium is the sum of all the multiply scattered fields

$$\mathbf{E}_s(\omega,\mathbf{x}) = \sum_{m=0}^{\infty} \mathbf{a}_m(\omega,\mathbf{x}). \tag{6-2.9}$$

Note that Eq. 6-2.9 is still a quantum mechanical expression (the multipole scattering amplitude was obtained by finding matrix elements of quantum mechanical operators). No connection with classical electrodynamics has been made yet. The connection comes when the number of scatterers becomes so large ($N >> 10^6$) that computing Eq. 6-2.9 becomes too time consuming. In certain cases, however, such as for an isotropic medium, one can show that summing up an infinite number of scattering diagrams leads to the Maxwell equations for a medium (this is done in Section 6.5).

6.3 Two Coupled Oscillators

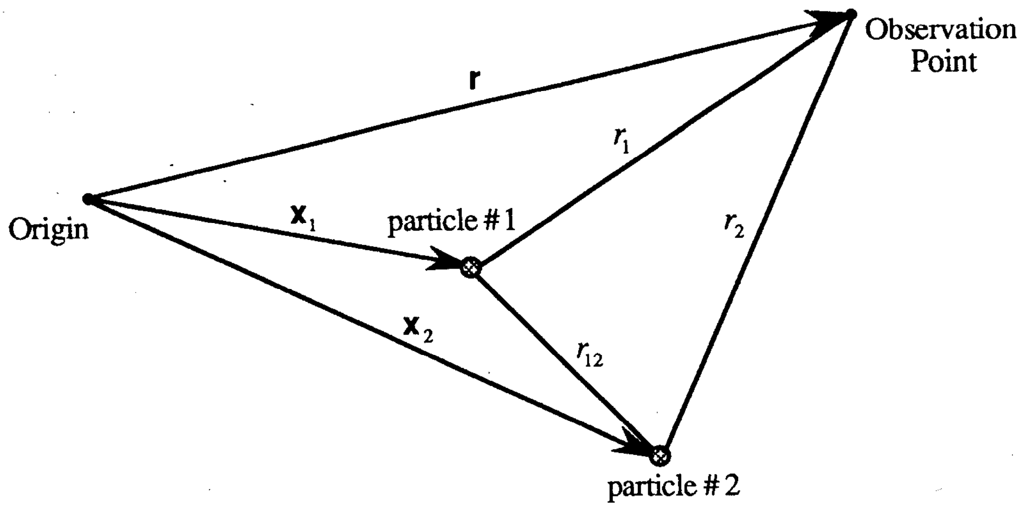

Fig. 6-3.1. Scattering geometry for two coupled oscillators.

For a simple example of multiple scattering scattering, consider the case of two identical particles situated a distance $r_{12} = |\mathbf{x}_1 - \mathbf{x}_2|$ apart as shown in Fig. 6-3.1. Assume, for further simplicity, that at some time $t = 0$ both particles are in the excited state and decay with a probability amplitude $F_0(t)$. This allows the zeroth order scattering term, $a_0(t)$, to be ignored along with all the spatial phase factors associated with it.

Then, for the frequency response given by Eq. 6-2.1, all of the higher order scattering terms can be computed through the use of the multiple scattering equation, Eq. 6-2.5. (Below, $r_1 = |\mathbf{r} - \mathbf{x}_1|$, $r_2 = |\mathbf{r} - \mathbf{x}_2|$, and the polarization matrix describing scattering from particle #1 to $\mathbf{r}$ has been assumed to be equal to the polarization matrix describing scattering from particle #2 to $\mathbf{r}$)

$$a_1(\omega,\mathbf{r}) = F_0(\omega)\frac{e^{ikr_1}}{r_1} + F_0(\omega)\frac{e^{ikr_2}}{r_2}$$

$$a_2(\omega,\mathbf{r}) = \left(F_0(\omega)\frac{e^{ikr_{12}}}{r_{12}}\right)\frac{e^{ikr_1}}{r_1}F(\mathbf{k}_f,\mathbf{k}_i) + \left(F_0(\omega)\frac{e^{ikr_{12}}}{r_{12}}\right)\frac{e^{ikr_2}}{r_2}F(\mathbf{k}_f,\mathbf{k}_i)$$

$$= F_0(\omega)\left[\frac{e^{ikr_{12}}}{r_{12}}F(\mathbf{k}_f,\mathbf{k}_i)\right]\left(\frac{e^{ikr_1}}{r_1} + \frac{e^{ikr_2}}{r_2}\right)$$

$$a_3(\omega,\mathbf{r}) = F_0(\omega)\left[\frac{e^{ikr_{12}}}{r_{12}}F(\mathbf{k}_f,\mathbf{k}_i)\right]^2\left(\frac{e^{ikr_1}}{r_1} + \frac{e^{ikr_2}}{r_2}\right)$$

$$a_m(\omega,\mathbf{r}) = F_0(\omega)\left[\frac{e^{ikr_{12}}}{r_{12}}F(\mathbf{k}_f,\mathbf{k}_i)\right]^{m-1}\left(\frac{e^{ikr_1}}{r_1} + \frac{e^{ikr_2}}{r_2}\right). \qquad (6\text{-}3.1)$$

The total scattered electric field is then

$$E_s(\omega,\mathbf{r}) = F_0(\omega)\left(\frac{e^{ikr_1}}{r_1} + \frac{e^{ikr_2}}{r_2}\right)\sum_{m=0}^{\infty}\left[\frac{e^{ikr_{12}}}{r_{12}}F(\mathbf{k}_f,\mathbf{k}_i)\right]^m$$

$$= \frac{F_0(\omega)\left(\frac{e^{ikr_1}}{r_1} + \frac{e^{ikr_2}}{r_2}\right)}{1 - \frac{e^{ikr_{12}}}{r_{12}}F(\mathbf{k}_f,\mathbf{k}_i)}. \qquad (6\text{-}3.2)$$

Evaluating this expression for dipole scattering using the spin averaged scattering amplitude, Eq. 5-1.48, gives interesting results. Eq. 6-3.2 is then valid for sigma polarized electric dipole fields or pi polarized magnetic dipole fields. Assuming $F_0(\omega)$ has the same resonance characteristics as the scattering amplitude

$$F_0(\omega) = F_0/(\omega - \omega_0 + i\Gamma/2\hbar), \qquad (6\text{-}3.3)$$

and for $r >> |\mathbf{x}_1|,|\mathbf{x}_2|$ Eq. 6-3.2 reduces to

$$E_s(\omega,r) = \frac{2F_0\left(e^{ikr}/r\right)e^{i\mathbf{k}\cdot(\mathbf{x}_1+\mathbf{x}_2)/2}\cos\left[\mathbf{k}\cdot(\mathbf{x}_1-\mathbf{x}_2)/2\right]}{\omega-(\omega_0-\omega_s)+i(\Gamma+\Gamma_s)/2\hbar} \tag{6-3.4}$$

where $\mathbf{k} = k(\mathbf{r}/r)$, and ω_s and Γ_s are a coupled oscillator frequency shift and decay rate speedup factor

$$\omega_s = \frac{1}{4}\left(\frac{2j_n+1}{2j_i+1}\right)\left(\frac{\Gamma_{rad}}{\hbar}\right)\frac{\cos(kr_{12})}{kr_{12}} \tag{6-3.5}$$

$$\Gamma_s = \frac{1}{2}\left(\frac{2j_n+1}{2j_i+1}\right)\Gamma_{rad}\frac{\sin(kr_{12})}{kr_{12}}. \tag{6-3.6}$$

This result shows that a pair of coupled oscillators will radiate fields with a natural frequency and natural linewidth that is different from an isolated oscillator. This is not surprising since, as shown in Section 3.7, a single oscillator interacting with its own electromagnetic field results in a frequency shift and a natural linewidth. In this problem there are two oscillators interacting with the electromagnetic fields generated by both oscillators.

For two ^{57}Fe nuclei, the coupled frequency shift and speedup rate are $(j_n = 3/2, j_i = 1/2)$

$$\omega_s = \frac{1}{2}\left(\frac{\Gamma_{rad}}{\hbar}\right)\frac{\cos(kr_{12})}{kr_{12}} \tag{6-3.7}$$

$$\Gamma_s = \Gamma_{rad}\frac{\sin(kr_{12})}{kr_{12}}. \tag{6-3.8}$$

As $kr_{12} \to 0$, the speedup rate goes to

$$\Gamma_s \to \Gamma_{rad}. \tag{6-3.9}$$

Since $\Gamma = \Gamma_{ic} + \Gamma_{rad}$, where Γ_{ic} is the decay rate due to internal conversion, then, when the separation between the oscillators is small compared to a wavelength, the radiative decay rate doubles. This confirms Dicke's supperadiant result that a symmetric state of two coupled oscillators has a radiative decay rate that is double that of a single oscillator.[5] However, as $kr_{12} \to 0$ the frequency shift becomes infinite. This is understandable because the electric field amplitude varies as $1/kr_{12}$. The particles are then bathed in a very high intensity electric field which will induce extremely large energy level shifts.

The frequency shift and speedup rate are also affected by the spatial separation of the particles--by increasing or decreasing the separation produces negative or positive frequency shifts and results in an increase or decrease of the the natural frequency. There is also an effect due to the angular momentum states of the particle. For very high angular momentum states and as $kr_{12} \rightarrow 0$, the speedup rate approaches $\Gamma_s \rightarrow 3\Gamma_{rad}/2$.

If the two particles are excited by an plane wave, the problem becomes slightly more complicated because the spatial phase of the plane wave must be taken into account. Performing computations similar to before, except now with an incoming plane wave

$$a_0(\omega,\mathbf{r}) = E_0 e^{i\mathbf{k}_i\cdot\mathbf{r}} \tag{6-3.10}$$

yields

$$E_s(\omega,\mathbf{r}) = E_0 e^{i\mathbf{k}_i\cdot\mathbf{r}} - E_0 \frac{1}{4}\left(\frac{2j_n+1}{2j_i+1}\right)\left(\frac{\Gamma_{rad}}{\hbar}\right)\frac{e^{ikr}}{kr} e^{-i\mathbf{H}\cdot(\mathbf{x}_1+\mathbf{x}_2)/2}$$

$$\times\left\{\cos[\mathbf{H}\cdot\mathbf{x}_{12}/2]\left(\frac{1}{R^+(\omega)}+\frac{1}{R^-(\omega)}\right)+\cos[(\mathbf{k}_f+\mathbf{k}_i)\cdot\mathbf{x}_{12}/2]\left(\frac{1}{R^+(\omega)}-\frac{1}{R^-(\omega)}\right)\right\} \tag{6-3.11}$$

where

$$R^+(\omega) = \omega - (\omega_0 - \omega_s) + i(\Gamma + \Gamma_s)/2\hbar \tag{6-3.12}$$

$$R^-(\omega) = \omega - (\omega_0 + \omega_s) + i(\Gamma - \Gamma_s)/2\hbar, \tag{6-3.13}$$

and $\mathbf{k}_f = k(\mathbf{r}/r)$, $\mathbf{H} = \mathbf{k}_f - \mathbf{k}_i$, $\mathbf{x}_{12} = \mathbf{x}_1 - \mathbf{x}_2$, and ω_s and $\Gamma_s$are given by Eqs. 6-3.5 and 6-3.6 . For this arrangement there are two normal modes that can exist. There is one mode in which there are negative frequency shifts and decay rate speedups, and another with just the reverse--positive frequency shifts and decay rate slowdowns.

6.4 Scattering Channel Fields

Multiple scattering computations can be simplified if scattering is examined only along the highly directional scattering channels where most of the radiation exits a medium (such as in the forward or Bragg directions for an isotropic medium or a crystal). For example, consider the case of a one dimensional line of scatterers, as shown in Fig. 6-4.1, where there is an incident plane wave traveling parallel to the line of scatters. The forward direction is a scattering channel direction since the spatial phase of a scattered wave from a particle located at z_η, $\phi_z = \mathbf{H}\cdot\mathbf{z}_\eta$, is always zero. The single scattered field observed at a distance far from any scatterer, $r >> z_\eta$, is then

$$a_1(\omega,r) = \sum_\eta \left(E_0 e^{i\mathbf{k}_i\cdot\mathbf{z}_\eta}\right)\left[\frac{e^{ikr_\eta}}{r_\eta}F\left(\mathbf{k}_f = \mathbf{k}_i\right)\right] \approx \sum_\eta \left(E_0 e^{i\mathbf{k}_i\cdot\mathbf{z}_\eta}\right)\left[\frac{e^{ikr}e^{-i\mathbf{k}_f\cdot\mathbf{z}_\eta}}{r}F\left(\mathbf{k}_f = \mathbf{k}_i\right)\right]$$

$$= \sum_\eta \left[E_0 \frac{e^{ikr}}{r}F\left(\mathbf{k}_f = \mathbf{k}_i\right)\right] = N_\eta E_0 \frac{e^{ikr}}{r}F\left(\mathbf{k}_f = \mathbf{k}_i\right) \tag{6-4.1}$$

where $r_\eta = r - z_\eta$, and N_η is the number of scatterers. All the single scattered fields have the same overall spatial phase factor, and therefore the net scattered field is a coherent sum of all of the single scattered fields.

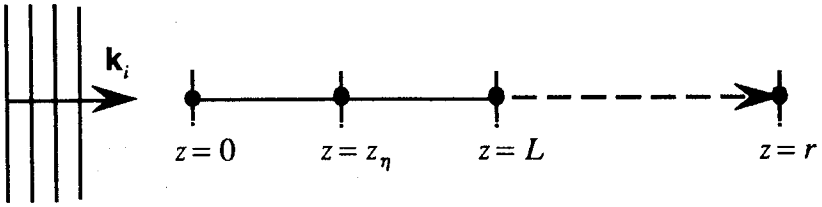

Fig. 6-4.1. Plane wave field incident upon a line of scatterers of length L.

For the double scattered fields,

$$a_2(\omega,r) = \sum_\eta \sum_{\eta'} \left[\frac{e^{ikr_{\eta\eta'}}}{r_{\eta\eta'}} e^{i\mathbf{k}_i\cdot\mathbf{z}_{\eta'}} F\left(\mathbf{k}_f = \mathbf{k}_i\right)\right]\left[\frac{e^{ikr_\eta}}{r_\eta}F\left(\mathbf{k}_f = \mathbf{k}_i\right)\right] \tag{6-4.2}$$

where $r_{\eta\eta'} = \left|z_\eta - z_{\eta'}\right|$. Since double scattering has been constrained to occur only in the forward direction (backscattering is ignored), $z_\eta > z_{\eta'}$ and thus $r_{\eta\eta'} = z_\eta - z_{\eta'}$. Then all of the doubled scattered fields also have the same overall spatial phase factor

$$a_2(\omega,r) = E_0 \frac{e^{ikr}}{r} \sum_{\eta\eta'} \frac{\left[F\left(\mathbf{k}_f = \mathbf{k}_i\right)\right]^2}{z_\eta - z_{\eta'}}. \tag{6-4.3}$$

By iteration, the total forward scattered electric field at the observation point is

$$E_s(\omega,r) = E_0 e^{ikr} + E_0 \frac{e^{ikr}}{r} F\left(\mathbf{k}_f = \mathbf{k}_i\right) \sum_\eta \left\{1 + \sum_{\eta'} \frac{F\left(\mathbf{k}_f = \mathbf{k}_i\right)}{z_\eta - z_{\eta'}} + \sum_{\eta'\eta''} \frac{\left[F\left(\mathbf{k}_f = \mathbf{k}_i\right)\right]^2}{\left(z_{\eta'} - z_{\eta''}\right)\left(z_\eta - z_{\eta'}\right)} + \cdots\right\}. \tag{6-4.4}$$

This infinite series expression is equivalent to the sum of an infinite number of scattering diagrams where the vector potential of each photon, except the incoming photon, is defined as a spherical wave (see Fig. 6-4.2). All photons travel in the same direction, and each photon can either exit the medium or scatter with a downstream particle. As seen before for a single particle, the sum over an infinite number of scattering diagrams can lead to frequency shifts and to changes in the natural radiative decay rate.

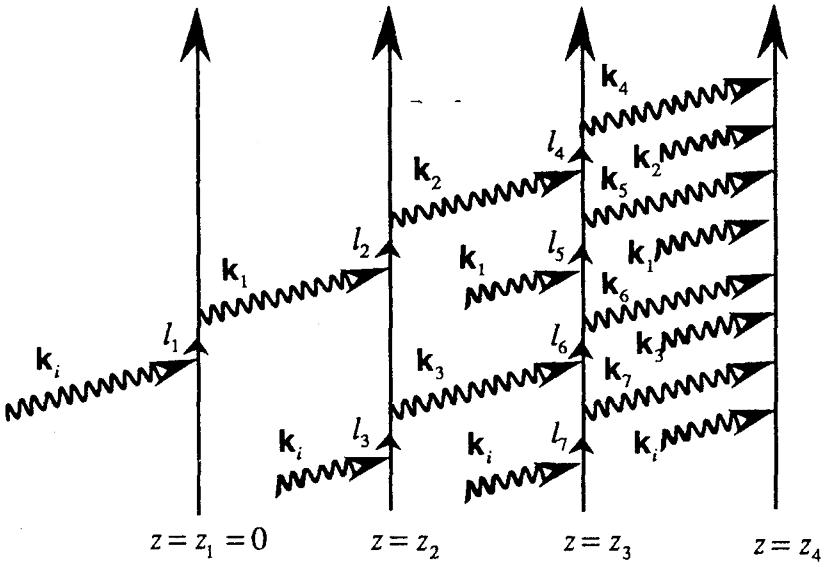

Fig. 6-4.2. Scattering diagram for multiple scattering along a scattering channel direction. All wavectors have the same magnitude and are in the same direction. The first four particles are shown with time represented by the vertical axis and intermediate states by l_j. (For convenience, the photon arrival time at each scatterer is not correctly drawn. Actually, photon $\mathbf{k}_i$ strikes all scatterers at the same time, photon $\mathbf{k}_1$ strikes all scatterers located at $z \geq z_2$ at the same time, etc.)

When there are many scatterers with an interparticle separation comparable to or less than the wavelength of the incoming field, the discrete line of particles can be approximated as a continuous linear distribution of particles. Eq. 6-4.4 can then be rewritten as

$$E_s(\omega,r) = E_0 e^{ikr} + E_0 \frac{e^{ikr}}{r} nF_\omega L \int_0^1 ds \left\{ 1 + nF_\omega \int_0^{1-\delta} \frac{1}{1-s'} + \left[nF_\omega\right]^2 \int_0^{1-\delta} \frac{ds'}{1-s'} \int_0^{1-\delta'} \frac{ds''}{1-s''} + \cdots \right\} \tag{6-4.5}$$

where $s = z/L$, $s' = z'/z$, $s'' = z''/z'$, etc., n is the number of particles per unit length, and $F_\omega = F(\mathbf{k}_f = \mathbf{k}_i)$. The small parameters in the upper limits, $\delta = d/z, \delta' = d/z', \delta'' = d/z''$, etc., are included to prevent the integrals from diverging. The quantity d is the average interparticle separation. The integral series can be evaluated to first order by making the approximation $\delta \approx d/L$. For such a case

$$E_s(\omega,r)=E_0e^{ikr}+\frac{E_0\dfrac{e^{ikr}}{r}nF\left(\mathbf{k}_f=\mathbf{k}_i\right)L}{1+nF\left(\mathbf{k}_f=\mathbf{k}_i\right)\ln\delta}. \tag{6-4.6}$$

Inserting the dipole scattering amplitude, Eq. 5-1.48, into the expression above gives

$$E_s(\omega,r)=E_0e^{ikr}-E_0\frac{e^{ikr}}{r}\frac{nL}{4\mathbf{k}_f}\left(\frac{2j_n+1}{2j_i+1}\right)\left(\frac{\Gamma_{rad}}{\hbar}\right)\frac{1}{\omega-\left(\omega_0+\omega_s\right)+i\Gamma/2\hbar} \tag{6-4.7}$$

where $$\omega_s=\frac{n}{4\mathbf{k}_f}\left(\frac{2j_n+1}{2j_i+1}\right)\left(\frac{\Gamma_{rad}}{\hbar}\right)\ln\delta. \tag{6-4.8}$$

This shows that, for forward scattering from a line of particles, there is no change in the natural linewidth, but there is a shift from the natural frequency of an isolated particle. The frequency shift diverges logarithmically with decreasing interparticle separation rather than linearly as was the case for the two particle system, but the reason for the divergence is the same--the electric field strength of spherical waves is very intense at small distances from the scatterer.

So far only scattering purely in the forward direction has been mentioned. Another way a wave can scatter and end up in the forward direction is to scatter in the backward direction and then scatter again into the forward direction. In doing so, the scattered wave can pick up a nonzero phase factor. For instance, for double scattering where the wave backscatters and then scatters into the forward direction, the field amplitude is that of Eq. 6-4.3 multiplied by the spatial phase factor: $-e^{i2k\left(z_\eta-z_{\eta'}\right)}$. For n^{th} order scattering there are $n!-1$ ways a field can scatter away and then back into the scattering channel direction--all of the amplitudes and associated phase factors for each order must then be evaluated. For an ordered line of scatterers (such as a linear lattice), all types of multiple scattering must be computed to determine the total scattered field--an extremely tedious task since all orders of scattering must be computed, and each order has $n!$ terms. However, if the line of scatterers is randomly ordered (such as an isotropic distribution of a large number of scatterers), the phase factors of fields scattered back into the scattering channel direction will be essentially random. In such a situation, these fields can be neglected because their contribution to the total scattered intensity will be down by a factor of $1/N$ compared to the intensity of the scattering channel fields (fields scattered purely in the scattering channel direction).

A plane or volume of a large number of ordered scatterers (such as a planar lattice or a crystal lattice) has more degrees of freedom than a line of scatterers. Because of the extra degrees of freedom, the intensity of scattering channel fields is a factor of N times greater than of multiply scattered fields scattered in directions other that the scattering channel direction--the nonscattering channel fields fields pick up additional phase factors that are essentially random for a many particle medium. Therefore, mainly the scattering channel fields will be investigated, and all other types of scattered fields will be neglected.

6.5 Plane Parallel Slab of Scatterers

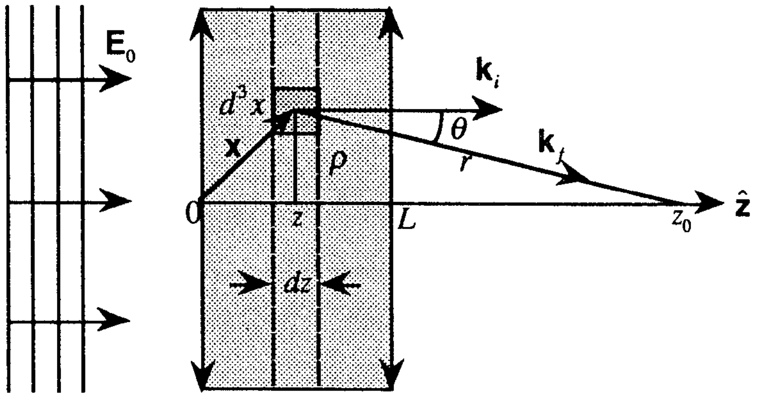

Fig. 6-5.1. Plane wave field incident upon a plane parallel slab of thickness L.[6]

The sum over the infinite number of scattering diagrams in Fig. 6-4.2 should, in the continuous limit, lead to a description of a scattered electric field that converges to the expression obtained by solving the Maxwell equations for a medium. This will be shown to be true for a plane parallel slab where boundary conditions are neglected.

In the continuous limit, the multiple scattering equations, Eq. 6-2.5, can be written in the form (for identical particles and for scattering channel fields)

$$a_1(\omega,z,z_0)dz = a_0(\omega,z,z_0)H(\omega,z,z_0)dz \qquad (6\text{-}5.1)$$

$$a_m(\omega,z,z_0)dz = \left[\int_0^z dz' a_{m-1}(\omega,z',z)\right]H(\omega,z,z_0)dz \qquad (6\text{-}5.2)$$

where z_0 is the observation point. This gives the m^{th} order field amplitude for a slice within the slab at position z of thickness dz by summing up all of the lower order field amplitudes of all preceding slices and multiplying by the frequency response at point z. The net scattering channel field at the position z in the medium is then

$$E_{scf}(\omega,z,z_0) = a_0(\omega,z,z_0) + \sum_{m=1}^{\infty}\int_0^z dz'\, a_m(\omega,z',z_0)\,. \tag{6-5.3}$$

For forward scattering within a line of scatterers, the frequency response observed at point z for a segment of thickness dz' located at point z' is

$$H(\omega,z',z)dz' = F(\mathbf{k}_f = \mathbf{k}_i)\frac{(n_l\, dz')}{z-z'} \tag{6-5.4}$$

where n_l is the number of particles per unit length. The frequency response for a slice of thickness dz' within a plane parallel slab is simpler. Consider a slab of thickness L and infinite in the dimensions transverse to the beam propagation direction as shown in Fig. 6-5.1. Jackson has shown that the sum of single scattered fields from a slice of thickness dz within the slab yields a net field with an amplitude that is independent of the distance from the slice[6]

$$dE_{slice} = \frac{2\pi i}{k}F(\mathbf{k}_f = \mathbf{k}_i)E_0 e^{ikz_0}(n\,dz) \tag{6-5.5}$$

where n is the number of scatterers per unit volume, and the incident field was a plane wave. The frequency response for a slice is then

$$H(\omega,z',z)\,dz' = \frac{2\pi i}{k}nF(\mathbf{k}_f = \mathbf{k}_i)dz'. \tag{6-5.6}$$

For forward scattering, the plane wave incident field can be written as

$$a_0(\omega,z,z_0) = a_0(\omega,z_0) = E_0(\omega)e^{ikz_0} \tag{6-5.7}$$

where the amplitude $E_0(\omega)$ is independent of z and z_0. The spatial phase factor e^{ikz} is ignored because, recalling from the previous section, for forward scattering the spatial phase of a scattered wave is zero. However, an overall phase factor e^{ikz_0} must be attached to the net scattering channel field to include the phase the field picks up in traveling from the slab to the observation point z_0. For such an incident plane wave field, using the multiple scattering equations for a medium, Eq. 6-5.2, the scattering channel field within the medium is

$$\begin{aligned} E_{scf}(\omega,z,z) &= a_0(\omega,z)\left\{1 + [i\varepsilon_0(\omega)k]\int_0^z \sum_{m=0}^{\infty}\frac{[i\varepsilon_0(\omega)kz]^m}{m!}dz\right\} \\ &= a_0(\omega,z)e^{i\varepsilon_0(\omega)kz} \end{aligned} \tag{6-5.8}$$

where $$\varepsilon_0(\omega) = \frac{2\pi}{k^2}nF(\mathbf{k}_f = \mathbf{k}_i). \tag{6-5.9}$$

This is precisely the solution to the Maxwell equations when neglecting boundary conditions (and it also agrees with the semiclassical results of Section 3.4). For instance, for a plane parallel slab of thickness L, the solution to the inhomogeneous wave equation for transverse electric fields, Eqs. 3-2.9 and 3-2.10, is

$$E_{Max}(\omega, L, z_0) = E_0(\omega) e^{in(\omega)kL} e^{ik(z_0 - L)} = E_{scf}(\omega, L, z_0) \qquad (6\text{-}5.10)$$

where the quantity $n(\omega) = 1 + \varepsilon_0(\omega)$ is the index of refraction of the medium, and the last phase factor, $e^{ik(z_0 - L)}$, takes care of propagation through free space to the point z_0. Since, in the many particle limit, the multiple scattering equations for scattering channel fields give the same answer as the inhomogeneous wave equation, for more complicated problems, such as including boundary conditions or examining dynamical diffraction in crystals, the inhomogeneous wave equation will be used for constructing the scattering channel fields. No attempt will be made to examine the multiple scattered fields not traveling in scattering channel directions--full dynamical scattering theory will not be investigated any further than the discussion in this chapter.

The frequency shifts and speedup rates are no longer clearly observable in Eq. 6-5.8. In some cases, calculating the scattered fields in the time domain allows these effects to be seen more clearly. One can then either take the Fourier transform of Eq. 6-5.8, or, equivalently, express the multiple scattering equations for scattering channel fields in the time domain

$$a_1(t, z, z_0)\,dz = \int_0^t a_0(t', z, z_0) H(t - t', z, z_0)\,dt'\,dz \qquad (6\text{-}5.11)$$

$$a_m(t, z, z_0)\,dz = \int_0^t \left[\int_0^z dz'\, a_{m-1}(t', z', z) \right] H(t - t', z, z_0)\,dt'\,dz \qquad (6\text{-}5.12)$$

and

$$E_{scf}(t, z, z_0) = a_0(t, z, z_0) + \sum_{m=1}^{\infty} \int_0^z dz'\, a_m(t, z', z_0)\,. \qquad (6\text{-}5.13)$$

As an example, multiple scattering of dipole fields will be examined where the incident plane wave field is a synchrotron pulse

$$a_0(\omega, z, z_0) = E_0 e^{ikz_0} \quad \text{or in time,} \quad a_0(t, z, z_0) = E_0 e^{ikz_0} \delta(t) \quad . \qquad (6\text{-}5.14)$$

For dipole fields

$$\varepsilon_0(\omega) kL = -(\Gamma_s / 4\hbar) / (\omega - \omega_0 + i\Gamma / 2\hbar) \qquad (6\text{-}5.15)$$

where

$$\Gamma_s / \hbar = n\sigma_0 (\Gamma / \hbar) L, \qquad (6\text{-}5.16)$$

L is the thickness of the slab, and σ_0 is the resonant cross section given by Eq. 5-1.52 (with the polarization factor set to unity). Inserting this factor into Eq. 6-5.8 and taking the Fourier transform will give the scattering channel field in the time domain. A contour integral must be performed to complete the Fourier transform, and Lynch, Holland, and Hamermesh have carefully described how to do this.[7]

The other approach involves evaluating the time response of the system. Taking the Fourier transform of the forward scattering amplitude (Eq. 5-1.48 with the polarization factor set to unity) by performing a simple contour integral where there is only one pole in the lower half complex z-plane gives

$$H(t,z',z) = -(\Gamma_s/4\hbar L)e^{-i\omega_0 t-\Gamma t/2\hbar}\theta(t) \qquad (6\text{-}5.17)$$

where

$$\theta(t) = \begin{cases} 1 & t \geq 0 \\ 0 & t < 0 \end{cases}. \qquad (6\text{-}5.18)$$

The multiple scattered field amplitudes are then

$$\sum_{m=1}^{\infty} a_m(t,z',z_0) = -E_0 e^{ikz_0}\frac{\Gamma_s}{4\hbar L}e^{-i\omega_0 t-\Gamma t/2\hbar}\left[1-\left(\frac{\Gamma_s zt}{4\hbar L}\right)+\frac{1}{(2!)^2}\left(\frac{\Gamma_s zt}{4\hbar L}\right)^2-\frac{1}{(3!)^2}\left(\frac{\Gamma_s zt}{4\hbar L}\right)^3+\cdots\right]$$

$$= -E_0 e^{ikz_0}(\Gamma_s/4\hbar L)e^{-i\omega_0 t-\Gamma t/2\hbar}J_0\left(\sqrt{\Gamma_s zt/\hbar L}\right)\theta(t) \qquad (6\text{-}5.19)$$

where the following Bessel function identity was used

$$J_0\left(2\sqrt{y}\right) = 1 - y + \frac{y^2}{(2!)^2} - \frac{y^3}{(3!)^2} + \cdots. \qquad (6\text{-}5.20)$$

Then, using the integral relationship for a Bessel function of order zero

$$\int uJ_0(u) = uJ_1(u) \qquad (6\text{-}5.21)$$

yields the scattering channel field

$$E_{scf}(t,L,z_0) = E_0 e^{ikz_0}\left\{\delta(t) - e^{-i\omega_0 t-\Gamma t/2\hbar}\frac{1}{2t}\int_0^{\sqrt{\Gamma_s t/\hbar}} uJ_0(u)\right\}\theta(t)$$

$$= E_0 e^{ikz_0}\left\{\delta(t) - e^{-i\omega_0 t-\Gamma t/2\hbar}\left(\frac{\Gamma_s}{2\hbar}\right)\frac{J_1\left(\sqrt{\Gamma_s t/\hbar}\right)}{\sqrt{\Gamma_s t/\hbar}}\right\}\theta(t). \qquad (6\text{-}5.22)$$

This is the same result Lynch, Holland, and Hamermesh would get if they were to substitute their ^{57}Co source with a broadband frequency source (such as a synchrotron pulse).[7, 8] There happens to be no frequency shifts for forward scattering through a plane parallel slab, but the natural decay rate is modified by a Bessel function (see Fig. 6-5.2). As $\Gamma_s \to 0$ the collection of particles within the slab behave independently instead of cooperatively, and the collective state decays with the natural lifetime of an isolated particle (kinematical scattering occurs). As Γ_s increases the lifetime of the collective state decreases. Thus, Γ_s indicates the extent a system has undergone homogeneous line broadening. The homogeneous broadened linewidth can be approximated as (after examining Eq. 6-5.8 more carefully)

$$\Gamma_{hom} = \begin{cases} \Gamma & ,\text{for } \Gamma_s << \Gamma \\ \Gamma\sqrt{\dfrac{1}{\ln 2}\left(\dfrac{\Gamma_s}{\Gamma}\right)-1} & ,\text{for } \Gamma_s >> \Gamma \end{cases}. \qquad (6\text{-}5.23)$$

Note that Γ_s in Eq. 6-5.16 depends upon a thickness parameter $T = n\sigma_0 L$. T must also be multiplied by an enrichment factor for samples that contain nonresonant particles and by a Lamb-Mössbauer factor to take into account vibrating scatterers.[9] The graphs below were calculated for a 100% enriched slab of ^{57}Fe nuclei with a Lamb-Mössbauer factor of unity and for no photoelectric absorption. If the photoelectric frequency response is constant over the frequency range of the dipole resonance, then Eq. 6-5.22 need only be multiplied by the factor $e^{i\mu_e(\omega_0)L/2}$ where $\mu_e(\omega_0)$ is the photoelectric absorption coefficient at the resonant frequency. The time spectra in Fig. 6-5.2 ignores the prompt delta-function pulse.

Two more examples of multiple scattering worked out in the time domain are given in Appendix B. In Appendix B.1, Lynch, Holland, and Hamermesh's solution is rederived for the problem where a ^{57}Co source excites a plane parallel slab of resonant scatterers. In Appendix B.2, the time domain multiple scattering equations are used for a case in which they turn out to be more convenient to use than the Fourier transform method. In this problem the dynamical phase between two widely separated resonance lines excited by a synchrotron pulse is examined.

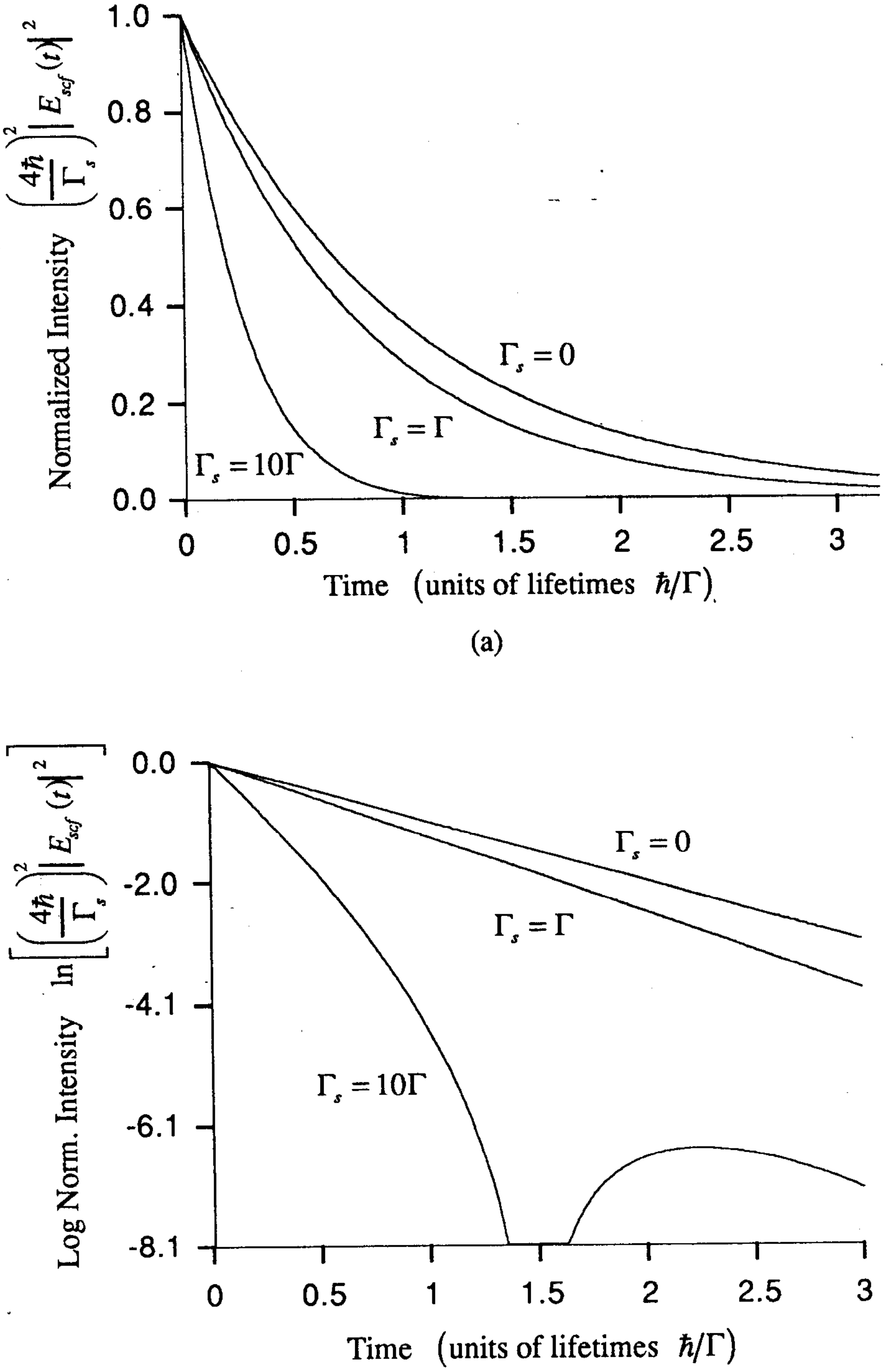

(a)

(b)

Fig 6-5.2. Time spectra of ^{57}Fe for various speedup rates: (a) linear scale, (b) log scale. The presence of dynamical beats becomes evident in the log plot for large speedups.

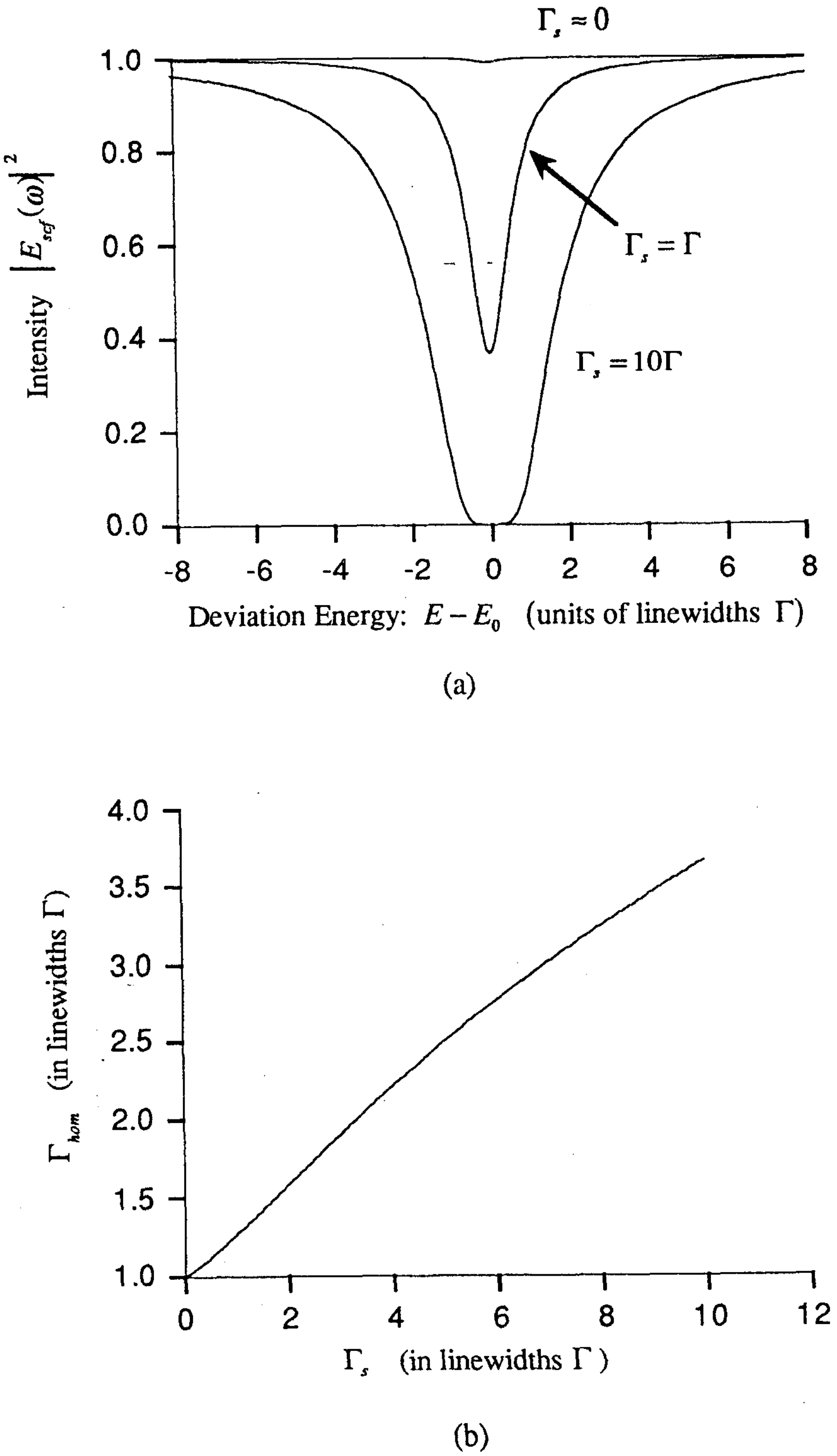

Fig 6-5.3. The decrease in the lifetime of the collective state, as shown in Fig 6-5.2 (a), corresponds, by the uncertainty principle, to a broadening of the linewidth in frequency space: (a) homogeneous line broadening due to multiple scattering, (b) homogeneous linewidth as a function of the speedup rate.

REFERENCES

[1] W. H. Zachariasen, *Theory of X-Ray Diffraction in Crystals* (Dover Publications, New York, 1945).

[2] R. W. James, *The Optical Principles of the Diffraction of X-Rays* (Ox Bow Press, Woodbridge, Connecticut, 1982).

[3] A. Papoulis, *The Fourier Integral and its Applications* (McGraw-Hill, New York, 1962).

[4] S. Ruby (private communications, 1991).

[5] R. H. Dicke, *Phys. Rev.* **93**, 99 (1954).

[6] J. D. Jackson, *Classical Electrodynamics* (Wiley, New York, 1975).

[7] F. J. Lynch, R. E. Holland, and M. Hamermesh, *Phys. Rev.* **120**, 513 (1960).

[8] Y. Kagan, A. M. Afanas'ev, and V. G. Kohn, *J. Phys. C* **12**, 615 (1979).

[9] S. Margulies and J. R. Ehrman, *Nucl. Instr. and Meth.* **12**, 131 (1961).

7. DYNAMICAL DIFFRACTION BY CRYSTALS

The underlying theory of the principles of dynamical diffraction in crystals was developed in the early 1900's independently by Darwin and Ewald. The two theories are quite different explanations of the same phenomenon. The Darwin-Prin's theory carefully examines the reflected and transmitted field amplitudes from each plane of atoms within a crystal in order to build up a total diffracted and transmitted amplitude (one ends up solving a set of coupled difference equations). On the other hand, the Ewald-Laue theory solves the Maxwell equations for a medium having a periodic index of refraction (one ends up solving a set of coupled dispersion equations). A well written discussion of both treatments can be found in James (as well as almost anything one desires to know about X-ray diffraction).[1] A good discussion of the Darwin-Prins treatment can be found in Warren[2] and the Ewald-Laue approach is well discussed in Zachariason[3] and in a paper by Batterman and Cole.[4] In the field of nuclear dynamical diffraction, the Darwin-Prins method has been extended by Hannon and Trammel,[5-8] and the Ewald-Laue approach has been utilized by Kagan and Afanas'ev.[9-11] The discussion in this chapter will concentrate on the Ewald-Laue method of dynamical diffraction theory.

7.1 Dispersion Relations for a Medium having a Tensor Index of Refraction

Solving the inhomogeneous wave equation for transverse electric fields in a medium, Eq. 3-2.11, gives insight into the nature of fields propagating through materials along scattering channels. Recall that the index effect, $2\boldsymbol{\varepsilon}_0$, is a tensor quantity proportional to the multipole scattering amplitude developed in Chapter 4. Thus, the inhomogeneous wave equation is also a tensor wave equation.

For an anisotropic medium, the spatially averaged index effect can be modeled as a continuous periodic function of the spatial coordinates (see Eqs. 3-4.18, 6-1.4, and 6-1.5):

$$2\boldsymbol{\varepsilon}_0(\mathbf{x},\omega) = \frac{4\pi}{k_{0\nu}^2 V_0}\sum_H \mathbf{F}_H e^{i\mathbf{H}\cdot\mathbf{x}} \qquad (7\text{-}1.1)$$

where a sum over all the possible scattering channels denoted by the index H is performed, and the magnitude of the scattered wavector within the medium is assumed to be approximately equal to the vacuum wavenumber: $k_f \approx k_{ov}$. The expression above shows that the index effect can be written as a Fourier series of the spatial frequency components of the scattering amplitude (the multipole scattering amplitude is given by Eq 4-3.63 or 4-3.64 with $\mathbf{x}_0 = 0$). Similarly, the electric field can be expressed as a sum of Fourier components. When this is done, the inhomogeneous wave equation transforms to

$$\left[\nabla \cdot \nabla \cdot + k_{0v}^2 + k_{0v}^2 \left(\frac{4\pi}{k_{ov}^2 V_0}\right) \sum\nolimits_{H'} \mathbf{F}_{H'} e^{i\mathbf{H}' \cdot \mathbf{x}}\right] \sum\nolimits_H \mathbf{E}_H e^{i\mathbf{k}_H \cdot \mathbf{x}} = 0,$$

and thus

$$\sum\nolimits_H \left(1 - \frac{\mathbf{k}_H \cdot \mathbf{k}_H}{k_{0v}^2}\right) \mathbf{E}_H e^{i\mathbf{k}_H \cdot \mathbf{x}} + \frac{4\pi}{k_{ov}^2 V_0} \sum\nolimits_S \sum\nolimits_{H'} \mathbf{F}_{H'} \mathbf{E}_S e^{i(\mathbf{k}_S + \mathbf{H}') \cdot \mathbf{x}} = 0. \tag{7-1.2}$$

The above equation can be satisfied if, term by term, the arguments of the exponentials are the same. They will be if one remains on the energy shell:

$$\mathbf{k}_S + \mathbf{H}' = \mathbf{k}_H. \tag{7-1.3}$$

This can also be seen through examining the Ewald sphere (or energy shell) construction in reciprocal lattice space, Fig. 7-1.1. The reciprocal lattice points, H and S, lie on the Ewald sphere, $\mathbf{k}_0$ is the forward scattered beam within the medium (reciprocal lattice vector is $H = 0$), and $\mathbf{k}_H$ and $\mathbf{k}_S$ are outgoing scattering directions. To satisfy Bragg's law, the incoming and outgoing wavectors must lie on the Ewald sphere. The relation in Eq. 7-1.3 shows that there are fields within the medium traveling in S-channels that are scattered by the spatial distribution of the index of refraction having spatial frequency components denoted by H', and these scattered fields end up traveling in the outgoing H-channel.

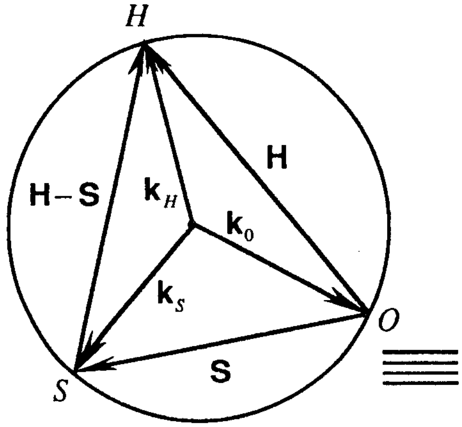

Fig. 7-1.1. Ewald sphere construction for scattering. $\mathbf{k}_0$ is the forward scattered wavector for fields scattering off crystal planes having reciprocal lattice vectors **H** and **S** to produce fields with wavectors $\mathbf{k}_H$ and $\mathbf{k}_S$.

From the Ewald sphere construction, one can see that $\mathbf{S}+\mathbf{H}'=\mathbf{H}$. Then, Eq. 7-1.2 reduces to

$$\left(1-\frac{\mathbf{k}_H\cdot\mathbf{k}_H}{k_{0\nu}^2}\right)E_\alpha^H+\sum_S\sum_\beta g_{\alpha\beta}^{HS}E_\beta^S=0 \tag{7-1.4}$$

where, using terminology similar to Kagan's,[9] the scattering tensor is defined as

$$g_{\alpha\beta}^{HS}=\frac{4\pi}{k_{0\nu}^2V_0}F_{\alpha\beta}^{(H-S)}, \tag{7-1.5}$$

and α and β are polarization indices of the electric field. Equation 7-1.4 is the dispersion equation for a medium having a tensor index of refraction.

7.2 The Scattering Tensor

The scattering tensor contains important polarization information about scattering processes. For the case of photoelectric scattering far from any bound state resonance or absorption edge, the scattering tensor is

$$\mathbf{g}^{HS}=\begin{pmatrix} g_{xx}^{HS} & g_{xy}^{HS} \\ g_{yx}^{HS} & g_{yy}^{HS} \end{pmatrix}=\left(\frac{4\pi}{k_{0\nu}^2V_0}\right)f^{H-S}P^{HS} \tag{7-2.1}$$

where the polarization independent part of the structure factor is, from Eq. 6-1.4 for n identical particles,

$$f^{H-S}=-r_e\sum_n\left(D_W(\mathbf{H}-\mathbf{S})f_0+f'-if''\right)e^{-i(\mathbf{H}-\mathbf{S})\cdot\mathbf{r}_n}, \tag{7-2.2}$$

and the polarization matrix is defined as

$$P^{HS}=\begin{pmatrix} P_{xx}^{HS} & P_{xy}^{HS} \\ P_{yx}^{HS} & P_{yy}^{HS} \end{pmatrix}=\begin{pmatrix} \hat{\boldsymbol{\varepsilon}}_x^S\cdot\hat{\boldsymbol{\varepsilon}}_x^H & \hat{\boldsymbol{\varepsilon}}_x^S\cdot\hat{\boldsymbol{\varepsilon}}_y^H \\ \hat{\boldsymbol{\varepsilon}}_y^S\cdot\hat{\boldsymbol{\varepsilon}}_x^H & \hat{\boldsymbol{\varepsilon}}_y^S\cdot\hat{\boldsymbol{\varepsilon}}_y^H \end{pmatrix} \tag{7-2.3}$$

where $\hat{\boldsymbol{\varepsilon}}_x^H$ and $\hat{\boldsymbol{\varepsilon}}_y^H$ are the two transverse polarizations of the scattered electric field with wavector $\mathbf{k}_H$, and the other two polarizations correspond to the wavector $\mathbf{k}_S$. The Debye-Waller factor, $D_W(\mathbf{H})$, is a function of the scattering vector and is given by Eq. 5-1.56.

The structure of the scattering tensor can be understood by examining some simple cases. For instance, for scattering from a transmission channel $(S=0)$ to a reflection channel (H),

$$\mathbf{g}^{H0}=\left(\frac{4\pi}{k_{0v}^2V_0}\right)f^{H}\begin{pmatrix}\hat{\boldsymbol{\varepsilon}}_x^0\cdot\hat{\boldsymbol{\varepsilon}}_x^H & \hat{\boldsymbol{\varepsilon}}_x^0\cdot\hat{\boldsymbol{\varepsilon}}_y^H\\ \hat{\boldsymbol{\varepsilon}}_y^0\cdot\hat{\boldsymbol{\varepsilon}}_x^H & \hat{\boldsymbol{\varepsilon}}_y^0\cdot\hat{\boldsymbol{\varepsilon}}_y^H\end{pmatrix}. \tag{7-2.4}$$

For the reverse process, scattering from a reflection channel $(S=H)$ to a transmission channel $(H=0)$,

$$\mathbf{g}^{0H}=\left(\frac{4\pi}{k_{0v}^2V_0}\right)f^{\overline{H}}\begin{pmatrix}\hat{\boldsymbol{\varepsilon}}_x^H\cdot\hat{\boldsymbol{\varepsilon}}_x^0 & \hat{\boldsymbol{\varepsilon}}_x^H\cdot\hat{\boldsymbol{\varepsilon}}_y^0\\ \hat{\boldsymbol{\varepsilon}}_y^H\cdot\hat{\boldsymbol{\varepsilon}}_x^0 & \hat{\boldsymbol{\varepsilon}}_y^H\cdot\hat{\boldsymbol{\varepsilon}}_y^0\end{pmatrix}. \tag{7-2.5}$$

For scattering from a transmission channel $(S=0)$ to a transmission channel $(H=0)$ [normal transmission through a material], or, for scattering from a reflection channel $(S=H)$ to a reflection channel (H) [normal transmission in the diffraction direction],

$$\mathbf{g}^{00}=\mathbf{g}^{HH}=\left(\frac{4\pi}{k_{0v}^2V_0}\right)f^{0}\begin{pmatrix}1 & 0\\ 0 & 1\end{pmatrix}. \tag{7-2.6}$$

Since the polarization basis of an electric field is orthonormal, the polarization matrices for transmission are diagonal. The polarization matrices for diffraction are diagonal only if a convenient polarization basis is chosen such as the sigma-pi basis used in Section 5.1 and shown in Fig. 5-1.1--in such a basis polarization mixing is no longer possible.

When the sigma-pi polarization basis discussed in Section 5.1 is used, the two electric field components completely decouple in the dispersion relation, and the dispersion relation reduces to two independent relations for each electric field component

$$\left(1-\frac{\mathbf{k}_H\cdot\mathbf{k}_H}{k_{0v}^2}\right)E_\alpha^H+\sum_S g_{\alpha\alpha}^{HS}E_\alpha^S=0. \tag{7-2.7}$$

For the electronic scattering described above or for spin averaged dipole scattering, the polarization matrices, P^{0H} and P^{H0}, are equivalent, and they are given by Eq. 5-1.47 for electric dipole scattering or Eq. 5-1.46 for magnetic dipole scattering. For spin averaged dipole scattering from q identical particles

$$f^{H-S}=-\frac{L_M(\mathbf{k}_i)L_M(\mathbf{k}_f)C}{4k_{0v}}\left(\frac{2j_n+1}{2j_i+1}\right)\frac{\Gamma_{rad}}{\hbar}\frac{1}{\omega_{\mathbf{k}_i}-\omega_0+i\Gamma/2\hbar}\sum_q e^{-i(\mathbf{H}-\mathbf{S})\cdot\mathbf{r}_q}. \tag{7-2.8}$$

The quantities $L_M(\mathbf{k}_i)$ and $L_M(\mathbf{k}_f)$ are the Lamb-Mössbauer factors that take into account the vibrations of the scatterers. From Eq. 4-3.66

$$L_M(\mathbf{k}_i)=\langle f_\alpha|e^{i\mathbf{k}_i\cdot\mathbf{u}}|i_\alpha\rangle,\quad L_M(\mathbf{k}_f)=\langle f_\alpha|e^{-i\mathbf{k}_f\cdot\mathbf{u}}|i_\alpha\rangle \tag{7-2.9}$$

where $|i_\alpha\rangle$ and $|f_\alpha\rangle$ are initial and final phonon states. The quantity C is the enrichment factor describing the concentration of resonant scatterers at the lattice sites.

In general, when multipole scattering is included, polarization mixing occurs in both the transmission and reflection channels. For nuclear scattering the scattering tensor in Eq. 7-2.1 has an angular independent structure factor defined as (from Eq. 5-1.4 for q identical particles and averaged over the initial state spins)

$$f^{H-S} = -(2\pi/k_{0v}) \frac{L_M(\mathbf{k}_i) L_M(\mathbf{k}_f) C \Gamma(L,\lambda)}{E_i - E_n + \hbar\omega_{\mathbf{k}_i} + i\Gamma_n/2} \frac{\langle j_f m_f LM | j_f L j_n m_n \rangle^2}{(2j_i + 1)} \sum_q e^{-i(\mathbf{H}-\mathbf{S})\cdot\mathbf{r}_q}, \quad (7\text{-}2.10)$$

and the polarization matrix is given by Eq. 5-1.5 with the substitution $\hat{\boldsymbol{\varepsilon}}^f_\alpha \rightarrow \hat{\boldsymbol{\varepsilon}}^H_\alpha$ and $\hat{\boldsymbol{\varepsilon}}^i_\alpha \rightarrow \hat{\boldsymbol{\varepsilon}}^S_\alpha$, where $\alpha = x, y$.

7.3 Linearized Dispersion Equations

The dispersion equations, Eq. 7-1.4, are a set of homogeneous nonlinear coupled field equations. The nonlinearity comes from the quadratic term k_H^2 and the polarization directions of the fields inside the medium represented in the polarization matrices. However, for X-ray photons, the dispersions equations can be linearized because most materials are essentially transparent to such photons. Since incoming X-ray photons are only slightly affected by the presence of a medium, the polarization directions of the fields inside a medium can be approximated as the polarization directions of the fields in vacuum. This is a common approximation used in dynamical diffraction theory.

If the index of refraction in the H channel is $\sqrt{1+2\varepsilon_H}$ where ε_H is a small complex number, then the quadratic term in the dispersion equation is $k_H^2 = (1+2\varepsilon_H)k_{0v}^2$ where k_{0v} is the vacuum wavenumber. The dispersion equation, Eq. 7-1.4, then reduces to the simpler form

$$2\varepsilon_H E_\alpha^H = \sum_{S\beta} g_{\alpha\beta}^{HS} E_\beta^S. \quad (7\text{-}3.1)$$

Making the further approximation that

$$k_H \approx (1+\varepsilon_H) k_{0v} \quad (7\text{-}3.2)$$

completes the linearization of the dispersion equations. This is shown for a two-beam (or two-channel) example in the following section.

7.4 Two-Beam Analytical Solution

In certain situations reasonably simple analytical expressions can be constructed for the scattered fields within a medium. This occurs for electronic scattering with a wise choice of the sigma and pi polarization vectors that diagonalize the scattering tensor. The multipole scattering tensor can also be diagonalized for certain orientations between the quantization axis of the scatterer and the scattering plane. For the two beam case where there are only two scattering channels, $S=0$ and $\mathrm{S}=H$, along which travel a forward scattered and a diffracted electric field, the decoupled dispersion relations can be written in the form

$$\begin{pmatrix} (g_{xx}^{00}-2\varepsilon_0) & g_{xx}^{01} & 0 & 0 \\ g_{xx}^{10} & (g_{xx}^{11}-2\varepsilon_1) & 0 & 0 \\ 0 & 0 & (g_{yy}^{00}-2\varepsilon_0) & g_{yy}^{01} \\ 0 & 0 & g_{yy}^{10} & (g_{yy}^{11}-2\varepsilon_1) \end{pmatrix} \begin{pmatrix} T_x \\ R_x \\ T_y \\ R_y \end{pmatrix} = \mathbf{G}\cdot\mathbf{v}=0. \quad (7\text{-}4.1)$$

where

$$\mathbf{T}=\mathbf{E}^{S=0} \quad (\text{transmitted field}) \quad (7\text{-}4.2)$$

$$\mathbf{R}=\mathbf{E}^{S=H} \quad (\text{diffracted, or reflected, field}). \quad (7\text{-}4.3)$$

$H\equiv 1$, and x,y denote the two transverse polarizations of the electric field (in the sigma and pi polarization basis shown in Fig. 5-1.1, $x=\sigma$, and $y=\pi$).

To solve the dispersion equation, a relationship between ε_0 and ε_1 must be found. This can be done by noting that refraction occurs for a wave entering a medium from free space

$$\mathbf{k}_0=\mathbf{k}_{0v}+k_{0v}\delta\hat{\mathbf{n}} \quad (7\text{-}4.4)$$

where $\mathbf{k}_{0v}$ is the vacuum wavector in the forward direction (all vacuum quantities will have the index v), $\hat{\mathbf{n}}$ is an interior normal to the crystal surface, and δ is a quantity describing how much refraction has taken place.

Using Eqs. 7-3.2 and 7-4.4, to first order in δ and ε_0 (to linearize the dispersion equations), one finds that

$$\delta=\varepsilon_0/\gamma_0 \quad (7\text{-}4.5)$$

where

$$\gamma_0=\hat{\mathbf{k}}_{0v}\cdot\hat{\mathbf{n}}. \quad (7\text{-}4.6)$$

Applying Bragg's law,

$$\mathbf{k}_1=\mathbf{k}_0+\mathbf{H}, \quad (7\text{-}4.7)$$

yields, to first order in $\varepsilon_1, \varepsilon_0$, and δ,

$$k_{0v}^2(1+2\varepsilon_1)=k_{0v}^2(1+2\varepsilon_0)+H^2+2(\mathbf{k}_{0v}+k_{0v}\delta\hat{\mathbf{n}})$$

which reduces to

$$\varepsilon_1=\varepsilon_0+\frac{\mathbf{H}\cdot(\mathbf{H}+2\mathbf{k}_{0v})}{2k_{0v}^2}+\delta(\hat{\mathbf{k}}_1-\hat{\mathbf{k}}_0)\cdot\hat{\mathbf{n}}$$

$$\approx\alpha_B/2+\varepsilon_0/b \tag{7-4.8}$$

where α_B is a deviation from Bragg parameter

$$\alpha_B=\mathbf{H}\cdot(\mathbf{H}+2\mathbf{k}_{0v})/k_{0v}^2. \tag{7-4.9}$$

The parameter b is an asymmetry factor

$$b=\gamma_0/\gamma_1 \tag{7-4.10}$$

where

$$\gamma_1=\hat{\mathbf{k}}_1\cdot\hat{\mathbf{n}}. \tag{7-4.11}$$

The α_B parameter describes how close a reciprocal lattice point must be to the Ewald sphere in order to still satisfy the Bragg condition. The parameter can be evaluated by examining how Bragg's law varies near the Ewald sphere

$$H=|\mathbf{k}_1-\mathbf{k}_0|=\sqrt{k_1^2+k_0^2-2k_1k_0\cos 2\theta_B}$$

$$\approx 2k_{0v}\sin\theta_B\left(1+\frac{\varepsilon_1+\varepsilon_0}{2}\right) \tag{7-4.12}$$

where $2\theta_B$ is the scattering angle between $\mathbf{k}_1$ and $\mathbf{k}_0$, and θ_B is the Bragg angle. Also note that

$$\mathbf{H}\cdot\mathbf{k}_{0v}=-Hk_{0v}\sin\theta_0 \tag{7-4.13}$$

where $\theta_0+\pi/2$ is the angle between $\mathbf{H}$ and $\mathbf{k}_{0v}$ (see Fig. 7-4.1). When the Bragg condition is satisfied, θ_0 is nearly equal to θ_B. Defining a deviation angle

$$\Delta\theta=\theta_0-\theta_B \tag{7-4.14}$$

that is a measure of the angular deviation from Bragg gives

$$\alpha_B=-2\Delta\theta\sin 2\theta_B-4(\Delta E/E)\sin^2\theta_B \tag{7-4.15}$$

where E is the incoming photon energy, and ΔE is the deviation of the Bragg energy from the incoming photon energy

$$\Delta E=E-E_B=\hbar c\left[k_{0v}-(k_1+k_0)/2\right]. \tag{7-4.16}$$

The Bragg energy has been defined to be proportional to the average wavenumber inside the medium. To remain close to the Bragg condition, either an angular or energy constraint must be satisfied: $\Delta\theta$ or ΔE must be close to zero. For instance, when examining the angular spectrum of a scattered field, the Bragg energy is set equal to the incoming photon

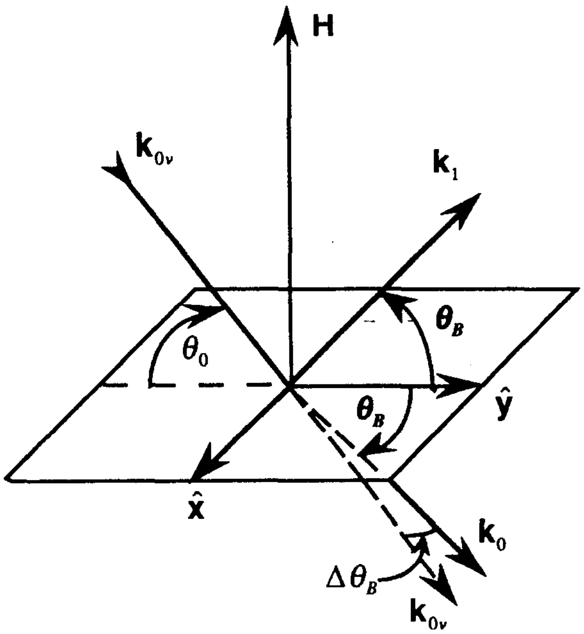

Fig. 7-4.1. Diffraction from crystal planes. The xy-plane is the crystal surface, and $\mathbf{H}$ is a reciprocal lattice vector perpendicular to the crystal planes. Present geometry shows a symmetric Bragg reflection $(b=-1)$. Incoming beam from vacuum, $\mathbf{k}_{0v}$, strikes the surface, and refraction produces outgoing beam, $\mathbf{k}_0$, shifted by $\Delta\theta_B$ from the incident angle θ_0.

energy, $E_B = E$ or $\Delta E = 0$, and the Bragg angle is obtained through Bragg's law and $\alpha_B = -2\Delta\theta \sin 2\theta_B$. When examining the energy spectrum of a scattered field, the Bragg angle is set equal to the incoming photon angle, $\theta_B = \theta_0$ or $\Delta\theta = 0$, and the Bragg energy is obtained from Bragg's law and $\alpha_B = -4(\Delta E/E)\sin^2\theta_B$. Bragg's law, Eq. 7-4.7, can be rewritten as the following expression:

$$E_B \sin\theta_B = \hbar c H/2 \tag{7-4.17}$$

where

$$H = 2\pi/d_{hkl}, \tag{7-4.18}$$

and d_{hkl} is the lattice spacing of the $[hkl]$ reflection.

The solution to Eq. 7-4.1 then reduces to solving a familiar eigenvalue-eigenvector problem. The characteristic equation is

$$\det(\mathbf{G}_{lin} - 2\varepsilon_0 \mathbf{I}) = 0 \tag{7-4.19}$$

where

$$\mathbf{G}_{lin} = \begin{pmatrix} g_{xx}^{00} & g_{xx}^{01} & \multicolumn{2}{c}{0} \\ g_{xx}^{10} & (bg_{xx}^{11} - b\alpha_B) & & \\ \multicolumn{2}{c}{0} & g_{yy}^{00} & g_{yy}^{01} \\ & & g_{yy}^{10} & (bg_{yy}^{11} - b\alpha_B) \end{pmatrix}. \tag{7-4.20}$$

The solution to the characteristic equation yields the four eigenvalues

$$\varepsilon_{0\beta}^{(1,2)} = \frac{1}{4}\left(g_{\beta\beta}^{00} + bg_{\beta\beta}^{11} - b\alpha_B\right) \pm \frac{1}{4}\sqrt{\left(g_{\beta\beta}^{00} - bg_{\beta\beta}^{11} + b\alpha_B\right)^2 + 4bg_{\beta\beta}^{01}g_{\beta\beta}^{10}} \tag{7-4.21}$$

where $\beta = x,y$.

To complete the solution to the inhomogeneous wave equation, boundary conditions must be supplied. In order to obtain analytical expressions to the reflected and transmitted fields, interfacial reflections at the entrant and exit crystal surfaces will be neglected. These reflections occur when a field crosses from one medium to another (such as from vacuum to the crystal medium). The Bragg and Laue solutions are given below using this approximation.

BRAGG CASE: At the top and bottom surfaces of the crystal (see Fig. 7-4.2), the boundary conditions are

$$\hat{\mathbf{n}} \cdot \mathbf{r} = 0: \qquad \mathbf{E}_{0v} = \mathbf{T} = \sum_{l=1}^{2} \sum_{\alpha} T_{\alpha}^{l} \hat{\boldsymbol{\varepsilon}}_{\alpha}^{0} \tag{7-4.22}$$

$$\hat{\mathbf{n}} \cdot \mathbf{r} = d: \qquad 0 = \mathbf{R} = e^{i(\mathbf{k}_{0v} + \mathbf{H}) \cdot \mathbf{r}} \sum_{l=1}^{2} \sum_{\alpha} R_{\alpha}^{l} e^{i\kappa_{\alpha}^{l} d} \hat{\boldsymbol{\varepsilon}}_{\alpha}^{H} \tag{7-4.23}$$

where

$$\mathbf{k}_0 = \mathbf{k}_{0v} + \kappa_{\alpha}^{l} \hat{\mathbf{n}} \tag{7-4.24}$$

$$\mathbf{k}_H \equiv \mathbf{k}_1 = \mathbf{k}_0 + \mathbf{H} \tag{7-4.25}$$

$$\kappa_{\alpha}^{l} = k_{0v} \varepsilon_{0\alpha}^{l} / \gamma_0 \tag{7-4.26}$$

$\alpha = x,y$, $l = 1,2$ is the eigenvector index, and $\mathbf{E}_{0v}$ is the incoming electric field from the vacuum. For Bragg diffraction and for no interfacial reflections, all of the incoming field scatters into the transmission channel, and, at the exit surface there is no incoming field scattering into the reflection channel.

For each eigenvalue in Eq. 7-4.21, there is a unique eigenvector

$$\mathbf{v}_{\alpha}^{l} = \begin{pmatrix} T_{\alpha}^{l} \\ R_{\alpha}^{l} \end{pmatrix}. \tag{7-4.27}$$

decreases. Thus, Γ_s indicates the extent a system has undergone homogeneous line broadening. The homogeneous broadened linewidth can be approximated as (after examining Eq. 6-5.8 more carefully)

$$\Gamma_{hom} = \begin{cases} \Gamma & \text{,for } \Gamma_s \ll \Gamma \\ \Gamma\sqrt{\dfrac{1}{\ln 2}\left(\dfrac{\Gamma_s}{\Gamma}\right) - 1} & \text{,for } \Gamma_s \gg \Gamma \end{cases}. \tag{6-5.23}$$

Note that Γ_s in Eq. 6-5.16 depends upon a thickness parameter $T = n\sigma_0 L$. T must also be multiplied by an enrichment factor for samples that contain nonresonant particles and by a Lamb-Mössbauer factor to take into account vibrating scatterers.[9] The graphs below were calculated for a 100% enriched slab of ^{57}Fe nuclei with a Lamb-Mössbauer factor of unity and for no photoelectric absorption. If the photoelectric frequency response is constant over the frequency range of the dipole resonance, then Eq. 6-5.22 need only be multiplied by the factor $e^{i\mu_e(\omega_0)L/2}$ where $\mu_e(\omega_0)$ is the photoelectric absorption coefficient at the resonant frequency. The time spectra in Fig. 6-5.2 ignores the prompt delta-function pulse.

Two more examples of multiple scattering worked out in the time domain are given in Appendix B. In Appendix B.1, Lynch, Holland, and Hamermesh's solution is rederived for the problem where a ^{57}Co source excites a plane parallel slab of resonant scatterers. In Appendix B.2, the time domain multiple scattering equations are used for a case in which they turn out to be more convenient to use than the Fourier transform method. In this problem the dynamical phase between two widely separated resonance lines excited by a synchrotron pulse is examined.

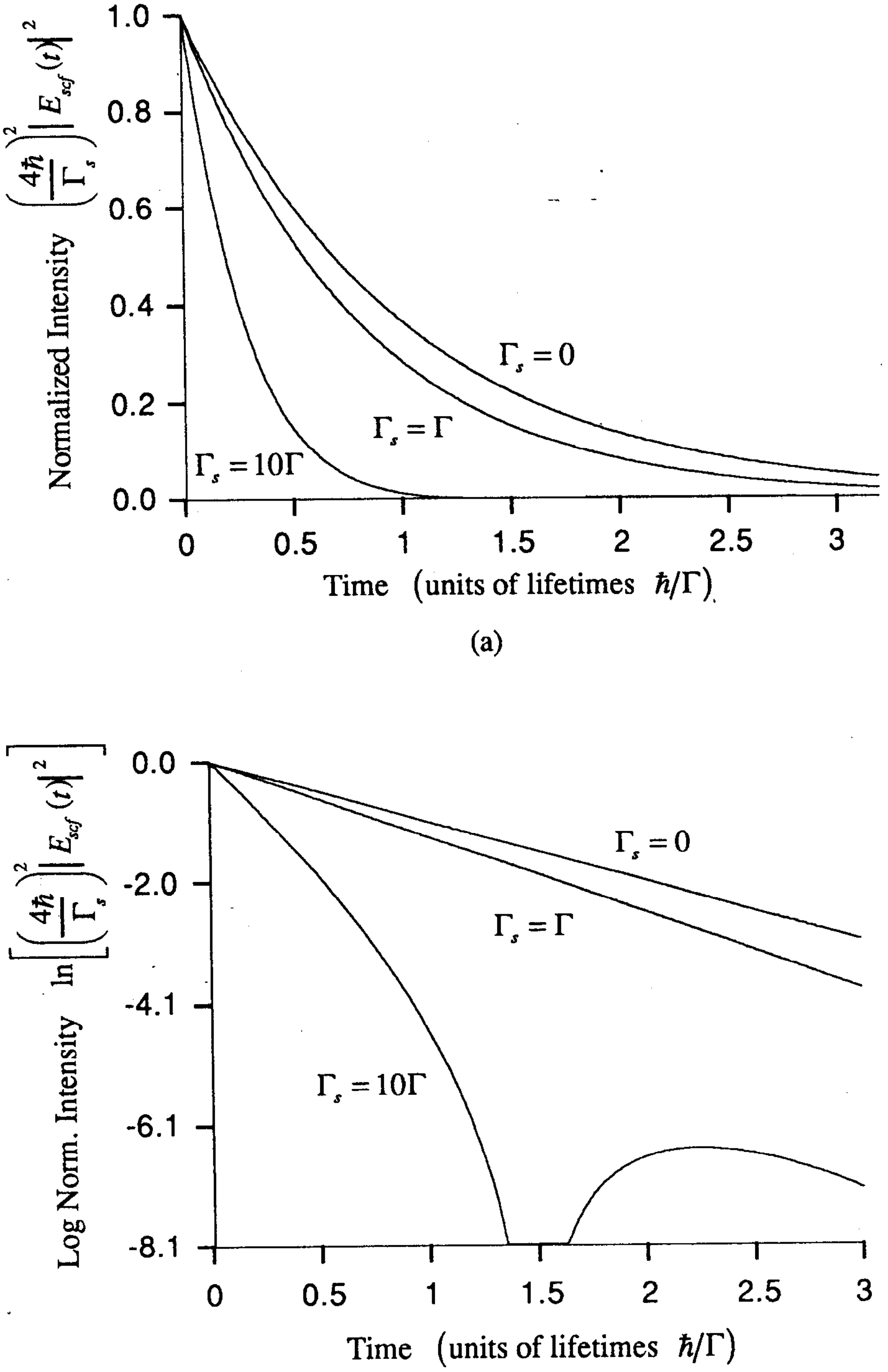

(a)

(b)

Fig 6-5.2. Time spectra of ^{57}Fe for various speedup rates: (a) linear scale, (b) log scale. The presence of dynamical beats becomes evident in the log plot for large speedups.

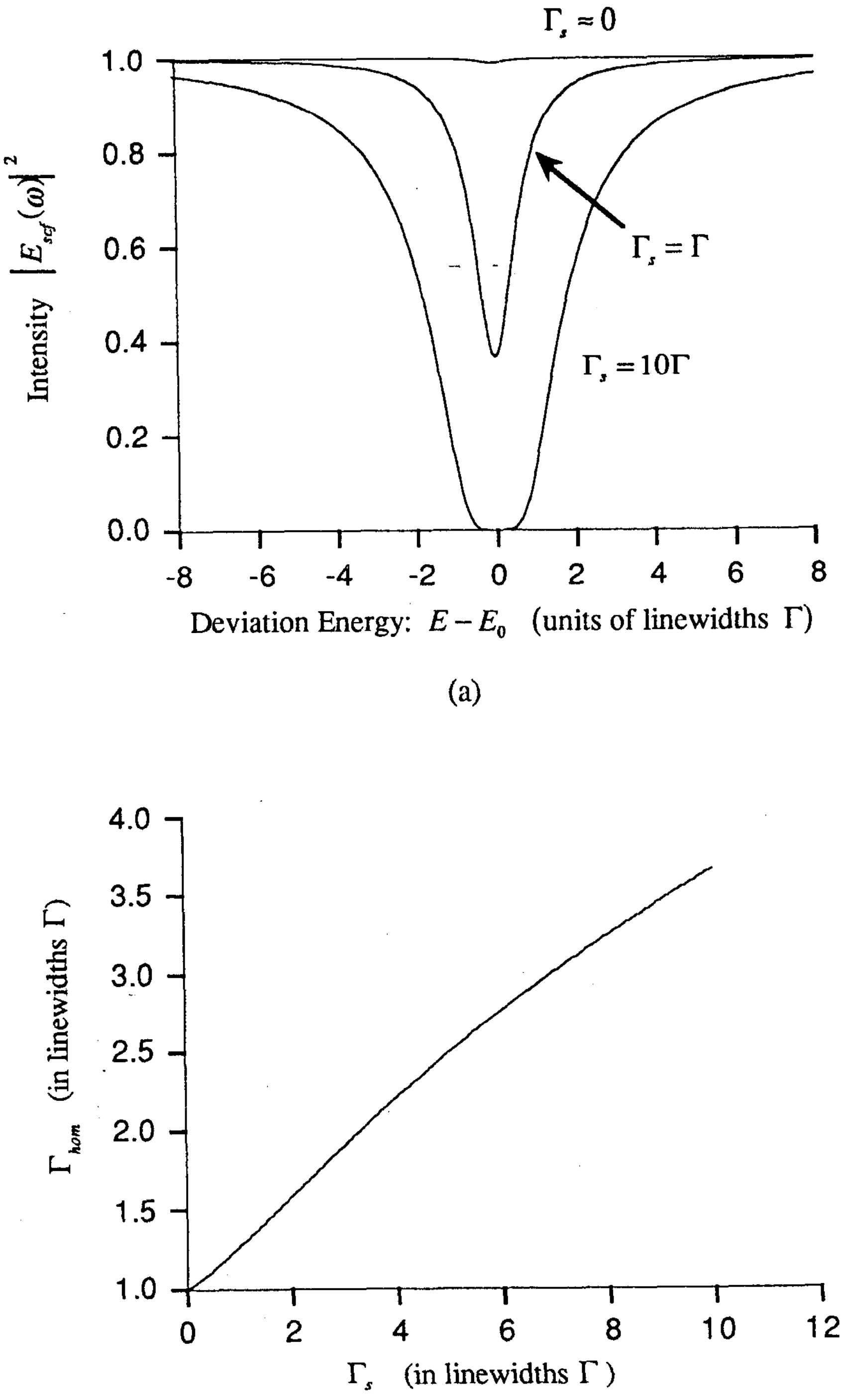

(a)

(b)

Fig 6-5.3. The decrease in the lifetime of the collective state, as shown in Fig 6-5.2 (a), corresponds, by the uncertainty principle, to a broadening of the linewidth in frequency space: (a) homogeneous line broadening due to multiple scattering, (b) homogeneous linewidth as a function of the speedup rate.

REFERENCES

[1] W. H. Zachariasen, *Theory of X-Ray Diffraction in Crystals* (Dover Publications, New York, 1945).

[2] R. W. James, *The Optical Principles of the Diffraction of X-Rays* (Ox Bow Press, Woodbridge, Connecticut, 1982).

[3] A. Papoulis, *The Fourier Integral and its Applications* (McGraw-Hill, New York, 1962).

[4] S. Ruby (private communications, 1991).

[5] R. H. Dicke, *Phys. Rev.* **93**, 99 (1954).

[6] J. D. Jackson, *Classical Electrodynamics* (Wiley, New York, 1975).

[7] F. J. Lynch, R. E. Holland, and M. Hamermesh, *Phys. Rev.* **120**, 513 (1960).

[8] Y. Kagan, A. M. Afanas'ev, and V. G. Kohn, *J. Phys. C* **12**, 615 (1979).

[9] S. Margulies and J. R. Ehrman, *Nucl. Instr. and Meth.* **12**, 131 (1961).

7. DYNAMICAL DIFFRACTION BY CRYSTALS

The underlying theory of the principles of dynamical diffraction in crystals was developed in the early 1900's independently by Darwin and Ewald. The two theories are quite different explanations of the same phenomenon. The Darwin-Prin's theory carefully examines the reflected and transmitted field amplitudes from each plane of atoms within a crystal in order to build up a total diffracted and transmitted amplitude (one ends up solving a set of coupled difference equations). On the other hand, the Ewald-Laue theory solves the Maxwell equations for a medium having a periodic index of refraction (one ends up solving a set of coupled dispersion equations). A well written discussion of both treatments can be found in James (as well as almost anything one desires to know about X-ray diffraction).[1] A good discussion of the Darwin-Prins treatment can be found in Warren[2] and the Ewald-Laue approach is well discussed in Zachariason[3] and in a paper by Batterman and Cole.[4] In the field of nuclear dynamical diffraction, the Darwin-Prins method has been extended by Hannon and Trammel,[5-8] and the Ewald-Laue approach has been utilized by Kagan and Afanas'ev.[9-11] The discussion in this chapter will concentrate on the Ewald-Laue method of dynamical diffraction theory.

7.1 Dispersion Relations for a Medium having a Tensor Index of Refraction

Solving the inhomogeneous wave equation for transverse electric fields in a medium, Eq. 3-2.11, gives insight into the nature of fields propagating through materials along scattering channels. Recall that the index effect, $2\boldsymbol{\varepsilon}_0$, is a tensor quantity proportional to the multipole scattering amplitude developed in Chapter 4. Thus, the inhomogeneous wave equation is also a tensor wave equation.

For an anisotropic medium, the spatially averaged index effect can be modeled as a continuous periodic function of the spatial coordinates (see Eqs. 3-4.18, 6-1.4, and 6-1.5):

$$2\boldsymbol{\varepsilon}_0(\mathbf{x},\omega)=\frac{4\pi}{k_{0\nu}^2 V_0}\sum_H \mathbf{F}_H e^{i\mathbf{H}\cdot\mathbf{x}} \tag{7-1.1}$$

where a sum over all the possible scattering channels denoted by the index H is performed, and the magnitude of the scattered wavector within the medium is assumed to be approximately equal to the vacuum wavenumber: $k_f \approx k_{ov}$. The expression above shows that the index effect can be written as a Fourier series of the spatial frequency components of the scattering amplitude (the multipole scattering amplitude is given by Eq 4-3.63 or 4-3.64 with $\mathbf{x}_0 = 0$). Similarly, the electric field can be expressed as a sum of Fourier components. When this is done, the inhomogeneous wave equation transforms to

$$\left[\nabla \cdot \nabla \cdot + k_{0v}^2 + k_{0v}^2 \left(\frac{4\pi}{k_{ov}^2 V_0}\right) \sum_{H'} \mathbf{F}_{H'} e^{i\mathbf{H}' \cdot \mathbf{x}}\right] \sum_H \mathbf{E}_H e^{i\mathbf{k}_H \cdot \mathbf{x}} = 0,$$

and thus

$$\sum_H \left(1 - \frac{\mathbf{k}_H \cdot \mathbf{k}_H}{k_{0v}^2}\right) \mathbf{E}_H e^{i\mathbf{k}_H \cdot \mathbf{x}} + \frac{4\pi}{k_{ov}^2 V_0} \sum_S \sum_{H'} \mathbf{F}_{H'} \mathbf{E}_S e^{i(\mathbf{k}_S + \mathbf{H}') \cdot \mathbf{x}} = 0. \tag{7-1.2}$$

The above equation can be satisfied if, term by term, the arguments of the exponentials are the same. They will be if one remains on the energy shell:

$$\mathbf{k}_S + \mathbf{H}' = \mathbf{k}_H. \tag{7-1.3}$$

This can also be seen through examining the Ewald sphere (or energy shell) construction in reciprocal lattice space, Fig. 7-1.1. The reciprocal lattice points, H and S, lie on the Ewald sphere, $\mathbf{k}_0$ is the forward scattered beam within the medium (reciprocal lattice vector is $H = 0$), and $\mathbf{k}_H$ and $\mathbf{k}_S$ are outgoing scattering directions. To satisfy Bragg's law, the incoming and outgoing wavectors must lie on the Ewald sphere. The relation in Eq. 7-1.3 shows that there are fields within the medium traveling in S-channels that are scattered by the spatial distribution of the index of refraction having spatial frequency components denoted by H', and these scattered fields end up traveling in the outgoing H-channel.

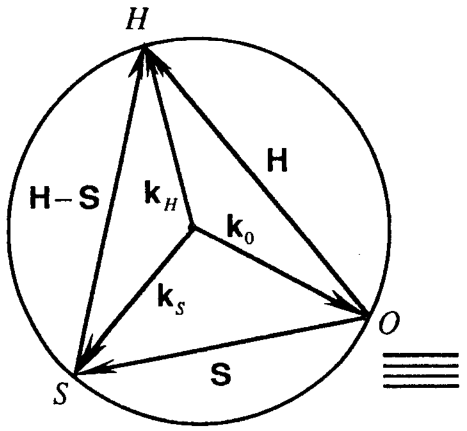

Fig. 7-1.1. Ewald sphere construction for scattering. $\mathbf{k}_0$ is the forward scattered wavector for fields scattering off crystal planes having reciprocal lattice vectors **H** and **S** to produce fields with wavectors $\mathbf{k}_H$ and $\mathbf{k}_S$.

From the Ewald sphere construction, one can see that $\mathbf{S}+\mathbf{H}'=\mathbf{H}$. Then, Eq. 7-1.2 reduces to

$$\left(1-\frac{\mathbf{k}_H\cdot\mathbf{k}_H}{k_{0\nu}^2}\right)E_\alpha^H+\sum_S\sum_\beta g_{\alpha\beta}^{HS}E_\beta^S=0 \tag{7-1.4}$$

where, using terminology similar to Kagan's,[9] the scattering tensor is defined as

$$g_{\alpha\beta}^{HS}=\frac{4\pi}{k_{0\nu}^2V_0}F_{\alpha\beta}^{(H-S)}, \tag{7-1.5}$$

and α and β are polarization indices of the electric field. Equation 7-1.4 is the dispersion equation for a medium having a tensor index of refraction.

7.2 The Scattering Tensor

The scattering tensor contains important polarization information about scattering processes. For the case of photoelectric scattering far from any bound state resonance or absorption edge, the scattering tensor is

$$\mathbf{g}^{HS}=\begin{pmatrix} g_{xx}^{HS} & g_{xy}^{HS} \\ g_{yx}^{HS} & g_{yy}^{HS}\end{pmatrix}=\left(\frac{4\pi}{k_{0\nu}^2V_0}\right)f^{H-S}P^{HS} \tag{7-2.1}$$

where the polarization independent part of the structure factor is, from Eq. 6-1.4 for n identical particles,

$$f^{H-S}=-r_e\sum_n\left(D_W(\mathbf{H}-\mathbf{S})f_0+f'-if''\right)e^{-i(\mathbf{H}-\mathbf{S})\cdot\mathbf{r}_n}, \tag{7-2.2}$$

and the polarization matrix is defined as

$$P^{HS}=\begin{pmatrix} P_{xx}^{HS} & P_{xy}^{HS} \\ P_{yx}^{HS} & P_{yy}^{HS}\end{pmatrix}=\begin{pmatrix} \hat{\boldsymbol{\varepsilon}}_x^S\cdot\hat{\boldsymbol{\varepsilon}}_x^H & \hat{\boldsymbol{\varepsilon}}_x^S\cdot\hat{\boldsymbol{\varepsilon}}_y^H \\ \hat{\boldsymbol{\varepsilon}}_y^S\cdot\hat{\boldsymbol{\varepsilon}}_x^H & \hat{\boldsymbol{\varepsilon}}_y^S\cdot\hat{\boldsymbol{\varepsilon}}_y^H\end{pmatrix} \tag{7-2.3}$$

where $\hat{\boldsymbol{\varepsilon}}_x^H$ and $\hat{\boldsymbol{\varepsilon}}_y^H$ are the two transverse polarizations of the scattered electric field with wavector $\mathbf{k}_H$, and the other two polarizations correspond to the wavector $\mathbf{k}_S$. The Debye-Waller factor, $D_W(\mathbf{H})$, is a function of the scattering vector and is given by Eq. 5-1.56.

The structure of the scattering tensor can be understood by examining some simple cases. For instance, for scattering from a transmission channel $(S=0)$ to a reflection channel (H),

$$\mathbf{g}^{H0} = \left(\frac{4\pi}{k_{0v}^2 V_0}\right) f^{H} \begin{pmatrix} \hat{\boldsymbol{\varepsilon}}_x^0 \cdot \hat{\boldsymbol{\varepsilon}}_x^H & \hat{\boldsymbol{\varepsilon}}_x^0 \cdot \hat{\boldsymbol{\varepsilon}}_y^H \\ \hat{\boldsymbol{\varepsilon}}_y^0 \cdot \hat{\boldsymbol{\varepsilon}}_x^H & \hat{\boldsymbol{\varepsilon}}_y^0 \cdot \hat{\boldsymbol{\varepsilon}}_y^H \end{pmatrix}. \tag{7-2.4}$$

For the reverse process, scattering from a reflection channel ($S = H$) to a transmission channel ($H = 0$),

$$\mathbf{g}^{0H} = \left(\frac{4\pi}{k_{0v}^2 V_0}\right) f^{\overline{H}} \begin{pmatrix} \hat{\boldsymbol{\varepsilon}}_x^H \cdot \hat{\boldsymbol{\varepsilon}}_x^0 & \hat{\boldsymbol{\varepsilon}}_x^H \cdot \hat{\boldsymbol{\varepsilon}}_y^0 \\ \hat{\boldsymbol{\varepsilon}}_y^H \cdot \hat{\boldsymbol{\varepsilon}}_x^0 & \hat{\boldsymbol{\varepsilon}}_y^H \cdot \hat{\boldsymbol{\varepsilon}}_y^0 \end{pmatrix}. \tag{7-2.5}$$

For scattering from a transmission channel ($S = 0$) to a transmission channel ($H = 0$) [normal transmission through a material], or, for scattering from a reflection channel ($S = H$) to a reflection channel (H) [normal transmission in the diffraction direction],

$$\mathbf{g}^{00} = \mathbf{g}^{HH} = \left(\frac{4\pi}{k_{0v}^2 V_0}\right) f^{0} \begin{pmatrix} 1 & 0 \\ 0 & 1 \end{pmatrix}. \tag{7-2.6}$$

Since the polarization basis of an electric field is orthonormal, the polarization matrices for transmission are diagonal. The polarization matrices for diffraction are diagonal only if a convenient polarization basis is chosen such as the sigma-pi basis used in Section 5.1 and shown in Fig. 5-1.1--in such a basis polarization mixing is no longer possible.

When the sigma-pi polarization basis discussed in Section 5.1 is used, the two electric field components completely decouple in the dispersion relation, and the dispersion relation reduces to two independent relations for each electric field component

$$\left(1 - \frac{\mathbf{k}_H \cdot \mathbf{k}_H}{k_{0v}^2}\right) E_\alpha^H + \sum_S g_{\alpha\alpha}^{HS} E_\alpha^S = 0. \tag{7-2.7}$$

For the electronic scattering described above or for spin averaged dipole scattering, the polarization matrices, P^{0H} and P^{H0}, are equivalent, and they are given by Eq. 5-1.47 for electric dipole scattering or Eq. 5-1.46 for magnetic dipole scattering. For spin averaged dipole scattering from q identical particles

$$f^{H-S} = -\frac{L_M(\mathbf{k}_i) L_M(\mathbf{k}_f) C}{4k_{0v}} \left(\frac{2j_n + 1}{2j_i + 1}\right) \frac{\Gamma_{rad}}{\hbar} \frac{1}{\omega_{\mathbf{k}_i} - \omega_0 + i\Gamma/2\hbar} \sum_q e^{-i(\mathbf{H}-\mathbf{S})\cdot\mathbf{r}_q}. \tag{7-2.8}$$

The quantities $L_M(\mathbf{k}_i)$ and $L_M(\mathbf{k}_f)$ are the Lamb-Mössbauer factors that take into account the vibrations of the scatterers. From Eq. 4-3.66

$$L_M(\mathbf{k}_i) = \langle f_\alpha | e^{i\mathbf{k}_i\cdot\mathbf{u}} | i_\alpha \rangle, \quad L_M(\mathbf{k}_f) = \langle f_\alpha | e^{-i\mathbf{k}_f\cdot\mathbf{u}} | i_\alpha \rangle \tag{7-2.9}$$

where $|i_\alpha\rangle$ and $|f_\alpha\rangle$ are initial and final phonon states. The quantity C is the enrichment factor describing the concentration of resonant scatterers at the lattice sites.

In general, when multipole scattering is included, polarization mixing occurs in both the transmission and reflection channels. For nuclear scattering the scattering tensor in Eq. 7-2.1 has an angular independent structure factor defined as (from Eq. 5-1.4 for q identical particles and averaged over the initial state spins)

$$f^{H-S} = -(2\pi/k_{0v})\frac{L_M(\mathbf{k}_i)L_M(\mathbf{k}_f)C\Gamma(L,\lambda)}{E_i - E_n + \hbar\omega_{\mathbf{k}_i} + i\Gamma_n/2}\frac{\langle j_f m_f LM | j_f L j_n m_n\rangle^2}{(2j_i+1)}\sum_q e^{-i(\mathbf{H}-\mathbf{S})\cdot\mathbf{r}_q}, \quad (7\text{-}2.10)$$

and the polarization matrix is given by Eq. 5-1.5 with the substitution $\hat{\boldsymbol{\varepsilon}}_\alpha^f \rightarrow \hat{\boldsymbol{\varepsilon}}_\alpha^H$ and $\hat{\boldsymbol{\varepsilon}}_\alpha^i \rightarrow \hat{\boldsymbol{\varepsilon}}_\alpha^S$, where $\alpha = x, y$.

7.3 Linearized Dispersion Equations

The dispersion equations, Eq. 7-1.4, are a set of homogeneous nonlinear coupled field equations. The nonlinearity comes from the quadratic term k_H^2 and the polarization directions of the fields inside the medium represented in the polarization matrices. However, for X-ray photons, the dispersions equations can be linearized because most materials are essentially transparent to such photons. Since incoming X-ray photons are only slightly affected by the presence of a medium, the polarization directions of the fields inside a medium can be approximated as the polarization directions of the fields in vacuum. This is a common approximation used in dynamical diffraction theory.

If the index of refraction in the H channel is $\sqrt{1+2\varepsilon_H}$ where ε_H is a small complex number, then the quadratic term in the dispersion equation is $k_H^2 = (1+2\varepsilon_H)k_{0v}^2$ where k_{0v} is the vacuum wavenumber. The dispersion equation, Eq. 7-1.4, then reduces to the simpler form

$$2\varepsilon_H E_\alpha^H = \sum_{S\beta} g_{\alpha\beta}^{HS} E_\beta^S. \quad (7\text{-}3.1)$$

Making the further approximation that

$$k_H \approx (1+\varepsilon_H)k_{0v} \quad (7\text{-}3.2)$$

completes the linearization of the dispersion equations. This is shown for a two-beam (or two-channel) example in the following section.

7.4 Two-Beam Analytical Solution

In certain situations reasonably simple analytical expressions can be constructed for the scattered fields within a medium. This occurs for electronic scattering with a wise choice of the sigma and pi polarization vectors that diagonalize the scattering tensor. The multipole scattering tensor can also be diagonalized for certain orientations between the quantization axis of the scatterer and the scattering plane. For the two beam case where there are only two scattering channels, $S=0$ and $S=H$, along which travel a forward scattered and a diffracted electric field, the decoupled dispersion relations can be written in the form

$$\begin{pmatrix} \begin{matrix} (g_{xx}^{00}-2\varepsilon_0) & g_{xx}^{01} \\ g_{xx}^{10} & (g_{xx}^{11}-2\varepsilon_1) \end{matrix} & 0 \\ 0 & \begin{matrix} (g_{yy}^{00}-2\varepsilon_0) & g_{yy}^{01} \\ g_{yy}^{10} & (g_{yy}^{11}-2\varepsilon_1) \end{matrix} \end{pmatrix} \begin{pmatrix} T_x \\ R_x \\ T_y \\ R_y \end{pmatrix} = \mathbf{G}\cdot\mathbf{v}=0. \quad (7\text{-}4.1)$$

where

$$\mathbf{T}=\mathbf{E}^{S=0} \qquad (\text{transmitted field}) \qquad (7\text{-}4.2)$$

$$\mathbf{R}=\mathbf{E}^{S=H} \qquad (\text{diffracted, or reflected, field}). \qquad (7\text{-}4.3)$$

$H\equiv 1$, and x,y denote the two transverse polarizations of the electric field (in the sigma and pi polarization basis shown in Fig. 5-1.1, $x=\sigma$, and $y=\pi$).

To solve the dispersion equation, a relationship between ε_0 and ε_1 must be found. This can be done by noting that refraction occurs for a wave entering a medium from free space

$$\mathbf{k}_0=\mathbf{k}_{0v}+k_{0v}\delta\hat{\mathbf{n}} \qquad (7\text{-}4.4)$$

where $\mathbf{k}_{0v}$ is the vacuum wavevector in the forward direction (all vacuum quantities will have the index v), $\hat{\mathbf{n}}$ is an interior normal to the crystal surface, and δ is a quantity describing how much refraction has taken place.

Using Eqs. 7-3.2 and 7-4.4, to first order in δ and ε_0 (to linearize the dispersion equations), one finds that

$$\delta=\varepsilon_0/\gamma_0 \qquad (7\text{-}4.5)$$

where $$\gamma_0=\hat{\mathbf{k}}_{0v}\cdot\hat{\mathbf{n}}. \qquad (7\text{-}4.6)$$

Applying Bragg's law,

$$\mathbf{k}_1=\mathbf{k}_0+\mathbf{H}, \qquad (7\text{-}4.7)$$

yields, to first order in $\varepsilon_1, \varepsilon_0$,and δ,

$$k_{0v}^2(1+2\varepsilon_1) = k_{0v}^2(1+2\varepsilon_0) + H^2 + 2\left(\mathbf{k}_{0v} + k_{0v}\delta\hat{\mathbf{n}}\right)$$

which reduces to

$$\begin{aligned}\varepsilon_1 &= \varepsilon_0 + \frac{\mathbf{H}\cdot(\mathbf{H}+2\mathbf{k}_{0v})}{2k_{0v}^2} + \delta\left(\hat{\mathbf{k}}_1 - \hat{\mathbf{k}}_0\right)\cdot\hat{\mathbf{n}} \\ &\approx \alpha_B/2 + \varepsilon_0/b \end{aligned} \tag{7-4.8}$$

where α_B is a deviation from Bragg parameter

$$\alpha_B = \mathbf{H}\cdot(\mathbf{H}+2\mathbf{k}_{0v})/k_{0v}^2. \tag{7-4.9}$$

The parameter b is an asymmetry factor

$$b = \gamma_0/\gamma_1 \tag{7-4.10}$$

where
$$\gamma_1 = \hat{\mathbf{k}}_1\cdot\hat{\mathbf{n}}. \tag{7-4.11}$$

The α_B parameter describes how close a reciprocal lattice point must be to the Ewald sphere in order to still satisfy the Bragg condition. The parameter can be evaluated by examining how Bragg's law varies near the Ewald sphere

$$\begin{aligned} H &= \left|\mathbf{k}_1 - \mathbf{k}_0\right| = \sqrt{k_1^2 + k_0^2 - 2k_1k_0\cos 2\theta_B} \\ &\approx 2k_{0v}\sin\theta_B\left(1+\frac{\varepsilon_1+\varepsilon_0}{2}\right) \end{aligned} \tag{7-4.12}$$

where $2\theta_B$ is the scattering angle between $\mathbf{k}_1$ and $\mathbf{k}_0$, and θ_B is the Bragg angle. Also note that

$$\mathbf{H}\cdot\mathbf{k}_{0v} = -Hk_{0v}\sin\theta_0 \tag{7-4.13}$$

where $\theta_0 + \pi/2$ is the angle between $\mathbf{H}$ and $\mathbf{k}_{0v}$ (see Fig. 7-4.1). When the Bragg condition is satisfied, θ_0 is nearly equal to θ_B. Defining a deviation angle

$$\Delta\theta = \theta_0 - \theta_B \tag{7-4.14}$$

that is a measure of the angular deviation from Bragg gives

$$\alpha_B = -2\Delta\theta\sin 2\theta_B - 4(\Delta E/E)\sin^2\theta_B \tag{7-4.15}$$

where E is the incoming photon energy, and ΔE is the deviation of the Bragg energy from the incoming photon energy

$$\Delta E = E - E_B = \hbar c\left[k_{0v} - (k_1 + k_0)/2\right]. \tag{7-4.16}$$

The Bragg energy has been defined to be proportional to the average wavenumber inside the medium. To remain close to the Bragg condition, either an angular or energy constraint must be satisfied: $\Delta\theta$ or ΔE must be close to zero. For instance, when examining the angular spectrum of a scattered field, the Bragg energy is set equal to the incoming photon

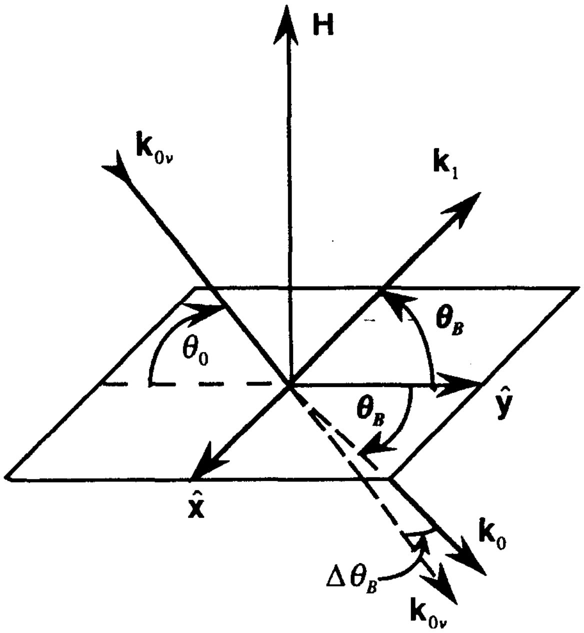

Fig. 7-4.1. Diffraction from crystal planes. The xy-plane is the crystal surface, and $\mathbf{H}$ is a reciprocal lattice vector perpendicular to the crystal planes. Present geometry shows a symmetric Bragg reflection ($b = -1$). Incoming beam from vacuum, $\mathbf{k}_{0v}$, strikes the surface, and refraction produces outgoing beam, $\mathbf{k}_0$, shifted by $\Delta\theta_B$ from the incident angle θ_0.

energy, $E_B = E$ or $\Delta E = 0$, and the Bragg angle is obtained through Bragg's law and $\alpha_B = -2\Delta\theta \sin 2\theta_B$. When examining the energy spectrum of a scattered field, the Bragg angle is set equal to the incoming photon angle, $\theta_B = \theta_0$ or $\Delta\theta = 0$, and the Bragg energy is obtained from Bragg's law and $\alpha_B = -4(\Delta E/E)\sin^2\theta_B$. Bragg's law, Eq. 7-4.7, can be rewritten as the following expression:

$$E_B \sin\theta_B = \hbar c H/2 \tag{7-4.17}$$

where

$$H = 2\pi/d_{hkl}, \tag{7-4.18}$$

and d_{hkl} is the lattice spacing of the $[h\,k\,l]$ reflection.

The solution to Eq. 7-4.1 then reduces to solving a familiar eigenvalue-eigenvector problem. The characteristic equation is

$$\det(\mathbf{G}_{lin} - 2\varepsilon_0 \mathbf{I}) = 0 \tag{7-4.19}$$

where

$$\mathbf{G}_{lin} = \begin{pmatrix} g^{00}_{xx} & g^{01}_{xx} & \multicolumn{2}{c}{0} \\ g^{10}_{xx} & (bg^{11}_{xx} - b\alpha_B) & & \\ & & g^{00}_{yy} & g^{01}_{yy} \\ \multicolumn{2}{c}{0} & g^{10}_{yy} & (bg^{11}_{yy} - b\alpha_B) \end{pmatrix}. \tag{7-4.20}$$

The solution to the characteristic equation yields the four eigenvalues

$$\varepsilon^{(1,2)}_{0\beta} = \frac{1}{4}\left(g^{00}_{\beta\beta} + bg^{11}_{\beta\beta} - b\alpha_B\right) \pm \frac{1}{4}\sqrt{\left(g^{00}_{\beta\beta} - bg^{11}_{\beta\beta} + b\alpha_B\right)^2 + 4bg^{01}_{\beta\beta}g^{10}_{\beta\beta}} \tag{7-4.21}$$

where $\beta = x, y$.

To complete the solution to the inhomogeneous wave equation, boundary conditions must be supplied. In order to obtain analytical expressions to the reflected and transmitted fields, interfacial reflections at the entrant and exit crystal surfaces will be neglected. These reflections occur when a field crosses from one medium to another (such as from vacuum to the crystal medium). The Bragg and Laue solutions are given below using this approximation.

BRAGG CASE: At the top and bottom surfaces of the crystal (see Fig. 7-4.2), the boundary conditions are

$$\hat{\mathbf{n}}\cdot\mathbf{r} = 0: \qquad \mathbf{E}_{0v} = \mathbf{T} = \sum_{l=1}^{2}\sum_{\alpha} T^l_\alpha \hat{\boldsymbol{\varepsilon}}^0_\alpha \tag{7-4.22}$$

$$\hat{\mathbf{n}}\cdot\mathbf{r} = d: \qquad 0 = \mathbf{R} = e^{i(\mathbf{k}_{0v}+\mathbf{H})\cdot\mathbf{r}} \sum_{l=1}^{2}\sum_{\alpha} R^l_\alpha e^{i\kappa^l_\alpha d} \hat{\boldsymbol{\varepsilon}}^H_\alpha \tag{7-4.23}$$

where

$$\mathbf{k}_0 = \mathbf{k}_{0v} + \kappa^l_\alpha \hat{\mathbf{n}} \tag{7-4.24}$$

$$\mathbf{k}_H \equiv \mathbf{k}_1 = \mathbf{k}_0 + \mathbf{H} \tag{7-4.25}$$

$$\kappa^l_\alpha = k_{0v}\varepsilon^l_{0\alpha}/\gamma_0 \tag{7-4.26}$$

$\alpha = x, y$, $l = 1, 2$ is the eigenvector index, and $\mathbf{E}_{0v}$ is the incoming electric field from the vacuum. For Bragg diffraction and for no interfacial reflections, all of the incoming field scatters into the transmission channel, and, at the exit surface there is no incoming field scattering into the reflection channel.

For each eigenvalue in Eq. 7-4.21, there is a unique eigenvector

$$\mathbf{v}^l_\alpha = \begin{pmatrix} T^l_\alpha \\ R^l_\alpha \end{pmatrix}. \tag{7-4.27}$$

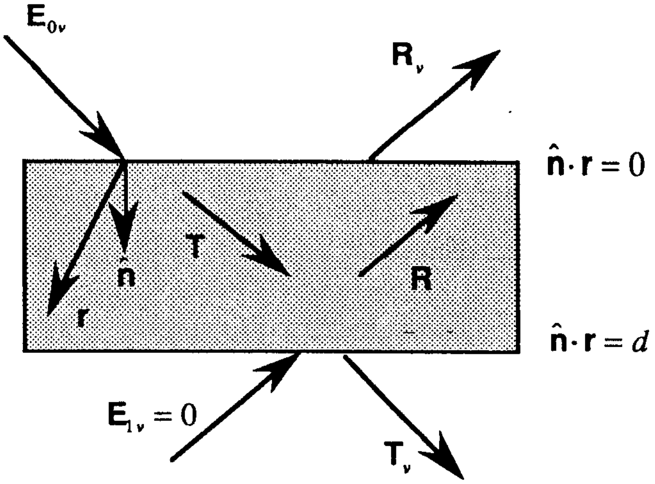

Fig. 7-4.2. Bragg diffraction geometry.

The reflection amplitudes can then be expressed in terms of the transmission amplitudes

$$R_\alpha^l = D_\alpha^l T_\alpha^l \tag{7-4.28}$$

where

$$D_\alpha^l = \left(v_\alpha^l\right)_2 / \left(v_\alpha^l\right)_1, \tag{7-4.29}$$

and $\left(v_\alpha^l\right)_i$ is the i^{th} component of $\mathbf{v}_\alpha^l$. Expressing the reflection amplitudes in terms of the transmission amplitudes enables one to solve a decoupled boundary value equation for the four transmission and four reflected wavefields inside the crystal

$$\mathbf{u}_{in} = \mathbf{B}_c \cdot \mathbf{w} \tag{7-4.30}$$

or, written out explicitly,

$$\begin{pmatrix} E_{0\nu x} \\ 0 \\ E_{0\nu y} \\ 0 \end{pmatrix} = \begin{pmatrix} \begin{matrix} 1 & 1 \\ D_x^1 e^{i\kappa_x^1 d} & D_x^2 e^{i\kappa_x^2 d} \end{matrix} & \huge 0 \\ \huge 0 & \begin{matrix} 1 & 1 \\ D_y^1 e^{i\kappa_y^1 d} & D_y^2 e^{i\kappa_y^2 d} \end{matrix} \end{pmatrix} \begin{pmatrix} T_x^1 \\ T_x^2 \\ T_y^1 \\ T_y^2 \end{pmatrix}. \tag{7-4.31}$$

After some algebra, the solution to the boundary condition equation can be written in the form

$$\begin{aligned} \mathbf{T}\left(\hat{\mathbf{n}}\cdot\mathbf{r}=z\right) &= e^{i\mathbf{k}_{0\nu}\cdot\mathbf{r}} \sum_{l=1}^{2} \sum_{\alpha} T_\alpha^l e^{i\kappa_\alpha^l z} \hat{\boldsymbol{\varepsilon}}_\alpha^0 \\ &= e^{i\mathbf{k}_{0\nu}\cdot\mathbf{r}} \sum_{\alpha} E_{0\nu\alpha} \hat{\boldsymbol{\varepsilon}}_\alpha^0 \frac{e^{i\left(\kappa_\alpha^1 z + \kappa_\alpha^2 d\right)}\left(g_{\alpha\alpha}^{00} - 2\varepsilon_{0\alpha}^2\right) - e^{i\left(\kappa_\alpha^2 z + \kappa_\alpha^1 d\right)}\left(g_{\alpha\alpha}^{00} - 2\varepsilon_{0\alpha}^1\right)}{e^{i\kappa_\alpha^2 d}\left(g_{\alpha\alpha}^{00} - 2\varepsilon_{0\alpha}^2\right) - e^{i\kappa_\alpha^1 d}\left(g_{\alpha\alpha}^{00} - 2\varepsilon_{0\alpha}^1\right)}, \end{aligned} \tag{7-4.32}$$

and, at the exit surface $z = d$,

$$\mathbf{T}(\hat{\mathbf{n}}\cdot\mathbf{r} = d) = e^{i\mathbf{k}_{0v}\cdot\mathbf{r}} \sum_{\alpha} E_{0v\alpha} \hat{\boldsymbol{\varepsilon}}_{\alpha}^{0} \frac{e^{i(\kappa_{\alpha}^{2}+\kappa_{\alpha}^{1})d}\left(2\varepsilon_{0\alpha}^{1} - 2\varepsilon_{0\alpha}^{2}\right)}{e^{i\kappa_{\alpha}^{2}d}\left(g_{\alpha\alpha}^{00} - 2\varepsilon_{0\alpha}^{2}\right) - e^{i\kappa_{\alpha}^{1}d}\left(g_{\alpha\alpha}^{00} - 2\varepsilon_{0\alpha}^{1}\right)}. \tag{7-4.33}$$

The reflection channel field is

$$\begin{aligned}\mathbf{R}(\hat{\mathbf{n}}\cdot\mathbf{r} = z) &= e^{i(\mathbf{k}_{0v}+\mathbf{H})\cdot\mathbf{r}} \sum_{l=1}^{2} \sum_{\alpha} D_{\alpha}^{l} T_{\alpha}^{l} e^{i\kappa_{\alpha}^{l} z} \hat{\boldsymbol{\varepsilon}}_{\alpha}^{H} \\ &= e^{i(\mathbf{k}_{0v}+\mathbf{H})\cdot\mathbf{r}} \sum_{\alpha} E_{0v\alpha} \hat{\boldsymbol{\varepsilon}}_{\alpha}^{H} \frac{b g_{\alpha\alpha}^{10}\left(e^{i(\kappa_{\alpha}^{2}d+\kappa_{\alpha}^{1}z)} - e^{i(\kappa_{\alpha}^{1}d+\kappa_{\alpha}^{2}z)}\right)}{e^{i\kappa_{\alpha}^{2}d}\left(g_{\alpha\alpha}^{00} - 2\varepsilon_{0\alpha}^{2}\right) - e^{i\kappa_{\alpha}^{1}d}\left(g_{\alpha\alpha}^{00} - 2\varepsilon_{0\alpha}^{1}\right)},\end{aligned} \tag{7-4.34}$$

and, at the entrant surface $z = 0$,

$$\mathbf{R}(\hat{\mathbf{n}}\cdot\mathbf{r} = 0) = e^{i(\mathbf{k}_{0v}+\mathbf{H})\cdot\mathbf{r}} \sum_{\alpha} E_{0v\alpha} \hat{\boldsymbol{\varepsilon}}_{\alpha}^{H} \frac{b g_{\alpha\alpha}^{10}\left(e^{i\kappa_{\alpha}^{2}d} - e^{i\kappa_{\alpha}^{1}d}\right)}{e^{i\kappa_{\alpha}^{2}d}\left(g_{\alpha\alpha}^{00} - 2\varepsilon_{0\alpha}^{2}\right) - e^{i\kappa_{\alpha}^{1}d}\left(g_{\alpha\alpha}^{00} - 2\varepsilon_{0\alpha}^{1}\right)}. \tag{7-4.35}$$

LAUE CASE: The boundary conditions for this case are (see Fig. 7-4.3)

$$\hat{\mathbf{n}}\cdot\mathbf{r} = 0: \qquad \mathbf{E}_{0v} = \mathbf{T} = \sum_{l=1}^{2} \sum_{\alpha} T_{\alpha}^{l} \hat{\boldsymbol{\varepsilon}}_{\alpha}^{0} \tag{7-4.36}$$

$$\hat{\mathbf{n}}\cdot\mathbf{r} = 0: \qquad 0 = \mathbf{R} = \sum_{l=1}^{2} \sum_{\alpha} R_{\alpha}^{l} \hat{\boldsymbol{\varepsilon}}_{\alpha}^{H}. \tag{7-4.37}$$

For Laue diffraction and for no interfacial reflections, all of the incoming field scatters into the transmission channel, and, at the entrant surface, there is no incoming field scattering into the reflection channel.

The boundary condition matrix for Laue diffraction is

$$\mathbf{B}_{c} = \begin{pmatrix} \begin{matrix} 1 & 1 \\ D_{x}^{1} & D_{x}^{2} \end{matrix} & \mathbf{0} \\ \mathbf{0} & \begin{matrix} 1 & 1 \\ D_{y}^{1} & D_{y}^{2} \end{matrix} \end{pmatrix}. \tag{7-4.38}$$

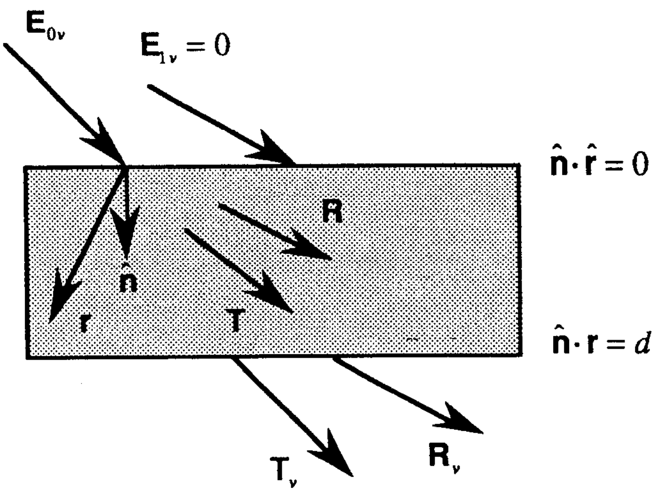

Fig. 7-4.3. Laue diffraction geometry.

Solving the boundary condition equation for the scattering channel field yields

$$\mathbf{T}(\hat{\mathbf{n}}\cdot\mathbf{r}=z)=e^{i\mathbf{k}_{0\nu}\cdot\mathbf{r}}\sum_{\alpha}E_{0\nu\alpha}\hat{\boldsymbol{\varepsilon}}_{\alpha}^{0}\frac{e^{i\kappa_{\alpha}^{1}z}\left(g_{\alpha\alpha}^{00}-2\varepsilon_{0\alpha}^{2}\right)-e^{i\kappa_{\alpha}^{2}z}\left(g_{\alpha\alpha}^{00}-2\varepsilon_{0\alpha}^{1}\right)}{\left(2\varepsilon_{0\alpha}^{1}-2\varepsilon_{0\alpha}^{2}\right)} \qquad (7\text{-}4.40)$$

$$\mathbf{R}(\hat{\mathbf{n}}\cdot\mathbf{r}=z)=e^{i(\mathbf{k}_{0\nu}+\mathbf{H})\cdot\mathbf{r}}\sum_{\alpha}E_{0\nu\alpha}\hat{\boldsymbol{\varepsilon}}_{\alpha}^{H}\frac{bg_{\alpha\alpha}^{10}\left(e^{i\kappa_{\alpha}^{2}z}-e^{i\kappa_{\alpha}^{1}z}\right)}{\left(2\varepsilon_{0\alpha}^{1}-2\varepsilon_{0\alpha}^{2}\right)}. \qquad (7\text{-}4.41)$$

7.5 Dynamical Characteristics of Angular Spectra

In kinematical diffraction theory the angular distribution of the scattered fields consists of delta function peaks situated at Bragg angles. In dynamical diffraction theory the angular width of the Bragg peaks are broadened due to multiple scattering. The angular distribution at a Bragg peak can be characterized by an η'_α parameter (or a y_α parameter described by Zachariasen)[3, 4]

$$\eta'_{\alpha}=\frac{[(1-b)/2]\operatorname{Re}\{g_{\alpha\alpha}^{00}\}+(b/2)\alpha_{B}}{\sqrt{|b|}\left|\operatorname{Re}\{g_{\alpha\alpha}^{10}\}\right|}. \qquad (7\text{-}5.1)$$

The above formula assumes that the scatterers in the crystal have space-inversion symmetry and that the origin is chosen at an inversion center (that is, the crystal is centrosymmetric and $g_{\alpha\alpha}^{10} = g_{\alpha\alpha}^{01}$). Also, forward scattering in the transmission channel is assumed to be identical to forward scattering in the reflection channel: $g_{\alpha\alpha}^{00} = g_{\alpha\alpha}^{11}$. For thick crystals most of the scattered intensity lies in the range $|\eta'_\alpha| < 1$ (see Figs. 7-5.1 and 7-5.2). Thus, an angular width, or Darwin width, of the diffracted beam can be defined as

$$\Delta\theta_D^\alpha = \frac{2\left|\mathrm{Re}\{g_{\alpha\alpha}^{10}\}\right|}{\sqrt{|b|}\sin 2\theta_B} = \frac{\Delta\theta_{Ds}^\alpha}{\sqrt{|b|}} \tag{7-5.2}$$

where $\Delta\theta_{Ds}^\alpha$ is the symmetric Darwin width for a thick crystal (this definition is useful mainly for Bragg diffraction as can be seen by examining Figs. 7-5.1 and 7-5.2). From Eq. 7-5.1 note that, for Bragg diffraction, the Darwin curve is not centered at the Bragg angle. There is an index of refraction shift from the Bragg angle where the center of the Darwin curve (the point $\eta'_\alpha = 0$) now lies at

$$\theta_c^\alpha = \theta_B + \frac{[(1-b)/2]\mathrm{Re}\{g_{\alpha\alpha}^{00}\}}{b\sin 2\theta_B}. \tag{7-5.3}$$

The electric field inside the crystal consists of traveling waves propagating perpendicular to the scattering vector, **H**, and standing waves with wavectors parallel to the scattering vector. Whether a standing wave field has its nodes or antinodes at the scattering planes depends upon the scattering angle and, thus, upon the η'_α parameter. When a standing wave has its antinodes lying at the scattering planes (that is, on the atoms) enhanced absorption occurs, and when it has its nodes lying at the scattering planes absorption processes are suppressed.

From the solution of the dispersion equation there turns out to be, for each scattering channel and for each polarization, two eigenwaves that are a function of the energy of the incident field and the deviation from Bragg, α_B (the two eigenwaves corresponds to the $l = 1$ and 2 solutions having eigenvalues given by Eq. 7-4.21). For Laue diffraction the two eigenwaves are damped exponentially with distance into the crystal. One wave has its nodes lying at the scattering planes (the alpha wave) and the other has its antinodes lying at the scattering planes (the beta wave).[4] Since the beta waves suffer enhanced absorption, these fields die out more quickly leaving only the alpha waves to contribute to the total field amplitude that exits a thick crystal. Since the alpha waves experience suppressed absorption, these fields can travel much further through crystals than would be expected when only photoelectric or resonant absorption is considered. This phenomena is the Borrmann effect--anomalous transmission through crystals.

For Bragg diffraction one eigenwave is damped exponentially while the other grows exponentially with distance inside the crystal. For photoelectric scattering they both have their nodes lying at the scattering planes when $\eta'_\alpha = -1$ and their antinodes lying at the scattering planes when $\eta'_\alpha = +1$.[1, 3, 4] Thus, as η'_α varies from -1 to $+1$, the electric field experiences suppressed absorption to enhanced absorption--this is the reason for the asymmetrical shape of the Darwin curve in Fig. 7-5.1. For resonant scattering the phase of the eigenwaves changes by π as the resonance curve is traversed from frequencies above the resonant frequency to those below the resonant frequency. Thus, the η'_α points where suppressed and enhanced absorption occur are at opposite sides of the Darwin curve when operating on opposite sides of the resonant curve--this is shown in Fig 7-5.3. As the absorption in the forward channel, $\mathrm{Im}\{g^{00}_{\alpha\alpha}\}$, becomes more predominant than the effective absorption resulting from scattering from the transmission to the reflection channel, $\mathrm{Im}\{g^{10}_{\alpha\alpha}\}$, the peak intensity shifts from $\eta'_\alpha = -1$ to $\eta'_\alpha = 0$, and the Darwin curve becomes more symmetrical. Since in general $\mathrm{Im}\{g^{00}_{\alpha\alpha}\} > \mathrm{Im}\{g^{10}_{\alpha\alpha}\}$, there is always a shift in the peak intensity towards $\eta'_\alpha = 0$.

The Borrmann effect is of particular interest in resonant scattering because absorption processes are always present and are usually predominant. For instance, for an isolated ^{57}Fe atom, internal conversion prevents the efficiency of photon production for a scattering event from being greater that 11%. However, by scattering off a lattice of ^{57}Fe atoms, the efficiency can be made much greater than 11% through the Borrmann effect.[12]

The figures below are rocking curves for pi polarized 14.4 keV radiation diffracting from a body centered cubic crystal of $\alpha-{}^{56}\mathrm{Fe}{}^{57}\mathrm{Fe}$ having a lattice spacing of 5 Å. There is one ^{56}Fe and ^{57}Fe atom per unit cell, and the ^{57}Fe atom lies at the center. No such iron crystal has yet been fabricated, but such a structure lets one examine resonant scattering by partially turning off the nonresonant photoelectric scattering. For instance, resonant nuclear diffraction is allowed for any combination of Miller indices that satisfies Bragg's law, but when the sum of the Miller indices is odd ($h+k+l=2n+1,\ n=0,1,2,\ldots$) photoelelectric diffraction is forbidden. For simplicity the resonant ^{57}Fe nuclei are assumed to have no internal hyperfine fields--they are therefore single line emitters (An iron crystal is inherently magnetic, but by adding impurities, such as was done for stainless steel or for YIG,[13] the internal fields can be suppressed. α - Fe naturally has a bcc crystal structure with a lattice spacing of 2.8665 Å. The lattice spacing of 5 Å is used as an attempt at approximating the larger unit cell constructed when impurities are added to produce a single line emitter.). Also, all Debye-Waller factors, Lamb-Mössbauer factors, and resonant enrichment factors have been set to unity.

Figures 7-5.1 and 7-5.2 are photoelectric rocking curves for the allowed $[0\ 0\ 2]$ reflection and for various thicknesses. Resonant nuclear scattering, though also allowed, is ignored in the calculations. In Fig. 7-5.1 the oscillations, or Pendellösung fringes, for the $10\mu m$ thick crystal are caused by the interference of the two eigenwaves traveling in the reflection channel. For $d = 1cm$ one of the eigenwaves has completely died off exponentially with distance which eliminates the possibility for interference between the eigenwaves to occur at the exit surface.

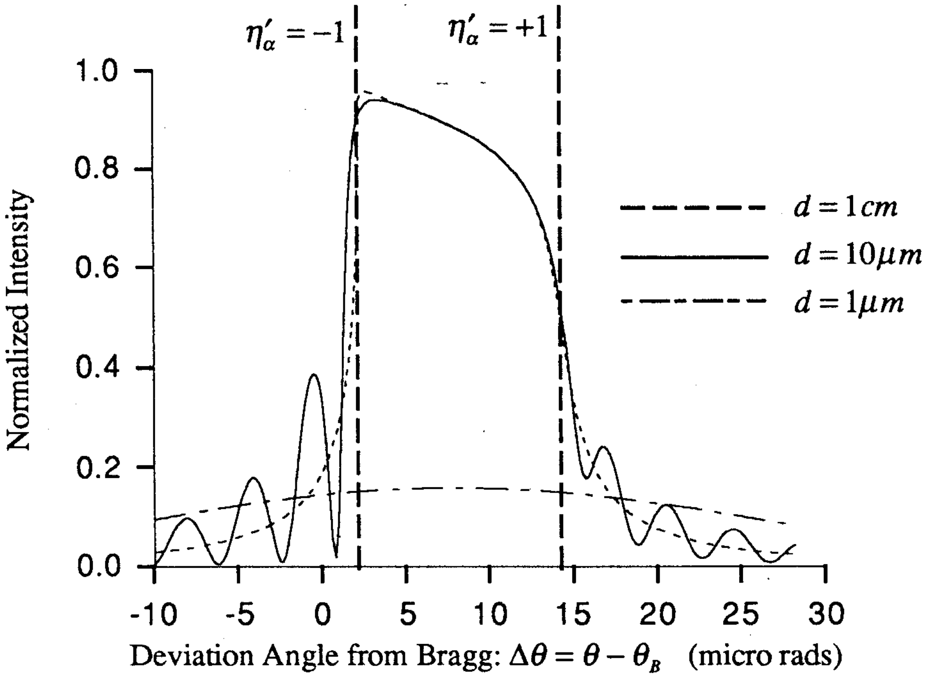

Fig. 7-5.1. Bragg diffraction rocking curves for $[0\,0\,2]$ reflection for various thicknesses. Only photoelectric scattering is being considered --resonant nuclear scattering is being ignored.

For Bragg diffraction the primary extinction length, or crystal penetration depth through which most of the transmission channel fields are reflected out of the crystal, can be approximated from Bragg's law, Eq. 7-4.17, as

$$d_{ext} = \frac{2\pi}{\Delta H} = \frac{2\pi}{H} \frac{\tan\theta_B}{\Delta\theta_w} \tag{7-5.4}$$

where $\Delta\theta_w$ is the angular width of the Darwin curve (full width at half maximum). This expression describes how much of a crystal is involved in diffraction by how far a reciprocal lattice point can be from the Ewald sphere before Bragg's law is seriously violated. For the crystal considered in this example, the Bragg angle for the $[0\,0\,2]$ reflection is 9.9° for 14.4 keV photons, and $2\pi/H = 5\text{Å}/2$. For $d = 1\text{cm}$ the Darwin width is $12\mu\text{rad}$, and thus $d_{ext} \approx 3.6\mu\text{m}$ and the crystal is several thousand extinction lengths thick. When $d = 10\mu\text{m}$ a far less number of planes contribute toward diffraction, thus the angular width is slightly broader than for the 1cm thick crystal. The extinction length is now approximately $3.3\mu m$, and the fields penetrate a far greater fraction of the crystal thickness. When $d = 1\mu m$, the Darwin width is $41\mu rad$ and the fields penetrate the entire thickness of the crystal: $d_{ext} \approx 1\mu m$.

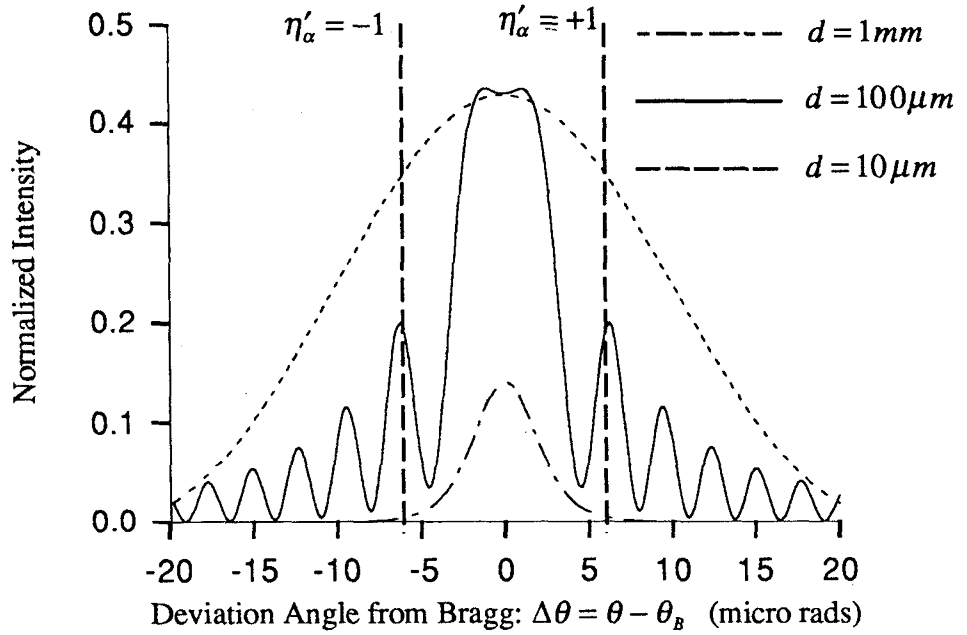

Fig. 7-5.2. Laue diffraction rocking curves for $[0\,0\,2]$ reflection for various thicknesses. Only photoelectric scattering is being considered--resonant nuclear scattering is being ignored.

The photoelectric absorption length for this crystal is roughly $0.5\mu m$. Thus, the Borrmann effect is readily seen in the Laue diffraction rocking curves in Fig. 7-5.2. When the crystal is $10\mu m$, or 20 absorption lengths thick, the transmitted intensity peaks at 40% whereas a value 9 orders of magnitude less would be expected if only photoelectric absorption was considered.

For pure resonant scattering when $\omega - \omega_0 = 0$, the Darwin width goes to zero since the scattering tensor becomes pure imaginary. The Borrmann effect persists at the center of the profile because the nodes of the fields inside the crystal lie at the scattering planes. Increasing the crystal thickness so that more planes contribute to reflecting the field out of the crystal pushes the peak reflectivity closer to unity. This effect is commonly referred to as the suppression of the inelastic channel.[9] Because the effective transmission absorption length is roughly 600 Å when the incoming field is on resonance, the transmitted field is quite negligible for the $10\mu m$ thick crystal used in Figs. 7-5.3 and 7-5.4.

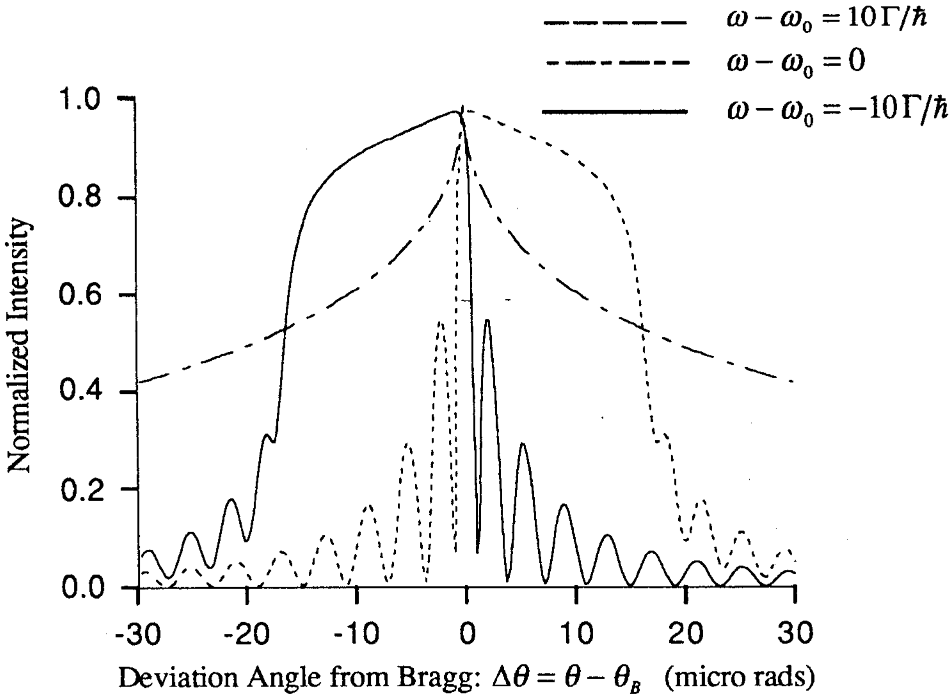

Fig. 7-5.3. Bragg diffraction rocking curves for $[0\ 0\ 1]$ reflection for various positions on the resonance curve. Only resonant nuclear scattering is being considered--photoelectric scattering is being ignored. Crystal thickness is $10\mu m$.

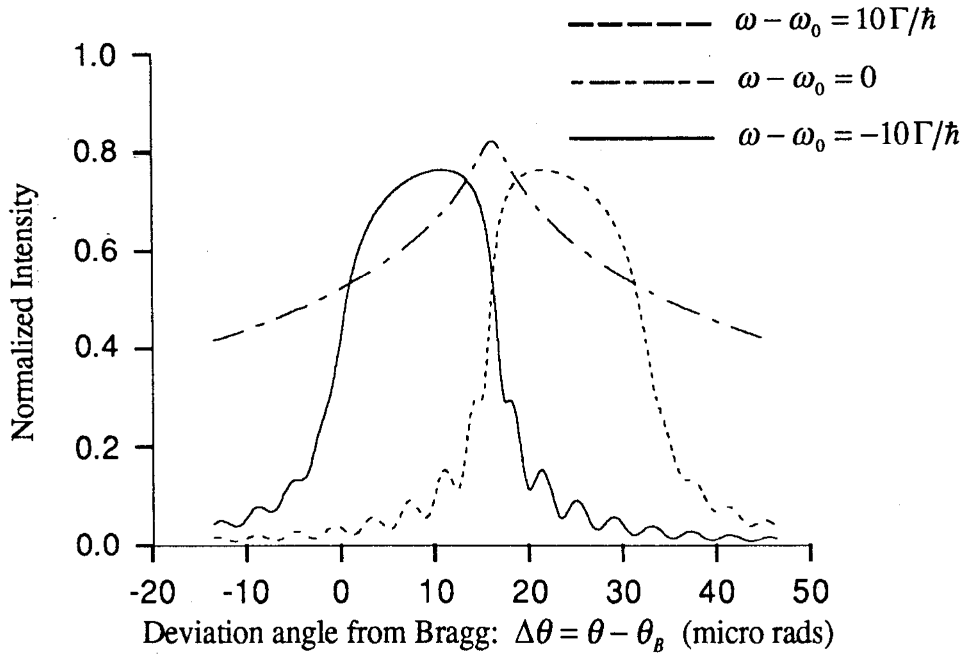

Fig. 7-5.4. Bragg diffraction rocking curves for $[0\ 0\ 1]$ reflection for various positions on the resonance curve. Both resonant nuclear and photoelectric scattering is considered. Crystal thickness is $10\mu m$. The point $\Delta\theta \approx 16\mu rad$ occurs at $\eta'_\alpha = \pm 1{,}0$ for the central curve (this is where the central curve peaks), at $\eta'_\alpha = -1$ for the curve on the right, and at $\eta'_\alpha = +1$ for the curve on the left.

7.6 Dynamical Characteristics of Energy Spectra

The expressions for the transmission and reflection channel fields are too complicated in their present form to see the dynamical effects of frequency shifts and speedup rates resulting from multiple scattering. Also, since there are now two eigenwaves traveling in a particular channel, ascribing a single frequency shift or speedup rate to an exiting field is no longer generally possible. However, in certain limiting cases in which only one predominant eigenwave manages to exit the crystal, one can easily examine the dynamical effects of multiple scattering. These limiting cases are described below.

CASE 1: Far Off Bragg.

When the direction of the incoming field is set to be far from any Bragg angle,

$$\alpha_B >> \left|g_{\alpha\alpha}^{00}\right| \text{ and } \left|g_{\alpha\alpha}^{10}\right|, \tag{7-6.1}$$

the eigenvalues reduce to

$$\varepsilon_{0\beta}^{(1,2)} = \frac{1}{4}\left[g_{\beta\beta}^{00}(1+b) - b\alpha_B\right] \pm \frac{1}{4}\left[\left|b\alpha_B\right| - g_{\beta\beta}^{00}(1-b)\frac{\left|b\alpha_B\right|}{b\alpha_B}\right] \tag{7-6.2}$$

for Bragg ($b<0$) and Laue ($b>0$) diffraction. For both Bragg and Laue diffraction, the reflection channel field is negligible, $\mathbf{R}(\omega)\approx 0$, since it falls off as $g_{\beta\beta}^{10}/\alpha_B$ while the transmission channel field reduces to

$$\mathbf{T}(\omega) = e^{i\mathbf{k}_{0\nu}\cdot\mathbf{r}}\sum_{\alpha} E_{0\nu\alpha}(\omega)\hat{\boldsymbol{\varepsilon}}_{\alpha}^{0} e^{i\left[g_{\alpha\alpha}^{00}(\omega)/2\right]k_{0\nu}L} \tag{7-6.3}$$

where

$$L = d/\gamma_0\,. \tag{7-6.4}$$

For combined resonant dipole and nonresonant scattering, the scattering tensor element for forward scattering is (from Eqs. 5-1.48 and 7-1.5)

$$g_{\alpha\alpha}^{00}(\omega)/2 = \frac{2\pi}{k_{0\nu}^{2}}nF\left(\mathbf{k}_f=\mathbf{k}_i\right) + \mu^{00}(\omega)/2k_{0\nu}\,. \tag{7-6.5}$$

The Lamb-Mössbauer and resonant enrichment factors have been included in the scattering amplitude, and $\mu^{00}(\omega)/k_{0\nu} = \left[g_{\alpha\alpha}^{00}(\omega)\right]_{nonres}$ is given by Eqs 7-2.1 and 7-2.2 for photoelectric scattering

$$\mu^{00}(\omega) = -\left(\frac{4\pi}{k_{0\nu}}\right)nr_e\left[D_W(0)f_0 + f'(\omega) - if''(\omega)\right] \tag{7-6.6}$$

(the imaginary part of $\mu^{00}(\omega)$ is the absorption coefficient). For the simple two-beam solution in Section 7.4, the expressions on the right side of Eq. 7-6.5 are independent of polarization since they describe forward scattering. Equation 7-6.3 is precisely the same solution as that obtained for the transmitted field from an isotropic medium in Section 6.5. The dynamical effects explored in that section then also apply equally well for this off-Bragg case.

CASE 2: Thin Crystal Approximation.

For the thin crystal approximation

$$k_{0v}\varepsilon_{0\beta}^{l}d/\gamma_0 << 1. \tag{7-6.7}$$

In this approximation, the transmission channel-fields for both Bragg and Laue diffraction are almost unity. Using the approximation $e^x \approx 1+x$ for $|x| << 1$ gives

$$\mathbf{T}_{Bragg}(\omega) = e^{i\mathbf{k}_{0v}\cdot\mathbf{r}}\sum_{\alpha} E_{0v\alpha}(\omega)\hat{\boldsymbol{\varepsilon}}_{\alpha}^{0}\frac{1+ik_{0v}L\left[g_{\alpha\alpha}^{00}(1+b)-b\alpha_B\right]/2}{1+ik_{0v}L\left(bg_{\alpha\alpha}^{00}-b\alpha_B\right)/2} \tag{7-6.8}$$

$$\mathbf{T}_{Laue}(\omega) = e^{i\mathbf{k}_{0v}\cdot\mathbf{r}}\sum_{\alpha} E_{0v\alpha}(\omega)\hat{\boldsymbol{\varepsilon}}_{\alpha}^{0}\left[1+ik_{0v}L\left(g_{\alpha\alpha}^{00}/2\right)\right]. \tag{7-6.9}$$

The solution for Laue transmission is equivalent to Case 1 (being far off Bragg) for a thin crystal, or equivalent to transmission through a thin isotropic slab. For combined resonant dipole and nonresonant scattering

$$\mathbf{T}_{Laue}(\omega) = e^{i\mathbf{k}_{0v}\cdot\mathbf{r}}\sum_{\alpha} E_{0v\alpha}(\omega)\hat{\boldsymbol{\varepsilon}}_{\alpha}^{0}\left[1-\frac{i\Gamma_s^{00}/4\hbar}{\omega-\omega_0+i\Gamma/2\hbar}+i\mu^{00}(\omega)L/2\right] \tag{7-6.10}$$

where, similar to the expression in Eq. 6-5.16 in section 6.5,

$$\Gamma_s^{00} = L_M(\mathbf{k}_i)L_M(\mathbf{k}_f=\mathbf{k}_i)Cn\sigma_0\Gamma L \tag{7-6.11}$$

and $L = d/\gamma_0$. Thus, for a thin crystal, Laue transmission channel fields exhibit no frequency shifts or decay rate speedups.

For Bragg scattering the transmission channel field is

$$\mathbf{T}_{Bragg}(\omega) = e^{i\mathbf{k}_{0v}\cdot\mathbf{r}}\sum_{\alpha} E_{0v\alpha}(\omega)\hat{\boldsymbol{\varepsilon}}_{\alpha}^{0}\left[\xi+\frac{ia[\xi b-(1+b)]}{\omega-\omega_0+i\Gamma/2\hbar-iab}\right] \tag{7-6.12}$$

where

$$a = \frac{\Gamma_s^{00}/4\hbar}{1+ib\mu^{00}(\omega)L/2-ib\alpha_B k_{0v}L/2} \tag{7-6.13}$$

and

$$\xi = \frac{1+i(1+b)\mu^{00}(\omega)L/2-ib\alpha_B k_{0v}L/2}{1+ib\mu^{00}(\omega)L/2-ib\alpha_B k_{0v}L/2}. \tag{7-6.14}$$

Since $\xi \approx 1$ in the thin crystal approximation, the transmitted field can be simplified to

$$\mathbf{T}_{Bragg}(\omega) = e^{i\mathbf{k}_{0\nu}\cdot\mathbf{r}} \sum_{\alpha} E_{0\nu\alpha}(\omega)\hat{\boldsymbol{\varepsilon}}_{\alpha}^{0}\left[1 - \frac{(\omega_s - i\Gamma_s/2\hbar)/b}{\omega - (\omega_0 + \omega_s) + i(\Gamma + \Gamma_s)/2\hbar}\right] \tag{7-6.15}$$

where
$$\omega_s = \mathrm{Re}\left\{\frac{ib(\Gamma_s^{00}/4\hbar)}{1 + ib\mu^{00}(\omega)L/2 - ib\alpha_B k_{0\nu}L/2}\right\}$$

$$= \frac{b(\Gamma_s^{00}/4\hbar)\left(\mathrm{Re}\{b\mu^{00}(\omega)\}L/2 - b\alpha_B k_{0\nu}L/2\right)}{\left(1 - \mathrm{Im}\{b\mu^{00}(\omega)\}L/2\right)^2 + \left(\mathrm{Re}\{b\mu^{00}(\omega)\}L/2 - b\alpha_B k_{0\nu}L/2\right)^2} \tag{7-6.16}$$

and
$$\Gamma_s = -\mathrm{Im}\left\{\frac{ib(\Gamma_s^{00}/2)}{1 + ib\mu^{00}(\omega)L/2 - ib\alpha_B k_{0\nu}L/2}\right\}$$

$$= \frac{-b(\Gamma_s^{00}/2)\left(1 - \mathrm{Im}\{b\mu^{00}(\omega)\}L/2\right)}{\left(1 - \mathrm{Im}\{b\mu^{00}(\omega)\}L/2\right)^2 + \left(\mathrm{Re}\{b\mu^{00}(\omega)\}L/2 - b\alpha_B k_{0\nu}L/2\right)^2}. \tag{7-6.17}$$

The second term in the brackets of Eq. 7-6.15 exhibits, in contrast to the transmitted field through an isotropic thin slab, a frequency shift, ω_s, and a speedup rate, Γ_s. However, since ω_s is proportional to the square of the crystal thickness, it is an exceedingly small quantity. The speedup rate is roughly proportional to the on-resonance thickness rate, $\Gamma_s \approx -b(\Gamma_s^{00}/2)$, for thin crystals.

Applying the thin crystal approximation to the reflection channel field for Bragg and Laue diffraction gives

$$\mathbf{R}_{Bragg}(\omega) = e^{i(\mathbf{k}_{0\nu}+\mathbf{H})\cdot\mathbf{r}} \sum_{\alpha} E_{0\nu\alpha}(\omega)\hat{\boldsymbol{\varepsilon}}_{\alpha}^{H} \frac{-ik_{0\nu}Lbg_{\alpha\alpha}^{10}/2}{1 + ik_{0\nu}L\left(bg_{\alpha\alpha}^{00} - b\alpha_B\right)/2} \tag{7-6.18}$$

$$\mathbf{R}_{Laue}(\omega) = e^{i(\mathbf{k}_{0\nu}+\mathbf{H})\cdot\mathbf{r}} \sum_{\alpha} E_{0\nu\alpha}(\omega)\hat{\boldsymbol{\varepsilon}}_{\alpha}^{H}\left(-ik_{0\nu}Lbg_{\alpha\alpha}^{10}/2\right). \tag{7-6.19}$$

For combined resonant dipole and nonresonant scattering the Laue diffracted field reduces to

$$\mathbf{R}_{Laue}(\omega) = e^{i(\mathbf{k}_{0\nu}+\mathbf{H})\cdot\mathbf{r}} \sum_{\alpha} E_{0\nu\alpha}(\omega)\hat{\boldsymbol{\varepsilon}}_{\alpha}^{H}\left[\frac{ib\Gamma_{s\alpha}^{10}/4\hbar}{\omega - \omega_0 + i\Gamma/2\hbar} - ib\mu_{\alpha}^{10}(\omega)L/2\right] \tag{7-6.20}$$

where, for resonant dipole scattering,

$$\Gamma_{s\alpha}^{10} = L_M(\mathbf{k}_i)L_M(\mathbf{k}_f)C\sigma_0\Gamma L(\mathbf{u}_\alpha^{H*}\cdot\mathbf{u}_\alpha^0)\frac{1}{V_0}\sum_n e^{-i\mathbf{H}\cdot\mathbf{r}_n} \tag{7-6.21}$$

and, for nonresonant photoelectric scattering,

$$\mu_\alpha^{10}(\omega) = -\left(\frac{4\pi}{k_{0\nu}V_0}\right)r_e(\hat{\boldsymbol{\varepsilon}}_\alpha^{H*}\cdot\hat{\boldsymbol{\varepsilon}}_\alpha^0)\sum_n\left[D_W(\mathbf{H})f_0 + f'(\omega) - if''(\omega)\right]e^{-i\mathbf{H}\cdot\mathbf{r}_n}. \tag{7-6.22}$$

Again, as was the case for the Laue transmission field, there are no frequency shifts or speedup rates for Laue diffraction from a thin crystal.

The Bragg diffracted field reduces to

$$\mathbf{R}_{Bragg}(\omega) = e^{i(\mathbf{k}_{0\nu}+\mathbf{H})\cdot\mathbf{r}}\sum_\alpha E_{0\nu\alpha}(\omega)\hat{\boldsymbol{\varepsilon}}_\alpha^H\left[\xi_\alpha' + \frac{ib(\xi_\alpha' a + a_\alpha')}{\omega - \omega_0 + i\Gamma/2\hbar - iab}\right] \tag{7-6.23}$$

where

$$a_\alpha' = \frac{\Gamma_{s\alpha}^{10}/4\hbar}{1 + ib\mu^{00}(\omega)L/2 - ib\alpha_B k_{0\nu}L/2} \tag{7-6.24}$$

and

$$\xi_\alpha' = \frac{-\mu_\alpha^{10}(\omega)L/2}{1 + ib\mu^{00}(\omega)L/2 - ib\alpha_B k_{0\nu}L/2} \tag{7-6.25}$$

and a is given by Eq. 7-6.13. This expression can also be simplified under some assumptions about the structure of the crystal lattice. If the lattice of resonant scatterers is different than the lattice of nonresonant scatterers, certain reflections may be found where, due to the geometrical structure factor, diffraction from resonant particles is allowed whereas diffraction from nonresonant particles is not allowed. This holds for certain iron crystals such as YIG, $FeBO_3$, and α - Fe_2O_3 enriched with ^{57}Fe. Under such conditions, $\xi_\alpha' = 0$, and the diffracted field simplified to

$$\mathbf{R}_{Bragg}(\omega) = e^{i(\mathbf{k}_{0\nu}+\mathbf{H})\cdot\mathbf{r}}\sum_\alpha E_{0\nu\alpha}(\omega)\hat{\boldsymbol{\varepsilon}}_\alpha^H\frac{(\omega_s - i\Gamma_s/2\hbar)(\Gamma_{s\alpha}^{10}/\Gamma_s^{00})}{\omega - (\omega_0 + \omega_s) + i(\Gamma + \Gamma_s)/2\hbar} \tag{7-6.26}$$

where Γ_s and ω_s are given by Eqs. 7-6.16 and 7-6.17. The frequency shift and speedup rate are the same as that for Bragg transmission through a thin crystal. Also note that these quantities are dependent upon forward scattering factors and not upon diffraction scattering factors, and they are polarization independent.

A crystal will also appear "thin" when the eigenvalues are near zero: $\varepsilon_{0\alpha}^l \approx 0$. The eigenvalues can be exactly zero for Bragg diffraction when $\alpha_B = 0$, $g_{\alpha\alpha}^{00} = g_{\alpha\alpha}^{11}$, and $g_{\alpha\alpha}^{00}g_{\alpha\alpha}^{11} = g_{\alpha\alpha}^{01}g_{\alpha\alpha}^{10}$. Under such conditions, an infinitely thick crystal will appear "thin" in the thin crystal approximation. And as $d \to \infty$, the transmission channel field becomes negligibly small and the reflection channel field goes to unity. These are the conditions for the suppression of the inelastic channel.[9] They result in an interesting demonstration of the Borrmann effect for resonant scattering where resonant absorption is completely suppressed in an infinitely thick crystal. Here an infinite number of planes contribute toward reflecting all of the incident field back out of the crystal--the reflectivity becomes unity. This Borrmann effect can be seen in Fig. 5-7.3 (at $\Delta\theta = 0$) for a crystal 3 primary extinction lengths thick (unity reflectivity is nearly achieved). However, note that the condition $g_{\alpha\alpha}^{00} g_{\alpha\alpha}^{11} = g_{\alpha\alpha}^{01} g_{\alpha\alpha}^{10}$ cannot be met for nonresonant scattering since the Debye-Waller factor for forward scattering (which is unity) is never equal to that for diffraction. Thus, unity reflectivity through the Borrmann effect can never be achieved for nonresonant scattering.

CASE 3: Thick Crystal Approximation.

In the thick crystal approximation

$$k_{0\nu} \varepsilon_{0\beta}^{l} d/\gamma_0 >> 1. \tag{7-6.27}$$

For Laue diffraction the two eigenwaves of each polarization in each scattering channel exponentially die off with distance into the crystal. Since both eigenwaves persist at the exit surface, ascribing a single frequency shift or speedup rate to the net exiting field is not possible. In addition, the analytical form of each eigenwave in Eqs. 7-4.40 and 7-4.41 cannot be further simplified other than that they approach zero as $d \rightarrow \infty$.

For Bragg diffraction one of the two eigenwaves exponentially dies off with distance while the other increases exponentially with distance. For the thick crystal approximation, the transmission channel field is negligibly small while the reflection channel field approaches

$$\mathbf{R}_{Bragg}(\omega) = e^{i(\mathbf{k}_{0\nu}+\mathbf{H})\cdot\mathbf{r}} \sum_{\alpha} E_{0\nu\alpha}(\omega) \hat{\boldsymbol{\varepsilon}}_{\alpha}^{H} \frac{b g_{\alpha\alpha}^{10}}{g_{\alpha\alpha}^{00} - 2\varepsilon_{0\alpha}^{(1,2)}} \tag{7-6.28}$$

where the eigenvalue that yields exponentially growing waves is chosen in the denominator. For combined resonant dipole and nonresonant scattering, the reflected field reduces to

$$\mathbf{R}_{Bragg}(\omega) = e^{i(\mathbf{k}_{0\nu}+\mathbf{H})\cdot\mathbf{r}} \sum_{\alpha} E_{0\nu\alpha}(\omega) \hat{\boldsymbol{\varepsilon}}_{\alpha}^{H} \left(b/\Omega_{s\alpha}\right)$$

$$\times\left[\omega - (\omega_0 + \omega_s) + i(\Gamma + \Gamma_s)/2\hbar \pm \sqrt{\left[\omega - (\omega_0 + \omega_s) + i(\Gamma + \Gamma_s)/2\hbar\right]^2 + \Omega_{s\alpha}^2/b}\right]$$

where (7-6.29)

$$\omega_s = \mathrm{Re}\left\{\frac{(1-b)\left(\Gamma_s^{00}/4\hbar\right)}{(1-b)\mu^{00}(\omega)L/2 + b\alpha_B k_{0v} L/2}\right\}$$

$$= \frac{(1-b)\left(\Gamma_s^{00}/4\hbar\right)\left[(1-b)\mathrm{Re}\left\{\mu^{00}(\omega)\right\}L/2 + b\alpha_B k_{0v} L/2\right]}{\left[(1-b)\mathrm{Re}\left\{\mu^{00}(\omega)\right\}L/2 + b\alpha_B k_{0v} L/2\right]^2 + \left[(1-b)\mathrm{Im}\left\{\mu^{00}(\omega)\right\}L/2\right]^2} \tag{7-6.30}$$

$$\Gamma_s = -\mathrm{Im}\left\{\frac{(1-b)\left(\Gamma_s^{00}/2\right)}{(1-b)\mu^{00}(\omega)L/2 + b\alpha_B k_{0v} L/2}\right\}$$

$$= \frac{(1-b)\left(\Gamma_s^{00}/2\right)\left[(1-b)\mathrm{Im}\left\{\mu^{00}(\omega)\right\}L/2\right]}{\left[(1-b)\mathrm{Re}\left\{\mu^{00}(\omega)\right\}L/2 + b\alpha_B k_{0v} L/2\right]^2 + \left[(1-b)\mathrm{Im}\left\{\mu^{00}(\omega)\right\}L/2\right]^2} \tag{7-6.31}$$

$$\Omega_{sa} = \left(\omega_s - i\Gamma_s/2\hbar\right)\left(\Gamma_{sa}^{10}/\Gamma_s^{00}\right)\left[2b/(1-b)\right]. \tag{7-6.32}$$

Γ_s^{00} and Γ_{sa}^{10} are given by Eqs. 7-6.11 and 7-6.21, and, as before, a reflection was chosen for a crystal structure that forbids nonresonant diffraction but allows resonant dipole diffraction. Though the crystal is infinitely thick, a length factor, L, was inserted for comparisons to previous calculations. All quantities computed for this case are actually independent of L.

The extrema in Eq. 7-6.30 occur at

$$\Delta\theta_M = \frac{1-b}{2b\sin 2\theta_B}\left(\mathrm{Re}\left\{g_{aa}^{00}(\omega)\right\} \pm \mathrm{Im}\left\{g_{aa}^{00}(\omega)\right\}\right)_{nonres} \tag{7-6.33}$$

where $\left[g_{aa}^{00}(\omega)\right]_{nonres} = \mu^{00}(\omega)/k_{0v}$ is a nonresonant scattering tensor element. The maximum frequency shift is then

$$\omega_s(\Delta\theta_M) = \frac{1}{k_{0v}L}\frac{\left(\Gamma_s^{00}/4\hbar\right)}{\mathrm{Im}\left\{g_{aa}^{00}(\omega)\right\}_{nonres}}. \tag{7-6.34}$$

The maximum speedup parameter occurs at the nonresonant Bragg peak:

$$2\left|\Omega_{sa}(\Delta\theta_P)\right| = \frac{1}{k_{0v}L}\frac{\left(\Gamma_s^{00}/\hbar\right)}{\mathrm{Im}\left\{g_{aa}^{00}(\omega)\right\}_{nonres}}\left(\Gamma_{sa}^{10}/\Gamma_s^{00}\right)\left[2b/(1-b)\right] \tag{7-6.35}$$

where the nonresonant Bragg peak is situated at

$$\Delta\theta_P = \frac{(1-b)\mathrm{Re}\left\{g_{aa}^{00}\right\}_{nonres}}{2b\sin 2\theta_B} \tag{7-6.36}$$

due to the index of refraction shift. The angular width of the speedup parameter, $2|\Omega_{s\alpha}|$, is (full width at half maximum)

$$\Delta\theta_{\Omega} = \frac{\sqrt{3}(1-b)\mathrm{Im}\{g_{\alpha\alpha}^{00}\}_{nonres}}{b\sin 2\theta_B}. \tag{7-6.37}$$

Because of the non-Lorentzian form of the reflected field, the quantities ω_s and Γ_s no longer fully represent a frequency shift and speedup rate, but, for certain ranges of α_B, they do roughly describe the magnitude of these dynamical effects. The non-Lorentzian characteristics of the energy spectrum embodied by Eq. 7-6.29 can be seen in Figs. 7.6-1 and 7.6-2 for various angles near the Bragg angle. The α–^{56}Fe^{57}Fe crystal examined earlier in Section 7-5 was used again in these calculations. Far from Bragg the energy spectrum asymptotically approaches the Lorentzian lineshape a single nucleus exhibits. On resonance and near the Bragg peak (which occurs at $\Delta\theta_P = 16\mu$rads) the collection of nuclei generate a field intensity with a cusp-like distribution and long tails centered at the natural frequency (this is where the Borrmann effect is predominant).

Plots of $\hbar\omega_s(\Delta\theta)$, the centroid of the energy spectrum, and the energy at the peak intensity versus the angle from Bragg are shown in Fig. 7-6.3. The centroid and $\omega_s(\Delta\theta)$ generally follow each other with discrepancies largest at the Bragg peak, and they converge to the energy of peak intensity at large deviations from Bragg (that is, deviations larger that two photoelectric Darwin widths--the photoelectric Darwin width for the α–^{56}Fe^{57}Fe infinitely thick crystal is roughly 12μrad for the $[0\ 0\ 2]$ nearest order allowed photoelectric reflection). The energy shifts represented by $\hbar\omega_s(\Delta\theta)$ and the centroid maximize very close to the Bragg peak positioned at $\Delta\theta_P$--at about three-fourths of a microrad from the peak for $\hbar\omega_s(\Delta\theta)$ and about 1μrad from the peak for the centroid.

The angular position of the on-resonance Bragg peak is totally determined by photoelectric forward scattering since the real part of the resonant forward scattering amplitude goes to zero (note that the first term in Eq. 7-6.33 is the index of refraction shift, $\Delta\theta_P$, for on resonance scattering). Therefore, the extrema of $\omega_s(\Delta\theta)$ are slightly shifted from $\Delta\theta_P$ since nonresonant photoelectric absorption is generally much smaller than nonresonant scattering: $(1-b)\mathrm{Im}\{\mu^{00}(\omega)/k_{0v}\}/2b\sin 2\theta_B \approx 3/4\,\mu$rad (note that $b=-1$,

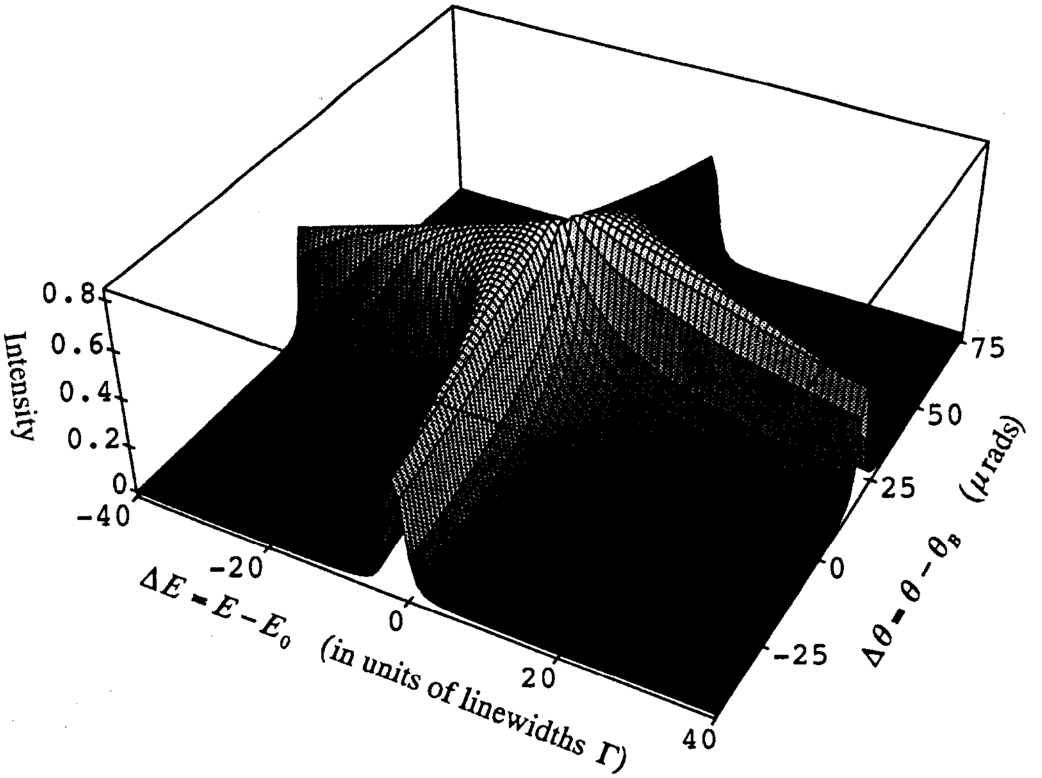

Fig. 7-6.1. Diffracted field intensity versus deviation angle from Bragg and deviation from the resonant energy.

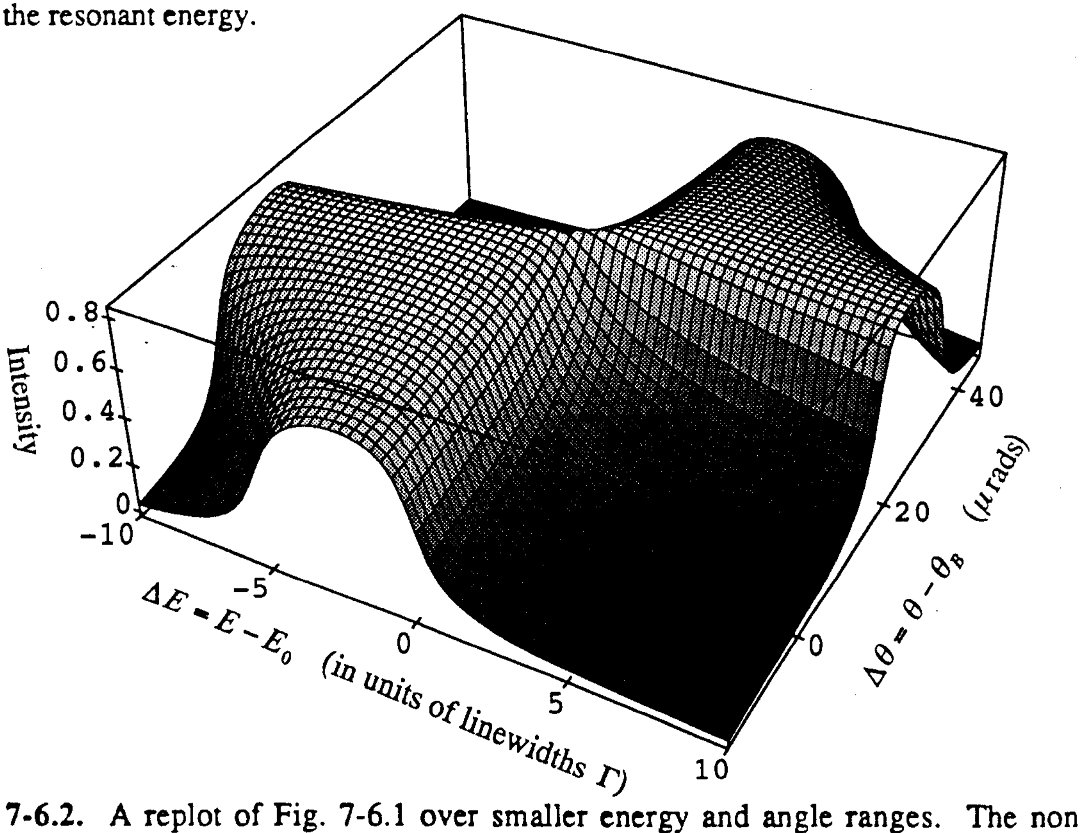

Fig. 7-6.2. A replot of Fig. 7-6.1 over smaller energy and angle ranges. The non-Lorentzian energy distribution is now clearly observable along with homogeneous line broadening and resonant energy shifts for these energy and angle ranges.

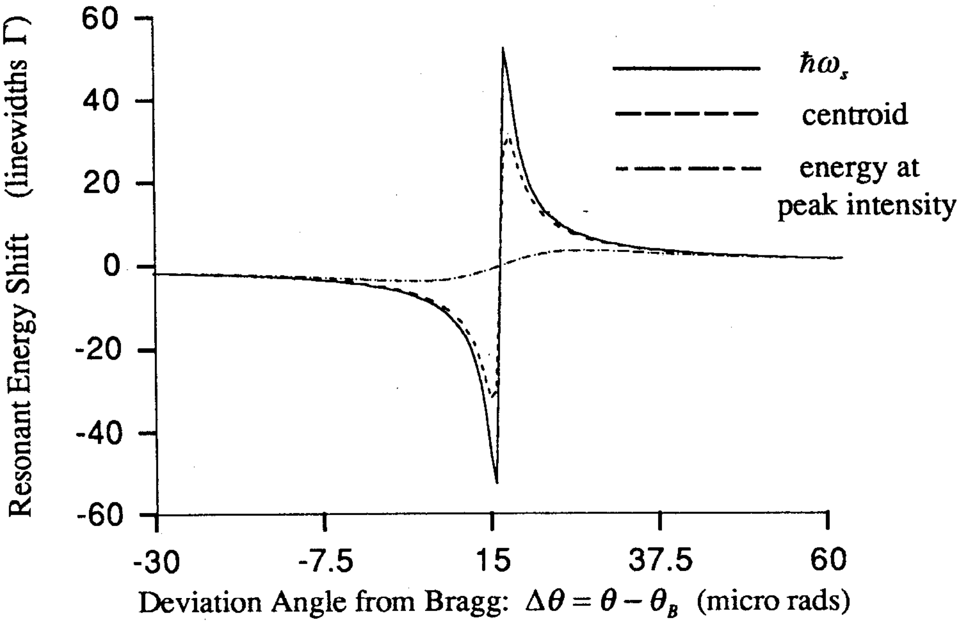

Fig. 7-6.3. Plots of $\omega_s(\Delta\theta)$, the centroid, and the energy at which the diffracted intensity peaks.

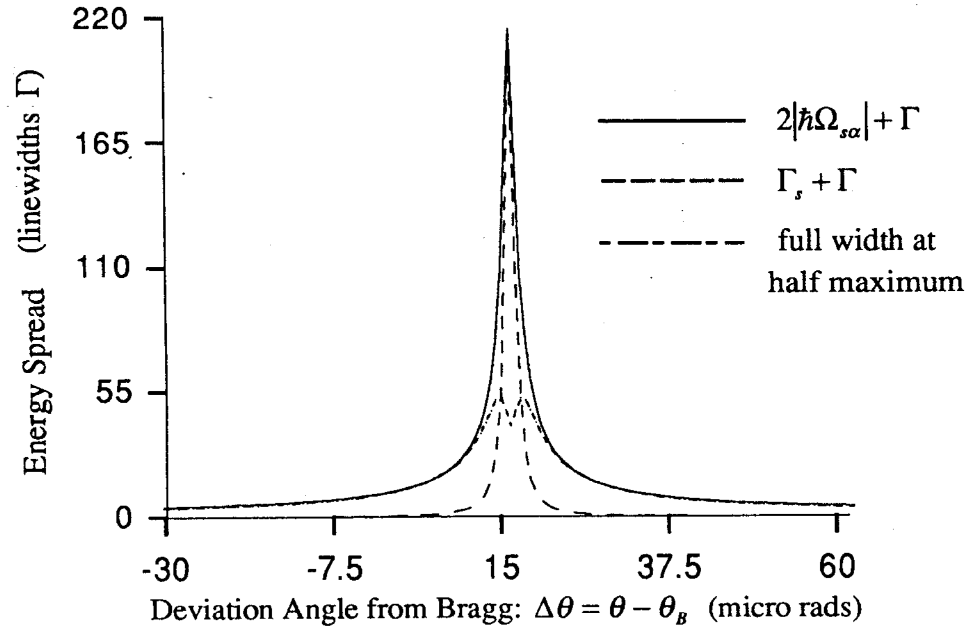

Fig. 7-6.4. Plots of speedup factors $2|\Omega_{s\alpha}|$ and Γ_s, and the full width at half maximum versus deviation angle.

$\theta_B \approx 4.9^\circ$, and $\mu^{00}(\omega)/k_{0v} \approx (-2.8+i0.13)\times 10^{-6}$ for the $[0\ 0\ 1]$ symmetric reflection of bcc $\alpha-{}^{56}\mathrm{Fe}{}^{57}\mathrm{Fe}$ having a lattice spacing of 5Å). The energy shift seen by examining the energy at which the field intensity is maximized has extrema that are roughly 15 times less than that for $\omega_s(\Delta\theta)$ and peaks (at about 11μrads) much further from the angular position of the on-resonant Bragg peak.

From Fig. 7-6.4 one can also see that $2|\Omega_{s\alpha}|+\Gamma$ approaches the full width at half maximum as the deviation angle progresses beyond half a photoelectric Darwin width. Thus, far off Bragg, the quantities ω_s and $2|\Omega_{s\alpha}|$ become good approximations for a frequency shift and speedup rate.

The dynamical quantities ω_s, Γ_s, and $2|\Omega_{s\alpha}|$ can be understood in another light by examining the diffracted intensity in the time domain. Fortunately, due to the efforts of Kohn,[10] an analytical expression for the Fourier transform of the diffracted field, Eq. 7-6.29, has been evaluated through contour integral methods for the case where the frequency spectrum of the incoming field is constant: $E_{0v\alpha}(\omega) = E_{0v\alpha}$ (as is the case for a synchrotron beam). The integral of interest is

$$I = \frac{1}{2\pi}\int_{-\infty}^{\infty} e^{-i\omega t}\left[(\omega - z_0) \pm \sqrt{(\omega - z_1)(\omega - z_2)}\right]d\omega \qquad (7\text{-}6.38)$$

where

$$z_0 = (\omega_0 + \omega_s) - i(\Gamma + \Gamma_s)/2\hbar \qquad (7\text{-}6.39)$$

$$z_{(1,2)} = (\omega_0 + \omega_s) - i(\Gamma + \Gamma_s)/2\hbar \pm \Omega'_{s\alpha} \qquad (7\text{-}6.40)$$

and

$$\Omega'_{s\alpha} = \mathrm{P}\left\{\sqrt{\Omega^2_{s\alpha}/b}\right\}. \qquad (7\text{-}6.41)$$

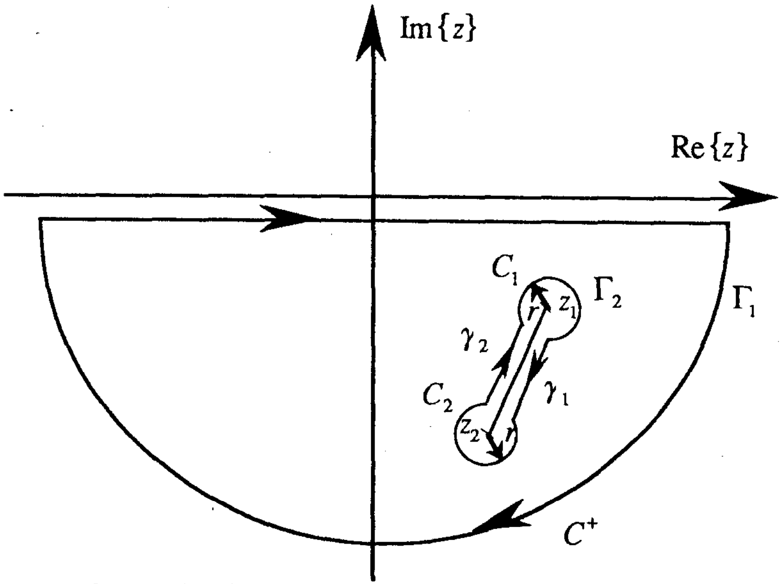

Fig. 7-6.5. Contour for evaluating the Fourier transform of the diffracted field from an infinitely thick crystal.

Since $\Omega_{s\alpha}$ is complex, the principal value of the square root in Eq. 7-6.41 must be evaluated.

Since ω_s is much smaller that the natural frequency and $\Omega_{s\alpha} \leq \left(\omega_s - i\Gamma_s/2\hbar\right)$ when examining only the real and imaginary parts separately, an appropriate contour to integrate over is shown in Fig. 7-6.5 which has a branch-cut between the two branch points z_1 and z_2. For this contour where ω is set to be complex valued

$$\left(\oint_{\Gamma_1} - \oint_{\Gamma_2}\right) e^{-izt}\left[\left(z - z_0\right) \pm \sqrt{\left(z - z_1\right)\left(z - z_2\right)}\right] dz = 0 \qquad (7\text{-}6.42)$$

since there are no poles in the region between the closed contours Γ_1 and Γ_2. The integral over arc C^+ of contour Γ_1 is zero by the Jordan Lemma (this can be seen by rewriting the argument of the integral in the form of a quotient of one over a polynomial of degree 1). The integral over the contour Γ_2 of the first term in the integral above also vanishes since it has no poles within the contour. Then

$$I = \pm\frac{1}{2\pi}\oint_{\Gamma_2} e^{-izt}\sqrt{\left(z - z_1\right)\left(z - z_2\right)}\, dz$$

$$= \pm\frac{1}{2\pi}\left(\int_{C_1} + \int_{C_2} + \int_{\gamma_1} + \int_{\gamma_2}\right) e^{-izt}\sqrt{\left(z - z_1\right)\left(z - z_2\right)}\, dz \qquad (7\text{-}6.43)$$

where C_1 and C_2 are two circles each of radius r, and γ_1 and γ_2 are two line segments on opposite sides of the branch-cut between the branch points z_1 and z_2. For the integral over circle C_1 let $z = z_1 + re^{i\theta}$. Then, since

$$\left|\int_{C_1} e^{-izt}\sqrt{\left(z - z_1\right)\left(z - z_2\right)}\, dz\right| < \left|2\pi r e^{-i(z_1 + r\sin\theta)t}\sqrt{re^{i\theta}\left(\Omega'_{s\alpha} + re^{i\theta}\right)}\right| \underset{r\to 0}{\rightarrow} 0,$$

the integral over C_1 vanishes as $r \to 0$ for $t > 0$. The same happens to the integral over the other circle C_2.

For the line segments let

$$z = \left[\frac{z_1 + z_2}{2}\right] + \left[\frac{z_1 - z_2}{2}\right] w. \qquad (7\text{-}6.44)$$

The principal value of the square root in the integral can then be expressed as

$$\sqrt{\left(z - z_1\right)\left(z - z_2\right)} = \Omega'_{s\alpha}\sqrt{1 - w^2}\, e^{\frac{i}{2}\left[\arg(-1+w) + \arg(1+w)\right]}. \qquad (7\text{-}6.45)$$

Then, along γ_1 from z_1 to z_2 the square root transforms to

$$\sqrt{\left(z - z_1\right)\left(z - z_2\right)} = i\Omega'_{s\alpha}\sqrt{1 - w^2} \qquad (7\text{-}6.46)$$

when w is set to $w = \lim_{\varepsilon\to 0} a + i\varepsilon$ where $|a| \leq 1$. Similarly, $w = \lim_{\varepsilon\to 0} a - i\varepsilon$ along γ_2 from z_2 to z_1 and thus

$$\sqrt{(z-z_1)(z-z_2)} = -i\Omega'_{s\alpha}\sqrt{1-w^2}\,. \tag{7-6.47}$$

Then

$$\begin{aligned} I &= \mp e^{-i(\omega_0+\omega_s)t} e^{-(\Gamma+\Gamma_s)t/2\hbar} \frac{i\Omega_{s\alpha}/b}{2\pi}\left(\int_{-1}^{1} - \int_{1}^{-1}\right)\sqrt{1-w^2}\, e^{-i\Omega'_{s\alpha}wt}\, dw \\ &= \mp e^{-i(\omega_0+\omega_s)t} e^{-(\Gamma+\Gamma_s)t/2\hbar} \frac{i\Omega_{s\alpha}/b}{\pi}\int_{-1}^{1}\sqrt{1-w^2}\cos(\Omega'_{s\alpha}wt)\,dw\,. \end{aligned} \tag{7-6.48}$$

With help from the integral tables in Abramowitz and Stegun,[14] the integral evaluates to

$$\int_{-1}^{1}\sqrt{1-w^2}\cos(\Omega'_{s\alpha}wt)\,dw = \pi\frac{J_1(\Omega'_{s\alpha}t)}{\Omega'_{s\alpha}t}. \tag{7-6.49}$$

The reflection channel field in the time domain is then

$$\mathbf{R}_{Bragg}(t) = e^{i(\mathbf{k}_{0v}+\mathbf{H})\cdot\mathbf{r}}\sum_{\alpha} E_{0v\alpha}\hat{\boldsymbol{\varepsilon}}_{\alpha}^{H} e^{-i(\omega_0+\omega_s)t} e^{-(\Gamma+\Gamma_s)t/2\hbar} i\Omega_{s\alpha}\frac{J_1(\Omega_{s\alpha}t)}{\Omega_{s\alpha}t}\theta(t). \tag{7-6.50}$$

The principal value of the square root expressed by $\Omega'_{s\alpha}$ has been dropped since $J_1(\Omega'_{s\alpha}t)/\Omega'_{s\alpha}t = J_1(\Omega_{s\alpha}t)/\Omega_{s\alpha}t$ (this can be seen by expanding the Bessel function in terms of a series expansion in $\Omega'_{s\alpha}t$). Also, the ± sign has been dropped because, as a result of the boundary conditions, the overall phase of the reflected field is indeterminable (though the phase can be determined when the reflection channel field interferes with another wave such as with the incoming field at the crystal surface). Examination of the reflected field reveals that it is frequency shifted by ω_s, and the natural decay rate is modified by a speedup factor Γ_s resulting only from forward scattering and by a speedup factor $\Omega_{s\alpha}$ resulting from diffraction.

The reason for the non-Lorentzian frequency response of the reflected field has now been isolated to the dynamical beat and speedup factor $J_1(\Omega_{s\alpha}t)/\Omega_{s\alpha}t$ in the time response. As a result, a decay rate attributed to the entire time response is no longer possible. However, the time behavior of the reflected field simplifies in the limits of the Bessel function for large and small arguments.[10] For instance, in the short time domain when $|\Omega_{s\alpha}t| << 1$

$$\mathbf{R}_{Bragg}(t) \approx e^{i(\mathbf{k}_{0v}+\mathbf{H})\cdot\mathbf{r}}\sum_{\alpha} E_{0v\alpha}\hat{\boldsymbol{\varepsilon}}_{\alpha}^{H} e^{-i(\omega_0+\omega_s)t} e^{-(\Gamma+\Gamma_s)t/2\hbar} i\frac{\Omega_{s\alpha}}{2}\theta(t), \tag{7-6.51}$$

and the reflected field suffers a frequency shift, ω_s, and a speedup, Γ_s, of the decay rate. In the long time domain when $|\Omega_{s\alpha}t| >> 1$

$$\mathbf{R}_{Bragg}(t) \approx e^{i(\mathbf{k}_{0\nu}+\mathbf{H})\cdot\mathbf{r}} \sum_{\alpha} E_{0\nu\alpha} \hat{\boldsymbol{\varepsilon}}_{\alpha}^{H} e^{-i(\omega_0+\omega_s)t} e^{-(\Gamma+\Gamma_s)t/2\hbar} i \sqrt{\frac{2}{\pi}} \frac{\cos\left(\Omega_{s\alpha} t - 3\pi/4\right)}{t\sqrt{\Omega_{s\alpha} t}} \theta(t). \qquad (7\text{-}6.52)$$

Since

$$\cos\left(\Omega_{s\alpha} t - 3\pi/4\right) = \left(e^{i\left(\mathrm{Re}\{\Omega_{s\alpha} t\} - 3\pi/4\right)} e^{-\mathrm{Im}\{\Omega_{s\alpha} t\}} + e^{-i\left(\mathrm{Re}\{\Omega_{s\alpha} t\} - 3\pi/4\right)} e^{+\mathrm{Im}\{\Omega_{s\alpha} t\}}\right) \Big/ 2$$

this long time limit exhibits both positive and negative frequency shifts and speedup and slowdown rates. However, since $\left|\mathrm{Im}\{\Omega_{s\alpha}\}\right| \le \Gamma_s/2\hbar$ there are never runaway solutions in which the reflected field grows exponentially with time. In fact, for the case in which $\left|\mathrm{Im}\{\Omega_{s\alpha}\}\right| = \Gamma_s/2\hbar$ the reflected field reduces to

$$\mathbf{R}_{Bragg}(t) \approx e^{i(\mathbf{k}_{0\nu}+\mathbf{H})\cdot\mathbf{r}} \sum_{\alpha} E_{0\nu\alpha} \hat{\boldsymbol{\varepsilon}}_{\alpha}^{H} i \frac{e^{i\pi/4}}{\sqrt{2\pi}} \frac{e^{-i\omega_0 t} e^{-\Gamma t/2\hbar}}{t\sqrt{\Omega_{s\alpha} t}} \theta(t). \qquad (7\text{-}6.53)$$

For this situation the reflected field intensity undergoes no frequency shift and decays faster than the natural decay rate by the factor $1/t^3$.

For the intermediate case in which $\left|\Omega_{s\alpha} t\right|$ is neither very large or small, an approximation of the decay behavior can be made using the result of the solution for the scattering channel field from an isotropic slab as a guide

$$\left|\mathbf{R}_{Bragg}(t)\right|^2 = C^2(\delta\theta) e^{-\left(\frac{\Gamma}{\hbar} + \frac{|\Omega_{s\alpha}|}{2\zeta(\delta\theta)\sqrt{\ln 2}}\right)t} \theta(t) \qquad (7\text{-}6.54)$$

where

$$\zeta(\delta\theta) = 1 + \frac{3}{2} \frac{|\delta\theta|}{|\delta\theta| + 25\mu rads}. \qquad (7\text{-}6.55)$$

Here, $\delta\theta$ is a measure of the angular deviation from the on-resonance Bragg peak (determined by the photoelectric index of refraction shift):

$$\delta\theta = \Delta\theta - \Delta\theta_P \qquad (7\text{-}6.56)$$

where $\Delta\theta_P$ is given by Eq. 7-6.36. For this estimate $\zeta(\delta\theta)$ is a function that varies from unity to 2.5 as the deviation angle varies from the center of the Bragg profile to far from Bragg. The coefficient $C(\delta\theta)$ rapidly varies from approximately 0.75 right on the Bragg peak to a plateau of 1.1 a few microrads from the Bragg peak.

Plots of normalized reflected intensity versus time are shown in Figs 7-6.6 to 7-6.8 for angular deviations from the Bragg peak of 0, 50, and 200 μrad respectively.

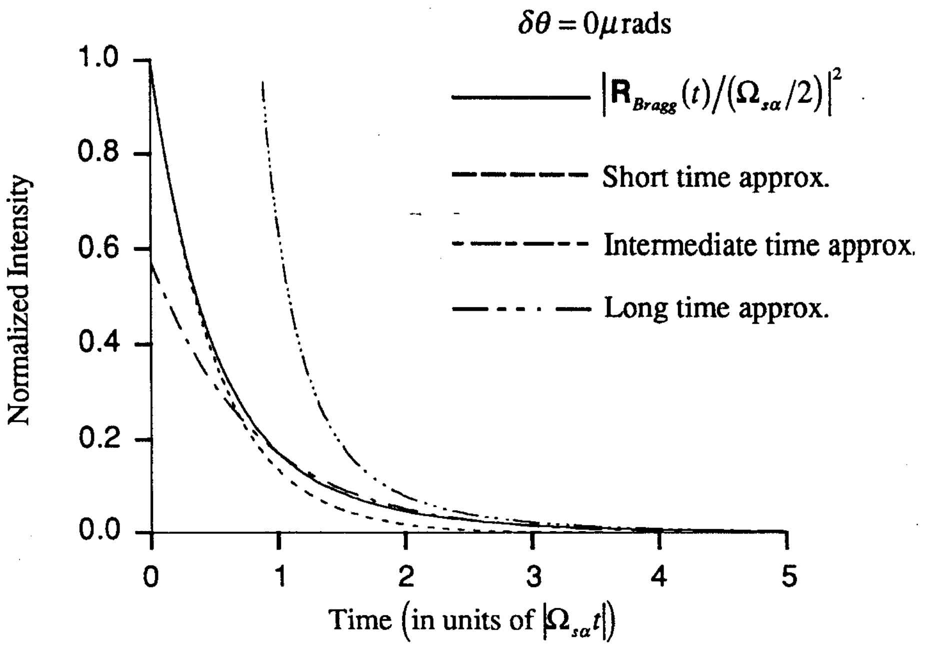

Fig. 7-6.6. Plots of normalized Bragg intensity versus $|\Omega_{s\alpha}t|$ (intensity is normalized by dividing by $|\Omega_{s\alpha}/2|^2$). The angular deviation from Bragg is 16μrad--this is right on the Bragg peak. The speedup factors are $1/2|\Omega_{s\alpha}| \approx \hbar/\Gamma_s \approx 0.66$ nsec.

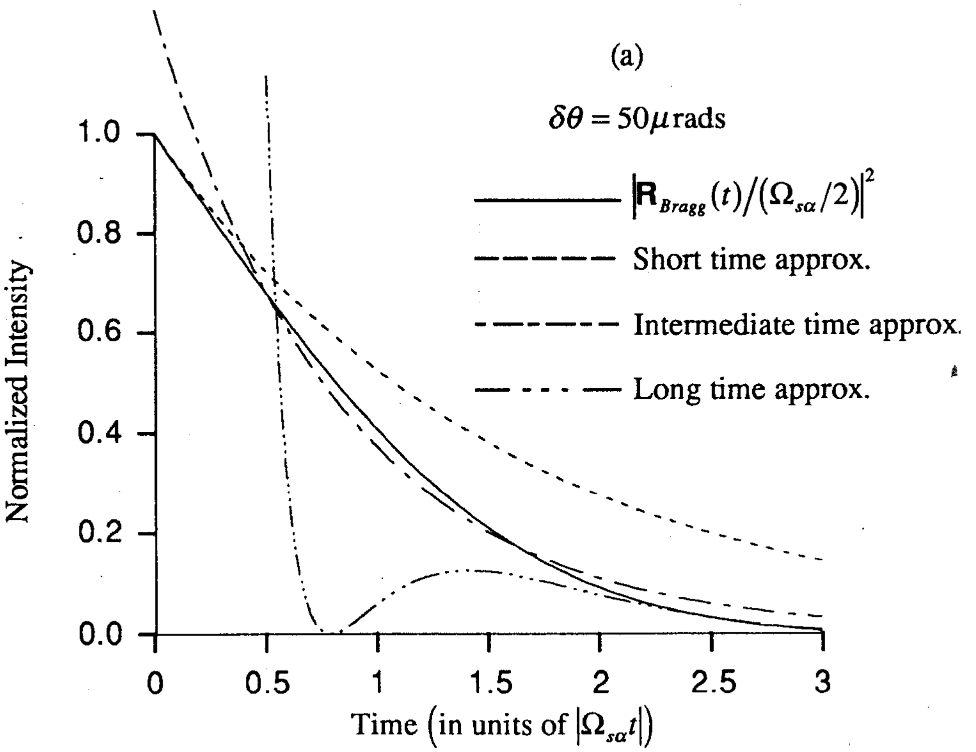

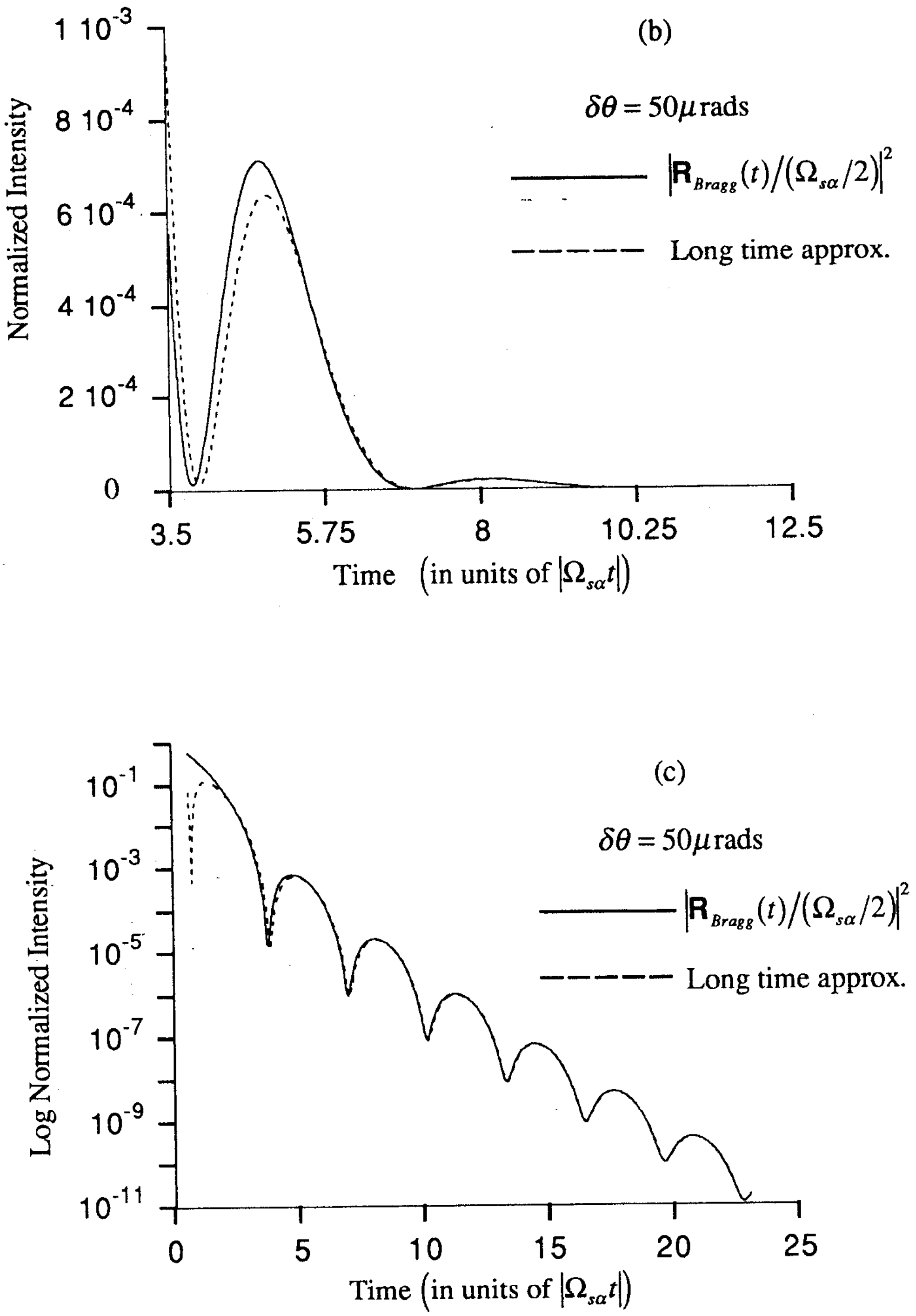

Fig. 7-6.7. The angular deviation from Bragg is 66μrad--this is 50μrad from the Bragg peak. The speedup factors are $1/2|\Omega_{s\alpha}| \approx 43$ nsec and $\hbar/\Gamma_s \approx 2.8$ μsec. The dynamical beats are now apparent at long times as can be seen in Figs. 7-6.7 (b) and (c).

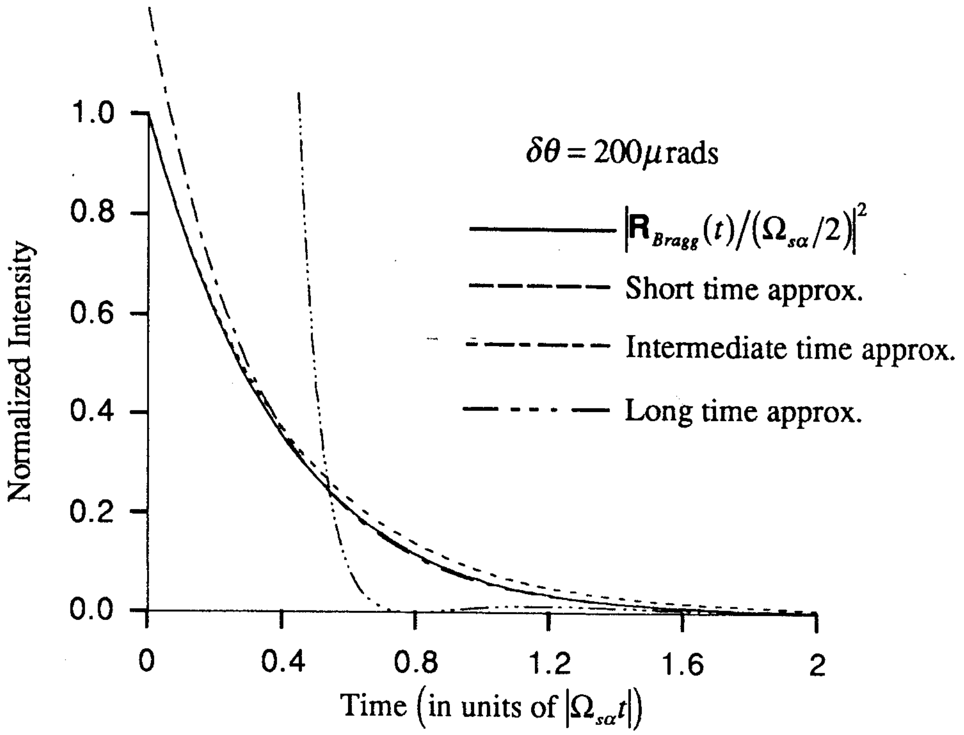

Fig. 7-6.8. The angular deviation from Bragg is 216μrad--this is 200μrad from the Bragg peak. The speedup factors are $1/2|\Omega_{s\alpha}| \approx 173$ nsec and $\hbar/\Gamma_s \approx 45$ μsec. Far from Bragg the field intensity decays with nearly the natural lifetime.

7.7 Dynamical Characteristics of Crystals with Hyperfine Split Spectra

To date, all crystals examined for nuclear resonant scattering have hyperfine split spectra rather than single line spectra. If the resonant lines for a particular crystal are very close together, the effects caused by interference between the various lines must be carefully examined in addition to any frequency shifts and speedup rates of each individual line. This significantly complicates the problem of analyzing the dynamical characteristics of the reflected field (in addition, no analytical form of the Bragg diffracted intensity in the time domain has been found).

If the resonant lines are far apart then the interference effects among the lines can be neglected, and the results of Sections 7.5 and 7.6 can be used for each individual line. For each individual line caused by a transition from an intermediate state $|n\rangle$ to a final state $|f\rangle$, the dynamical quantities ω_s, Γ_s, and $\Omega_{s\alpha}$ are given by Eqs. 7-6.30, 7-6.31, and 7-6.32 with substitution of $\Gamma_s^{00}/k_{0v}L$ and $\Gamma_{s\alpha}^{10}/k_{0v}L$ by

$$\Gamma^{00}_{s(fn)}/k_{0v}L = \frac{(4\pi)^2}{k^3_{0v}} nL_M(\mathbf{k}_i)L_M(\mathbf{k}_f = \mathbf{k}_i)C\Gamma_{rad}\frac{\langle j_f m_f LM | j_f L j_n m_n\rangle^2}{(2j_i+1)}P^{00}_{LM} \qquad (7\text{-}7.1)$$

and

$$\Gamma^{10}_{s\alpha(fn)}/k_{0v}L = \frac{(4\pi)^2}{k^3_{0v}} L_M(\mathbf{k}_i)L_M(\mathbf{k}_f)C\Gamma_{rad}\frac{\langle j_f m_f LM | j_f L j_n m_n\rangle^2}{(2j_i+1)}P^{10}_{LM}\frac{1}{V_0}\sum_q e^{-i\mathbf{H}\cdot\mathbf{r}_q}. \qquad (7\text{-}7.2)$$

where P^{HS}_{LM} is a polarization matrix described in Section 7-2.

Plots of $\omega_s(\Delta\theta)$ and $2|\Omega_{s\alpha}(\Delta\theta)|$ are shown below for three different crystals: α-Fe_2O_3, $FeBO_3$, and YIG (only for the d1-site). All these crystals have been used for nuclear resonant scattering experiments, and they all exhibit hyperfine split six line spectra. They can all be grown with enriched ^{57}Fe atoms, and they all have the property, because of either antiferromagnetic ordering or a ferromagnetic sublattice structure, where photoelectric diffraction for certain lattice planes is forbidden whereas resonant nuclear diffraction is allowed. The plots where constructed for the case in which the polarization matrix P^{HS}_{LM} diagonalizes: there is an applied magnetic field oriented perpendicular to the scattering plane. For lines $(\ell_1,\ell_2,\ell_3,\ell_4,\ell_5,\ell_6)$, $\mathrm{Re}(P^{10}_{1,\pm1})_{\sigma\sigma} = (3/16\pi)\cos 2\theta_B(1,0,1,1,0,1)$ for incoming horizontally polarized fields, and $(P^{10}_{10})_{\pi\pi} = (3/16\pi)(0,2,0,0,2,0)$ for

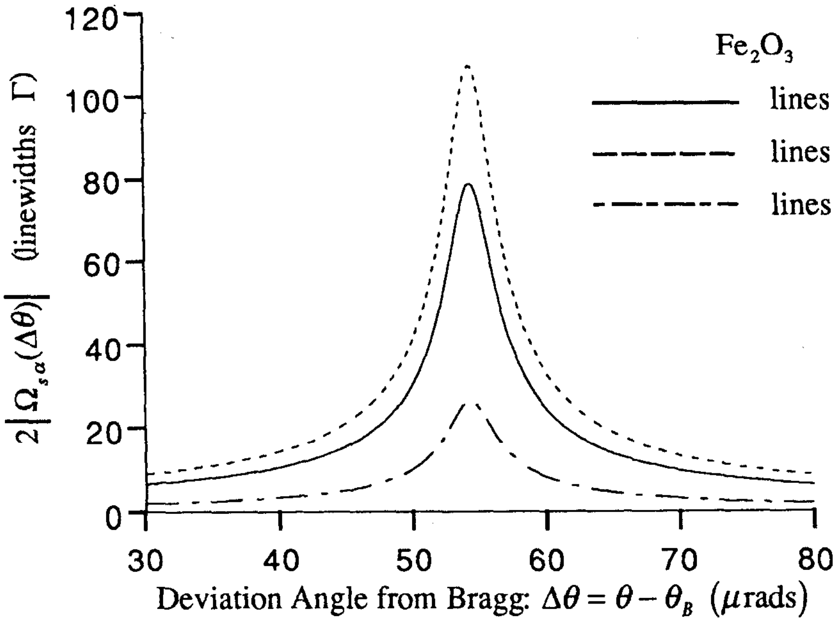

(a)

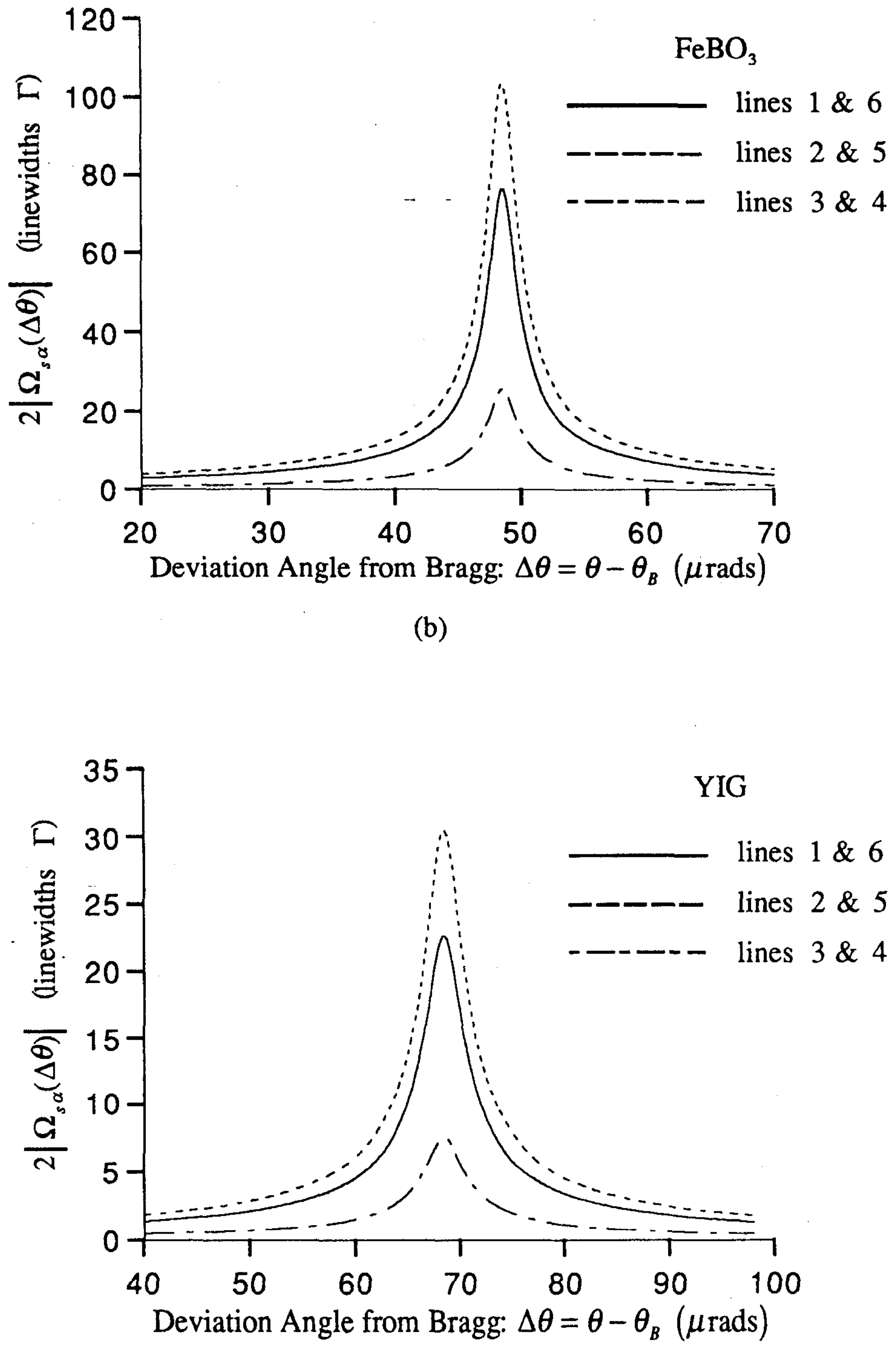

(b)

(c)

Fig. 7-7.1. Homogeneous line broadening parameter, or decay rate speedup factor, for the various hyperfine split lines of:(a) α - Fe_2O_3, (b) $FeBO_3$, and (c) YIG.

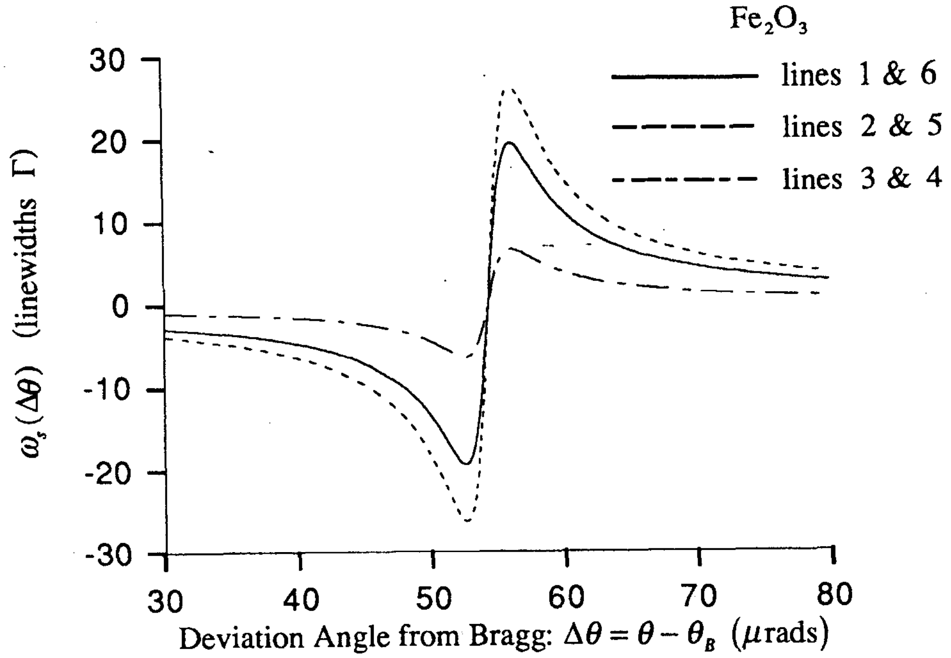

Fe_2O_3
lines 1 & 6
lines 2 & 5
lines 3 & 4
30
20
10
0
-10
-20
-30
$\omega_s(\Delta\theta)$ (linewidths Γ)
30
40
50
60
70
80
Deviation Angle from Bragg: $\Delta\theta = \theta - \theta_B$ (μrads)

(a)

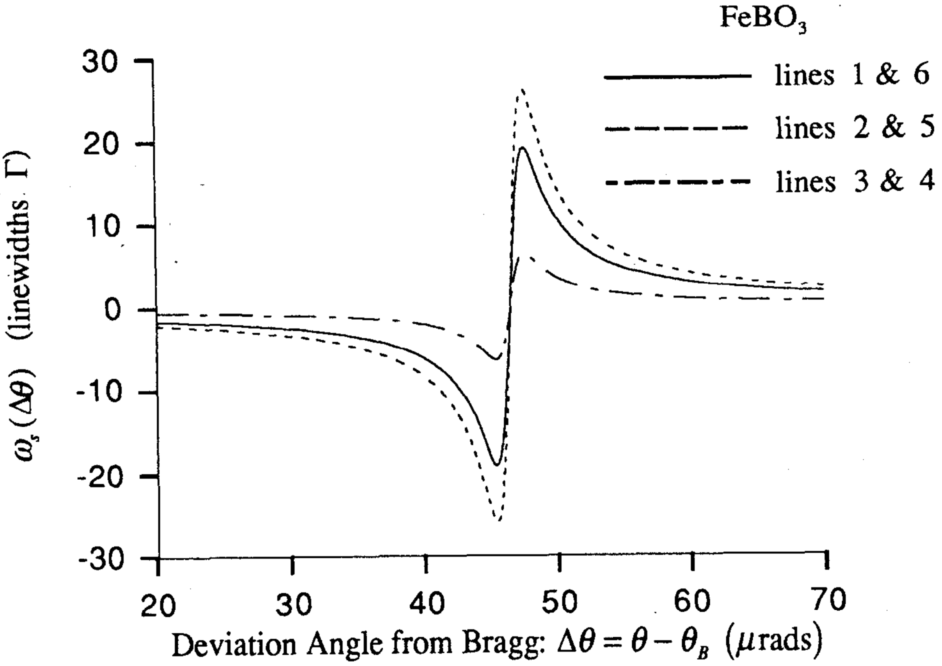

$FeBO_3$
lines 1 & 6
lines 2 & 5
lines 3 & 4
30
20
10
0
-10
-20
-30
$\omega_s(\Delta\theta)$ (linewidths Γ)
20
30
40
50
60
70
Deviation Angle from Bragg: $\Delta\theta = \theta - \theta_B$ (μrads)

(b)

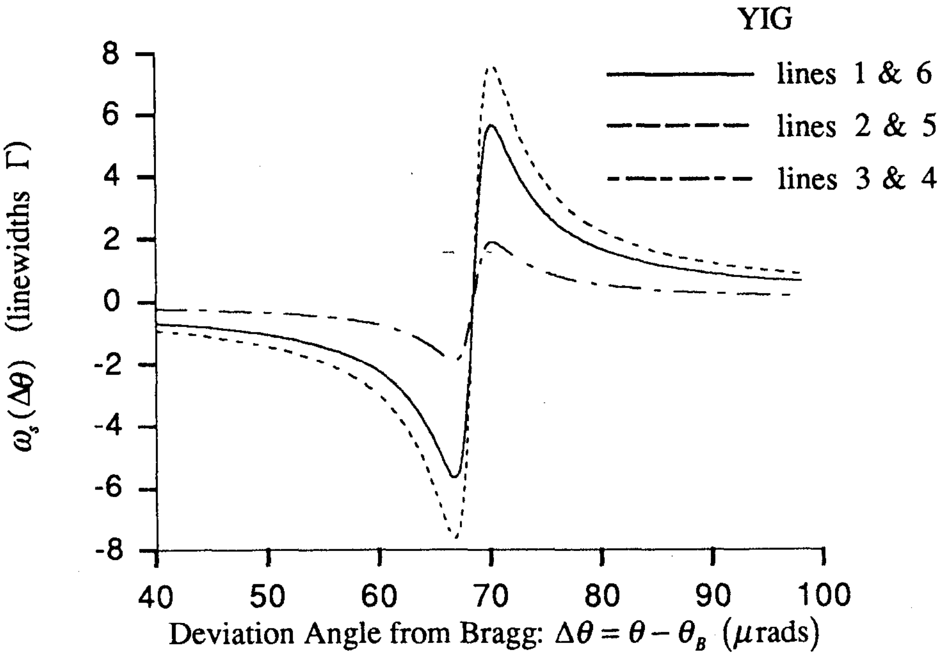

(c)

Fig. 7-7.2. Resonant frequency shift for the various hyperfine split lines of: (a) α-Fe_2O_3, (b) $FeBO_3$, and (c) YIG.

lines $(\ell_1,\ell_2,\ell_3,\ell_4,\ell_5,\ell_6)$ are $(1,2/3,1/3,1/3,2/3,1)$. The Lamb-Mössbauer and resonant enrichment factors have been set to unity: $L_M(\mathbf{k}_i)L_M(\mathbf{k}_f)=1$ and $C=1$. The resonant energy is 14.4125 keV, the resonant linewidth is 4.67×10^{-9} eV, and $j_i = 1/2$. The $[1\,1\,1]$ reflection from α-Fe_2O_3 and $FeBO_3$ have Bragg angles of 5.4° and 5.1° respectively. The Bragg angle of the $[0\;0\;2]$ reflection from YIG is 4.0°.

Since the photoelectric absorption due to the spectator oxygen atoms is small compared to the iron atoms for α-Fe_2O_3 and $FeBO_3$, the extrema in the frequency shift and speedup parameter characterized by Eqs. 7-6.34 and 7-6.35 are nearly identical as can be seen in Figs. 7-7.1 (a) and (b) (the extrema are naturally independent of unit cell volume and crystal thickness, but, if the photoelectric absorption of the spectator atoms is completely neglected, they also become independent of the number of resonant nuclei per unit cell). However, YIG has many more spectator atoms (32 other iron atoms, 24 yittrium atoms, and 96 oxygen atoms). The photoelectric absorption from these spectator atoms significantly limits the maximum frequency shift and speedup.

The angular range over which there is a moderate speedup is described by Eq. 7-6.37. By decreasing the Bragg angle (such as by increasing the lattice spacing) or by increasing the photoelectric absorption (such as by increasing the number of resonant nuclei per unit cell), the angular range for moderate speedup can be greatly extended. However, increasing the photoelectric absorption by increasing the number of spectator atoms instead of the number of resonant nuclei will decrease the maximum speedup.

7.8 Numerical Solutions of the Linearized Dispersion Relations

The analytical two beam solution of the linearized dispersion equation was possible because the polarization matrices were diagonal for a particular eigenpolarization basis. The dispersion equation decoupled into two relations for each eigenpolarization, and this resulted in simple analytical solutions for the transmitted and diffracted fields. The eigenpolarizations for nonresonant photoelectric scattering are the sigma and pi polarizations since mainly Thomson scattering occurs. For resonant magnetic dipole scattering with an applied magnetic field perpendicular to the scattering plane, the eigenpolarizations are also the sigma and pi polarizations. When the applied magnetic field is parallel to the scattering plane and horizontally oriented (Case 3 in Section 5.1) the eigenpolarizations are the right and left circular polarizations (however, a polarization matrix must be reconstructed in this basis since the polarization matrices in the linear basis represented by Eqs. 5-1.19 and 5-1.20 no longer apply).

In general eigenpolarizations for resonant scattering are not easy to find for an arbitrary orientation of the quantum axis. Therefore the polarization matrices are usually constructed in a simple polarization basis (such as the sigma and pi basis), and then one proceeds to solve the dispersion equations (which may no longer be uncoupled) through numerical techniques. This involves solving the characteristic eigenvalue equation expressed in Eq. 7-4.19 where

$$\mathbf{G}_{lin}=\begin{pmatrix} g_{xx}^{00} & g_{xx}^{01} & g_{xy}^{00} & g_{xy}^{01} \\ g_{xx}^{10} & \left(bg_{xx}^{11}-b\alpha_B\right) & g_{xy}^{10} & g_{xy}^{11} \\ g_{yx}^{00} & g_{yx}^{01} & g_{yy}^{00} & g_{yy}^{01} \\ g_{yx}^{10} & g_{yx}^{11} & g_{yy}^{10} & \left(bg_{yy}^{11}-b\alpha_B\right) \end{pmatrix}. \qquad (7\text{-}8.1)$$

The G_{lin}-matrix is a $2n\times 2n$ matrix where n is the number of scattering channels (or beams as it is termed in the literature). For the two-beam case G_{lin} is a 4×4 matrix, but when there are many umveg, or simultaneous, reflections G_{lin} can rapidly become very large to the point where a fast computer is a necessary tool for solving the characteristic equation. Resonant umveg reflections are not explored in this paper, thus the largest G_{lin}-matrix investigated is the linearized 4×4 matrix shown above. With the help of readily available computer programs (such as EISPACK or the NAG eigenvector-eigenvalue routines) numerically solving the dispersion equation for both the eigenvalues and eigenvectors is a straightforward procedure. However, insight into the dynamics of the scattering process is lost. This insight can be partly recovered by examining simple analytical solutions such as those presented in Sections 7-3 to 7-7.

When the incoming photon beam is near the surface grazing angle of the crystal, the boundary conditions described in Section 7-4 are no longer adequate--the specular reflection off the crystal surface is no longer negligible. One must now properly insure that the normal components of the **D** and **B** fields and the tangential components of the **E** and **H** fields of the Maxwell equations are continuous across the top and bottom surfaces of the crystal. When this is done for the two-beam case, instead of having 4 eigenvalues to solve for, there are now 8 to find. Four come from solving the characteristic equation in Eq. 7-4.19, and four more come from solving two separate dispersion equations describing fields propagating through the crystal that have been internally reflected from the top and bottom surface of the crystal. The continuity boundary conditions yields 16 equations (eight involving the transmission channel eigenwaves and eight involving the reflection channel eigenwaves). They can be reduced to 8 equations by eliminating the exiting fields and the specularly reflected field.[15] Resonant grazing angle scattering from crystals is also not explored in this thesis.

7.9 Nonlinear Dispersion Equation

The linearized dispersion equation is valid in the limit of finite and nonzero asymmetry factors. As $b \rightarrow 0$ or as $b \rightarrow \pm\infty$ (that is, when the forward scattered or diffracted field propagates nearly parallel to the crystal surface), the nonlinear dispersion equation presented in Eq. 7-1.4 may be required. This involves finding the solution to a quadratic characteristic equation.[15]

Projecting the wavectors within the crystal onto unit vectors normal and parallel to the crystal surface ($\hat{\mathbf{n}}$ and $\hat{\mathbf{u}}$ respectively) produces a nonlinear characteristic dispersion relation in terms of the projection of the transmission channel wavector onto the surface normal:

$$k_{0\hat{n}} = \mathbf{k}_0 \cdot \hat{\mathbf{n}}. \tag{7-9.1}$$

Noting that $\mathbf{k}_1 = \mathbf{k}_0 + \mathbf{H}_1$ (Bragg's law) gives

$$\mathbf{k}_1 \cdot \mathbf{k}_1 / k_{0v}^2 = k_{0\hat{n}}^2 + k_{0\hat{n}}\left(2H_{1\hat{n}}/k_{0v}\right) + \left(H_{1\hat{n}}/k_{0v}\right)^2 + k_{1\hat{u}}^2. \tag{7-9.2}$$

The quadratic characteristic relation is then

$$\left(k_{0\hat{n}}^2 \mathbf{B}_2 + k_{0\hat{n}} \mathbf{B}_1 + \mathbf{B}_0 - \mathbf{G}\right)\boldsymbol{\upsilon} = 0 \tag{7-9.3}$$

where

$$\mathbf{B}_2 = \begin{pmatrix} 1 & & & \\ & 1 & & 0 \\ 0 & & 1 & \\ & & & 1 \end{pmatrix}, \quad \mathbf{B}_1 = \begin{pmatrix} 0 & & & \\ & 0 & & 0 \\ 0 & & 2H_{1\hat{n}}/k_{0v} & \\ & & & 2H_{1\hat{n}}/k_{0v} \end{pmatrix},$$

$$\mathbf{B}_0 = \begin{pmatrix} -1 & & & \\ & -1 & & 0 \\ 0 & & (H_{1\hat{n}}/k_{0v})^2 + k_{1\hat{u}}^2 - 1 & \\ & & & (H_{1\hat{n}}/k_{0v})^2 + k_{1\hat{u}}^2 - 1 \end{pmatrix},$$

$$\mathbf{G} = \begin{pmatrix} g_{xx}^{00} & g_{xx}^{01} & g_{xy}^{00} & g_{xy}^{01} \\ g_{xx}^{10} & g_{xx}^{11} & g_{xy}^{10} & g_{xy}^{11} \\ g_{yx}^{00} & g_{yx}^{01} & g_{yy}^{00} & g_{yy}^{01} \\ g_{yx}^{10} & g_{yx}^{11} & g_{yy}^{10} & g_{yy}^{11} \end{pmatrix}, \text{ and } \boldsymbol{\upsilon} = \begin{pmatrix} T_x \\ T_y \\ R_x \\ R_y \end{pmatrix}. \tag{7-9.4}$$

By defining an eigenvector $\boldsymbol{\omega}$ such that

$$\boldsymbol{\upsilon} = k_{0\hat{n}} \boldsymbol{\omega} \tag{7-9.5}$$

allows the quadratic characteristic equation to be modified to

$$k_{0\hat{n}} \mathbf{B}_1 \mathbf{B}_2^{-1} \boldsymbol{\upsilon} + \left(\mathbf{B}_0 - \mathbf{G}\right)\mathbf{B}_2^{-1} k_{0\hat{n}} \boldsymbol{\omega} = -k_{0\hat{n}}^2 \boldsymbol{\upsilon}. \tag{7-9.6}$$

This relation becomes linear in $k_{0\hat{n}}$ when both sides of the equation are divided by that parameter. The new linear characteristic equation to be solved for is then

$$\left(\mathbf{Q} - k_{0\hat{n}} \mathrm{I}\right)\mathbf{b} = 0 \tag{7-9.7}$$

where

$$\mathbf{Q} = \begin{pmatrix} -\mathbf{B}_1 \mathbf{B}_2^{-1} & -(\mathbf{B}_0 - \mathbf{G})\mathbf{B}_2^{-1} \\ \mathrm{I} & \mathbf{0} \end{pmatrix} \tag{7-9.8}$$

$$\mathbf{b} = \begin{pmatrix} \boldsymbol{\upsilon} \\ \boldsymbol{\omega} \end{pmatrix} \tag{7-9.9}$$

and I is the identity matrix.

Since the B and G-matrices are of order 4, the Q-matrix is of order 8. Then the linear characteristic equation will give 8 eigenvalues, $k_{0\hat{n}}^{\ell}$, and eigenvectors, $\mathbf{b}^{\ell}$. The first four elements of the eigenvector $\mathbf{b}^{\ell}$ yields $\boldsymbol{\upsilon}^{\ell}$ which is the desired eigenvector for the nonlinear dispersion equation. The boundary conditions are found by the same method explained in Section 7.8: ensuring that the normal components of **D** and **B** and the tangential components of **E** and **H** are continuous across the crystal interfaces. Instead of there being 16 eigenwaves inside the crystal that exists for the linearized dispersion relation with simple boundary conditions, there are now 32 eigenwaves traveling inside the crystal--16 for each polarization and 8 for each scattering channel direction.

When examining highly asymmetric reflections (which are also not explored in this thesis) one may need to solve the nonlinear dispersion equation rather that the linearized dispersion equation.

7.10 Umweganregung, or Simultaneous, Reflections

In the previous sections only 2-beam diffraction was investigated. However, n-beam diffraction from a crystal can occur when more than one set of crystal planes reflect the incident beam into the same outgoing direction. These umweganregung (umveg for short) reflections occur simultaneously with the primary reflection. The Ewald sphere for a 3-beam diffraction case is shown in Fig. 7-1.1. In the figure, $\mathbf{k}_0$ is shown to scatter into the $\mathbf{k}_H$ direction due to planes having a primary scattering vector $\mathbf{H}$. Simultaneously, $\mathbf{k}_0$ is scattered into the $\mathbf{k}_S$ direction due to planes having a scattering vector $\mathbf{S}$, and then $\mathbf{k}_S$ is scattered into the $\mathbf{k}_H$ direction due to planes having a scattering vector $\mathbf{H}-\mathbf{S}$.

Bragg's law for satisfying both the primary **H** reflection and the secondary **S** reflection can be obtained by studying the scattering geometry shown in Fig. 7-10.1. The scattering plane $(\hat{\mathbf{x}}, \hat{\mathbf{y}})$ consists of $\mathbf{k}_0$, $\mathbf{H}$, and $\mathbf{k}_H$, and $\mathbf{H}$ points in the $\hat{\mathbf{z}}$-direction. **S** is a secondary reciprocal lattice vector that makes and angle θ_S with respect to $\mathbf{H}$:

$$\hat{\mathbf{S}} = \sin\theta_S \cos\phi\, \hat{\mathbf{x}} + \sin\theta_S \sin\phi\, \hat{\mathbf{y}} + \cos\theta_S\, \hat{\mathbf{z}}. \tag{7-10.1}$$

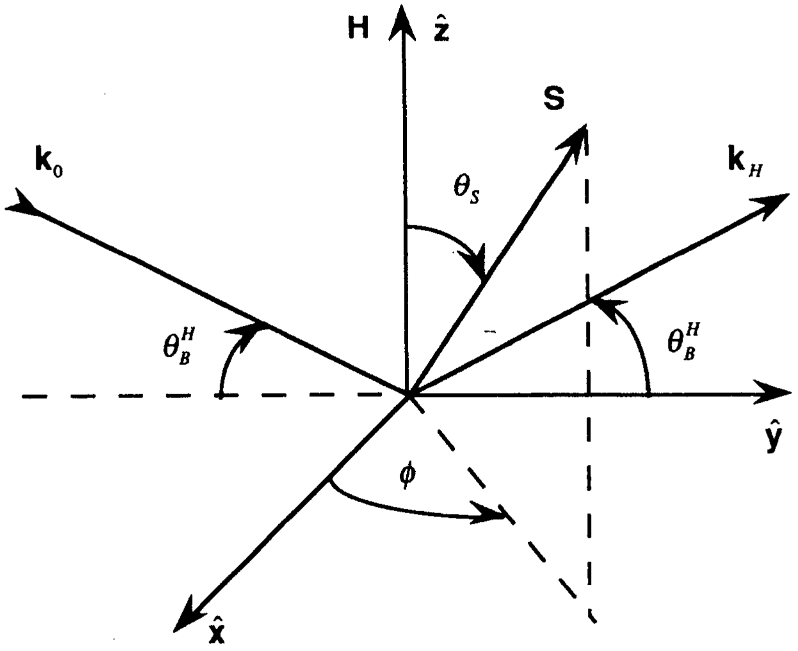

Fig. 7-10.1 Scattering geometry for 3-beam diffraction.

The Bragg angle between $\mathbf{H}$ and $\mathbf{k}_H$ is $90°-\theta_B^H$, and the Bragg angle between $\mathbf{S}$ and $\mathbf{k}_H$ is $90°-\theta_B^S$. Then, from Fig. 7-10.1,

$$\sin\theta_B^S = \hat{\mathbf{k}}_H \cdot \hat{\mathbf{S}} = \sin\theta_B^H \cos\theta_S + \cos\theta_B^H \sin\theta_S \sin\phi . \tag{7-10.2}$$

Bragg's law for each of the separate reflections is (recall Eq. 7-4.17)

$$\sin\theta_B^H = \hbar c H/2E_B \qquad \text{and} \qquad \sin\theta_B^S = \hbar c S/2E_B . \tag{7-10.3}$$

The azimuthal angle for which both of these reflections occur simultaneously is then

$$\sin\phi = \frac{\hbar c}{2E_B \sin\theta_S}\left(\frac{L - H\cos\theta_S}{\sqrt{1-(\hbar c H/2E_B)^2}}\right), \tag{7-10.4}$$

and the energy at which this occurs is

$$E_B = \frac{\hbar c}{2}\sqrt{\left(\frac{L - H\cos\theta_S}{\sin\theta_S \sin\phi}\right)^2 + H^2} . \tag{7-10.5}$$

Umveg reflections can show up as undesirable glitches in crystallography experiments. Or, they can be useful as precise energy calibration markers. As a result, knowledge of the intensity of umveg reflections is valuable information. As a first order approximation, the intensity of an umveg reflection is proportional to the product of the structure factors of the umveg's two sets of reflections:

$$I_{umveg} \approx F_S F_{H-S} \tag{7-10.6}$$

where F is the structure factor of a unit cell (see Eqs. 6-1.4 and 6-1.5).[16] More about these umveg reflections are discussed in Section 9.5 where they are used as energy calibration markers and where ϕ-energy graphs are constructed to chart out the regions that should be avoided.

REFERENCES

[1] R. W. James, *The Optical Principles of the Diffraction of X-Rays* (Ox Bow Press, Woodbridge, Connecticut, 1982).

[2] B. E. Warren, *X-Ray Diffraction* (Dover, New York, 1990).

[3] W. H. Zachariasen, *Theory of X-Ray Diffraction in Crystals* (Dover, New York, 1945).

[4] B. W. Batterman and H. Cole, *Rev. Mod. Phys.* **36**, 681 (1964).

[5] J. P. Hannon and G. T. Trammell, *Phys. Rev.* **169**, 169 (1968).

[6] J. P. Hannon and G. T. Trammell, *Phys. Rev.* **186**, 306 (1969).

[7] J. P. Hannon, N. J. Carron, and G. T. Trammell, *Phys. Rev. B* **9**, 2791 (1974).

[8] J. P. Hannon, N. J. Carron, and G. T. Trammell, *Phys. Rev. B* **9**, 2810 (1974).

[9] A. M. Afanas'ev and Y. Kagan, *Sov. Phys. JETP* **21**, 215 (1965).

[10] Y. Kagan, A. M. Afanas'ev, and I. P. Perstnev, *Sov. Phys. JETP* **27**, 819 (1968).

[11] Y. Kagan, A. M. Afanas'ev, and V. G. Kohn, *J. Phys. C* **12**, 615 (1979).

[12] H. J. Maurus, U. van Bürck, G. V. Smirnov, and R. L. Mössbauer, *J. Phys. C* **17**, 1991 (1984).

[13] I. S. Lyubutin, E. F. Makarov, and V. A. Povitskii, *Sov. Phys. JETP* **26**, 44 (1967).

[14] M. Abramowitz and I. A. Stegun, *Handbook of Mathematical Functions* (National Bureau of Standards, Washington D.C., 1972).

[15] R. Colella, *Acta Cryst.* **A30**, 413 (1974).

[16] Q. Shen, *Acta Cryst.* **A42**, 525 (1986).

8. NUMERICAL ANALYSIS PROCEDURES

8.1 Crystal Structure of Fe_2O_3, $FeBO_3$, and YIG

The principle crystals used in the field of nuclear resonance scattering have been hematite ($\alpha-Fe_2O_3$),[1-4] rhombohedral iron borate ($FeBO_3$),[5-7] yittrium iron garnet (YIG),[8, 9] and orthorhombic iron borate (Fe_3BO_6)[10, 11] (and, to a lesser extent, potassium ferrocyanide ($K_4Fe(CN)_6 \cdot 3H_2O$),[12] sodium nitroprusside ($Na_2Fe(CN)_5NO \cdot 2H_2O$),[13] ^{157}Te crystals,[14] and mosaic ^{119}Sn crystals[15] -- these crystals have very large mosaic spreads, and perfect crystals of these compounds are difficult to fabricate). All these crystals (except for the mosaic ^{119}Sn crystals) have the feature that, for certain crystallographic reflections, nonresonant photoelectric diffraction is forbidden whereas resonant nuclear diffraction is allowed.[16] This feature allows the nonresonant background to be significantly reduced in order to observe the nuclear signal.

$\alpha-Fe_2O_3$ and $FeBO_3$ both have a rhombohedral calcite crystal structure (space group $R\bar{3}c - D^6_{3d}$)[17-19] and exhibit a canted antiferromagnet system[20-23] (see Fig. 8.1-1). They each have two molecules per unit cell which lead to the formation of magnetic sublattices below the Néel temperature (948°K for $\alpha-Fe_2O_3$ and 348°K for $FeBO_3$).[20, 23] The magnetic moments lie within the (1 1 1) plane with two adjacent planes being antiferromagnetically coupled (however, below the Morin temperature of 253°K the $\alpha-Fe_2O_3$ magnetic moments align themselves perpendicular to the (1 1 1) planes[24]). Because the antiferromagnetic moments are canted, there is a small ferromagnetic moment lying within the (1 1 1) plane. The ferromagnetic moments will align themselves parallel to an external magnetic field, therefore, an applied external magnetic field can be used to orient the antiferromagnetic moments (an alignment field of about 1 kGauss[25, 26] is needed for $\alpha-Fe_2O_3$ and only several Gauss (~ 5Gauss)[22, 27] is needed for $FeBO_3$).

Because of the antiferromagnet sublattice structure, resonant nuclear reflections are allowed from certain lattice planes whereas photoelectric reflections are forbidden. For instance, from planes A and B for the crystals in Fig. 8.1-1, the electric fields are reflected 180° out of phase. However, since the magnetic moments lie in nearly antiparallel directions for the two planes, the polarization of the reflected fields for each hyperfine line for the two planes is different (for perfect antiferromagnets, the polarizations are

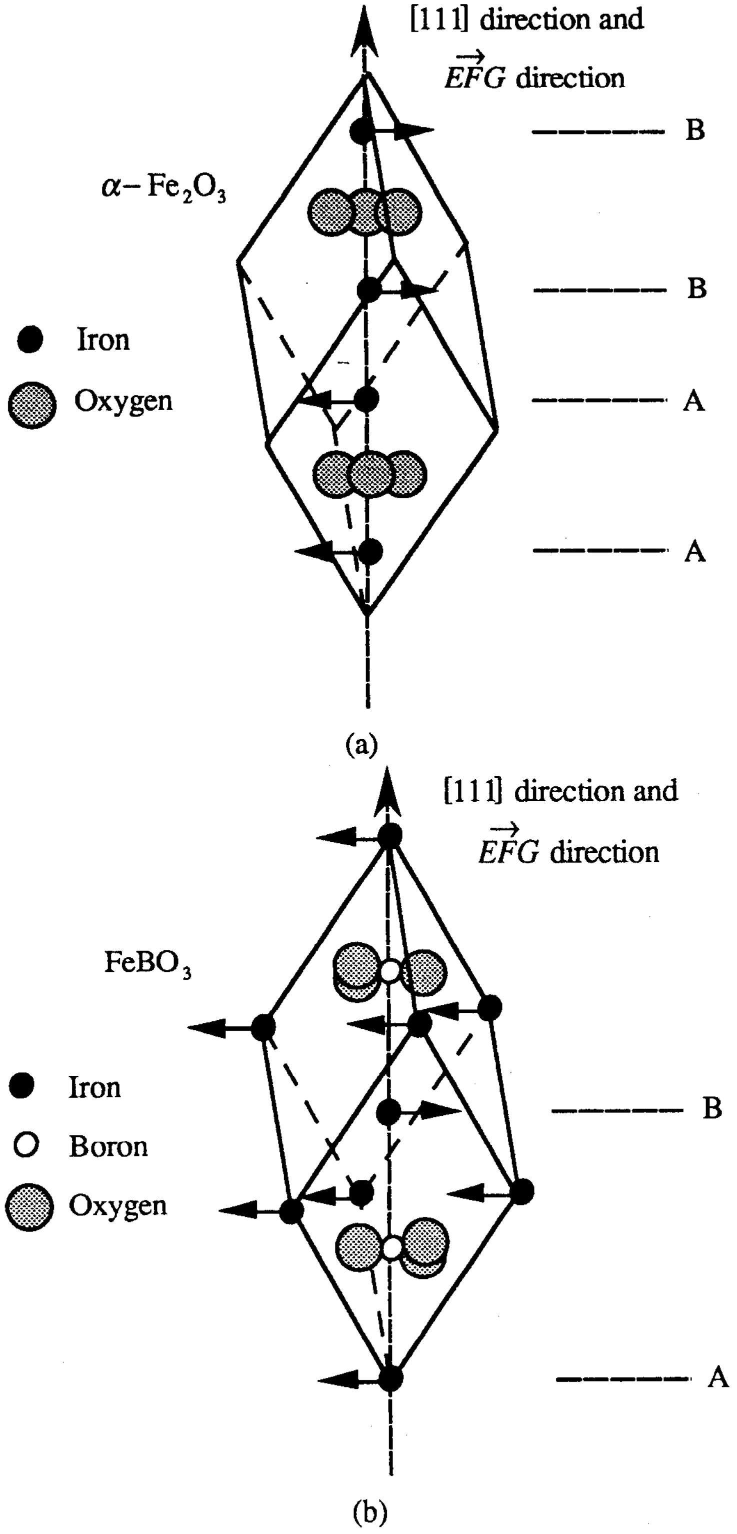

Fig. 8.1-1. Antiferromagnetic structure of (a) $\alpha-Fe_2O_3$ and (b) $FeBO_3$. The electric field gradients lie perpendicular to the (1 1 1) planes. Planes A and B have magnetic moments in antiparallel directions.

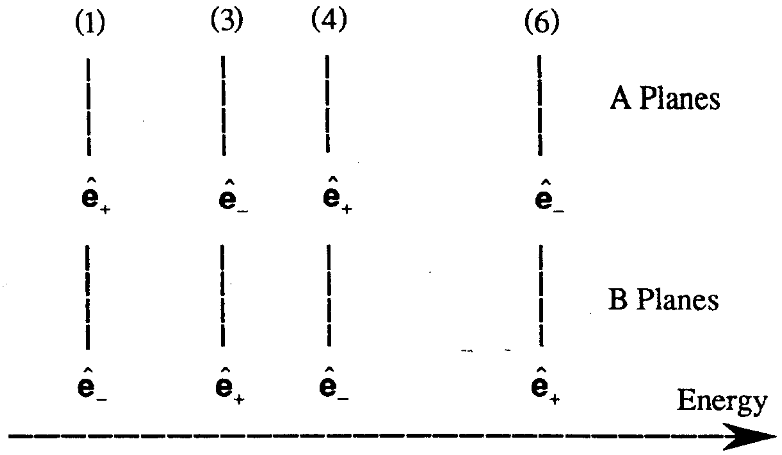

Fig. 8.1-2. Hyperfine energy spectrum illustrating the case where the applied magnetic field is perpendicular to the scattering plane (only hyperfine lines 1,3,4, and 6 are then possible). For small canting and Bragg angles, the polarization of each hyperfine line of the reflected field can be approximated as right and left circularly polarized: $\hat{e}_-$ and $\hat{e}_+$. Since the internal hyperfine fields are identical for the iron atoms in the A and B planes (except for the direction of the internal magnetic fields), the hyperfine lines from the two planes overlap with a 180° phase difference due to the position of atoms within the unit cell. However, due to polarization differences, there is no cancellation of the fields reflected from the two planes.

orthogonal--see Fig. 8.1-2). Complete cancellation of the reflected fields is then no longer possible.

YIG $(Y_3Fe_5O_{12})$ is the crystal examined in this thesis. Even though it has a cubic crystal structure, its unit cell is much more complex than the rhombohedral structure of the other crystals. YIG belongs to the space group Ia3d - O_h^{10}, and it has 96 O^{3-} ions located at the h - sites, 24 Y^{2+} located at the c - sites, and 40 Fe^{3+} ions located at the a and d - sites.[28] During the 1960's and 1970's when magnetic bubbles appeared to be a promising way to store megabytes of information, the technology was developed to grow high quality YIG crystal films on GGG (gadolinium gallium garnet) substrates by liquid-phase epitaxy methods. Because these YIG films can be grown nearly free of dislocations and other crystal defects and with very uniform lattice spacings, YIG is an attractive choice for nuclear resonant diffraction experiments.

YIG is a ferrimagnet below the Curie temperature of 559°K for ceramic materials and 549.2°K for YIG films grown from $PbO - V_2O_5$ fluxes.[29] The easy direction of magnetization is the [111] direction, though alignment fields of 100 Gauss are sufficient to orient the magnetic moments to the [001] direction. The d - site iron atoms are surrounded by a distorted oxygen tetrahedron stretched along a fourfold inversion axis oriented in the [001] direction, and the a - site iron atoms are surrounded by a distorted octahedron

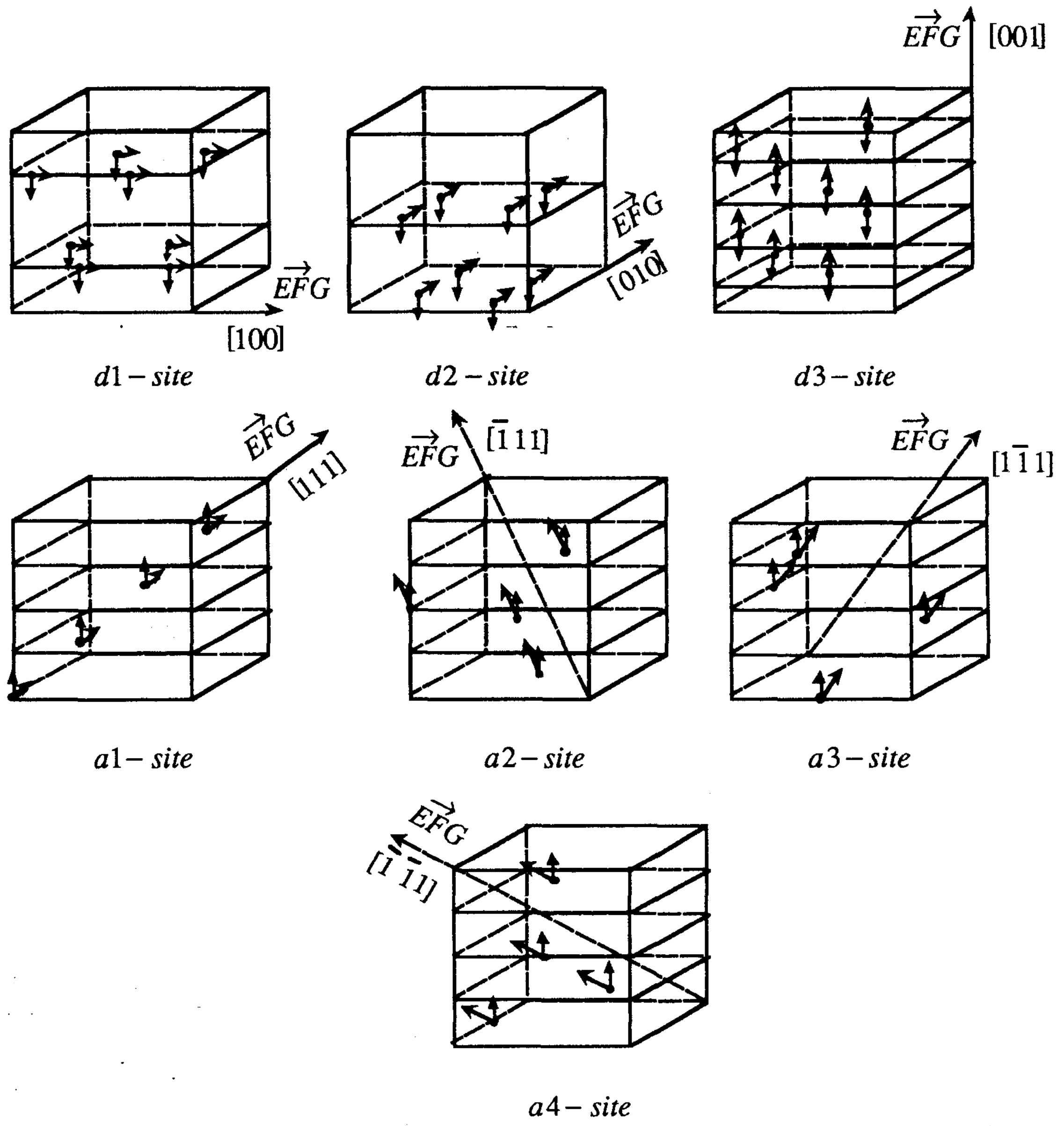

Fig. 8-1.3. Orientation of magnetic moments, (↑), and electric field gradients, (↑), for the seven magnetic sublattices of YIG. To orient the magnetic moments, there is an applied magnetic field in the [001] direction.

stretched along a threefold symmetry axis oriented in the [111] direction. The electric field gradients formed within these distorted oxygen polyhedra lie along the symmetry axis. The seven ferromagnetic sublattices within the YIG unit cell are shown in Fig. 8-1.3 with the orientation of the magnetic moments and electric field gradients.[30, 31]

For the experiments done in this thesis, crystal planes were chosen where all the a – site reflections were forbidden and all the d – site reflections were allowed except for the $d3$ – site. Therefore, ferromagnetic ordering was utilized to examine nuclear resonant scattering instead of antiferromagnetic ordering as was used for the $\alpha-\mathrm{Fe_2O_3}$ and $\mathrm{FeBO_3}$ crystals. Nonzero reflected fields now occur because of different electric quadrupole shifts between the $d-$sites rather than because of polarization differences that occur for antiferromagnetic crystals (See Fig. 8-1.4).

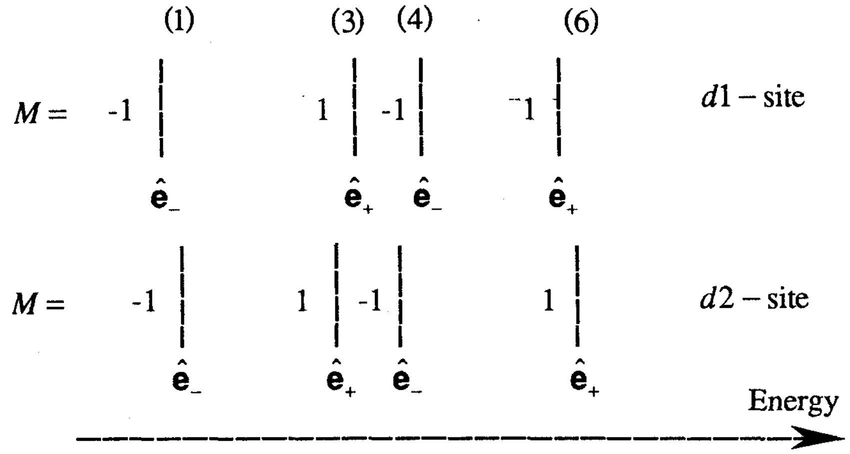

Fig. 8-1.4. Hyperfine energy spectrum illustrating the case where the applied magnetic field is parallel to the scattering plane.[32] For small Bragg angles the polarization of each hyperfine line can be approximated as right and left circularly polarized: $\hat{\mathbf{e}}_-$ and $\hat{\mathbf{e}}_+$. The magnetic moments of the two sites are parallel, but the electric field gradients are in perpendicular directions. This introduces small differences in the electric quadrupole field which show up as different quadrupole shifts in the hyperfine lines for each $d-$site.

8.2 Crystallography

To orient a general crystal for diffraction, an orientation matrix must be found that can perform the transformation of a vector in reciprocal space to an orthogonal lab coordinate system. Let there be a vector $\mathbf{v}$ in reciprocal space with basis axes $\left(\hat{\mathbf{a}}^*, \hat{\mathbf{b}}^*, \hat{\mathbf{c}}^*\right)$:

$$\mathbf{v} = \mathbf{h}^{\mathrm{T}}\hat{\mathbf{r}}^* = h\hat{\mathbf{a}}^* + k\hat{\mathbf{b}}^* + \ell\hat{\mathbf{c}}^* \qquad (8\text{-}2.1)$$

where $\hat{\mathbf{r}}^* = \hat{\mathbf{a}}^* + \hat{\mathbf{b}}^* + \hat{\mathbf{c}}^*$ is a unit radial vector in reciprocal space and $\mathbf{h}^{\mathrm{T}} = (h,k,\ell)$ is a row vector containing the Miller indices, or reciprocal space coordinates, of the reciprocal vector $\mathbf{v}$. Let the laboratory system have a fixed orthogonal basis $\left(\hat{\mathbf{x}}_L, \hat{\mathbf{y}}_L, \hat{\mathbf{z}}_L\right)$ (see Fig. 8-2.1). The problem is then to find the components of $\mathbf{v}$ in the lab space.

A solution can be found if there are three known reflections from the crystal. Then there are three reciprocal vectors $\mathbf{v}_1$, $\mathbf{v}_2$, and $\mathbf{v}_3$ which are known to point in some direction in lab space--their components in lab space are then known. This is summarized

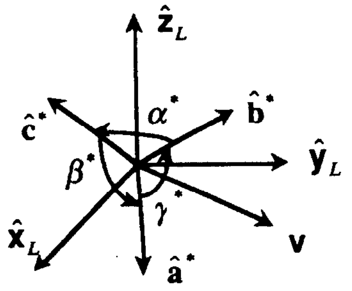

Fig. 8-2.1. Vector **v** in reciprocal and lab space.

by the following relation:[33]

$$\left.\begin{array}{l} \mathrm{v}_{1L}=\mathrm{v}_1 \\ \mathrm{v}_{2L}=\mathrm{v}_2 \\ \mathrm{v}_{3L}=\mathrm{v}_3 \end{array}\right\} \Rightarrow \begin{pmatrix} h_{1L} & k_{1L} & \ell_{1L} \\ h_{2L} & k_{2L} & \ell_{2L} \\ h_{3L} & k_{3L} & \ell_{3L} \end{pmatrix} \begin{pmatrix} \hat{\mathrm{x}}_L \\ \hat{\mathrm{y}}_L \\ \hat{\mathrm{z}}_L \end{pmatrix} = \begin{pmatrix} h_1 & k_1 & \ell_1 \\ h_2 & k_2 & \ell_2 \\ h_3 & k_3 & \ell_3 \end{pmatrix} \begin{pmatrix} \hat{\mathrm{a}}^* \\ \hat{\mathrm{b}}^* \\ \hat{\mathrm{c}}^* \end{pmatrix}$$

or
$$\mathbf{H}_L^{\mathrm{T}}\hat{\mathbf{r}}_L = \mathbf{H}^{\mathrm{T}}\hat{\mathbf{r}}^* \qquad (8.2\text{-}2)$$

(the superscript T denotes the transpose of the matrix, and vectors are always column vectors). The coordinate axes then transform as

$$\hat{\mathbf{r}}_L = \mathbf{U}'\hat{\mathbf{r}}^* \qquad (8\text{-}2.3)$$

where
$$\mathbf{U}' = \left(\mathbf{H}_L^{\mathrm{T}}\right)^{-1}\mathbf{H}^{\mathrm{T}}. \qquad (8\text{-}2.4)$$

From Eqs. 8-2.2 and 8-2.3, one also gets a relationship detailing how the coordinates transform:

$$\mathbf{h}_L^{\mathrm{T}}\mathbf{U}' = \mathbf{h}^{\mathrm{T}} \qquad (8\text{-}2.5)$$

which leads to

$$\mathbf{h}_L = \left(\mathbf{U}'^{-1}\right)^{\mathrm{T}}\mathbf{h} \qquad (8\text{-}2.6)$$

or
$$\mathbf{h}_L = \mathbf{U}\mathbf{h} \qquad (8\text{-}2.7)$$

where
$$\mathbf{U} = \mathbf{H}_L\mathbf{H}^{-1}. \qquad (8\text{-}2.8)$$

As expected, the coordinates transform in an inverse way to the axes since $\mathbf{U}^{\mathrm{T}} = \mathbf{U}'^{-1}$. Thus, from a knowledge of the elements of $\mathbf{H}_L$ and $\mathbf{H}^{-1}$ for three reciprocal vectors, the components of any reciprocal vector can be obtained in terms of lab coordinates by using Eq. 8-2.7.

The determination of the orientation matrix can be simplified if a primary reflection, $\mathbf{h}_p$, is known and a secondary reflection, $\mathbf{h}_s$, lies in the scattering plane such that $\mathbf{h}_s \cdot \mathbf{k}_f > 0$ where $\mathbf{k}_f$ is the scattered wavector of the primary reflection (see Fig. 8-2.2). The third reciprocal vector can be found by taking the cross product between the primary

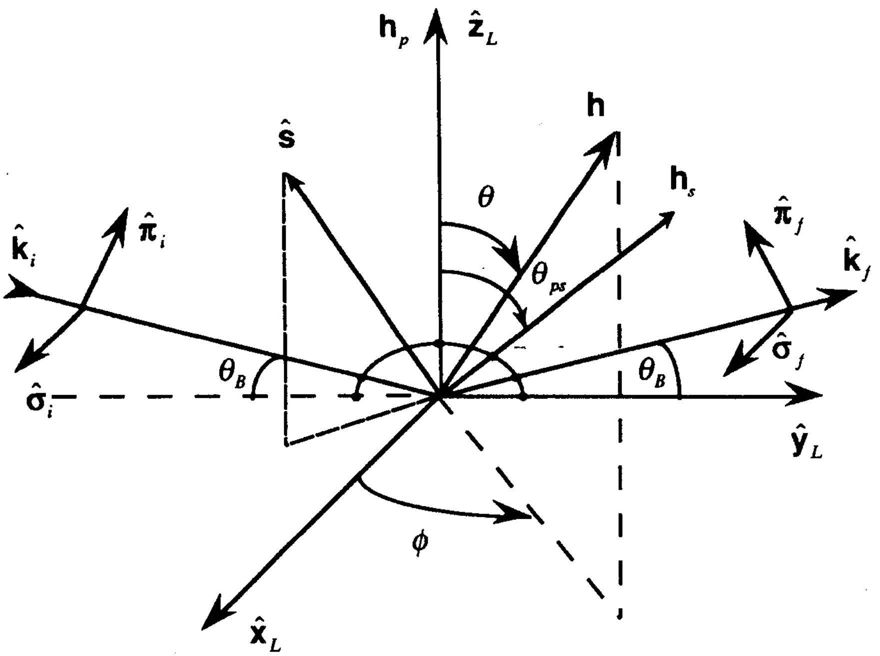

Fig. 8-2.2. Orientation geometry for diffraction. $\mathbf{k}_i, \mathbf{k}_f, \mathbf{h}_p, \mathbf{h}_s, \hat{\mathbf{y}}_L$, and $\hat{\mathbf{z}}_L$ all lie in the scattering plane. $\mathbf{k}_f$ diffracts from planes perpendicular to $\mathbf{h}_p$, $\mathbf{h}_p$ is parallel to $\hat{\mathbf{z}}_L$, $\hat{\mathbf{x}}_L$ is perpendicular to the scattering plane, and $\hat{\mathbf{s}}$ is the outward surface normal of the crystal. $(\hat{\mathbf{x}}_L, \hat{\mathbf{y}}_L, \hat{\mathbf{z}}_L)$ lab system is fixed in space and never rotates--same for $\mathbf{k}_i$ since it comes from a fixed source. $\mathbf{h}_p, \mathbf{h}_s, \mathbf{k}_f$, and $\hat{\mathbf{s}}$ all rotate with crystal as it is oriented in space. $\mathbf{h}$ is the desired reflection and is always eventually oriented to lie in the $\hat{\mathbf{z}}_L$-direction.

and secondary reciprocal vectors. Cross products can be done only in spaces with an orthonormal basis, therefore, for crystals with noncubic structure, such as rhombohedral crystals, one must project the reciprocal basis onto an orthonormal basis, then take the cross product, and then project the results back into reciprocal space. The matrix that transforms a reciprocal vector to an orthogonal space with basis $(\hat{\mathbf{x}}_0, \hat{\mathbf{y}}_0, \hat{\mathbf{z}}_0)$ is[34, 35]

$$\mathbf{B} = \begin{pmatrix} a^* & b^* \cos\gamma^* & c^* \cos\beta^* \\ 0 & b^* \sin\gamma^* & -c^* \sin\beta^* \cos\alpha \\ 0 & 0 & 1/c \end{pmatrix} \qquad (8\text{-}2.9)$$

$$\mathbf{B}^{-1} = \begin{pmatrix} a\sin\beta\sin\gamma^* & -a\sin\beta\cos\gamma^* & a\cos\beta \\ 0 & b\sin\alpha & b\cos\alpha \\ 0 & 0 & c \end{pmatrix} \qquad (8\text{-}2.10)$$

where $(\hat{\mathbf{a}}, \hat{\mathbf{b}}, \hat{\mathbf{c}})$ are the direct crystal axes with interaxis angles α, β, γ where $\cos\alpha = \hat{\mathbf{b}} \cdot \hat{\mathbf{c}}$, $\cos\beta = \hat{\mathbf{c}} \cdot \hat{\mathbf{a}}$, $\cos\gamma = \hat{\mathbf{a}} \cdot \hat{\mathbf{b}}$, and $(\hat{\mathbf{a}}^*, \hat{\mathbf{b}}^*, \hat{\mathbf{c}}^*)$ are the reciprocal lattice axes with interaxis reciprocal angles α^*, β^*, γ^* defined in a similar manner. In the orthogonal space $\hat{\mathbf{x}}_0$, $\hat{\mathbf{y}}_0$, $\hat{\mathbf{a}}^*$, and $\hat{\mathbf{b}}^*$ all lie in a plane perpendicular to $\hat{\mathbf{z}}_0$, and $\hat{\mathbf{a}}^*$ is parallel to $\hat{\mathbf{x}}_0$.

A third reflection is then

$$\mathbf{h}_3 = \mathbf{h}_p \times \mathbf{h}_s = \mathbf{B}^{-1}\left[\left(\mathbf{B}\mathbf{h}_p\right) \times \left(\mathbf{B}\mathbf{h}_s\right)\right]. \tag{8-2.11}$$

From Fig. 8-2.2, the lab coordinates of the reciprocal vectors can easily be seen. The primary reflection is in the $\hat{\mathbf{z}}_L$-direction, the third reflection is in the $\hat{\mathbf{x}}_L$-direction, and the secondary reflection is

$$\mathbf{h}_{sL} = \left|\mathbf{h}_s\right|\left(\sin\theta_{ps}\hat{\mathbf{y}}_L + \cos\theta_{ps}\hat{\mathbf{z}}_L\right) \tag{8-2.12}$$

where

$$\cos\theta_{ps} = \mathbf{h}_p \cdot \mathbf{h}_s / \left|\mathbf{h}_p\right|\left|\mathbf{h}_s\right|. \tag{8-2.13}$$

To take the dot product of two vectors in a nonorthogonal basis, the two vectors must again be transformed to an orthogonal space in which the dot product can be properly taken:

$$\mathbf{h}_p \cdot \mathbf{h}_s = \left(\mathbf{B}\mathbf{h}_p\right)^{\mathrm{T}} \cdot \left(\mathbf{B}\mathbf{h}_s\right). \tag{8-2.14}$$

Note that the dot product relationship gives the metric for reciprocal space:

$$\mathbf{B}^{\mathrm{T}}\mathbf{B} = \begin{pmatrix} \mathbf{a}^* \cdot \mathbf{a}^* & \mathbf{a}^* \cdot \mathbf{b}^* & \mathbf{a}^* \cdot \mathbf{c}^* \\ \mathbf{a}^* \cdot \mathbf{b}^* & \mathbf{b}^* \cdot \mathbf{b}^* & \mathbf{b}^* \cdot \mathbf{c}^* \\ \mathbf{a}^* \cdot \mathbf{c}^* & \mathbf{b}^* \cdot \mathbf{c}^* & \mathbf{c}^* \cdot \mathbf{c}^* \end{pmatrix} = \mathbf{G}^{-1}. \tag{8-2.15}$$

The dot product can then be written in the familiar way for the dot product of two vectors within a space defined by a metric $\mathbf{G}$:

$$\mathbf{h}_p \cdot \mathbf{h}_s = h_{p\mu} G^{\mu\nu} h_{s\nu} \tag{8-2.16}$$

where $h_{p\mu}$ and $h_{s\nu}$ are the covariant components of the vectors $\mathbf{h}_p$ and $\mathbf{h}_s$ (that is, they are the components of those vectors in reciprocal space), and $G^{\mu\nu}$ are the contravariant elements of the metric for the direct crystal axes space (that is, they are the elements of the reciprocal space metric $\mathbf{G}^{-1}$). The cross product given in Eq. 8-2.11 can also be written in terms of the metric as[36]

$$\left(\mathbf{h}_p \times \mathbf{h}_s\right)_\ell = G_{\ell i}\varepsilon^{ijk} h_{pj} h_{sk} \tag{8-2.17}$$

where ε^{ijk} is the contravariant antisymmetric tensor for a space with metric $\mathbf{G}^{-1}$:

$$\varepsilon^{ijk} = \begin{cases} \sqrt{\det\left|\mathbf{G}^{-1}\right|} & \text{if } i,j,k \text{ is a cyclic permutation of } 1,2,3 \\ -\sqrt{\det\left|\mathbf{G}^{-1}\right|} & \text{if } i,j,k \text{ is a cyclic permutation of } 2,1,3 \\ 0 & \text{otherwise} \end{cases} \tag{8-2.18}$$

and $G_{\ell i}$ are the covariant elements of the metric for the direct crystal axes space (that is, they are the elements of the metric $\mathbf{G}$).

The orientation matrix $\mathbf{U}$ can now be constructed since $\mathbf{H}_L$ and $\mathbf{H}$ are completely determined:

$$\mathbf{H}_L = \begin{pmatrix} 0 & 0 & \left|\mathbf{h}_3\right| \\ 0 & \left|\mathbf{h}_s\right|\sin\theta_{ps} & 0 \\ \left|\mathbf{h}_p\right| & \left|\mathbf{h}_s\right|\cos\theta_{ps} & 0 \end{pmatrix} \tag{8.2-19}$$

$$\mathbf{H} = \begin{pmatrix} h_p & h_s & h_3 \\ k_p & k_s & k_3 \\ \ell_p & \ell_s & \ell_3 \end{pmatrix} \tag{8-2.20}$$

and

$$\mathbf{U} = \mathbf{H}_L\mathbf{H}^{-1}. \tag{8-2.21}$$

The Fortran code, **Orient_cryst**, embodying all of this section's discussion on orienting a general crystal follows. The subroutine uses the same framework as Busing and Levy's Algol program designed for 3 and 4-circle diffractometers.[35] In addition to what has been discussed, the subroutine can perform rotations about the desired reflection, $\mathbf{h}$, and rotations about the incoming photon direction, $\mathbf{k}_i$, that preserve the Bragg condition.

The subroutine must be linked with another subroutine package called EIS_LIN_PACK. This package contains the popular LINPACK code for solving simultaneous equations and the EISPACK code for solving eigenvalue problems.[37, 38] They were obtained from the National Energy Software Center at Argonne National Laboratory. The subroutine **Lineq** in LINPACK was used to find the inverse matrix $\mathbf{H}^{-1}$ for constructing the orientation matrix.

In the Fortran code below, and in the EWALD code that follows later, to preserve space, several lines of code are piled up onto a single line. A semicolon (never used in actual Fortran code) separates each line of code.

```
      Subroutine Orient_cryst(Ee,a,alpha,hp,hs,h,S,Uo,sigmai,pii,sigmaf,pif,b)
c This Subroutine sets up the Crystal Orientation for Diffraction. Uo is the Net Orientation Matrix -- to
c Transform any Reciprocal Lattice Vector to the Orthogonal Lab Coordinate System, Operate Uo on it:
c                          V_lab = Uo(dot)V_recip.
c VARIABLES:
c  a(i) = Crystal Lattice Spacings a,b,c (cm) ; alpha(i) = Crystal Lattice angles alpha,beta,gamma (deg)
c  Vo = Unit Cell Volume (cm**3)  ; Ee = Incoming Photon Energy (Ev) ; hp,hs = Primary and Secondary
c  Reciprocal Lattice Vectors  ; S = Outward Surface Direction  ; h = Desired Reciprocal Lattice Scattering
c  Vector  ; Ki,Kf = Incoming and Diffracted wavectors (1/Angstrom)  ; sigma,pi = sigma and pi
c  polarization vectors  ; Bragg = Bragg Angle (radians)  ; b = Asymmetry Factor
c  PhiKi,phiH = azimuthal rotation angles about Ki and h directions (deg)
c  psi = azimuthal rotation angle about h after azimuthal rotation about Ki has been done.
c  NOTE:
c(1)  The Lab coordinate system is determined by Ki and its polarization vectors.
c(2)  PhiKi = rotation of a plane perpendicular to Ki direction. For example, phiKi = 90 deg ==> h rotates
c         from Lab_z to a vector lying in [Lab_x,Lab_y] plane.  PhiH = azimuthal rotation of plane
c         perpendicular to h direction.  PhiKi,PhiH rotations both preserve Bragg's Condition.
c  LINK:     Link with EIS_LIN_PACK
c D.E.Brown 1990            (SSRL/STANFORD)
     Real*8    **Everything possible** (all Matrices are 3x3 arrays)
      Common /stup/ hbarc,sinBragg,Vo,phiKi,phiH,psi,Ki,Kf,kis
     Common /Lab/ x_Lab,y_Lab,z_Lab  ;  Common /conv/ rad,pi
c Construct a matrix Bo that transforms from non-orthogonal axes to an orthogonal axes system.
c Boi is the inverse of Bo.
     Call Generate_Bo(a,alpha,Vo,Bo,Boi)
c Determining angle between hs and hp which gives orientation of hs in Lab coordinate system
     Call General_Dot(hp,hp,Bo,hpp)  ; Call General_Dot(hs,hs,Bo,hss)
     Call General_Dot(hp,hs,Bo,hps)  ; Call General_Dot(S,S,Bo,ss)
     hpp = Dsqrt(hpp)  ; hss = Dsqrt(hss)  ; ss  = Dsqrt(ss)
     cosps = hps/(hpp*hss)      ! angle between hs and hp  ; sinps = Dsqrt(1.0d0 - cosps**2)
c To construct a third vector, take cross product of hs and hp
     Call General_Cross(hs,hp,Bo,Boi,h3)  ; Call General_Dot(h3,h3,Bo,h33)  ; h33 = Dsqrt(h33)
c One can now construct the Orientation Matrix U that transforms any vector in reciprocal coordinate space to
c the Lab coordinate space. Note that: hp is in Lab_z direction, hs = cosps(Lab_z) + sinps(Lab_y), and h3 is in
c Lab_x direction.
      Call Lab_Vectors(hpp,hss,h33,sinps,cosps,hplab,hslab,h3lab)
      Call Orientation(hp,hs,h3,hplab,hslab,h3lab,U)
c Computation of the Bragg angle of the Desired Reflection.  Note that hmag = 1.0/d(hkl) ,
c where d(hkl) = interplaner spacing for indices h,k,l (units = angstroms)
     Call General_Dot(h,h,Bo,hmag)           ; hmag = Dsqrt(hmag)
     sinBragg = pi*hbarc*hmag*1.0d8/Ee  ; cosBragg = Dsqrt(1.0 - sinBragg**2)
c The h reflection is desired. Then rotate h so that is is pointing in the Lab_z direction--h will point in the
c direction hp used to be directed. To Do this, transform h to Lab system, h --> Uh = hLab.  From its polar and
c azimuthal angles, one can now rotate h to point in the Lab_z direction--and one can rotate all of the other
c vectorsattached to the crystal system with rotatation matrix Rz.
      Call Mv(U,h,hLab)  ; Call Polar(hLab,x_Lab,y_Lab,z_Lab,theta,phi)  ; Call Generate_Rz(theta,phi,Rz)
c Now, the crystal can be rotated about h and Ki and still preserve the Bragg condition.  The Rkh matrix
c performs this rotation.  First the crystal is rotated azimuthally about h, and then azimuthally about Ki.  The
c Rpsi matrix performs an addition azimuthal rotation about h after the rotation Rkh has been done (necessary
c only when a rotation about Ki has been done). Uo is the Net Orientation Matrix. First it transforms reciprocal
c lattic vector to Lab system.  Then it rotates it by Rz in aligning h to point in the +z_Lab direction.  Then it
c makes Rkh Bragg preserving rotation.
      Call Generate_Rkh(phiH*rad,phiKi*rad,cosBragg,sinBragg,Rkh)  ; Call MM(Rz,U,dum2)
      If(phiKi .Eq. 0.0) Then  ; Call MM(Rkh,dum2,Uo)     ! Uo is the Net Orientation Matrix
      Else  ; Call Generate_Rpsi(psi*rad,Rz,Rkh,hLab,Rpsi)  ; Call MM(Rkh,dum2,dum3)  ; Call MM(Rpsi,dum3,Uo)
      Endif
c The Diffracted wavevector can now be determined from Bragg's law h = Kf - Ki, as well as the asymmetry
c factor b = ki(dot)n/Kf(dot)n where n = inward surface normal.
      Call Mv(Uo,h,hLab)  ; Call Mv(Uo,S,SLab)  ; Ko = Ee*1.0d-8/hbarc
      Do 1 I=1,3
        Ki(i) = Ko*(cosBragg*y_Lab(i) - sinBragg*z_Lab(i))  ; Kf(i) = 2.0*pi*hLab(i) + Ki(i)
  1     pii(i) = sinBragg*y_Lab(i) + cosBragg*z_Lab(i)        ; sigmai(i) = x_Lab(i)
      Call Cross(Kf,z_Lab,sigmaf,norm)          !diffracted sigma polarization
      Call Cross(sigmaf,Kf,pif,norm)            !diffracted pi polarization
```

```
    Call Dot(Ki,SLab,kis) ; Call Dot(Kf,SLab,kfs) ; b = kis/kfs ; kis = kis/(ss*Ko)
    Do 5 I=1,3
5    Ki(i) = Ki(i)/Ko ; Kf(i) = Kf(i)/Ko
    Return
    End
***********************************************************************************************
    Subroutine Generate_Rz(theta,phi,Rz)
c This subroutine rotates crystal so that the desired reciprocal lattice scattering vector is in the Lab_z direction.
c Rz = the rotation matrix that does this. First, crystal is rotated azimuthally by phi so that desired vector lies in
c (+x_Lab,+z_Lab) plane. Then, crystal is rotated polarly by theta so that the vector lies points in the +z_Lab
c direction.
    cost = Dcos(theta)   ; sint = Dsin(theta) ; cosp = Dcos(phi)   ; sinp = Dsin(phi)
    Rz(1,1) = cost*cosp  ; Rz(2,1) = -sinp    ; Rz(3,1) = sint*cosp
    Rz(1,2) = cost*sinp  ; Rz(2,2) = cosp     ; Rz(3,2) = sint*sinp
    Rz(1,3) = -sint      ; Rz(2,3) = 0.0d0    ; Rz(3,3) = cost
    Return
***********************************************************************************************
    Subroutine Generate_Rkh(pH,pK,cosb,sinb,Rkh)
c This subroutine constructs Rotation Matrix Rkh that performs Bragg-preserving rotations first by pH about
c the reciprocal scattering vector and then by pK about the incident photon direction. All rotations obey right
c hand rule.
    cosh = Dcos(pH)      ; sinh = Dsin(pH) ; cosk = Dcos(pK)    ; sink = Dsin(pK)
     Rkh(1,1) =  cosk*cosh + sinb*sink*sinh ; Rkh(2,1) = -sinb*sink*cosh + (sinb**2*cosk + cosb**2)*sinh
     Rkh(3,1) = -cosb*sink*cosh + cosb*sinb*(cosk - 1.0d0)*sinh
     Rkh(1,2) = -cosk*sinh + sinb*sink*cosh ; Rkh(2,2) =  sinb*sink*sinh + (sinb**2*cosk + cosb**2)*cosh
     Rkh(3,2) =  cosb*sink*sinh + cosb*sinb*(cosk - 1.0d0)*cosh
     Rkh(1,3) =  cosb*sink ; Rkh(2,3) =  cosb*sinb*(cosk - 1.0d0) ; Rkh(3,3) =  cosb**2*cosk + sinb**2
    Return
***********************************************************************************************
     Subroutine Generate_Rpsi(psi,Rz,Rkh,h,Rpsi)
c This subroutine does a crystal plane normal rotation--that is, a rotation about the scattering vector h. The
c Zs-direction is in the h-direction, Xs = h(cross)z_lab, Ys = h(cross)Xs.
     Call Mv(Rz,h,dum)  ! Rotate h to Lab_z direction ; Call Mv(Rkh,dum,h)  ! Rotate h around itself and Ki
     hx = h(1) ; hy = h(2) ; hz = h(3) ; d1 = Dsqrt(hx**2 + hy**2) ; d2 = Dsqrt(hx**2 + hy**2 + hz**2)
c Transform to [Xs,Ys,Zs] system
     R(1,1) =  hy/d1  ; R(2,1) =  hz*hx/(d1*d2)            ; R(3,1) =  hx/d2
     R(1,2) = -hx/d1  ; R(2,2) =  hz*hy/(d1*d2)            ; R(3,2) =  hy/d2
     R(1,3) =  0.0d0  ; R(2,3) = -(hx**2 + hy**2)/(d1*d2)  ; R(3,3) =  hz/d2
c Perform azimuthal psi rotation in [Xs,Ys] plane (right-handed sense)
     Rpsi(1,1) =  Dcos(psi) ; Rpsi(2,1) =  Dsin(psi) ; Rpsi(3,1) =  0.0d0
     Rpsi(1,2) = -Dsin(psi) ; Rpsi(2,2) =  Dcos(psi) ; Rpsi(3,2) =  0.0d0
     Rpsi(1,3) =  0.0d0     ; Rpsi(2,3) =  0.0d0     ; Rpsi(3,3) =  1.0d0
c Inverse Transform back to Lab [Note that R(inverse) = R(transpose) since R is an orthogonal matrix]
     RT(1,1) =  hy/d1              ; RT(2,1) = -hx/d1              ; RT(3,1) =  0.0d0
     RT(1,2) =  hz*hx/(d1*d2)      ; RT(2,2) =  hz*hy/(d1*d2)      ; RT(3,2) = -(hx**2 + hy**2)/(d1*d2)
     RT(1,3) =  hx/d2              ; RT(2,3) =  hy/d2              ; RT(3,3) =  hz/d2
     Call MM(Rpsi,R,dum1)          ; Call MM(RT,dum1,Rpsi)
     Return
***********************************************************************************************
      Subroutine Generate_Bo(a,alpha,Vo,Bo,Boi)
c This subroutine generates the matrix Bo that transforms crystal reciprocal lattice vectors from their crystal
c bases system to an orthogonal coordinate system. In this way dot and cross products of reciprocal lattice
c vectors can be performed.
c VARIABLES:
c  b(i) = Reciprocal Lattice Spacings a*,b*,c* (1/cm) ; cosb(i) = Cosine of Reciprocal Lattice Angles
c  alpha*,beta*,gamma* ; Boi(i,j) = Inverse of Bo(i,j) ; Vo = Volume of Unit Cell (cm**3)
     Common /conv/ rad
     Do 1 I=1,3
       a(i) = a(i)*1.0d8         ! Conversion from cm to Angstroms ; cosa(i) = Dcos(alpha(i)*rad)
1      sina(i) = Dsin(alpha(i)*rad)
      V = Dsqrt(1.0d0 - cosa(1)**2 - cosa(2)**2 - cosa(3)**2 + 2.0*cosa(1)*cosa(2)*cosa(3))
      Vo = V*a(1)*a(2)*a(3)*(1.0d-8)**3
      Do 5 I=1,3
        j = i + 1 ; If(j .Gt. 3) j = 1 ; k = j + 1 ; If(k .Gt. 3) k = 1
```

```
      cosb(i) = (cosa(j)*cosa(k) - cosa(i))/(sina(j)*sina(k))  ;  sinb(i) = Dsqrt(1.0d0 - cosb(i)**2)
5     b(i)   = sina(i)/(a(i)*V)
    Bo(1,1) =  b(1)                   ; Bo(2,1) =  0.0d0                  ; Bo(3,1) =  0.0d0
    Bo(1,2) =  b(2)*cosb(3)           ; Bo(2,2) =  b(2)*sinb(3)           ; Bo(3,2) =  0.0d0
    Bo(1,3) =  b(3)*cosb(2)           ; Bo(2,3) = -b(3)*sinb(2)*cosa(1)   ; Bo(3,3) =  1.0d0/a(3)
    Boi(1,1) =  1.0d0/b(1)            ; Boi(2,1) =  0.0d0                 ; Boi(3,1) =  0.0d0
    Boi(1,2) = -a(1)*sina(2)*cosb(3)  ; Boi(2,2) =  a(2)*sina(1)          ; Boi(3,2) =  0.0d0
    Boi(1,3) =  a(1)*cosa(2)          ; Boi(2,3) =  a(2)*cosa(1)          ; Boi(3,3) =  a(3)
    Return
****************************************************************************************************
    Subroutine Orientation(h1,h2,h3,h1L,h2L,h3L,U)
c This subroutine constructs the Orientation Matrix U that allows one to transform from the crystal reciprocal
c coordinate space to Lab orthogonal coordinate space: (Lab vector) V_lab = U (dot) V_recip.
    nd = 3  ! # of rows  ;  nr = 3  ! # of columns  ;  n = 3  ! order of matrix
    Do 1 I=1,3
      H(i,1) = h1(i)    ;  H(i,2) = h2(i)    ;  H(i,3) = h3(i)
      HL(i,1) = h1L(i)  ;  HL(i,2) = h2L(i)  ;  HL(i,3) = h3L(i)
      Do 1 J=1,3
1       b(i,j) = 0.0d0
    b(1,1) = 1.0d0    ;  b(2,2) = 1.0d0    ;  b(3,3) = 1.0d0
    Call Lineq(H,b,Hinv,nd,n,nr,aa,ierr)  ;  Call MM(HL,Hinv,U)
    Return
****************************************************************************************************
    Subroutine Lab_Vectors(hpp,hss,h33,sinps,cosps,h1,h2,h3)
c This subroutine uses the reciprocal lattice vectors in reciprocal space to construct Lab vectors in Lab space.
c Note that this subroutine has taken a special case -- 2 reciprocal lattice vectors lie in the scattering plane and
c one points in the Lab_z direction.  However, if one were to know beforehand the directions of all 3
c vectors h1,h2,h3 in lab space (pointing in general directions), their lab components could be inserted in this
c subroutine, and no other modifications need be done in this program (except some calculations are no longer
c necessary, such as calculating sinps,cosps,etc. ).
c hpp = magnitude of hp, hss = magnitude of hs, h33 = mag. of h3
    Common /Lab/ x_Lab,y_Lab,z_Lab
    h1(1) = 0.0d0  ;  h1(2) = 0.0d0       ;  h1(3) = hpp
    h2(1) = 0.0d0  ;  h2(2) = hss*sinps   ;  h2(3) = hss*cosps
    h3(1) = h33    ;  h3(2) = 0.0d0       ;  h3(3) = 0.0d0
    x_Lab(1) = 1.0d0  ;  x_Lab(2) = 0.0d0  ;  x_Lab(3) = 0.0d0
    y_Lab(1) = 0.0d0  ;  y_Lab(2) = 1.0d0  ;  y_Lab(3) = 0.0d0
    z_Lab(1) = 0.0d0  ;  z_Lab(2) = 0.0d0  ;  z_Lab(3) = 1.0d0
    Return
****************************************************************************************************
    Subroutine General_Cross(u,v,B,Bi,uv)
c This subroutine takes the general cross product of vectors u,v defined in a non-orthogonal coordinate system.
c Bi = inverse of B
    Call Mv(B,u,Bu)        ;  Call Mv(B,v,Bv)  ;  Call Cross(Bu,Bv,BuBv,norm)  ;  Call Cross(u,v,uv,uvmag)
    Call Mv(Bi,BuBv,uv)  ;  Call Dot(uv,uv,norm)
    Do 1 I=1,3                                ! Giving uv a magnitude equal
1     uv(i) = uvmag*uv(i)/Dsqrt(norm)         ! to magn. of cross product of indices of u,v
    Return
****************************************************************************************************
    Subroutine General_Dot(u,v,B,uv)
c This subroutine takes the general dot product of vectors u,v defined in a non-orthogonal coordinate system.
    Call Mv(B,u,Bu)  ;  Call Mv(B,v,Bv)  ;  Call Dot(Bu,Bv,uv)
    Return
****************************************************************************************************
    Subroutine Polar(v,x,y,z,theta,phi)
c  This Subroutine determines the azimuthal and polar angles of a vector "v" in a coordinate system with basis
c vectors x,y,z theta = polar angle, phi = azimuthal angle      -180 < phi < 180,  0 < theta < 180
****************************************************************************************************
    Subroutine MM(A,B,C)
c This subroutine performs matrix multiplication C = A*B
****************************************************************************************************
    Subroutine Mv(A,x,Ax)
c This subroutine multiplies column vector x by 3x3 matrix A to obtain column vector Ax :   Ax = A*x
****************************************************************************************************
```

```
      Subroutine Cross(u,v,w,norm)
c This Subroutine computes the Cross Product of two vectors "u" and "v" in orthogonal space.  Returns a unit
c vector "w" and its length "norm"
**************************************************************************************************************
      Subroutine Dot(u,v,w)
c This Subroutine computes the Dot product of two vectors "u" and "v" in orthogonal space:   w = u*v
**************************************************************************************************************
```

8.3 Ewald Program

The EWALD code that follows computes the reflection and transmission amplitudes from a crystal using the Ewald-Laue dynamical diffraction theory.[39-41] The main program **Ewald** controls the calculation by calling the appropriate subroutines. An initialization subroutine is called (Initialize) to set up the dynamical diffraction calculation, and instructions are returned (via iflg) to compute either an energy or angle spectrum over a desired range. Program Ewald then makes calls to subroutine Dispersion at each appropriate energy or angle value. Dispersion returns the reflection and transmission coefficients R and T directly, and it returns the reflected and transmitted electric field amplitudes indirectly through the common block /ts/. When energy spectra are calculated, time spectra can also be determined by taking the Fourier transform of the electric field amplitudes. Since fast Fourier transform routines are quite ubiquitous, the routine that did calculations for EWALD is not shown here--the actual routine used was an adapted version of Brigham's well known Fortran code.[42]

Subroutine **Initialize** reads in the relevant information contained in the files nuclear.dat and atompos.dat, and it initializes physical constants to be used in further calculations. The important physical constants pertinent to ^{57}Fe used in EWALD are the total lifetime, 140.95 nsecs,[43] the internal conversion coefficient, 8.23,[43] and the magnetic moments of the ground and excited states: 0.09024 nm and -0.1549 nm. The ground state magnetic moment was measured by Locher and Geschwind though electron-nuclear double resonance techniques[44] while the excited state magnetic moment was found by Preston, Hanna, and Heberle through Mössbauer measurements.[45]

Calls are made to **Orient_cryst** to get the orientation matrix, U, and, for each site, to **YIG_basis** to construct the quantum coordinate system (Hx,Hy,Hz) where Hz is in the direction of the internal magnetic field. Thus, for multi-site crystals, no universal quantum axis is constructed--their internal magnetic field defines what type of scattering occurs. Using the orientation matrix, the quantum coordinate system, and the information from the data files, an eigenvector representing the nuclear scattering tensor elements for each polarization combination, quantum level, and site is constructed along with associated eigenvalues. **Eigenvector** is essentially $\mathbf{g}^{\mathrm{HS}}/2$ in Eq. 7-2.1 for magnetic dipole scattering without the resonance denominator.

ElectStrFact is also called to compute the photoelectric structure factor (the contents of the subroutine are not shown here since the calculations are straightforward). Since the photoelectric structure factor is essentially constant over the energy range of the hyperfine nuclear resonance, $\approx 10^{-6}\,\mathrm{eV}$, they only need to be calculated once. In computing the photoelectric structure factor presented in Eq. 7-2.2, the value for f_0 came from a mean atomic scattering factor (calculated from self-consistent or variational wavefunctions) tabulated in International Tables for X-Ray Crystallography[46] and in Warren.[47] The value for f' came from a database (set up by Sean Brennan at SSRL) of Cromer and Liberman's relativistic Hartree-Fock calculations,[48] and the value for f'' came from a compilation of x-ray cross section measurements contained in McMaster.[49] Compton scattering was also included by adding the incoherent cross section values contained in McMaster to f''. Since the anomalous scattering factors, f' and f'', are insensitive to the scattering angle when operating far from any absorption edge or bound state resonance, the angular dependence of these terms was neglected.

Subroutine **Polarmat** constructs photoelectric and nuclear magnetic dipole polarization matrices for the incident and scattered electric fields. The photoelectric polarization matrix is equivalent to the Thomson polarization matrix given by Eq. 5-1.3. Construction of the magnetic dipole polarization matrix is more involved. Once the spherical unit vectors are calculated through the appropriate cross products outlined in Section 5.1, the vector spherical harmonics can be constructed. Translating from program symbols to those used in Section 5.1:

$$\mathsf{Y10i} = \sqrt{8\pi/3}\,\mathbf{Y}_{10}^{(0)}\left(\Omega_{\mathbf{k}_i}\right) = i\sin\theta_{\mathbf{k}_i}\hat{\boldsymbol{\phi}}_{\mathbf{k}_i} \tag{8-3.1}$$

$$\mathsf{Y11i} = \sqrt{16\pi/3}\,\mathbf{Y}_{11}^{(0)}\left(\Omega_{\mathbf{k}_i}\right) = e^{i\phi_{\mathbf{k}_i}}\left(\hat{\boldsymbol{\theta}}_{\mathbf{k}_i} + i\cos\theta_{\mathbf{k}_i}\hat{\boldsymbol{\phi}}_{\mathbf{k}_i}\right). \tag{8-3.2}$$

If nuclear level mixing did not occur, then the final polarization matrices could be constructed in the form given by Eq. 5-1.5. However, to include nuclear level mixing the matrices must be constructed as described in Section 5.2 and given by Eq. 5-2.30. Therefore, **Polarmat** only finds all of the possible dot products between polarizations and vector spherical harmonics in preparation for making the final polarization matrix given by Eq. 5-2.30.

The coefficients c_{nq} in Eq. 5-2.29 are calculated by the subroutine **Splitting** through diagonalizing the unperturbed Hamiltonian given in Section 5-2. Once the